CHARACTERIZATION OF GRAPHENE OXIDE OBTAINED FROM MODIFICATIONS OF HUMMERS' METHOD AND ITS APPLICATION FOR REINFORCING TEXTILES

Jordi Aixart Forés

UNIVERSITAT ROVIRA i VIRGILI

Characterization of graphene oxide obtained from modifications of Hummers' method and its application for reinforcing textiles

JORDI AIXART FORÉS

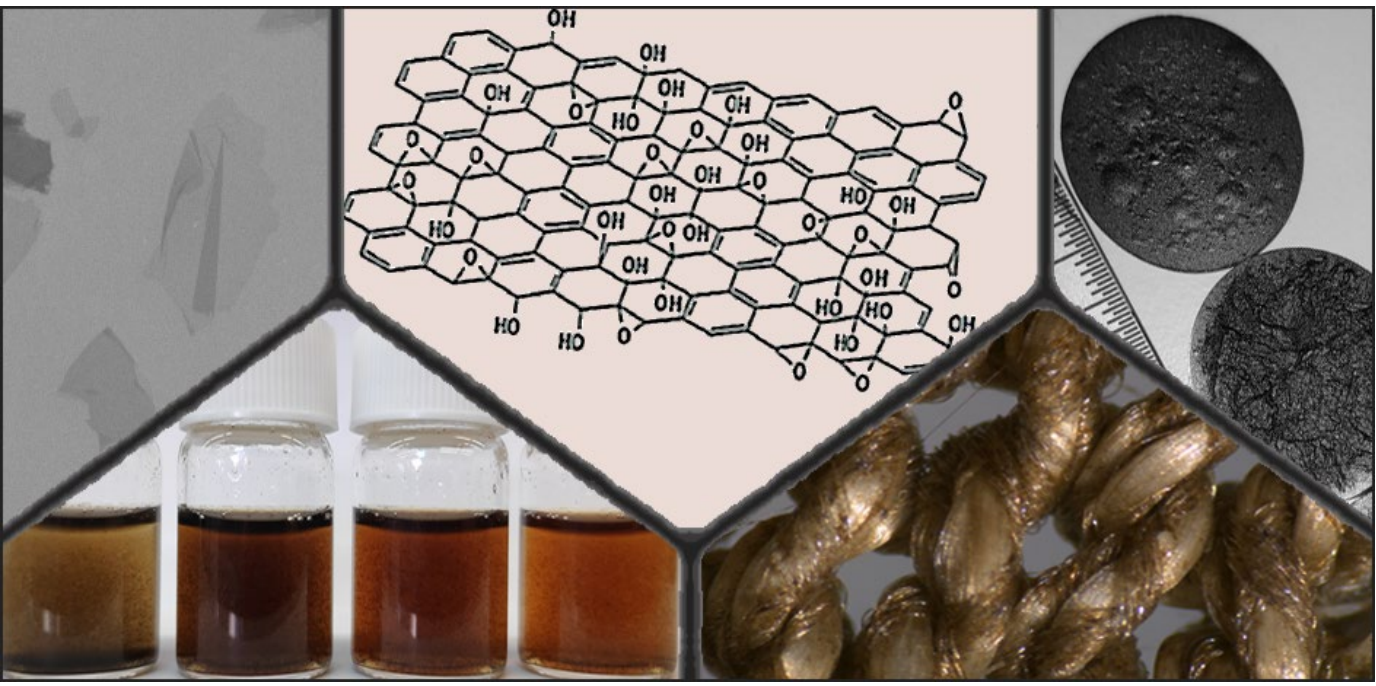

DOCTORAL THESIS
2021

JORDI AIXART FORÉS

Characterization of graphene oxide obtained from modifications of Hummers' method and its application for reinforcing textiles

DOCTORAL THESIS

SUPERVISED BY

Prof. Francesc Díaz
Dr. Joan Rosell-Llompart

Doctoral program in Nanoscience, Materials and Chemical Engineering
Department of Physical and Inorganic Chemistry
Department of Chemical Engineering

UNIVERSITAT ROVIRA i VIRGILI

Tarragona - 2021

UNIVERSITAT ROVIRA I VIRGILI
CHARACTERIZATION OF GRAPHENE OXIDE OBTAINED FROM MODIFICATIONS OF HUMMERS' METHOD AND ITS APPLICATION FOR REINFORCING TEXTILES
Jordi Aixart Forés

UNIVERSITAT ROVIRA i VIRGILI

WE STATE that the present study, entitled “Characterization of graphene oxide obtained from modifications of Hummers’ method and its application for reinforcing textiles.”, presented by Jordi Aixart Forés for the award of the degree of Doctor, has been carried out under our supervision at the Department of Physical and Inorganic Chemistry and the Department of Chemical Engineering of this university.

Tarragona, August 30th, 2021

Doctoral Thesis Supervisors:

Francisco Manuel Díaz González - DNI 33816818X (AUT)
Digitally signed by Francisco Manuel Díaz González - DNI 33816818X (AUT)
Date: 2021.08.30 15:37:12 +02'00'

Prof. Francesc Díaz

Joan Rosell Llompart - DNI 35039930 M (AUT)
Firmado digitalmente por Joan Rosell Llompart - DNI 35039930M (AUT)
Fecha: 2021.08.30 15:29:02 +02'00'

Dr. Joan Rosell-Llompart

UNIVERSITAT ROVIRA I VIRGILI
CHARACTERIZATION OF GRAPHENE OXIDE OBTAINED FROM MODIFICATIONS OF HUMMERS' METHOD AND ITS APPLICATION FOR REINFORCING TEXTILES
Jordi Aixart Forés

ACKNOWLEDGMENTS

I firstly want to thank my supervisors Dr. Joan Rosell and Prof. Quico Díaz for their support and guidance through all these years. Their excellency during this thesis, undoubtably made possible its realization.

The elaboration of this thesis has been a long and tough path, full of ups and downs. For this reason, I must thank my friends and mentors Dr. María Rivero and Dr. Nicolás Coca, whose scientific experience, brilliance, and their excellent advises during my days of despair, have served as a fundamental pillar to the full completion of this thesis. I also want to thank all my office colleagues and important friends Víctor Llamas, Laia Gil, Roger Miró, Ander Eguskiza and Albert Ferriol for their joyful attitude and charming friendship. Also, to my best colleague David Nieto, his radiating happiness has brightened my scientific career since the master's degree.

The work performed in this thesis has been possible thanks to the financial support of Lenard BCN. I want to thank all the people involved in the project: JM, JC, MP, FT, JR, and FD for their contribution, not only in the development of the project but also in educating me in valuable strategies and forms of the company environment.

Also, thanks to my coworkers of Eurecat, FiCMA and DEW: Josep Maria Serres, Nicolette Bakker and Eszter Bodnár, for their countless support always when I needed it.

Finally, thanks to my family and everyone who had trust in me.

UNIVERSITAT ROVIRA I VIRGILI
CHARACTERIZATION OF GRAPHENE OXIDE OBTAINED FROM MODIFICATIONS OF HUMMERS' METHOD AND ITS APPLICATION FOR REINFORCING TEXTILES
Jordi Aixart Forés

PUBLICATIONS

Paper I

J. Aixart, F. Díaz, J. Llorca, J. Rosell-Llompart, Increasing reaction time in Hummers' method towards well exfoliated graphene oxide of low oxidation degree, Ceramics International 47 (2021) 22130–22137. https://doi.org/10.1016/j.ceramint.2021.04.235.

Paper II

J. Aixart, F. Díaz, J. Llorca, J. Rosell-Llompart, The effect of reaction temperature in Hummers' method on graphene oxide's chemistry and morphology and the crucial effect of washing and exfoliating techniques the GO dispersions. (In progress)

UNIVERSITAT ROVIRA I VIRGILI
CHARACTERIZATION OF GRAPHENE OXIDE OBTAINED FROM MODIFICATIONS OF HUMMERS' METHOD AND ITS APPLICATION FOR REINFORCING TEXTILES
Jordi Aixart Forés

CONTENTS

ACRONYMS

AFM - Atomic Force Microscopy

BE - Binding Energy

C/O ratio - Carbon to oxygen ratio

CVD - Chemical Vapor Deposition

DTG - Derivative Thermogravimetric curve

EDS - Energy-dispersive X-ray Spectroscopy

FWHM - Full Width at Half-Maximum

GIC - Graphite Intercalation Compound

GO - Graphene Oxide

HOPG - Highly Oriented Pyrolytic Graphite

HRTEM - High-Resolution Transmission Electron Microscopy

Lc - Column Length

OD - Oxidation Debris

OM - Optical Microscopy

PGO - Pristine Graphite Oxide

ptGO - Post-treated Graphene Oxide

PU - Polyurethane

rGO - Reduced Graphene Oxide

SEM - Scanning Electron Microscopy

SSNMR - Solid State Nuclear Magnetic Resonance

TGA - Thermogravimetric analysis

XPS - X-Ray Photoelectron Spectroscopy

XRD - X-Ray Diffraction

UNIVERSITAT ROVIRA I VIRGILI
CHARACTERIZATION OF GRAPHENE OXIDE OBTAINED FROM MODIFICATIONS OF HUMMERS' METHOD AND ITS APPLICATION FOR REINFORCING TEXTILES
Jordi Aixart Forés

SUMMARY

Graphene Oxide (GO) is a novel nanomaterial related to the well-known graphene. It is often obtained from the chemical oxidation of graphite and consists in graphene layers with different oxygen functionalities. Its popularity lies in the ease of production, scalability, and affinity with water, which facilitates its handling and application. It can be partially reconverted to graphene via chemical reduction, or it can be used as a material itself, as its oxygen functionalities have huge potential in numerous applications.

The most widely used reaction for the obtention of GO is the Hummers method, where graphite is oxidized using strong oxidants in acid media. The result is an aqueous dispersion of GO flakes which contain chemical richness consisting in different functional groups, mainly epoxides, hydroxyls, carbonyls, carboxyls and organosulfates.

GO is a delicate nanomaterial whose chemistry and morphology of the flakes strongly depends on the Hummers' reaction parameters. Surprisingly, it is common to see studies where GO is used in an application without much description of its preparation. This has led to numerous studies about application of GO but also to a clear need for fundamental research on the preparation and characterization of GO.

In this thesis, fundamental studies have been made about Hummers' method and the morphological and chemical characteristics of the GO flakes. Different GOs have been obtained by modifications of reaction time and temperature in Hummers' method. The obtained GOs have been characterized and their different morphological and chemical properties have been described and interpreted. Subsequently, the same GOs were subjected to intense purification procedures and exfoliation, observing that these procedures, commonly used in the literature, have an important effect on the characteristics of the GOs, causing shattering of the GO flakes into smaller pieces while reducing the

chemical richness of the GOs relative to their state prior to the treatments. With our modifications of the Hummers method, GOs with tailorable morphology and chemistry have been obtained.

Finally, this thesis project has been made possible thanks to an industrial R&D collaboration with a technical-textiles company. Some of the main results are, therefore, also described. GO has been applied to textiles to improve their mechanical strength. The large-scale production and application of GO to textiles has been demonstrated using industrial equipment at pilot scale, obtaining fabrics coated with GO with about 50% improved mechanical resistance to puncture.

UNIVERSITAT ROVIRA I VIRGILI
CHARACTERIZATION OF GRAPHENE OXIDE OBTAINED FROM MODIFICATIONS OF HUMMERS' METHOD AND ITS APPLICATION FOR REINFORCING TEXTILES
Jordi Aixart Forés

1 INTRODUCTION

1.1. THE RISE OF GRAPHENE

Graphene is a two-dimensional monolayer of carbon atoms packed into a honeycomb lattice. It is the basic building block for graphitic materials of all other dimensionalities: fullerenes, carbon nanotubes and graphite are other carbon structures that can be built from the graphene honeycomb structure (Figure 1) [1].

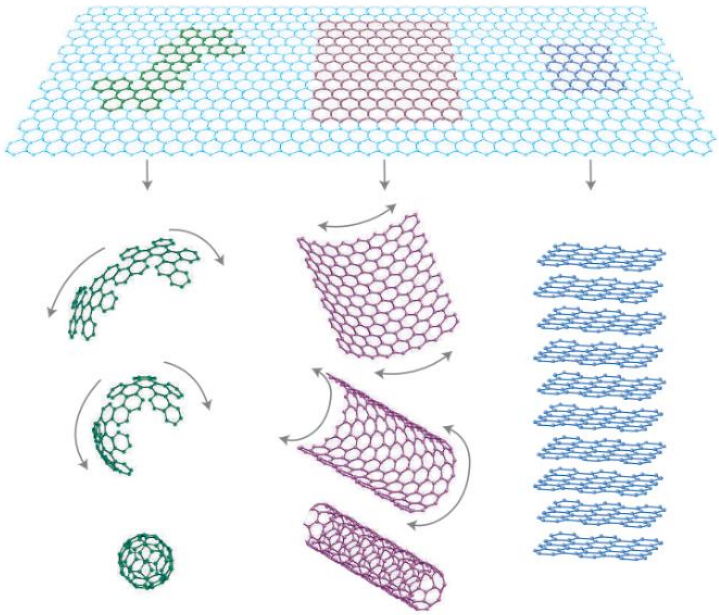

Figure 1: Graphene (top) shown as the 2D building block for carbon materials of other dimensionalities. It can be wrapped to form 0D fullerenes (left), rolled into 1D carbon nanotubes (middle), and stacked to form 3D graphite. Reproduced from [1] with permission from Springer Nature.

Graphene first appeared in the technical literature in 1986 in a publication of Boehm et al. [2], combining the word graphite and the suffix “-ene” which refers to polycyclic aromatic hydrocarbons. Before that, some researchers had found, without being aware, graphene-like structures [3]. But it was in 2004 when Novoselov, Geim, and coworkers reported graphene as a strictly two-dimensional carbon material, with the aim of investigating its electronic properties in transistors [4]. As these authors claimed in their 2007 review “The rise of graphene”, graphene rapidly gained popularity and opened the field of new physics and potential applications of a new class of materials known as two-dimensional (2D) materials, which are characterized by being one atom thick [1]. Attesting to the importance of such contribution, Geim and Novoselov won the Nobel prize in physics in 2010 for their experiments regarding graphene [5].

Among the most popular characteristics of graphene are its mechanical and electronic properties along the plane. With a high Young’s modulus of 0.5 TPa, it has a breaking strength 200 times higher than steel [6]. It also has an unusually high electron mobility of $4 \cdot 10^{-4}$ $cm^2 \cdot V^{-1} \cdot s^{-1}$ at room temperature [7]. A graphene monolayer absorbs a 2.3% of white light [8], being able to be used in optoelectronic applications. For thermal properties, graphene shows a high heat conductivity, around $5 \cdot 10^3$ $W \cdot m^{-1} \cdot K^{-1}$ [9].

1.1.1. Preparation of graphene

Graphene monolayers can be made by three principal methods. The first method proposed was originally reported by Novoselov et al. [4], consisting in micromechanical cleavage, which is also known as the Scotch tape method. The process consists in repeatedly exfoliating carbon sheets from graphite crystals by applying Scotch tape and dissolving the resulting fragments in

acetone. After depositing the dispersion on a substrate, some sheets consist of single carbon-atom layers, namely graphene [10] (Figure 2). The advantage of this “home-made” method is its low cost, but in general, achieving a graphene monolayer with desired dimensions and placement is not possible, as a huge distribution of differently sized particles is obtained [11], in addition of being a slow production, lab-scale methodology.

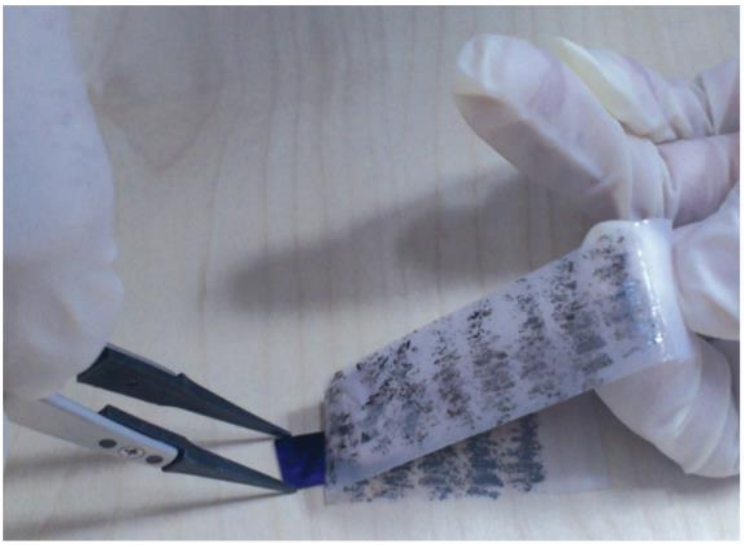

Figure 2: Scotch tape method of graphene synthesis from graphite. Reproduced from [10] *with permission from Springer Nature.*

A second method consist of the direct synthesis of graphene on a silicon carbide (SiC) substrate. Graphene is grown on the silicon or carbon faces of a SiC wafer by sublimating Si atoms and leaving a graphitized surface [12]. Such graphene can have very high quality, with crystallites about hundreds of micrometers in lateral size [13]. The drawbacks of this method are the high cost of SiC wafers and the high temperatures needed to sublimate Si (above 1000 ºC).

A third method consist in the growth of graphene films by chemical vapor deposition (CVD) on copper films [14]. This process typically continues with the transfer of the graphene layer from the copper support to the desired substrate. The transfer method consists in spin-coating poly (methyl methacrylate) (PMMA) on the graphene layer, etching the Cu substrate, placement of the graphene/PMMA on the final substrate, and removal of the PMMA [15]. With the CVD method, square meters of graphene have been already obtained [16]. Despite the high quality of the graphene obtained, this process is still expensive due to high energy consumption and because the Cu foil must be etched. Furthermore, when graphene grows on the Cu foil, it starts depositing on random spots that conjoin as the graphene layers grow, forming islands. The zones where these islands encounter one another tend to disrupt the hexagonal lattice of graphene, producing grain boundary defects, which are "weak" zones where all the properties of the material are hindered [17]. An example high-resolution transmission electron microscopy (HRTEM) image of a grain boundary defect can be observed in Figure 3.

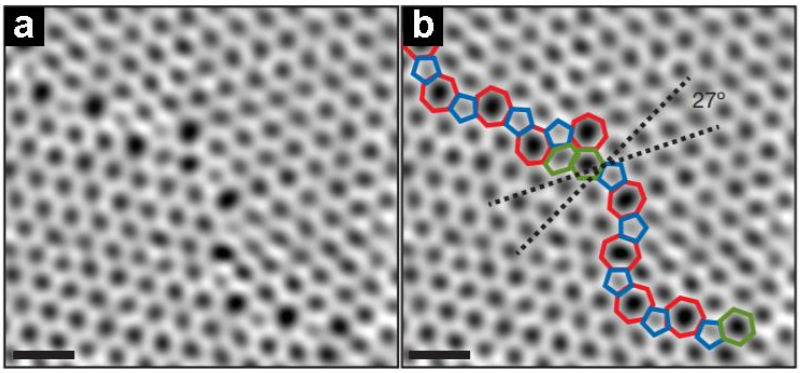

Figure 3: Grain boundary defects of graphene grown on Cu by CVD. a) Original HRTEM image. b) Same image with the non-hexagonal arrangement of carbon atoms shown, with the angles of growth of each layer. The scalebar is 5 Å. Adapted from [17] *with permission from Springer Nature.*

1.1.2. Graphene oxide (GO) and reduced graphene oxide (rGO): quantity over quality

Apart from the three methods described above for producing pristine graphene in relatively high quality, bulk chemistry methods have been developed via a liquid phase exfoliation of graphite, which are capable of yielding much larger quantities of "graphene" with lesser quality [18]. The main method is the *graphite oxide route*, where graphite is oxidized to graphene oxide (GO) in aqueous solution, and then it is reduced to reduced graphene oxide (rGO) [19].

The wet chemical method via the graphite oxide route has been explored to mass produce graphene at the expense of obtaining a graphenic material with less quality [20], [21], [22]. Graphite oxide was known from much earlier than graphene, since the XIX century, when it was obtained by oxidation of graphite [23]. In this method, graphite is initially oxidized in an acidic mixture forming hydrophilic graphite oxide, which possesses large amounts of oxygen-containing functional groups attached onto the basal planes and edges of graphite. Their functionalities make graphite oxide easily exfoliated in solvent (water) to form a stable GO dispersion. GO can be partially reduced to a graphene-like material by removing the oxygen functionalities and recovering the conjugated structure as rGO [24]. In these cases, intensive efforts are usually followed to preserve the properties of the graphitic layers without inducing a large amount of defects, controlling the aggressiveness of the oxidation [25].

The advantages of this liquid-phase production of GO are that the chemical process uses inexpensive graphite as raw material and that the obtained product, hydrophilic GO, can form stable aqueous colloids, facilitating the processability of the material [26]. However, the oxidation of graphite is so aggressive that the obtained GO loses the excellent electronic properties of

graphene, making it an insulator due to the transformation of the planar sp^2-hybridized geometry to distorted sp^3-hybridized geometry [27]. GO must be reduced to restore the aromatic graphene networks, but parts of the structure that had been irreversibly damaged in the oxidation cannot be healed. For this reason, the literature refers to this material as rGO instead of graphene. An image of the process can be seen in Figure 4 where the structure of graphene, GO and rGO are compared [28].

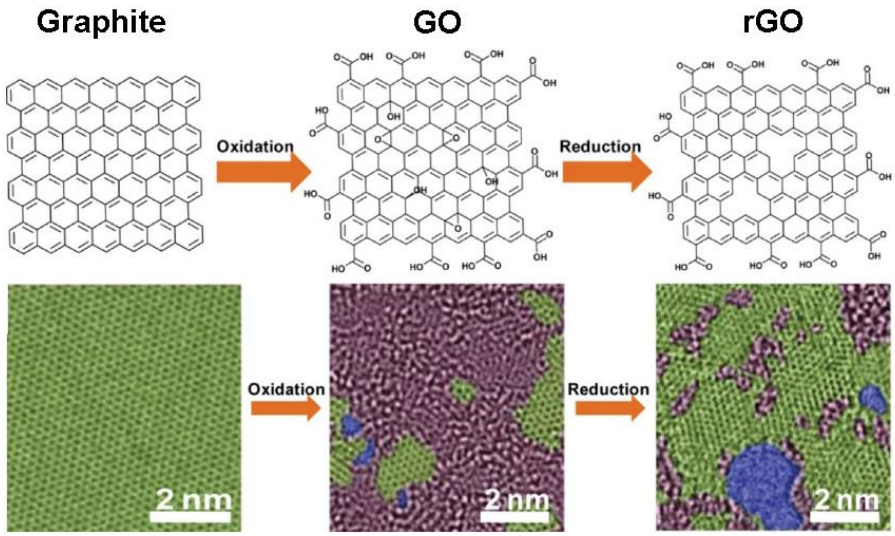

Figure 4: Procedure of oxidation of graphite to GO and reduction to rGO. Above: the changes in the structural models; below: colored HRTEM images showing the atomic structures (from left to right) of graphene, GO and rGO. The green, purple, and blue areas depict sp^2 domains, oxidized domains, and holes, respectively. Adapted from [28] *with permission from Elsevier.*

GO can be reduced chemically and thermally, obtaining products that resemble graphene in different structural degrees, with also different electrical, thermal, and mechanical properties [29], [30]. Among the chemical agents used to reduce GO to rGO, the most widely used is hydrazine (N_2H_4) [31], although the less dangerous and toxic reducers sodium borohydride ($NaBH_4$) [32] and

hydriodic acid (HI) [33] can be used. Electrochemical reduction can be also achieved in a simple electrochemical cell [34]. Between thermal approaches, hydrothermal reduction partially recovers the sp^2 structure while removing functional groups [35]. Thermal annealing under inert atmosphere is also effective in removing the functionalities but it leads to highly defective rGO [36].

It must be noted that, despite graphene's properties worsen when the number of defects in the structure increases, the defective structure is convenient in some applications, for example in fuel cells [37] or in sensor devices [38].

In fact, over the years, even graphene oxide has shown to be particularly interesting as a material itself, in fields where oxygen functionalities in the graphene layer are convenient.

1.1.3. Structure of GO. From the atomic to the micron scale

The actual chemical structure of GO has been in discussion for many years. The incorporation of oxygen into the structure is clear, but the divalent character of oxygen causes it to interact with carbon in multiple ways, being introduced in the carbon grid with the formation of different kind of covalent bonds.

1.1.3.1. The structural models of GO

Back in 1939, the first structural model proposed was by the hand of Hofmann and Holst [39]. In their model, oxygen was inserted in the aromatic basal plane exclusively as epoxide groups, spread over both sides of the plane in a random disposition (Figure 5a). They estimated a net molecular formula of C_2O. In 1946, Ruess extended the structural model of GO with the incorporation of hydroxyl groups into the basal plane, a concept supported by their findings of hydrogen in GO samples (Figure 5b). They also altered the basal plane

structure to a hybrid sp^2-sp^3 system [40]. In 1969, Scholz and Boehm proposed a new model where they removed all epoxides and formulated a regular structure of sequences of plane sp^2 cyclohexanes terminated with ketones and linked by open sp^3 rings decorated with hydroxyls (Figure 5c) [41]. A fourth remarkable model was proposed by Nakajima and Matsuo in 1994, inspired by their X-Ray Diffraction (XRD) results of interlayer distance [42]. They concluded that the main functional group were tertiary alcohols on both sides of the planes, which expanded the interlayer distance upon hydration (Figure 5d).

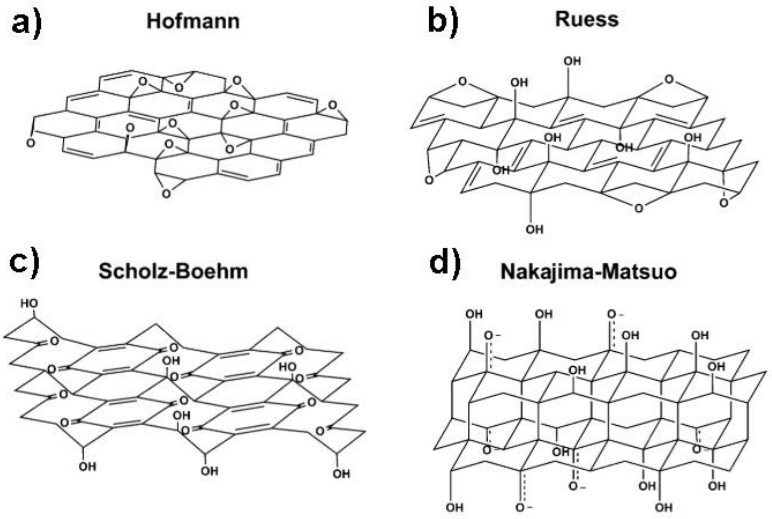

Figure 5: Main models of GO structure of the XX century that have been overcome at present. Adapted from [43] *with permission from Royal Society of Chemistry.*

These models were a good basis to start understanding the chemical functionality and structure of GO, but they err on simplicity and regularity. More recent models rejected regular structures and focused on alternatives based on an amorphous structure combining the functional possibilities of the previously proposed regular structures. It was in this line of thought that the most famous

and accepted structural model until nowadays was proposed by Lerf and Klinowski [44] in 1998 (Figure 6).

Parting from initial studies of characterization of GO using solid state nuclear magnetic resonance (SSNMR) spectroscopy [45], Lerf and Klinowski performed a study using ^{13}C NMR [44] where they observed three signals at 60, 70 and 130 ppm which they attributed to alcohols, epoxides and C=C bonds. In their following paper, based on these findings, they formulated the structure shown in Figure 6.

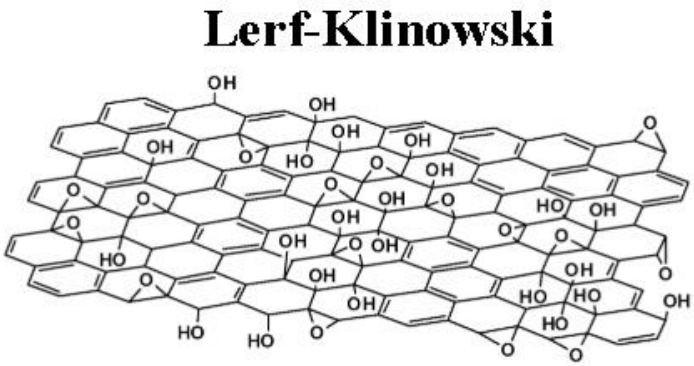

Figure 6: Lerf-Klinowski structural model. Adapted from [43] *with permission from Royal Society of Chemistry.*

Even though the Lerf-Klinowski structural model is nowadays the most widely accepted model for GO, research from the last decade clearly indicates that the real structure of GO differs from this still simplistic model, which does not consider the edges and defects of the aromatic structure and possible C-C cleavage due to over-oxidation. We had to await until 2016 when a new, more realistic structure was proposed by Dimiev and Tour [46]. In the Dimiev-Tour structure (Figure 7), epoxides and tertiary alcohols are also present in both sides of the basal plane. The edges and holes are decorated with ketones and

carboxyls, and there is presence of covalent sulfates. They also considered the presence of graphitic unoxidized domains.

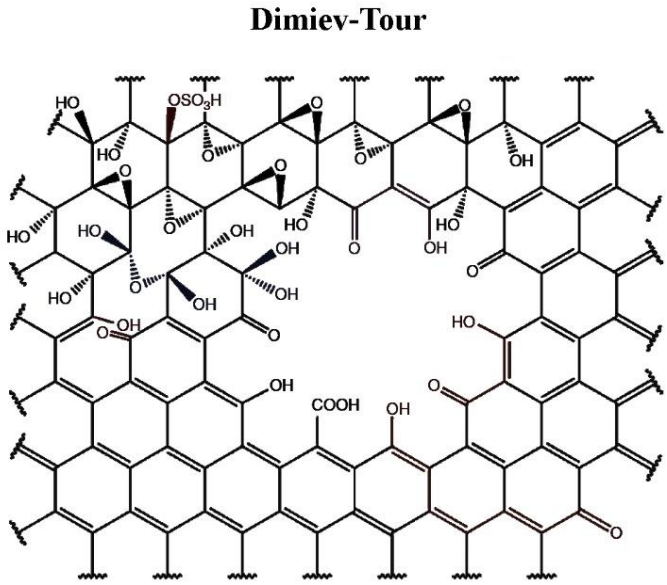

Figure 7: Structure of GO proposed by Dimiev and Tour. Adapted from [46] *with permission from John Wiley and Sons.*

In 2020, Brisebois et al. [47] created a new structural model of GO (Figure 8) considering all the contributions from the previous authors and conclusions of new studies. In their model, they considered all the plausible functional groups that can exist in GO, specifying the degree of oxidation and sulfur content. Thus, this is the clearer structural model to understand the chemical richness of GO from a generic point of view.

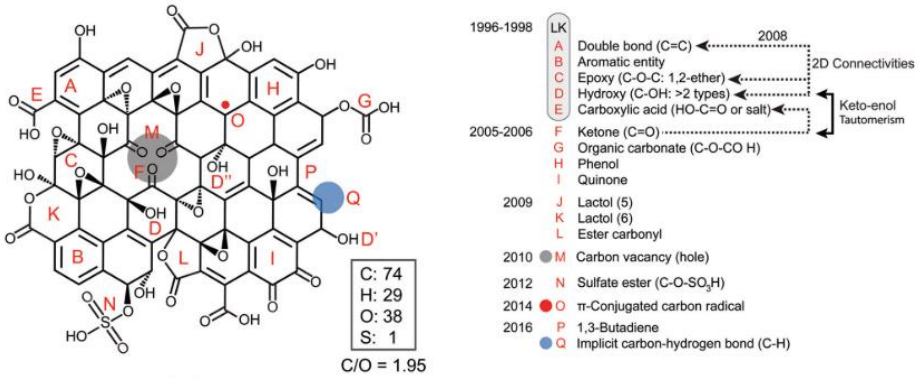

Figure 8: Structural model of a standard GO formulated by Brisebois et al. Adapted from [47] *with permission from Royal Society of Chemistry.*

1.1.3.2. Graphitic domains and holes in the structure

In the structure of graphene oxide, there exists oxygen-free areas called graphitic domains, where the structure of sp^2-hybridized carbon atoms remains in form of islands of pristine graphene. This atomic hierarchy has been observed using HRTEM.

In 2010, the first aberration-corrected HRTEM images of rGO were reported by Gómez-Navarro et al. [48]. In their study, they found areas with clear crystalline graphenic character in form of islands. These images can be observed in Figure 9.

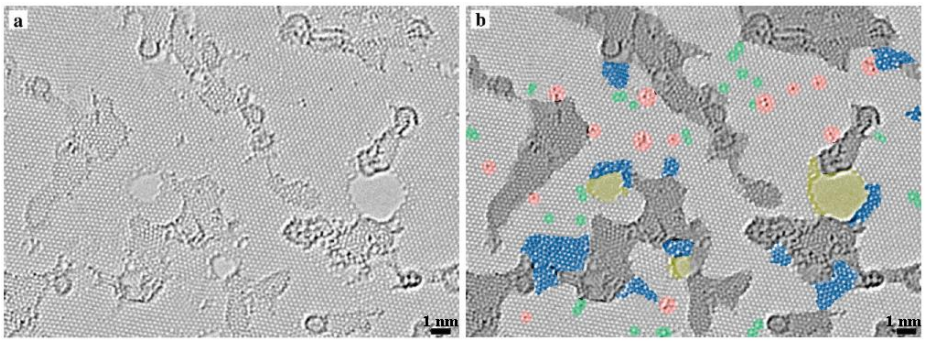

Figure 9: Atomic resolution aberration corrected HRTEM image of rGO. a) Original image. b) With color added highlighting the important features. The original honeycomb graphenic structure is displaying in the original color. Contaminated areas are shaded in dark gray, including oxygen functionalities. Blue regions are disordered carbon networks, identified as remnants of the oxidation-reduction process. Red spots are individual atomic substitutions. Green areas indicate topological defects as single bond rotations or dislocation cores. Holes are colored in yellow. Reproduced from [48] *with permission from American Chemical Society.*

Within these graphenic areas, there exist a visible amount of topology defects, which include oxygen remnant functionalities, disordered carbon networks, atomic substitutions, and permanent damage in form of holes in the structure.

The case of GO, which is more defective, up to 40%, is somewhat more chaotic. In Figure 10, a HRTEM image of a GO monolayer can be observed [49]. In that case, the observed structure had a high fraction of amorphous domain caused by the high amount of oxygen functionalities, with only small islands of intact graphenic domain. In the image, graphitic islands can be identified as the typical honeycomb structure, while the rest of the flake is shown with an amorphous structure. Holes are also generated from permanent destruction of the structure during the oxidation process and generation of CO_2. Dimiev et al. [50] proposed that the observable graphitic domains are not formed during the synthesis but afterwards by the mobility of hydroxyls through the carbon grid, bunching up

together and forming these two separated domains of highly oxidized carbon and pure sp^2 graphitic domains. The mobility of oxygen functional groups was also demonstrated by Kumar et al. in hydrothermally processed GO [51]. The dominance of amorphous domain over graphitic domains determines the electrical insulation of GO, while in the case of rGO where graphitic domains prevail, the electrical conductivity can be as high as for graphite [52].

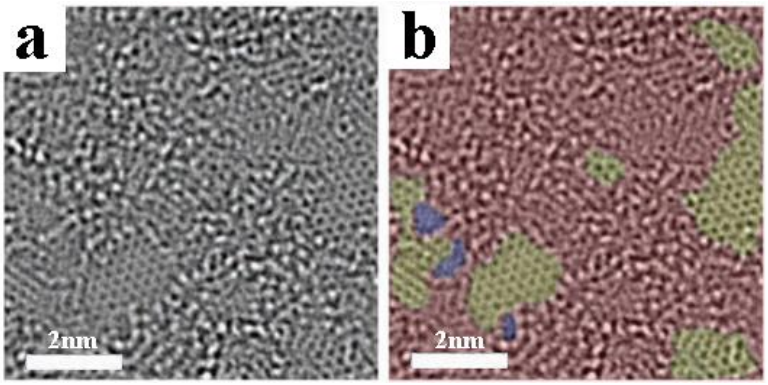

Figure 10: HRTEM image of a GO monolayer. a) Original image. b) The same image colored, being the graphenic areas in yellow, the amorphous oxidized areas in red and holes in blue. Reproduced from [49] *with permission of John Wiley and Sons.*

In conclusion, HRTEM studies of GO have been essential to reveal one of the most important characteristics of GO, namely the coexistence of well oxidized domains and intact graphitic domains, in addition to the possible formation of permanent holes in the structure. In the case of GO, the oxidized domains prevail, reducing the presence of graphitic domains to mere islands. In the case of rGO, part of the graphitic structure is recovered, and the situation reverses, being then when the oxidized domains are reduced to islands and the graphitic structure evolves to a continuous framework.

1.1.3.3. The stacking of GO monolayers

GO monolayers assemble into a layered bulk material after drying. The separation between each layer depends on the intercalants between them, including functional groups, impurities, and water molecules.

In Figure 11a, an example of an atomic structure of multilayered GO with intercalated water molecules is shown, reproduced from [53]. The calculated structure shows how water molecules intercalate between the layers, expanding them. In the same study, the authors calculated the interlayer distance of GOs with different chemical composition (Figure 11b). Their calculations show that the interatomic distance increases with the percentage of water inserted, but that there are no significative differences caused by the functionalization, which have an impact only if the percentage of water is near 0.

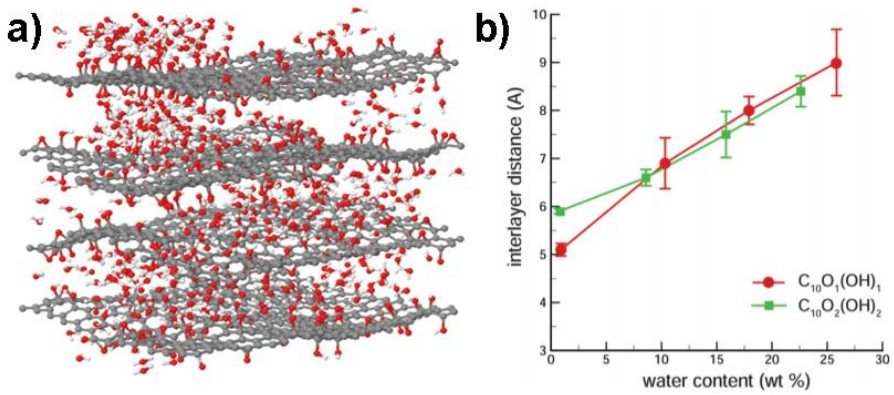

Figure 11: a) Atomic structure of hydrated multilayer GO containing a 25% of water. b) variation of interlayer distance as a function of water content for GO with two different C/O ratios: 1 hydroxyl and 1 epoxide per 10 carbon atoms (red line) and 2 hydroxyls and 2 epoxides per 10 carbon atoms (green line). Adapted from [53] *with permission from American Chemical Society.*

In the Figure 11a, the functional groups added for the calculation are only hydroxyls and epoxides. Today we know that covalently-bound sulfates are part of the structure in most GO samples [46], [47], and that they might contribute importantly to the interlayer distance of GO, adding to the contribution from the other functional groups [54].

We now consider epoxides (C-O-C), hydroxyls (C-OH) and organosulfates (C-OSO_2-O-C) as the functional groups that can be situated on the basal planes of GO. These groups consist in different number of atoms, and they are bound to the carbon grid in different manners. This will lead to each kind of group occupying a different volume in the structure of GO, contributing in different degrees to the interlaminar separation. In Figure 12, a schematic illustration of a graphenic monolayer with the mentioned functional groups is represented, where the lengths of the functional groups have been calculated using the interatomic angles and distances of (i) organosulfates [55], (ii) hydroxyls and (iii) epoxides [56].

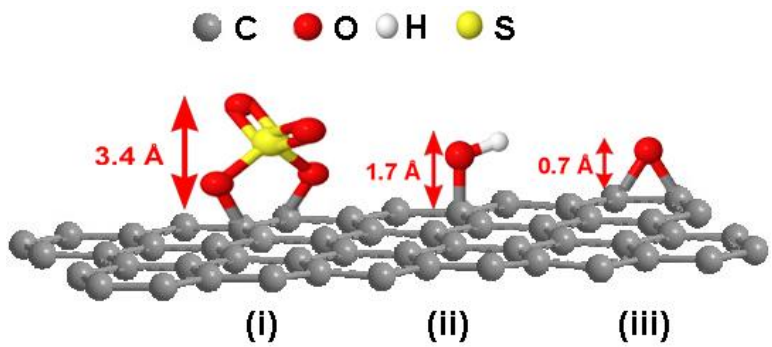

Figure 12: Schematic illustration of the common functional groups found on the basal plane of GO. (i) organosulfates, (ii) hydroxyls and (iii) epoxides are represented with their total length calculated from the graphenic layer.

In Figure 12, Organosulfate groups are the most voluminous, with lengths around 3.4 Å. Hydroxyls follow with a length of 1.7 Å. Epoxides, being the less

voluminous functional group, have a length of 0.7 Å. Recalling that the interlayer distance of most GOs ranges from 7.5 to 12.5 Å, the presence of a high quantity of voluminous organosulfates is relevant. Organosulfates are also able to form hydrogen bonds with water molecules (i.e., retaining them).

Apart from this, the most important factor that determines the interplanar distance between GO monolayers is the amount of water retained in the structure, even in dry samples, due to the hydrophilicity of GO that causes the water molecules to be present in high amount in the structure, forming hydrogen bonds with the negatively charged functional groups present in GO [57]. As H_2O molecules have a kinetic diameter of 2.6 Å [58], their incorporation between the GO layers will have a major impact on the total separation, as total water content in dry GO can be as high as a 25% of its weight (As seen by Thermogravimetric analyses (TGA)).

The combined contribution of the relative presence of the functional groups existent in the basal plane and the retention of water molecules in the structure, which is also reliant in the absolute quantity of functional groups, will determine the interlayer distance between GO planes. Hence, from the interlayer distance of our GOs quantified by XRD, we can have an approximate notion of the oxidation and exfoliation degrees of samples prepared with different conditions.

1.1.3.4. GO monolayers stacked into flakes

GO is usually handled as a dispersion of individual GO particles in water dispersion. This dispersion is usually observed as a distribution of particles with “flake” morphology and different lateral sizes. Despite the theoretical affinity of GO monolayers for water, the flakes have different thicknesses, reflecting different numbers of constituent GO monolayers. Commonly, the flakes have lateral dimensions of tens of microns, and thicknesses ranging from few to

hundreds of nanometers. These dimensions allow an individual GO flake to be easily observable using common microscopy techniques.

In Figure 13a, a GO flake micrograph is shown, as obtained by Atomic Force Microscopy (AFM). The morphology can be well determined, with the inclusion of small wrinkles. In Figure 13b the height profile of the black lines is represented, observing a flake thickness around 2.25 nm. In this case, this would be a single monolayer of GO.

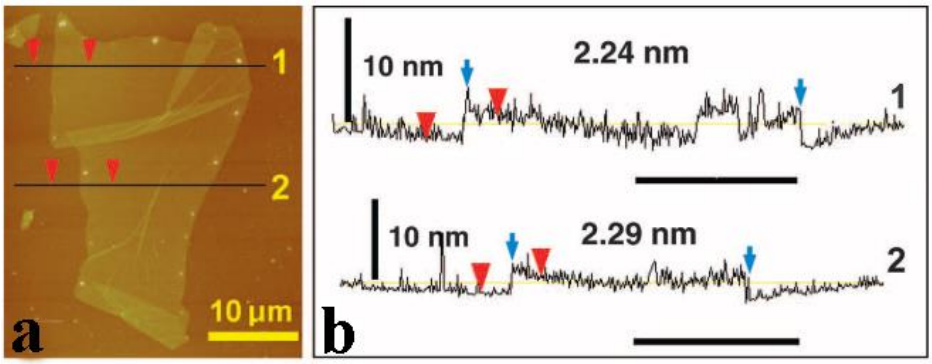

Figure 13: a) AFM image of a GO flake. b) Height profile of the marked lines in a). Reproduced from [59] *with permission from The American Association for the Advancement of Science.*

1.1.4. Properties and applications of GO and rGO

Aside from the ease of preparation of GO, the oxygenated groups are advantageous over graphene in many cases. The higher solubility and the possibility of the functionalization of the surface are some of the characteristics that make GO a promising material. Consequently, GO and rGO have found a place in many and diverse fields, which are summarized in Figure 14 [60].

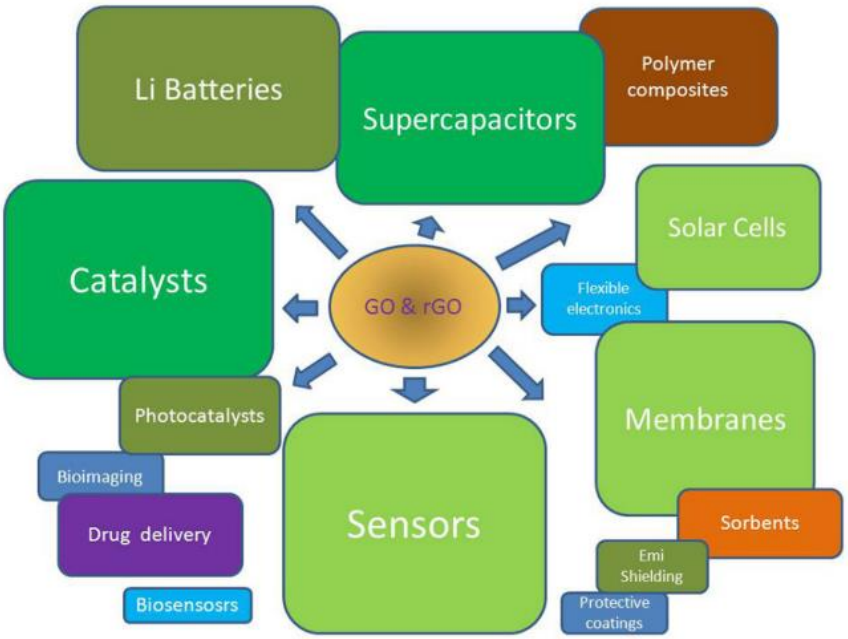

Figure 14: Applications of GO and rGO. Size of blocks gives an estimation of the impact of the number of publications of these materials in the corresponding areas. Reproduced with permission from [60].

The mechanical performance of GO is undoubtably worse than that of graphene. For example, a Young's modulus of 200 GPa has been reported for GO [61], which, although impressive, is still an order of magnitude lower than for graphene (0.5 TPa) [6]. However, GO finds a great opportunity in polymer composites [62], where the crosslinking of the oxygen functional groups between GO and the polymer increases the tensile strength of the resultant composite [63], [64]. Interesting studies have been performed increasing the mechanical properties of polyvinyl alcohol (PVA) [65], polyurethane (PU) [66] and polylactic acid (PLA) [67] using GO as a nanofiller.

The disruption of the sp^2 aromatic structure by the insertion of oxygen inhibits the electrical conductivity of GO, making it electrically resistive (10^{10} Ω/sq) [68]. For this reason, in most electrical applications, rGO is used instead of GO [69].

Thus, in energy applications, supercapacitors [70], lithium ion batteries [71], and stretchable electronics [72] have been designed using rGO.

Thanks to its high transparency combined with good electrical properties, rGO is used in low-cost flexible solar cells to define transparent electron transport layers [73]. They can also be used as photocatalysts when incorporating semiconductor nanocrystals into the structure of chemically modified GO and rGO, enabling reaction pathways [74]. The liquid crystal behavior of concentrated GO is also interesting for functional materials, such as fibers, aerogels and electrodes [75].

The thermal conductivity of GO ranges from 0.5 to 1 $W \cdot m^{-1} \cdot K^{-1}$ making it not ideal for most applications that require good thermal properties [76]. However, it finds a niche in applications where high thermal insulation are sought, like in-home insulation, as part of GO/concrete composites [77] and flame retardants [78].

Membranes is another promising application field for GO. The self-deposition of GO from solutions leads to the formation of uniform papers of GO. Such films have shown permeability for water molecules while retaining other molecules [79], making GO membranes promising candidates to be used in filters for water treatment, with the capability to control the adsorption of organic molecules as a function of the surface chemistry of the GOs [80], [81]. Additionally, when GO solutions are freeze-dried, sponge-like materials with high volume can be obtained, also referred to as aerogels or hydrogels, which exhibit high sorption capacity for oils and different pollutants present in wastewaters [82].

Finally, GO has been used in chemical and biochemical sensors [83]. It can be used to coat plasmonic nanoparticles [84] and being functionalized with proteins, DNA and antibodies [85], reaching unnumerable possibilities in modern nanobiotechnology.

1.1.5. Tuning GO chemistry

Many of the applications for GO rely on the presence of functional groups. Removing oxygen functional groups from GO is one way to modify its chemistry and tune its characteristics for desired applications. Another way is the addition of functional groups to graphene oxide directly by chemical reactions on available (oxygen free) sites [86], [87].

The carboxylic groups often present on the edges of GO layers offer a wide range of possible reactions. The carboxylic group is usually activated by thionyl chloride ($SOCl_2$) [88]. Then, reaction of the acid chloride with amines and alcohols lead to amides [89] and esters [90], respectively, that improved the interactions of GO monolayers with nanoparticles, enhancing their biocompatibility. Reaction with cysteamine, which is a simple molecule with an amine at one end of the carbon chain and a thiol at the other, permits the thiolation of GO [91]. Thiols are known to form strong bonds with gold nanoparticles and surfaces.

Amination results from the reaction of activated hydroxyls (with hydrobromic acid, HBr) with an amine [92]. The resulting GO shows an increase in the electrical conductivity and reduction of the work-function of the material. Aminated GO has also been observed to present less cytotoxicity [93]. The dispersibility in organic solvents can also be tailored with the introduction of amines with different chain length [94].

Strong nucleophiles can react with epoxides causing ring-opening and the addition of a new functional group, for example a hydrazone group [95]. Finally, GO can be non-covalently functionalized with molecules with aromatic parts, i.e., phenyls, that will attach to the hexagonal lattice via π-π stacking [96].

1.2. SYNTHESIS OF GO. PREPARATION METHODS AND MECHANISM OF FORMATION

The first reported synthesis about the oxidation of graphite was presented by Brodie in 1855 [23]. In the Brodie's method, potassium chlorate ($KClO_3$) was used in fuming nitric acid to treat graphite, obtaining a compound that was referred as "graphitic acid". In 1898, Staudenmaier presented a new protocol with the aim of avoiding dangerous reagents and gaseous chlorine-containing by-products [97]. Using exfoliated graphite as a precursor, he maintained $KClO_3$ as oxidant but in a mixture of concentrated nitric and sulfuric acid, and performed the reaction at room temperature. The reaction was faster than the one proposed by Brodie, and Staudenmaier never observed any explosion following his method, which was one of the dangers in Brodie's method.

In the following years, various researchers tried several modifications of these methods in order to obtain less hazardous and more efficient processes [98], [99], [100]. It was in 1957 when the most famous method in the oxidation of graphite appeared, by the hand of Hummers and Offeman [101]. In their work they applied, for the first-time, potassium permanganate ($KMnO_4$) as an oxidant, and they used powdered graphite flakes in an anhydrous mixture of sodium nitrate ($NaNO_3$) diluted in concentrated sulfuric acid. The permanganate was added in portions keeping the temperature below 20 ºC. Then, the temperature was increased to 35 ºC for a reaction time of 30 min. The pasty product was afterwards diluted in water, experiencing a temperature increase to 98 ºC. After 15 minutes more water was added, and the reaction ended with the neutralization of the residual permanganate with hydrogen peroxide (H_2O_2).

As can be imagined, the use of different methods and kinds of oxidants will determine the physical and chemical properties of the GOs [102], [103]. In the early procedures of the GO synthesis, very few differences were observed in the various products [104]. Today, after having reproduced those syntheses,

we know that the produced GOs differ to some extent [105], [106], [107], the main differences being:

- In the Brodie's method, the product obtained would be what is nowadays called a graphite intercalation compound of sulfuric acid (H_2SO_4-GIC), instead of actual GO [108].
- The purification of GOs prepared by Staudenmaier and Hummers methods are tedious. Staudenmaier method presents insoluble $KClO_3$ salts, which are difficult to separate from GO particles. Hummers' method results in a considerable amount of sulfur in the product, demonstrated to be bound covalently to the structure in form of organosulfate [109].
- The chemical composition varies in the GOs obtained by the three methods, but the oxidation degree follows a trend of decreasing C/O ratio in the order Brodie > Staudenmaier > Hummers [107], [110].

Following the timeline of new methods to prepare GO, the next important procedure was presented in 1934 by Thiele [111]. He used electrochemical oxidation of graphite in concentrated sulfuric acid, applying high current density. This method has been further researched and has gained great popularity nowadays [112], [113]. The advantages of this procedure are the avoidance of oxidant impurities (apart from the intercalated sulfuric acid) and a higher control on the oxidation degree of the GO sheets, which is proportional to the current applied [114]. The drawback is a low capacity to oxidize, i.e., the oxidation can be controlled but only a low percentage of oxygen gets incorporated into the structure. For this reason, the procedure is generally slower than the main chemical syntheses [115].

The next innovative contribution in the field of GO syntheses took place much more recently, specifically in 2010, when Marcano et al. [116] published what is probably the most popular modification of Hummers' method. In their synthesis, they excluded $NaNO_3$ from the reagents, they doubled the amount of $KMnO_4$, and they performed the reaction in an acid mixture 9:1 of

H_2SO_4/H_3PO_4. The main advantages of their method are (i) the complete removal of NOx toxic gases generated in Hummers' method and (ii) the yield of a higher fraction of well-oxidized carbon, i.e., less unoxidized graphite particles in the final product. Also, they claim a better conservation of the aromatic structure with less carbon cleavage caused by the oxidation. The main disadvantage is the very high amount of $KMnO_4$ used, with a ratio of 6 g of $KMnO_4$ per 1 g of graphite, doubling the amount used in the original Hummers' method, a change with clear negative economic and environmental repercussions.

Another modern and interesting publication appeared in 2015 when Peng et al. presented a new and environmentally friendly method [117]. In their paper, the original potassium permanganate used in Hummers' method was substituted by potassium ferrate (K_2FeO_4). The particularity of their "green" approach is mainly the avoidance of contaminant manganese residues by the generation of iron sulfates instead, which are much easier to treat and recycle. The quality of their GO was also determined to be as good as that obtained by the other methods. The main drawback of this method is the high cost of K_2FeO_4 in comparison to $KMnO_4$ [118].

Summing up, the growing popularity of GO is stimulating the search for new synthesis approaches and modifications of the existent methods to overcome their limitations and to achieve high scalability and controllable procedures capable of producing large quantities of GO with tailorable chemistry [119].

1.2.1. The Original Hummers' Method

Among the methods just presented, Hummers' method is the most widely used by the scientific community due to the short reaction time and its easiness. Also, this method avoids the generation of hazardous chlorine gases and possible explosions during the reaction.

As mentioned above, Hummers and Offeman reported in 1957 the first successful oxidation of graphite using potassium permanganate in a mixture of concentrated sulfuric acid and sodium nitrate ($NaNO_3$) in anhydrous conditions [101]. Their process started with the stirring of 100 g of graphite powder -325 mesh and 50 g of $NaNO_3$ into 2.3 L of sulfuric acid 93%. This mix was firstly cooled to 0 ºC in an ice bath. Then, under constant stirring, 300 g of potassium permanganate ($KMnO_4$) were added to the suspension, controlling the rate of addition to prevent exceeding 20 ºC. Then, the ice bath was removed, and the temperature of the reaction was brought to 35 ºC, where it was maintained for 30 minutes. At the end of that time, 4.6 L of water were added, causing violent effervescence and an increase of the temperature to 98 ºC. The suspension was maintained at this temperature for 15 minutes, and then it was further diluted with 14 L of water. The reaction ended by the addition of hydrogen peroxide (H_2O_2) to reduce the residual permanganate. Finally, they filtered the obtained graphite oxide, and the solid cake was washed intensively with water.

It is also worth mentioning that the effectiveness of Hummers and Offeman's procedure relays on the small particle size of graphite used [120], [121]. When large-particle-size graphite is oxidized with the same conditions, an incompletely oxidized graphite-GO hybrid is obtained [122]. The reason behind this is the low diffusion rate of the oxidizers into the graphitic interlayer.

1.2.2. Mechanism of oxidation in the oxidation of Graphite to Graphite Oxide

Most of the studies that inquired about the mechanism of formation and the structure of GO have been theoretical until recently. In these studies, the primary aim was to understand how oxygen is introduced in the graphitic lattice and how this affects the honeycomb pristine structure.

We summarize here some important ideas. For example, the cracks on GO flakes which are observable by electron microscope have been attributed to the strain generated by epoxy rings in the graphitic structure [123]. Epoxides are 3-atom member triangular rings that, in general, are highly reactive due to the strain of the bond angles. This scenario will inevitably lead to ring opening in parts of the structure and the consequent loss of aromaticity and the weakening of C-C bonds.

Another interesting study [124] suggested that, in general terms, the graphite source used to produce GO following any of the methods cannot be considered as pure crystalline graphite and the presence of defects and discontinuities in some parts of the graphitic structure and at the edges of the planes must be accepted. These defects will be the starting loci for the oxidation wherefrom the formation of functional groups will propagate to the basal planes.

These studies help to understand the structure of GO and the formation mechanisms. However, they usually consider the precursor to be a single graphene layer, while the reaction occurs to multiple stacked layers in what we know as graphite. In a recent paper Boukhalov et al. [125] demonstrate the significant difference in the oxidation mechanism between single-layer graphene and bulk graphite, considering the formation of CO_2 and the necessary role of water to transform epoxy groups to hydroxyls and to intercalate between the graphitic layers.

The best developed mechanism of formation of graphene oxide from graphite using the reaction conditions of Hummers' method is probably Dimiev et al.'s, as described in various publications [109], [126], [127], [128], [50]. In the following section, their ideas are presented and summarized.

1.2.2.1. The oxidation mechanism in Hummers' method

In the reaction corresponding to the oxidation of graphite to graphene oxide (GO), the following three steps can be identified, after each of which the product can be isolated and observed:

- Step 1: Intercalation of sulfuric acid in the graphite structure, forming a sulfuric acid- Graphite Intercalation Compound (H_2SO_4-GIC).
- Step 2: Conversion of the H_2SO_4-GIC to pristine graphite oxide (PGO).
- Step 3: Conversion of the PGO to GO by the addition of water.

- **Step 1: intercalation of H_2SO_4 in the graphite galleries.**

The first step, the intercalation of sulfuric acid into the graphite structure forming H_2SO_4-GIC, begins immediately after exposure of the graphite to the acidic oxidizing medium. In this step, graphite acquires a characteristic blue color (Figure 15). Ideally, in this stage all the graphene planes in the flake are separated by H_2SO_4 molecules. This H_2SO_4-GIC particle can be separated and observed as in Figure 15. In the micrograph, the blue part corresponds to the unoxidized H_2SO_4-GIC, while the brown edges are already oxidized by the $KMnO_4$.

It is also important to mention that this H_2SO_4-GIC is formed when using any of the known oxidation methods of graphite: the Brodie and Staudenmaier methods involving $KClO_3/H_2SO_4$, the new green approach involving K_2FeO_4/H_2SO_4 [122] and also the electrochemical methods of graphite oxidation in H_2SO_4 [129], [130]. So, the formation of H_2SO_4-GIC is not exclusive to the Hummers' method.

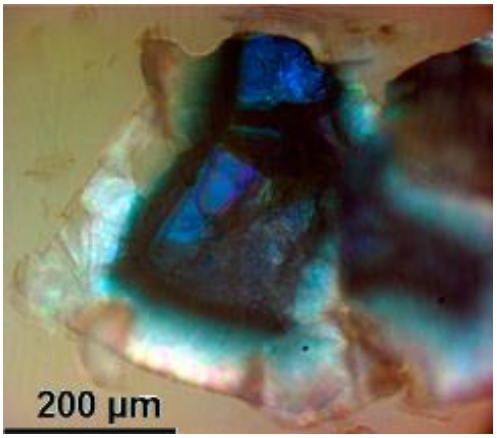

Figure 15: Optical reflection microphotograph of a graphite flake isolated from step 1. Note blue color in the center corresponding to graphite with intercalated H_2SO_4 and brown edges as already oxidized GO. Adapted from [127] *with permission from the American Chemical Society.*

The ability of the acidic oxidizing media to intercalate in graphite is the first necessary condition for the successful oxidation of graphite, which is the second step of the reaction, which starts due the oxidation capability of the MnO_4^- ions.

In this step, $NaNO_3$ plays the role of helping the intercalation of $KMnO_4$ and H_2SO_4, expanding the interlayer distance of the graphitic galleries and permitting a better oxidation of the basal planes [131]. Hummers' method is also possible without $NaNO_3$, leading to GO with similar characteristics [132].

- **Step 2: Oxidation of H_2SO_4-GIC to pristine graphite oxide (PGO).**

This step involves the full insertion of the oxidizing agent into the graphite galleries and the reaction between the oxidizer and the graphite planes.

As shown in Figure 15, the reaction of oxidation occurs from the edges to the center of the flakes, as the characteristic blue color of H_2SO_4-GIC turns into a brownish color corresponding to the stage 2 PGO, indicating this edge-to-center reaction progression.

Regarding the oxidizing agent that acts in this step, we know that permanganate is a necessary compound in Hummers' method, as no GO is obtained with its absence. In the past, there was some debate on which was the actual manganese-related oxidant. Some authors suggested that the oxidizer was manganese heptaoxide (Mn_2O_7) [43] while others argued that the oxidizer could be the permanganyl ion (MnO_3^+) [127]. Both compounds are now believed to be present in the reaction, as shown in Scheme 1. The presence of manganese heptaoxide is easily observable during the reaction as the mixture turns into a green color characteristic of this compound [133].

Scheme 1. Formation of manganese heptaoxide and permanganyl ion.

$$KMnO_4 + 3H_2SO_4 \longrightarrow K^+ + \boldsymbol{MnO_3^+} + H_3O^+ + 3HSO_4^-$$

$$MnO_3^+ + MnO_4^- \longrightarrow \boldsymbol{Mn_2O_7}$$

However, it was recently proposed that the manganese compound does not directly react with H_2SO_4-GIC, and that the incorporation of oxygen to the carbon atoms would in fact be carried by H_2O molecules present in the mixture (as concentrated acid contains a 2-5 %wt of water molecules) [50]. In this view, the true role of the Mn-based species is to accept the electrons generated by the incorporation of water molecules to graphite, creating an electrochemical potential to the acid mixture, but not forming direct bonds with graphite. The proposed oxidation mechanism is shown in Figure 16, where a H_2O molecule is added to a carbon atom (1), forming an oxonium intermediate cation (2) (-OH_2^+). The electronic density moves through the aromatic honeycomb until

finding a Mn(VII) compound that accepts the electron. It is especially important to note that with this mechanism, the Mn(VII) species do not necessary need to be in contact with the water-carbon reactive spot, the electron density can move through the graphenic layer until finding the electron acceptor. Afterwards, the intermediate cation transforms to a hydroxyl via deprotonation (3). The structure can be further oxidized again with another water molecule (4), that ultimately transforms to another hydroxyl (5), forming the first functional group of the oxidation of graphite, the vicinal diols.

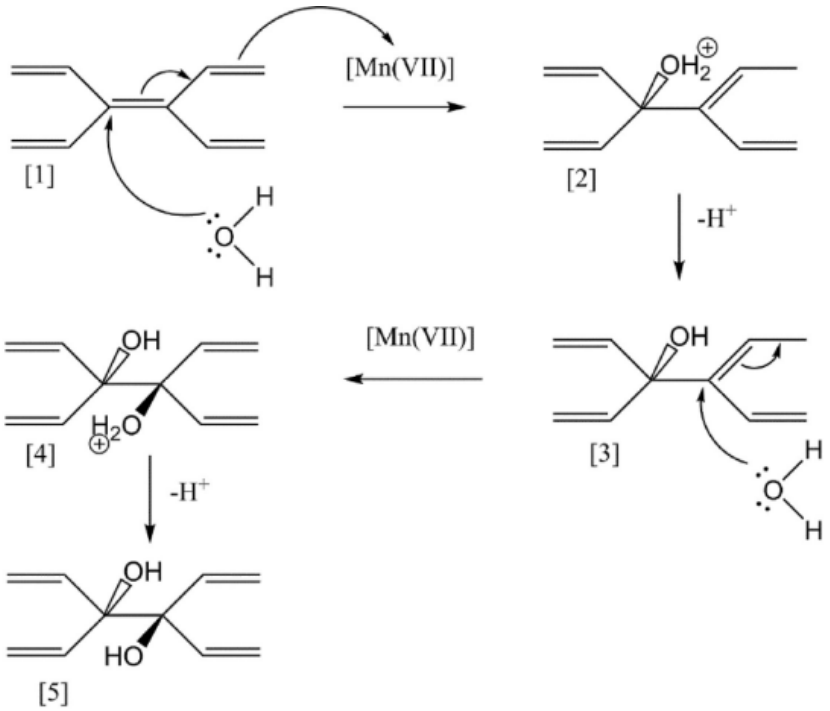

Figure 16: Mechanism of the oxidation of graphite with water molecules, with the Mn-based species accepting electrons from the graphene honeycomb. Reproduced from [50] *with permission from Elsevier.*

The suggestion that the Mn(VII) only acts as an electron acceptor is supported by the fact that GO can be also obtained in electrochemical processes where graphite is dispersed in a sulfuric acid dilution without $KMnO_4$ or other oxidants [129], [130], [134].

Following the reaction chain, the generated diols would transform easily to epoxides and organosulfates:

Epoxides and vicinal diols are well-related functional groups that can reversibly transform one into the other. Taniguchi et al. [135] proposed that the transformation of epoxides to hydroxyls are driven by variation of the pH of the medium. The mechanism of such transformations is shown in Figure 17. An epoxide as attacked by OH^- as a nucleophile in basic conditions (a), leading to the opening of the ring with the insertion of a new oxygen and the attack of the existent O^- to a water molecule (b), this leads to the formation of vicinal diols (c). In acid conditions, vicinal diols can react with a hydronium molecule (H_3O^+) forming an intermediate cation that can abandon the structure in form of a water molecule (f). The remaining hydroxyl reacts with the neighbor carbocation (e) closing the ring (d). The remaining acidic proton will be captured by a water molecule.

It must be pointed that the formation of epoxides from vicinal diols might be promoted by manganese heptaoxide, as several epoxidation organic reactions by this compound have been studied [136], and this would explain why epoxides are the main functional group of GO [109]. Strain caused by new generated tetrahedral sp^3 carbons in a flat sp^2 lattice could also favor the stability of epoxides, as they maintain the flat conformation of the carbon atoms in the graphenic lattice [137], [138].

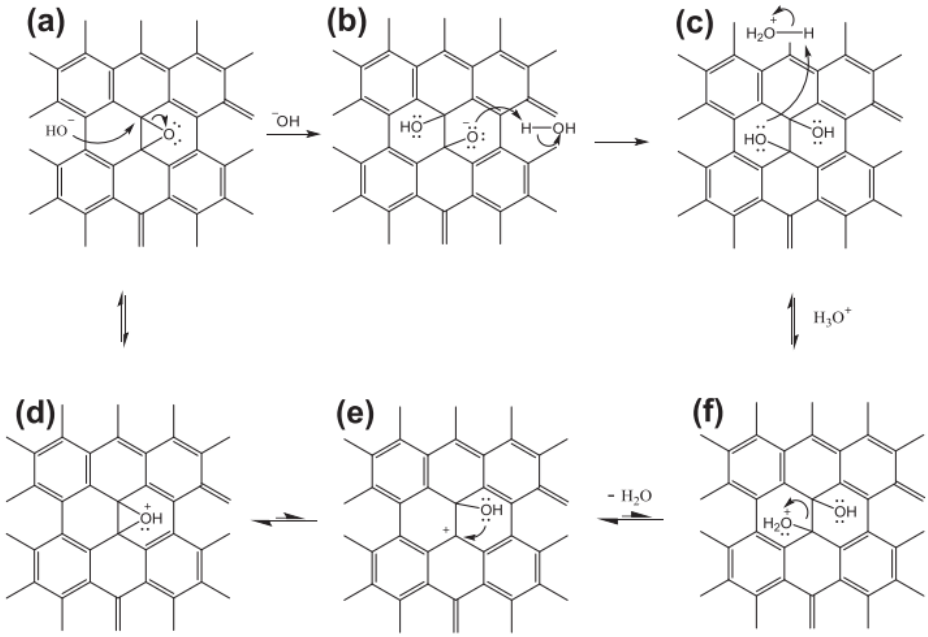

Figure 17: Transformation of epoxides to vicinal diols and vice versa proposed by Taniguchi et al. Reproduced from [135] *with permission from Elsevier.*

Organosulfates can be generated in a parallel route from neighboring epoxides as shown in Figure 18. The transformation of epoxides to organosulfates through ring-opening is thermodynamically favorable [139]. Two neighboring epoxides receive the addition of a molecule of dihydrogen sulfate, while one of the epoxides opens in a typical ring opening reaction, with the formation of a monosulfate (2). The intermediate monosulfate rapidly attacks the adjacent epoxide as a nucleophile, with the formation of a cyclic sulfate, called a covalent sulfate (3). This species is more stable and persists further treatments with water, being still present in the final product. Part of these organosulfates, however, are hydrolyzed upon exposure of GO to water, as organosulfates are also very reactive [140]. Water molecules act as nucleophiles causing a ring opening which is the reverse reaction of the organosulfate formation (4). The hydrolysis continues to the monosulfate generated previously and another nucleophilic attack occurs, with the generation of two vicinal diols (5).

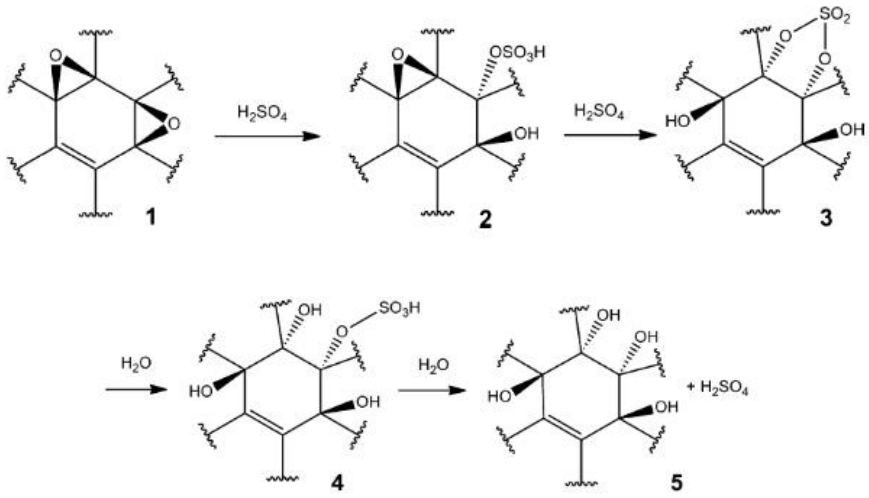

Figure 18: Formation and hydrolysis of organosulfates. Adapted from [46] *with permission from John Wiley and Sons.*

The formation of carbonyls and carboxyls succeeds easily at the edges of the flakes and at any defect that may exist in the aromatic structure [109]. We know that commercial graphite flakes are composed of multiple crystallites that are stacked forming an individual flake [141], [142]. These crystallites will also have crystallographic defects such as grain boundary defects, line defects, or hydrogen-terminated vacancies [143], which will be the first spots to be attacked by the oxidants. However, the ratio of edges and defects to the total aromatic surface is still low, and this is reflected by the limited number of carbonyls and carboxyls observed in the final GO.

However, they can also be formed by the cleavage of epoxides and vicinal diols [138], [144]. A schematic representation of the C-C cleavage with the formation of carbonyls and carboxyls from two neighboring epoxides is shown in Figure 19.

Figure 19: Schematic formation of carbonyls (b) and carboxyls (c) from two neighboring epoxides (a). Reproduced from [144] *with permission from Elsevier.*

Finally, esters and lactols can also be found in GO, due to transformations of carboxylic acids with separated hydroxyls in the case of esters (Figure 20a) and from carbonyls and internal hydroxyls in the case of lactols (Figure 20b).

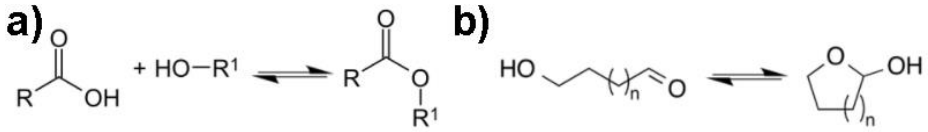

Figure 20: General reactions for the formation of a) esters and b) lactols. Images adapted from Wikipedia.

- **Step 3: delamination of Pristine Graphite Oxide (PGO) to Graphene Oxide (GO) and termination with H_2O_2.**

Until this step, the reaction conditions were maintained anhydrous with some degree of water present in the sulfuric acid. At this point, pristine graphene oxide (PGO) would have a characteristic chemical composition mainly based in epoxides and organosulfates covalently bounded to the structure [109], [145]. These functional groups undergo extensive transformation upon exposure to water [146].

When PGO is exposed to water, the chemical composition of the as-synthesized material transforms radically, as water has a nucleophilic character that attacks electrophilic centers in the structure. Then, all the reactions shown in step 2, which occurred in a low degree in that stage develop heavily, with the development of all the functional groups and resulting in the chemical richness of GO. The functional group formation is accompanied by the self-exfoliation of the GO layers [124] into GO flakes.

H_2O_2 is used in the termination of the reaction by reducing the remaining permanganate thus stopping its oxidating power. However, it was recently demonstrated that the addition of H_2O_2 also affects the chemistry of GO [147], as it reduces the oxo-functional groups of GO, obtaining lesser oxidation degree in samples where much H_2O_2 was used to neutralize the reaction, while a higher chemical richness when the addition of H_2O_2 was avoided.

1.2.3. Generation of small polycyclic molecules: One- and Two-Component Structural Model

The two-component structural model of GO proposed in 2011 by Rourke et al. [148] has enjoyed huge popularity. According to the model, the GO generated in the oxidation reaction of graphite would consist in two kinds of specimens: (i) slightly oxidized graphite oxide and (ii) small polycyclic organic molecules. These small polycyclic molecules would be adsorbed on the surface of graphite oxide. In Rourke et al.'s publication, the small molecules are named "oxidation debris" (OD). This term has gained considerable notoriety in the technical literature. The OD would be adsorbed onto the GO surface and would be stable in water. The desorption could be achieved by the addition of a strong base and the increase of the pH. It was in these conditions where the authors observed and characterized these small polycyclic molecules. A representation of the two-component structural model proposed by Rourke is shown in Figure 21.

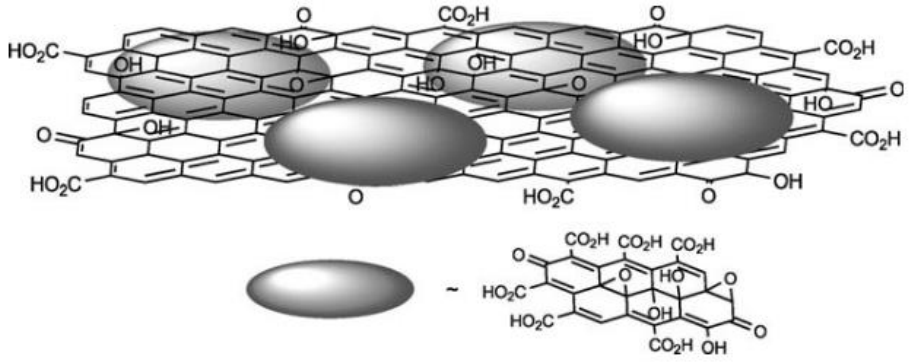

Figure 21: Representation of the two-component structural model of Rourke. GO would consist in a mildly oxidized graphene layer covered by highly oxidized and relatively small molecules: the oxidative debris. Reproduced from [148] *with permission from John Wiley and Sons.*

After that study, several research groups used this model to explain their conclusions about properties observed on GO. For example, the model has been used to exclusively explain its fluorescence [149] and electrochemical properties [150]. Some authors performed interesting studies about the formation and control of the OD [151], [152], which seems to strengthen this theory.

However, Dimiev et al. questioned this model in 2015 with a counter-study pointing out its incongruences [128]. In Dimiev's paper, the presence of OD under basic conditions is attributed to an actual disintegration of a single GO layer due to strong nucleophilic attacks caused by OH^- ions, which has been confirmed by studies where base-washed GO caused its cleavage [153], [154].

Rourke et al. responded to Dimiev et al.'s criticisms by arguing in favor to the two-component structural model principles [155]. The debate is still ongoing, with division between authors that consider GO as a unique and fragile structure that tends to cleave into smaller pieces (one-component structural

model) [156], [157] and authors that consider GO as a mildly oxidized structure covered with detachable oxidation debris (two-component structural model) [158], [159].

1.2.4. Purification of Graphite Oxide and washing procedures

In the large-scale production of GO, the synthesis itself is not the most critical step. The bottleneck is in the purification steps that follow the reaction. Purification of GO is performed by several washing procedures in water to remove the acids and heavy metals impurities. Also, when washed, GO product exfoliates into thinner sheets forming a very stable colloidal solution [160]. This adds more difficulties to the purification protocols as small GO sheets do not sediment and tend to clog the pores of filters.

Principal routes of purification were established in the early days of GO preparation [101]. The purification step always starts with a dilution of the acids present in the mixture using large quantities of water.

After the dilution step, sedimentation-decantation cycles are the easiest method to separate GO from the contaminants remaining from the reaction. After each cycle, as the pH of the medium increases, the affinity of GO with water increases [161] and the time for sedimentation lasts longer. The reason is the high negative charge present in the GO sheets due to its oxygen functional groups [20], [162]. This negative electrostatic charge present in GO sheets facilitates their dispersion due to the interaction with water molecules, but at the same time, when the pH decreases or impurity ions still exist in the dispersion, the affinity for water lessens, the dispersibility of GO decreases, and the sedimentation is shortened. In order to accelerate the process, HCl is usually used to wash GO as it reduces the pH and facilitates its sedimentation [163]. HCl has been the substance of choice for this aim due to the easiness of its

washing afterwards and the monitoring of its concentration through pH measurement.

Purification processes usually repeat some dilution/sedimentation cycles until the nearly complete removal of reagent impurities. Then, GO is further washed by filtration [164], centrifugation [165] or dialysis [166] to remove the HCl and obtain pure GO in water.

Both centrifugation and dialysis may be adequate to purify small amounts of GO. In the case of centrifugation, high centrifugation speeds or times are needed, not suitable for processing large batches of GOs. Also, many cycles of centrifuging-redispersing are needed to fully wash GO, wasting a lot of water. Moreover, in every centrifugation step, undeposited GO flakes, presumably with the highest oxidation and exfoliation degrees, are inevitably lost in the discarded water [167]. Dialysis, on the other hand, has the drawback of being very slow, usually taking weeks to effectively remove all the ions, with the constant need to change the water used.

Filtration can usually be accomplished in less time. After the washing of the reagent impurities with HCl, dead-end filtration or crossflow filtration can be used [164], [168]. In dead-end filtration, the water flows through a filter, whereas in crossflow filtration, the solution flows parallel to the filter. Vacuum-assisted filtration can also be used, but, at high concentrations, the filter cake gelates in water and rapidly blocks the flow of solvent through the filter [169].

1.3. THE IMPORTANCE OF CONTROLLING GO REACTION PROCEDURES

1.3.1. Needs in GO research

Interest in GO arose from the discovery of graphene, and its growing popularity is clearly reflected by the number of scientific contributions that have been published in the last decade and a half. Figure 22 displays the number of publications resulting from searching by "Graphene Oxide" in Scopus. Since 2006, when the first article was published, the number of entries has grown exponentially at the beginning, and is still growing nowadays.

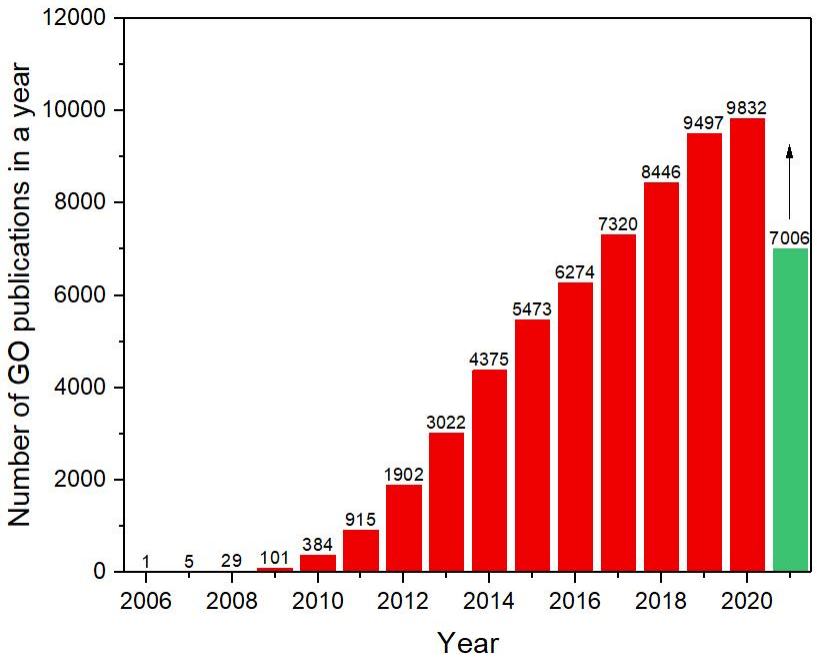

Figure 22: Number of GO publications in a year, as obtained by searching "Graphene Oxide" in Scopus. Data consulted on 22-08-2021.

For a trendy scientific topic, great number of contributions comes inevitably with a rush by authors wanting to produce an original study and be the first publish it. For GO, this rush is visible in publications where the authors apply GO in some uncommon applications, but often ignore the characterization of the material.

It is common to read in the technical literature that the GO *"has been prepared by a modification of Hummer's method"* or purchased from somewhere. In these cases, important information about the synthesis conditions is typically neglected. Many authors find an extravagant application and compare the properties of their material by varying typical parameters such as GO concentration or the application methodology. For example, we can find articles where GO has been applied as a nanofiller to a polymer used in the aerospace industry [170], in ocular regenerative medicine [171] or in protective facial masks against Covid-19 [172]. But they use a generic GO with unknown chemical characteristics. This raises questions such as: How can someone be sure that the GO they will prepare in their lab can accomplish the same or similar results? And how can someone get better results if they control the parameters which they did not?

In the previous sections, we concluded that GO is a compound with very complex chemical behavior. There exist different ways to obtain it from graphite: it can be oxidized chemically using different reagents or electrochemically using different voltages. The result is a graphitic material with oxygen bound covalently. In this form, the C/O ratio is commonly reported to have an approximate measure of the degree of oxidation of the graphite. However, each GO has at least four main functional groups: epoxides, hydroxyls, carbonyls and carboxyls, whose relative abundances can undoubtably vary in each reaction step.

We would be lucky if the variability of GO ended here. However, after performing the reaction, GO must be purified. Quenching with water is the most common way to do it, but as-synthesized GO also reacts with water. After the

purification, we obtain graphite oxide of different sizes, which must be exfoliated. Exfoliating the graphite oxide in water can be done through different methods, from shaking manually a vial containing it or by sonicating it. The method used shatters GO into small pieces to an extent which depends on the method used. Finally, GO is also pH sensitive, and their dispersions are metastable, so it degrades over time at ambient temperature. Storage conditions and time can therefore also play a role on the composition and chemical makeup of the GO.

In sum, it is unreasonable to use GO in a research study without giving details about the reaction, purification procedures, as well as post-treatments. Buying commercial solid GO may be correct in terms of reproducibility. However, considering that solid GO is the coarsest kind of GO, as it must be intensely sonicated to be redispersed, better results could be obtained by opting for synthesizing it by oneself. The widespread synthesis of GO therefore also justifies the careful study of the reaction parameters, as well as their safety margins.

1.3.2. The parameters to control in Hummers' method

1.3.2.1. Graphite sources

In Hummers' method, the common graphite size used is -325 mesh, which corresponds to sieved particles of less than 44 µm [173]. This size of graphite flakes was already used by Hummers et al. [101]. However, this procedure (using graphite with common graphite sizes) leads to large amounts of unreacted graphite, due to the slow penetrability of the oxidants [122].

Graphite -100 mesh (less than 150 µm particle size) and -2000 mesh (less than 6.5 µm particle size) were later used in Hummers' method, resulting in an

important variability of the oxidation degree, and C/O ratios of 2.70 and 1.67, respectively [174]. Graphite powders with the same size but different crystallinity also leads of GO with different oxidation degree [175], [176].

Expanded graphite, which is a thermally treated graphite that has an increased interlayer distance, has also been used in Hummers' method to facilitate the intercalation of the oxidizers [177], obtaining a higher oxidation degree and the total reaction of graphite to GO. Highly Oriented Pyrolytic Graphite (HOPG), which is the kind of graphite with larger monocrystalline graphene layers, can be used to obtain large monolayers of GO with mild oxidation [178]. GO has been also synthesized from graphite waste produced by the diamond industry [179] and from graphitized coconut shell [180], obtaining GO in both cases.

Despite not being a graphite source, it is also possible to perform the oxidation reaction to dried GO [181]. The result is a GO with a higher oxidation degree after each repetition until the total oxidation of the carbon structure to CO_2.

In conclusion, GO can be fabricated from all graphitized sources, obtaining a material that fits in the definition of GO, although, at the same time, small variations in the characteristics of the graphite source often leads to GO with differentiable properties such as oxidation degree.

1.3.2.2. Parameters that control the degree of oxidation of graphite to GO: time, temperature, and concentration of oxidizers

The main parameters usually varied in Hummers' method are reaction time, temperature, and concentration of the oxidizers (grams of $KMnO_4$ and $NaNO_3$ per gram of graphite). These parameters can be varied to obtain GOs with different degree of oxidation [182], [183], [184]. The effect of increasing time, temperature, and concentration of oxidizers lead, in general, to a higher reactivity. Therefore, combining them can be of special interest to accurately

tailor the chemistry of GO product. In several publications, these three parameters have been studied, together or separately, providing details about the GO product obtained in each case [182], [183], [184].

Reaction temperature is by far the most widely studied parameter [19], [185], [186], where higher reaction temperatures result in a higher degree of oxidation. It was already shown by Charpy in 1909 [99] that the oxidation of graphite can easily lead to over-oxidation, observing a higher weight loss when the temperature of the reaction increased. At room temperature, graphite was oxidized to GO with almost no weight loss. At 45 ºC, a small amount of graphite was lost in form of CO_2 [134], but at 100 ºC almost 50% of graphite was converted into CO_2. He also observed that the weight loss at high temperatures could be controlled by limiting the amount of $KMnO_4$ used in the reaction.

It has also been shown that increasing reaction time at a given temperature also favors the oxidation of graphite to GO. Formation of CO_2 has been detected during the reaction whatever the reaction time is [187], provided a high enough amount of oxidizers is present [188]. By controlling the amount of oxidizers, the oxidation of graphite is limited to a certain point regardless the increase of reaction time. This behavior was observed by Hontoria-Lucas et al. [189]. In their work, using Staudenmayer's method, performing the reaction during 240 h they found a ceiling of the oxidation at 120 h of reaction, with no further evolution of the elemental composition after that time.

Apart from the C/O ratio, controlling the above-mentioned reaction parameters may also affect the morphology of the GO flakes. It has been reported that prolonged oxidation breaks GO flakes into smaller pieces [190]. The same happens when increasing reaction temperature, where small increments in the reaction temperature lead to a greater exfoliation of the flakes [191]. The reason in both cases may be the more effective intercalation of the oxidizers and the formation of new functionalities on the basal planes of the GOs [124], forming more hydrophilic spots, increasing the negative potential of the surface of the

monolayers [192] and favoring their spontaneous separation in water dispersions.

The chemistry of the GOs can be also controlled with these parameters. Maintaining a low temperature in all the reaction steps favors the formation of first-stage functional groups, which are epoxides (C-O-C) and organosulfates (C-O-SO_3) [192], [185], which are reactive and can develop into hydroxyls (C-OH). The organosulfates are known to be easily hydrolyzed by nucleophilic attack of water molecules at high temperatures [193], [145] (being totally hydrolyzed at 98º C). Carboxylic acids (O-C-OH) tend to easily decompose at high temperatures forming CO_2 [194], [195]. However, in some studies, a higher content of carboxyls have been found when the temperature of the reaction was increased [181], [185], [196]. On the other hand, Epoxides may transform to hydroxyls in acidic medium via ring-opening, favored by high temperatures [197], [195], [135].

In conclusion, reaction time and temperature are the key parameters to obtain GO with controllable degree of oxidation. The content of oxidizers only play a role as a limiting reagent, as the oxidation stops when they are totally consumed [187], [189].

1.3.2.3. Purification

GO is usually purified using water, with firstly increases the temperature of the acidic mix. Reaching high temperatures due to the addition of water also the chemistry of the obtained GO, causing the hydrolysis of epoxides and sulfonates to carboxylic acids [197].

The chemistry modification of GO can be observed during the washing steps, as GO has a bright-yellow color initially, which darkens and evolves to a brownish black under prolonged exposure of water in the washing procedures.

The color change also matches with the neutralization of the acidity of the reaction media.

Using other solvents for purification also have an important effect on the final chemistry of GO [109]. GOs washed with organic solvents such as methanol or trifluoroacetic acid had a higher content of epoxides and sulfonates, indicating that water used on washing perform a nucleophilic attack to some of these groups.

A total purification of GO without degradation of its chemistry is one of the major challenges of the production of reasonably high quantities of GO. Several methods exist but the 2D nature of the GO particles hinders all these methods in some way.

1.3.2.4. Post-treatments

After the purification procedures of GO, the obtained product is accurately known as graphite oxide, with the oxidized monolayers still stacked into large particles. To exfoliate these particles to monolayered graphene oxide, the most common methods performed in laboratory involve strong stirring [198], [199], [200], separation of the non-exfoliated particles by centrifugation [116], [201], or sonication [202], [203], [204]. Exfoliation is an important step to obtain GO flakes with the desired size characteristics [205], [206].

When sonication is applied, not only it succeeds at exfoliating the graphite oxide to GO, it also breaks large surface particles into smaller fragments [207], [208], [209]. The main explanation about why GO flakes break under sonication is that the large flakes obtained after the reaction have weak spots, possibly characterized by high concentration of functional groups, that are susceptible to be mechanically broken [210], [211], [212]. An image of the possible process is shown in Figure 23, where the cleavage of a chain of oxo-functional groups

is proposed due to hydrothermal treatment. Mechanical cleavage during sonication could act in the same manner.

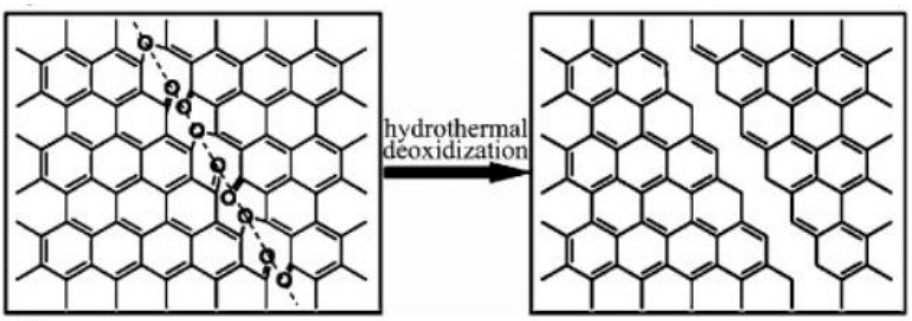

Figure 23: Cleavage of the oxidized spots on GO due to hydrothermal deoxidation. Mechanical cleavage could happen in the same way. Reproduced from [210] *with permission from John Wiley and Sons.*

The GO particles' size influenced the mechanical properties of GO bulk structures made of assembled dispositions of the flakes [207], [208], [213]. The consensus is that large GO flakes are better in properties than small GO flakes if they are exfoliated. Therefore, when undertaking mechanical exfoliation of graphite oxide for a particular application, the effect of time and power on the fragmentation of the GO particles into smaller pieces should be considered. Other side-effects must be considered when selecting the exfoliation protocol. For example, ultrasonic exfoliation not only cleaves GO into smaller particles, but also affects the chemistry of the obtained GO [214], degrading the less stable functional groups.

1.3.2.5. pH stability

The pK_a values calculated for GO dispersions varies from 2.0 to 4.0, depending on their oxidation degree. These values indicate that GO is a stronger acid than

most of the typical molecules with one carboxylic acid [215]. The origin of this high acidity may be conjugated hydroxyls and phenols, that can delocalize negative charges and stabilize the carboxylate ion [216].

However, the characteristic acidity of GO goes beyond simple pK_a values. One interesting study [126] was carried by performing titrations with additions of NaOH and reversing the titration by adding HCl after different times. The results are shown in Figure 24. In Figure 24a NaOH is added to the dispersion of GO until reaching a pH=10 (black line). Then, immediately, the reverse titration with HCl is performed (red line), reversing the equilibrium. Figure 24b, however, the same addition of NaOH is carried on, but the dispersion is let rest 6h before reversing the pH. The result is that less amount of acid is needed, indicating that the titration started with less pH; therefore, GO much have generated H^+ during the rest time. The effect is increased in Figure 24c where the addition of HCl started after 15h and heating the dispersion at 60 ºC. In that case, the GO structure auto-generated many H^+ to acidify the pH of the dispersion from 10 to 8. In Figure 24d, this decrease of the pH as a function of time is depicted.

Then, it has been demonstrated that in aqueous solutions, there is an acidification kinetics of GO associated to a chemical reaction, suggesting that H^+ are generated in basic conditions.

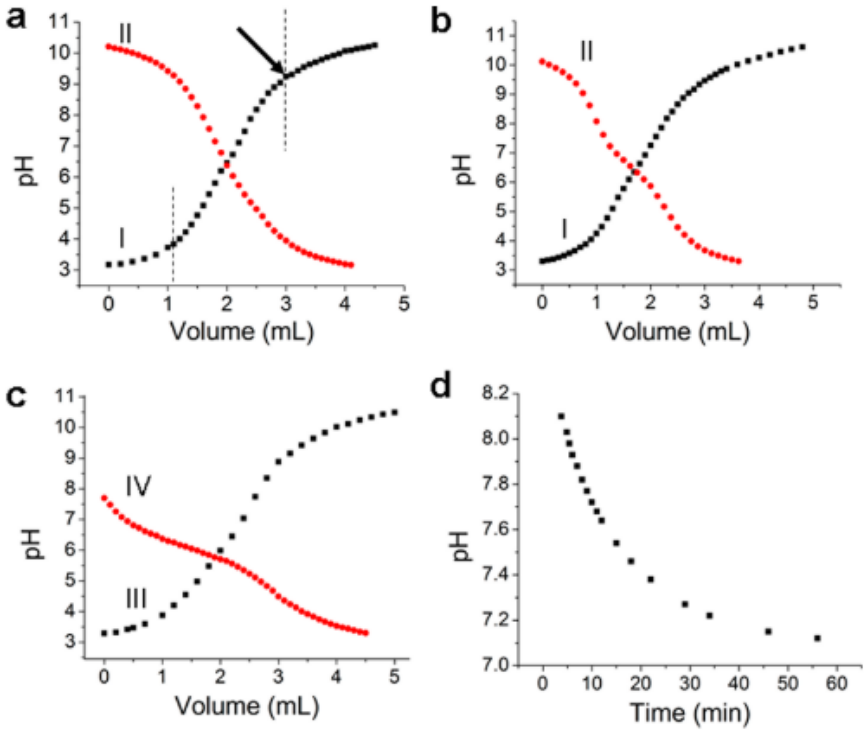

Figure 24: Titration of GO curves. Black lines in a-c represent the forward addition of NaOH. Red lines represent the reverse titration, by adding HCl. In a) the reverse titration was performed immediately after the addition of NaOH, in b) after 6 h and in c) after 15h heating at 60 ºC. d) The change in pH of GO with time after the addition of NaOH. Reproduced from [126] *with permission from American Chemical Society.*

The functional groups responsible of the H^+ generation could be the vicinal diols, which undergo irreversible transformations generating H_3O^+ because of a nucleophilic attack of the hydroxide anions to tertiary alcohols [126]. The acidity of alcohols is caused by the stability of the conjugate base due to the delocalization of the negative charge over the area of a graphitic domain.

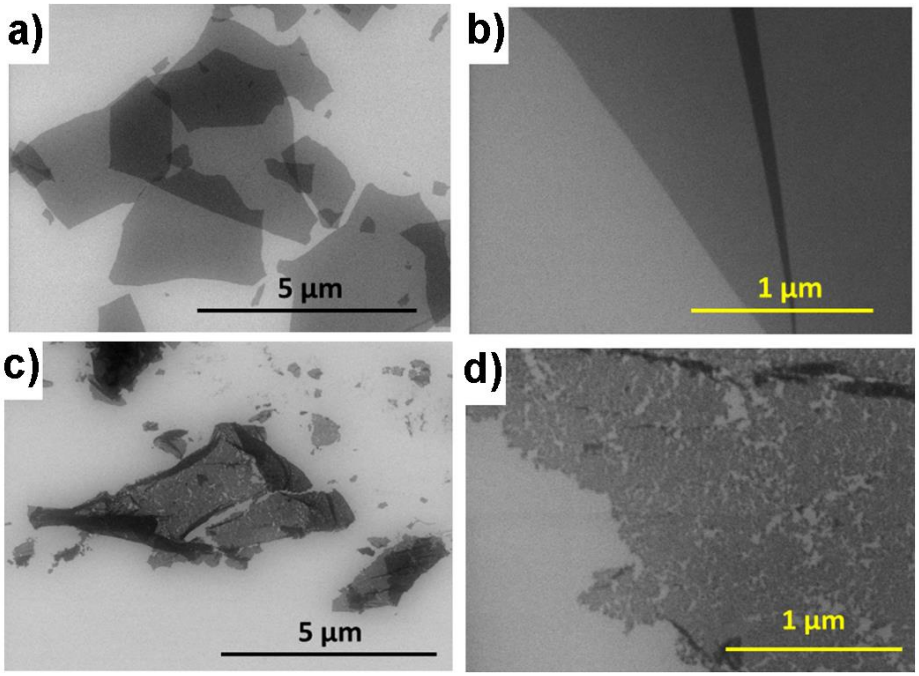

Figure 25: SEM images of GO flakes. a) and b) are pristine GO flakes, showing smooth edges. c) and d) are GO flakes treated with NaOH, where the disintegration driven by the strong-base treatment can be observed. Reproduced from [128] *with permission from Elsevier.*

Effects of NaOH treatment on the morphology of flakes has been also investigated [128]. Morphology of GO flakes before (Figure 25a-b) and after (Figure 25c-d) treatment with NaOH have been observed by SEM, showing a clear disintegration of the base-treated flakes if compared with untreated flakes.

In conclusion, the functional groups on the GO structure develop when the pH is increased with the release of more protons, indicating that the chemical composition is susceptible to changes after modifying the pH of the medium. Also, nucleophilic attacks by OH^- induce the cleavage of the oxidized domains, which may occur in chain reactions [217], further fragmentating the GO flakes. Then, the simple washing of GO with water, leaving dispersions with pH=7, may

deteriorate its chemistry. Being more recommendable to store the synthesized GO in acid conditions.

1.3.2.6. Ageing

GO is a metastable material, comprising oxygen functional groups that can be considered active sites and be involved in various reactions, even at low temperatures [218], [219]. It has been found that GO functional groups degrade with the passing of time, even when stored after drying to solid state [220]. The epoxides groups, theoretically, as they have a strained ring system, tend to degenerate to hydroxyls, which releases the stress by recovering the regular tetrahedron angles of carbon atoms. These spontaneous chemical modifications would have a relaxation time of few days, driven by the availability of hydrogen species [221]. In water dispersion, the decomposition of GO functional groups accelerates due to nucleophilic attacks of the water molecules [222].

What is also very interesting and relevant is the tendency of oxygen atoms to diffuse through the carbon lattice, forming oxidized and non-oxidized domains, pairing reacting species susceptible to form O_2 and H_2O [223].

In conclusion, storing GO dispersions under low pH, at low temperature, and while avoiding light exposure should be recommended to preserve the fine chemistry that possesses after the reaction.

1.4. APPLICATION OF GO ON TEXTILES

In the recent years, textiles have been in the focus of new developments. New functionalities of textile products are sought nowadays, where novel nanomaterials can find application. Graphene derivatives have been used in textiles improving characteristics such as electrical conduction [224], thermal regulation [225], flame resistance [226], antimicrobial action [227], UV protection [227], etc.

Three main methods exist to produce graphene-based textiles. The first consists in the coating of conventional fabrics or yarns with GO [228], with the possible following reduction to rGO (Figure 26a), which is interesting for its electric properties. The second consists in the CVD synthesis of graphene on a Cu mesh followed by the acid removal of the metal, leaving a fabric structure based on graphene [229] (Figure 26b). The third method consists in the preparation of GO fibers through extrusion in a coagulation bath [230] (Figure 26c), where reduction can optionally be performed to obtain rGO fibers.

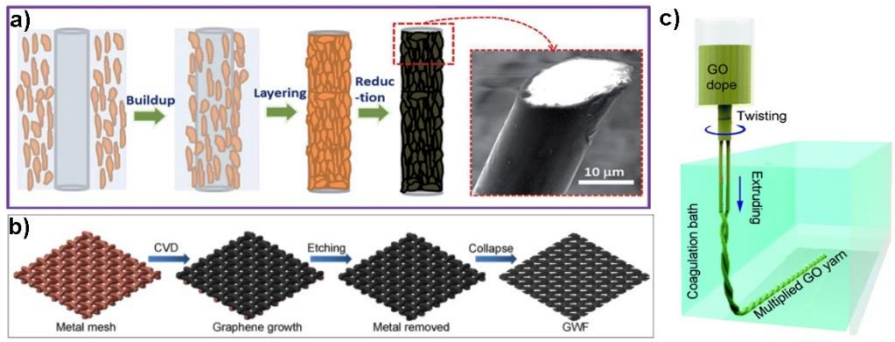

Figure 26: Principal methods to produce graphene-based fabrics. a) Coating of fabrics with GO, followed by reduction. Reproduced from [228] *with permission form RSC publishing b) Synthesis of graphene on a Cu mesh followed by etching. Reproduced from* [229] *with permission from Springer Nature. c) Formation of GO fibers by extrusion in a coagulation bath. Reproduced from* [230] *with permission from The Royal Society of Chemistry.*

From these methods, the most widely employed is the first one, due to its ease, scalability, and low prize of GO. The possibility of using GO as an aqueous ink makes it easy to be used in the textile industry as typical inks and colorants are already used. In the technical literature, the preferred method for coating textiles with GO is dip-coating. With this approach, the fabric is submerged in a GO solution and then the fabric is dried. GO has a negatively charged structure that interacts with the functional groups of the fabrics, increasing the fixation of GO; so, typically, a good coating is achieved with this technique. However, to boost the fixation of GO and avoid its shedding, different chemicals and processes are employed. For example, Bovine Serum Albumin (BSA), can be absorbed on the fabrics, leaving a positive charge that helps the posterior electrostatic attachment of the (negatively charged) GO thanks to its negative charge [231]. Plasma treatment of the fabric has been also used with the same purpose [232]. The use of resins, such as polyurethane (PU) has also been reported to increase the adhesion of GO [233].

Thermoplastic PU has been widely used in various applications such as coatings, elastomers, foams, and adhesives. It has a block copolymer structure, with polyol and isocyanate functional groups [234]. When GO is added to a PU matrix, cross-linking of GO with PU takes place, forming a rigid composite with increased mechanical strength [235]. Water-based PU is used in the textile industry to coat fabrics, obtaining a transparent and flexible film adapted to the morphology of the fabric which increases the longevity of the fabrics by protecting the microfibers from defibering. Therefore, PU can be also used to fix GO to the fabric, gaining on the fixation of GO and forming a PU+GO composite with increased strength.

2 AIMS OF THE THESIS

The research performed in the development of this thesis was financed by an industrial R&D project focused on the application of graphene oxide (GO) to textiles to improve their mechanical properties.

As researching on the industrial application of a material can be troublesome due to the unavailability of industrial equipment and the need for collaborators availabilities, we decided to make fundamental research on GO as a material itself, to contribute to the literature with substantial studies.

GO is a widely used graphene-like nanomaterial. Its promising applications and easiness of preparation in a non-specialized laboratory makes GO investigation accessible to all kinds of researchers. This availability is, of course, beneficious for science, but at the same time, has led to a large number of publications where GO has been used on its own or in combination with other materials being described as a product obtained by the Hummers' method reaction, without much more information about the reaction conditions that we know that affect its chemistry. In addition, the characterization section of these publications is usually limited to confirming the presence of GO, without any information about degree of oxidation or other important chemical features. On top of that, some authors proceed to purification techniques which involve the use of acids, centrifugation, or sonication, which are known to affect the physicochemical integrity of graphite oxide, yet do not provide much description and/or analyses on the transformations of their GO over the preparation steps. In sum, we have detected a lack of knowledge in the technical literature, regarding the physicochemical properties of GO prepared with variations of the typical reaction conditions and before applying any post-treatment.

This situation motivated us to drive our thesis aims toward fundamental research on the GO synthesis via the original Hummers' method and an exhaustive characterization of the product obtained to study its dependence on

synthesis conditions, trying to avoid the processing of the material that changes its properties, or at least, keeping them constant in all the samples.

Our main aim was to synthesize GO via modifications of the reaction parameters time and temperature of Hummers' method, and to thoroughly characterize the GO product to establish how these parameters affect the morphology and chemistry of GO.

When we tried to purify the obtained GOs, we realized that the post-treatments used for purification were also affecting the chemistry and morphology of the prepared GOs. For this reason, we also found interesting to study how our post-treatments affected our GOs prepared with different reaction conditions. Therefore, we have identified three thesis fundamental research aims:

- The effect of the reaction time on the chemistry and morphology of GO flakes obtained by Hummers' method.
- The effect of the reaction temperature on the chemistry and morphology of GO flakes obtained by Hummers' method.
- The effect of the extensive washing with water and strong agitation post-treatments on the chemistry and morphology of the GOs flakes obtained by Hummers' method under different reaction times and temperatures.

Additionally, we have performed a study in the line of the earlier-mentioned industrial textile project, to put in context the work performed in three years of research. The aim of this part of the research was:

- To coat a textile with GO to enhance its mechanical resistance to the puncture, with the scale-up of the application to typical coating methods of the textile industry.

The contents of thesis are then divided in two parts: an exhaustive investigation on the preparation and characterization of GO and its application on textiles during the research project. The two parts are separable as the two research

lines were conducted separately. Also, many of the results obtained for the application of GO on textiles have not been presented, due to confidentiality matters, limiting the weight of this part in the thesis to a unique chapter. The research presented in the thesis is then related to the preparation and characterization of GOs with different physicochemical properties.

3 EXPERIMENTAL TECHNIQUES

Summary: In this chapter, we describe the experimental techniques used in the development of this thesis. The first part of the chapter is intended to introduce the characterization techniques used for the morphological and chemical characterizations of the GOs prepared. Their appropriateness and capabilities for GO characterization were established in the literature review of Chapter 1. For the morphological characterization, we employed reflection optical microscopy (OM) and scanning electron microscopy (SEM). Thermogravimetric analyses (TGA) were conducted to determine the thermal stability. The structural analysis was determined by X-ray diffraction (XRD). The chemistry of the samples was determined by energy-dispersive X-ray spectroscopy (EDS) and by X-ray photoelectron spectroscopy (XPS). With EDS atomic concentration of the bulk samples was obtained while with XPS, we obtained the atomic concentration and chemical composition of the surface. Finally, Raman spectroscopy was used as complementary techniques to confirm the nature of the GOs. The second part of this chapter addresses the synthesis method selected for the obtention of GO and the variations we performed to procure GOs with different characteristics in terms of chemistry and morphology.

3.1. CHARACTERIZATION TECHNIQUES

3.1.1. Optical Microscopy (OM)

Optical visibility is an important feature of two-dimensional nanomaterials, such as graphene and graphene oxide. With optical microscopy, it is relatively easy to obtain information about the position, lateral dimensions, and thickness of the specimen. Revealing the dimensions and position of GO flakes is crucial when it refers to their application to devices in form of thin films [236].

Optical microscopy covers a wide range of light microscopy methods, such as transmitted and reflected light, fluorescence, and laser microscopy methods. Advances in resolution, speed of acquisition and digital imaging have enabled microscopists to acquire quantitative measurements of specimens efficiently [237], [238].

An optical microscope uses visible light, with wavelengths from 400-650 nm and a series of lenses to magnify specimens. As light passes through the sample, light is absorbed, reflected or diffracted. The differences in intensity of light are detected forming an image against a bright background.

3.1.1.1. Reflection optical microscopy and interference effects of light.

Reflected light microscopy is used when the light is unable to pass through the specimens. It is then directed onto the surface of the sample and returned to the microscope objective. The range of applications of this technique is enormous including the observation of metals, ceramics, minerals, polymers and semiconductors.

When observing thin particles under optical microscopy, it is common to observe colors on transparent, colorless or lightly colored substances. These colors are caused by interference effects of light, which is the same phenomenon that is found when we observe colors on soap bubbles, spilled oil on water or on some glass surfaces [239]. When incident white light reaches the surface of a thin film, part of the light is reflected, and part of the light is transmitted. When the transmitted light reaches the bottom, the situation repeats, with a new split into reflected and transmitted lights. The wavelengths reflected from the upper and lower boundaries return in the direction of the emission and interfere constructively or destructively in function of depending on the thickness of the thin film, its refractive index, and the angle of the incident light. A scheme of the process can be observed in Figure 27. From white light, only wavelengths that interfere constructively will be observable in form of a unique color. In the situation of Figure 27, the blue wave interferes constructively from the reflections of the upper and lower boundary of the thin film, while the green wave interferes destructively. Thus, in this example, considering the color of the waves as the color associated to their wavelengths, the thin film will appear blue when observed with reflection optical microscopy.

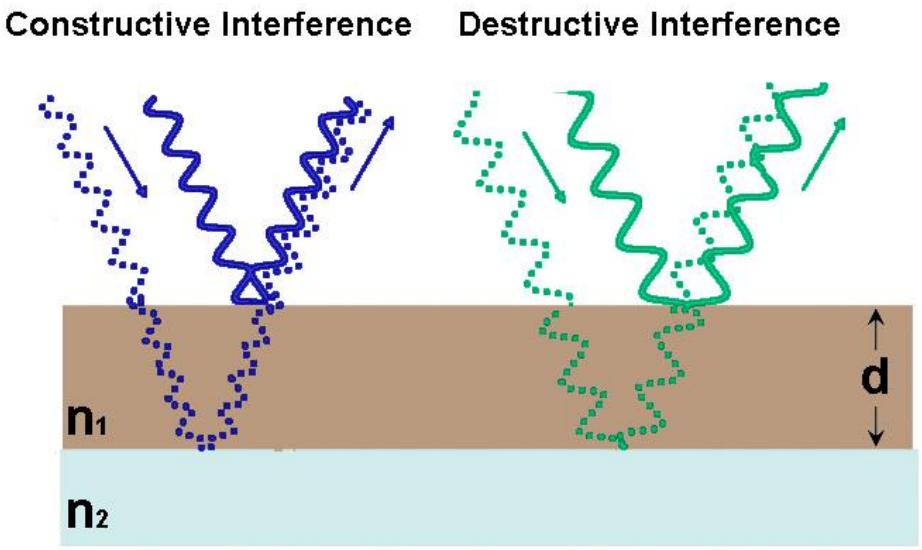

Figure 27: Interference of light from the upper and lower boundary of a thin film. Constructive interference occurs when both reflected lights are in phase and destructive interference occurs when they are not.

In a distribution of GO flakes, the lateral size of the particles typically extends to various orders of magnitude. Flakes of less than 100 nm can coexist with large flakes of more than 100 µm.

From these, large lateral dimensions had been presumed to be beneficial for GO since the beginnings of graphene [68], [240]. The isolation of flakes with a specific size is of great relevance in the field of micro and nano applications [241]. However, obtaining size-sorted GO suspensions is nontrivial. Many accurate post-treatments involving sonication, centrifugation and filtration procedures are needed.

With OM, one can obtain a first assessment of the distributions of particles that conform the dispersions, paying attention to the thicknesses of the flakes, and visualize unexfoliated particles of graphite oxide. Using OM, large areas of a surface can be scanned quickly, obtaining qualitative information in a matter of minutes. Using visible light as emitting source is beneficial when we observe

GO flakes, being able to have an approach about the thickness of the flakes as a function of the color and opacity of the flakes.

Using thin film optics theory, the colors that GO displays based on optical reflectance, have been investigated [242]. Figure 28a shows the calculated colors for graphene oxide as a function of its thickness. The observable color of the flake (or thin film) varies versus its thickness, following the color arrangement of the visible spectrum. The optical appearance that GO shows is due to interference phenomena of light when white light (comprising all visible wavelengths) is used. This study was centered on observing GO flakes deposited on a 270 nm thick SiO_2/Si substrate (Figure 27b).

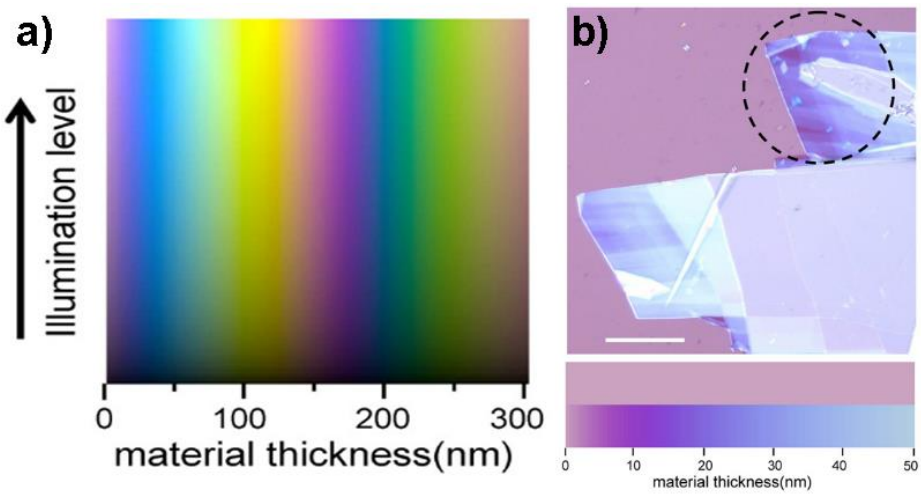

Figure 28: a) Two-dimensional color image calculated as a function of the thickness of graphene oxide deposited on SiO_2/Si layer. Apparent colors change as a function of thickness due to interference phenomena of light. b) Optical micrograph of GO flakes on a 270 nm thick Si/SiO_2 substrate. Adapted from [242] *with permission from IOP Publishing.*

In the case of few-layer GO flakes dielectric substrates must be used in order to enhance contrast, allowing the identification of single-layer flakes [243],

[244]. On “thick” GOs (more than 50 nm), the importance of the substrate is greatly reduced [245].

3.1.1.2. Preparation of the samples and instrumentation used

For the optical microscopy techniques performed in this thesis, samples were prepared by drop-casting of 2.5 mL of the corresponding GO dispersions covering the whole surface of a standard glass microscopy slides. The microscopy slides were first cleaned by bath sonication in a solution of 30% H_2SO_4. This increased the hydrophilicity of the slides [246] due to the attachment of hydroxyl groups to the surface of the glass, permitting a better wettability. Afterwards, the slides were rinsed with deionized water and left to dry at 85 ºC. After the drop-casting of the samples, they were let dry at room temperature but in a box covered with a holed parafilm, in order to slow down the evaporation rate and avoid the formation of coffee rings [247].

Reflection optical microscopy images were obtained using a Leica DM 2500 confocal microscope with a halogen white light source and a 50x Leica objective (NA 0.75 – WD 0.37 mm). Digital images were captured with a PixeLink PL-A662 camera, coupled to the microscope. Samples were mounted on a high-precision monitored 3D-stage, which was used to control the recorded position. For most measurements, the typical scanned area size was 500 µm x 500 µm, consisting in a montage of 2596 high-resolution individual images.

3.1.2. Scanning Electron Microscopy (SEM)

Scanning Electron microscopy (SEM) is a microscopy technique that uses a focused beam of electrons instead of light. Using electrons instead of light allows to have images of higher resolution, achieving magnifications up to 300.000x. The interaction between the electron beam and the surface of the

sample generates several signals that can be used to obtain different information about the topography and composition of the sample. These signals are secondary electrons, backscattered electrons, Auger electrons, X-rays and visible photons [248].

When the electron beam reaches the sample, they collide with the electrons of the surface, changing their path with an energy loss and producing the ionization of the electrons of the atoms. The ionized electrons leave the atom with low kinetic energy and are detected by a specific detector. These electrons are called secondary electrons and they are generated only by superficial atoms, giving information about the topography of the sample. Other electrons of the beam are scattered backwards once they collide with the atomic nucleus of the atoms of the samples. These are called backscattered electrons and give information about the atomic composition of the sample, as the interaction of the electrons with the atomic nucleus depends on the atomic number *"Z"*. Compositional information can be obtained from the characteristic X-rays generated from the interaction of the incident electrons with the electronic shell of the atoms. Other less used signals are Auger electrons, non-characteristic continuum X-rays and cathodoluminescence. All these physical processes are represented in Figure 29.

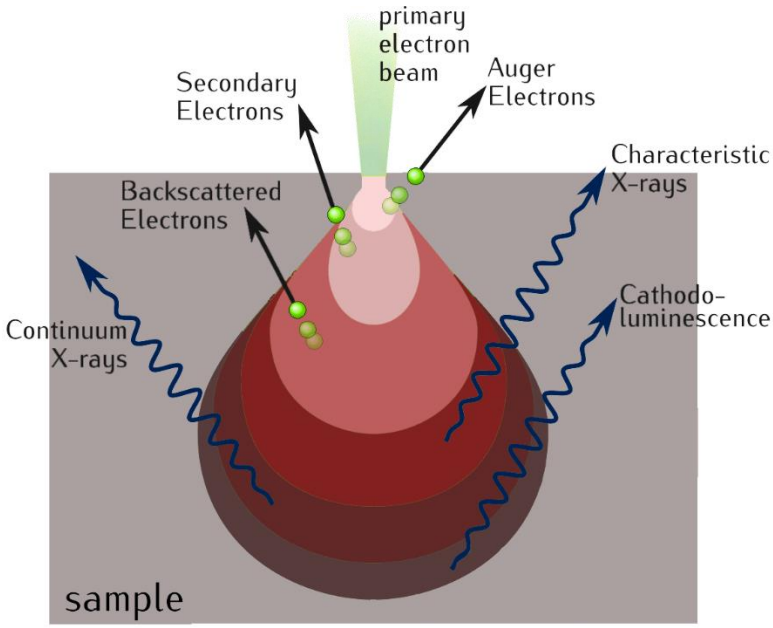

Figure 29: Scheme of the signals generated by the interaction of the electron beam with a sample.

The possibility of scanning large surface areas allows SEM to analyze simultaneously hundreds of different flakes on the same sample, while providing information about the distribution of the flake size, morphology and even number of carbon layers in fully exfoliated samples. GO flakes occasionally form wrinkles or folds [249]. In Figure 25b we could observe an untreated GO flake that has a smooth edge and a fold in the middle of it [128] while in Figure 25c the damaged flake treated with base also show wrinkles.

3.1.2.1. Preparation of the samples and instrumentation used

In this thesis, a FEI Quanta 600 ESEM was used to capture high resolution SEM images of the dispersed GO flakes, using high vacuum and an operating voltage of 2 keV.

Dispersions of the GOs were prepared in a concentration of 1 ppm performing 4 predilutions from the starting concentration of 3 mg/mL. Milli-Q water was used to avoid the formation of salt microcrystals in the dried samples. 125 µL of each sample was then deposited by drop-casting on a diced silicon substrate of 1 cm^2. The samples were dried at room temperature in a petri dish covered with a holed parafilm tape, in order to slow down the evaporation rate, increase the ordering of flakes and to avoid the formation of coffee rings [247].

Images at 500x magnification were obtained, comprising numerous flakes per image. For each flake, the number of pixels that formed its shape was obtained manually using the image software Adobe Photoshop CS3.

3.1.3. Energy-Dispersive X-ray Spectroscopy (EDS)

Energy-dispersive x-ray spectroscopy (EDS) is a spectroscopic microanalysis technique used for the identification of chemical elements present in a sample, quantitatively or qualitatively. This technique is commonly hosted inside scanning electron microscopes (SEM) and transmission electron microscopes (TEM). When an electron beam is focused on the sample in either a SEM or TEM, the electrons from the beam penetrate the sample and interact with the atoms present in the sample producing characteristic X-rays [250].

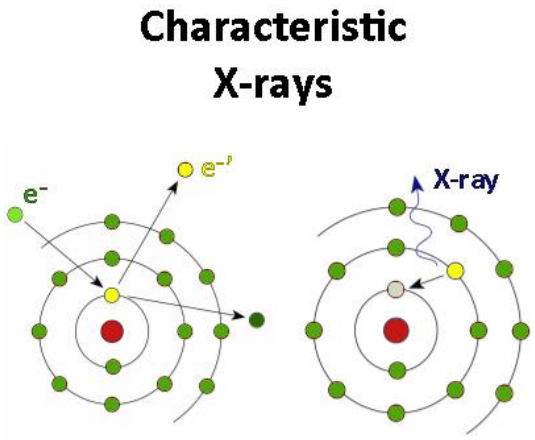

Figure 30: Scheme of the generation of characteristic X-rays, by the interaction of an electron to the electronic shell of an atom.

Characteristic X-rays are formed by the electrons of the inner shell of the atom. One incident electron interacts with an inner shell electron, ejecting it in an elastic collision. Then, an outer electron replaces the vacancy, releasing the energy difference as an X-ray (Figure 30). This discrete value of energy is intrinsic of each atom.

The X-rays generated are detected by an Energy Dispersive detector, displaying the signal as a spectrum. The combination of the characteristic X-rays detected permit the identification and quantification of the atomic elements of the sample.

For GO, with EDS the relative quantity of carbon and oxygen can be determined despite the quantification of these low-Z elements tend to be inaccurate [251]. Sulfur usually found on GO can be also quantified [252], [253], [254]. Lastly, EDS is also useful to detect the presence of impurities remaining from the oxidation reaction [255].

3.1.3.1. Preparation of the samples and instrumentation used

In this thesis, a FIB-SEM Thermo Scientific Scios 2 Dualbeam coupled to a Thermo Scientific Pathfinder X-ray microanalysis detector was used to record the EDS spectra, operating at a voltage of 25 kV.

Samples were prepared from GO dispersions with a concentration of 3 mg/mL. 111 µL of each GO were deposited by drop-casting on a silicon diced substrate of 1 cm^2. The samples were let dry in a hot plate at 40 ºC. The drop-casting procedure was repeated 6 times for a total deposition of 2 mg in each sample, guaranteeing enough thickness to avoid the detection of the silicon substrate due to a high penetration of the electron beam.

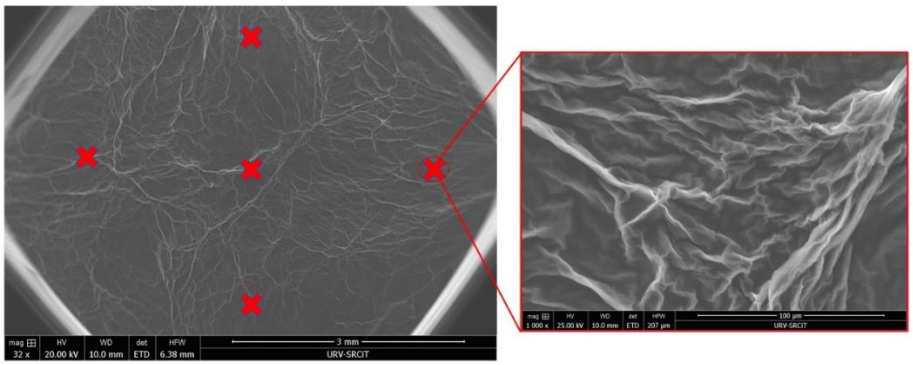

Figure 31: On the left, a low-magnification SEM image of a sample of GO used for the EDX analysis. Wrinkles can be observed as the characteristic assembly of dried bulk GO. 5 measurements were performed in separated zones as shown in the image. In each spot, magnification was increased to 1000x, as shown on the right, to record the EDX spectrum.

For each sample, 5 spectra were recorded at different positions of the sample with a magnification of 1000x. The 5 spectra were averaged into one spectrum per sample. In Figure 31, an example of one analyzed sample is shown, red crosses of the left image indicate the different zones that were magnified to

1000x, as shown in the image on the right, and analyzed to obtain 5 spectra of different zones of the sample.

3.1.4. X-ray Photoelectron Spectroscopy (XPS)

X-ray Photoelectron Spectroscopy (XPS) is a widely used technique for characterization of the chemistry of GO. It provides information about the characteristic atomic bonds of each element. XPS is a useful technique for the recognition of functional groups, absorbed contaminants or other chemical modifications present in the surface [256]. XPS has two important advantages when it is applied to GO: it provides elemental content of the outer chemical layer of a sample (3-5 nm) and it can quantify the different oxygen functional groups on the structure.

XPS is based on the photoelectric effect. The internal electronic levels of the atom are excited with an X-ray beam. The interaction between the X-rays and the electrons causes the emission of photoelectrons with a kinetic energy that provides information about the energy of each level, and thus, the nature of the emitting atom.

In the photoemission process (Figure 32), an atom or molecule absorbs an X-ray photon, ejecting an electron. The kinetic energy of the ejected electron depends upon the energy of the X-ray, the binding energy of the electron and the work function. The binding energy depends upon the element from which the electron is emitted, the orbital from which is ejected and the chemical environment of the atom from which the electron is emitted [257]. XPS spectra are recorded by counting the photoelectrons over a range of kinetic energies. Peaks appear in the spectrum from emitted electrons of a characteristic energy, enabling the identification and quantification of all the present elements, in exception of hydrogen.

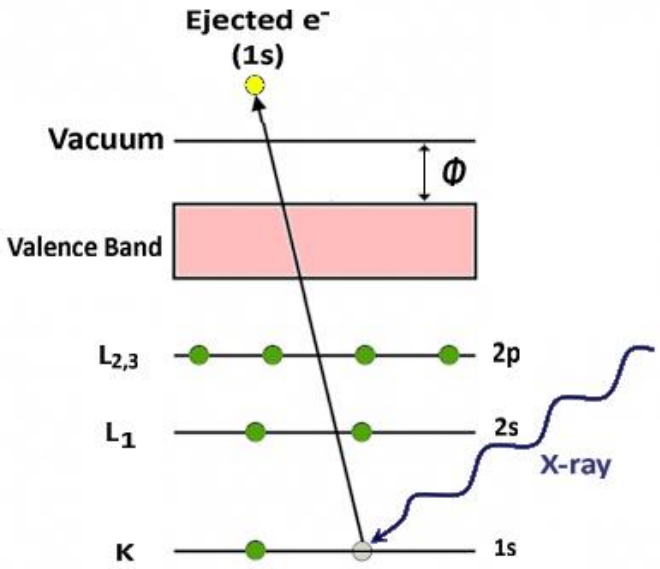

Figure 32: The photoemission process for the incidence of an X-ray to the electronic shell of an atom. The interaction of a given energy X-ray with an 1s electron causes its ejection with a characteristic kinetic energy.

For GO, the elemental quantification is determined by running a survey spectrum (a scan from 1200 to 0 eV) where all elements constituting the samples can be detected. The most valuable information, which is the different chemical states of the carbon atoms, is obtained from the C 1s spectrum. The energy of the C 1s orbital varies as a function of the type of bonds that C forms with other elements, thus allowing their relative abundance to be quantified.

In the C 1s spectrum of graphite, we encounter a single band centered around 284.8 eV [258], which is the typical band of the graphitic framework, including C-C, C=C and C-H bonds (Figure 33a). The asymmetry of the peak is due to the presence of a minor component around 286 eV originated from deviations from the pure sp^2 graphitic carbon structure [259]. As part of the GO basis, this band will be present in all the GO samples with high intensity.

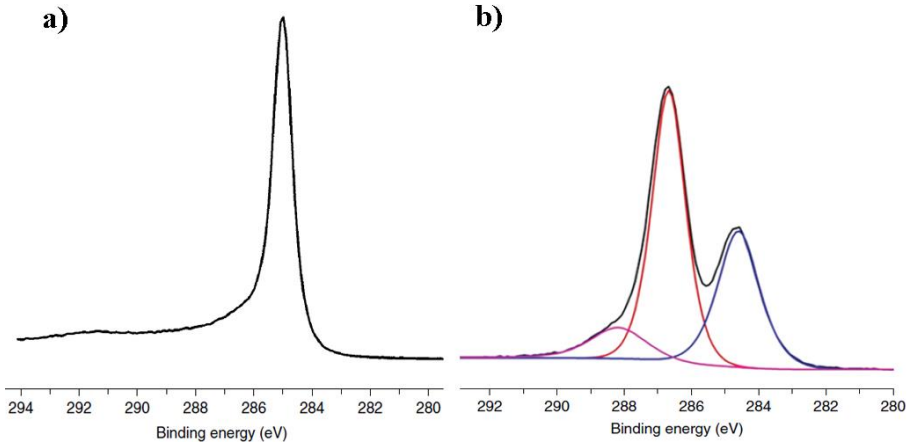

Figure 33.a) C 1s XPS spectrum of graphite. b) C 1s XPS spectrum of graphene oxide. Reproduced from [259].

The C 1s spectrum of GO is composed by three apparent components (Figure 33b). Again, the peak at 284.8 eV is assigned to the graphitic domains, as long they are not chemically bound to oxygen atoms. Even if the carbon is not pure sp^2, it will generate a signal in this area. The most intense peak is centered at 286.5 eV and it is attributed to the carbon atoms of epoxides (C-O-C) and tertiary alcohols (C-OH). These two components are entangled and cannot be separated due to the large number of configurations that can be found in GO, leading to peak broadening. Lastly, the 289.2 eV signal is usually attributed to carboxylic acid/ester groups (O-C=O) [259].

In the literature, different ways of deconvoluting the integral C 1s spectra can be found [260], [255], [261], where the C 1s spectra is deconvoluted in all sort of functional groups that may be present in GO. However, the low binding energy shift between similar functional groups makes these deconvolutions highly speculative, even for comparative purposes.

3.1.4.1. Preparation of the samples and instrumentation used

XPS samples were prepared by drop-casting of 125 µL of the corresponding GO dispersions with a concentration of 3 mg/mL on a Si 1x1 cm^2 diced substrate and dried at room temperature.

The samples were shipped to the XPS laboratory of Prof. Jordi Llorca, at Universitat Politècnica de Catalunya (UPC), Barcelona (Spain). The XPS is a SPECS system equipped with a XR50 source operating at 250 W, and a Phoibos 150 MCD-9 detector. The pass energy of the hemispherical analyzer was set at 20 eV and the energy step of high-resolution spectra was set at 0.1 eV. Binding energy (BE) values were referred to the C 1s C-H sp^3 peak at 284.8 eV. Data processing was performed with the CasaXPS software. Atomic fractions were calculated using peak areas normalized based on acquisition parameters after background subtraction, experimental sensitivity factors and transmission factors provided by the manufacturer.

3.1.5. Thermogravimetric Analysis (TGA)

Thermogravimetry is a technique consisting in the measure of the mass variation of a material as a function of temperature and/or time, generally in a controlled atmosphere [262]. These changes might be due to different processes, as phase transitions, oxidation or reduction reactions or thermal decomposition of the material, etc., that will be detected by an accurate thermobalance.

GO prepared via Hummers' method has a main weight loss for GO around 180-200 ºC [263]. TGA coupled with mass spectrometry (TGA-MS) can be used to analyze the gases formed during the thermal decomposition, being able to attribute different processes of decomposition as a function of temperature [264]. An example of a TGA-MS analysis is shown in Figure 34. There are two

clear decomposition peaks, during the main decomposition peak situated at 153 ºC, H_2O, CO_2 and CO are formed. During the secondary decomposition peak at 240 ºC, SO_2 is primarily detected in addition to water. These results clearly indicate that firstly, the oxo-functional groups are decomposed, and then, the organosulfates decompose.

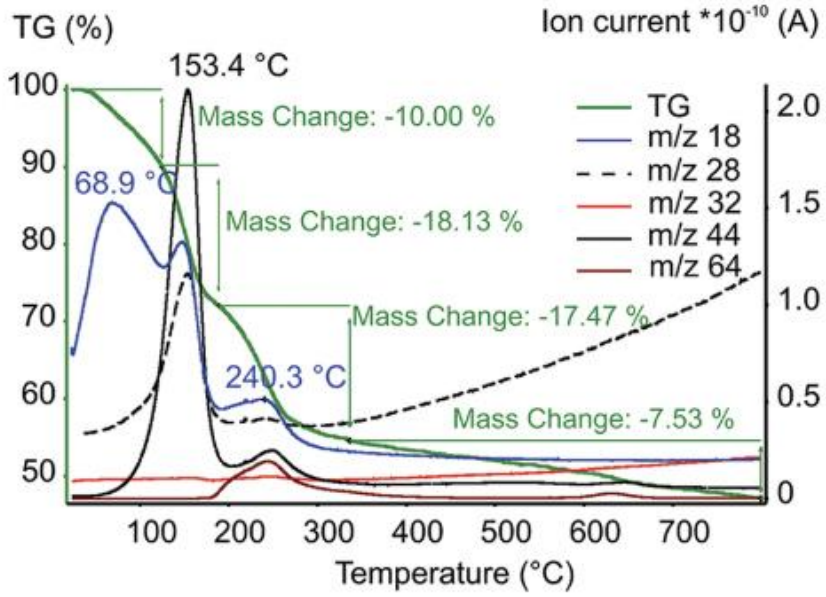

Figure 34. TGA-MS analysis obtained for GO with the m/z data obtained for the gases formed during decomposition. m/z= 18 (H_2O), m/z= 28 (CO), m/z= 32 (He), m/z= 44 (CO_2) and m/z= 64 (SO_2). Reproduced from [264] *with permission of American Chemical Society.*

3.1.5.1. Preparation of the samples and instrumentation used

GO samples for TGA were prepared from GO dilutions dried at room temperature. The obtained paper-like products were shattered into small pieces. Then, 5 mg of each GO were placed in a platinum crucible and introduced into the furnace. Same weight of calcined alumina was used as a reference. Two kinds of experiments were performed: (i) a fast overview, using a 10 ºC/min ramp from a starting temperature of 25 ºC to 1400 ºC. (ii) A focused experiment in the decomposition zones, using a slow ramp of temperature of 2.5 ºC/min from 25 ºC to 400 ºC. These last experiments were performed by triplicate and the weight loss information, and the temperature of decomposition were averaged for those three measurements.

Thermogravimetric analyses were performed for each sample with a thermobalance *TA Instruments SDT 2960.* With these tests, weight loss curves were obtained for each GO sample.

3.1.6. X-ray diffraction (XRD)

X-ray diffraction (XRD) is a technique that provides information about the structure of crystalline materials in a non-destructive interaction of X-rays with the sample [265]. X-rays are electromagnetic radiation with wavelengths in the range of 0.1-5 Å. This range is in the same order of magnitude than the typical interatomic distance in solids. For this reason, when the X-ray beam penetrates the sample, part of the beam is absorbed, transmitted, or scattered, and part is reflected elastically. Elastic interactions occur with the electron cloud of the atoms and the X-rays are diffracted to certain directions.

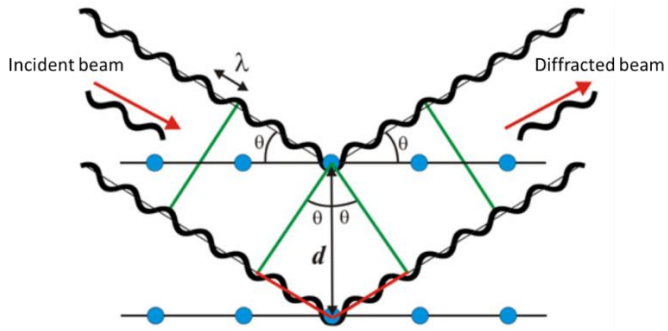

Figure 35: Schematic representation of constructive X-rays diffracted by a crystalline structure.

X-rays diffracted by different atomic planes can be amplified by constructive interference, as shown in Figure 35. The conditions for diffraction are described by the Bragg's law:

$$n\lambda = 2d\ sin\theta$$

Where "n" is an integer, "λ" is the wavelength of the X-rays, "d" is the spacing between planes in the atomic lattice of the sample and "θ" is the diffraction angle.

Furthermore, with XRD, the size of sub-micrometer crystallites can be determined following the Scherrer equation [266]:

$$L = \frac{K\lambda}{\beta cos\theta}$$

Where L is the size of the crystallite in the direction of the corresponding peak, K is a shape factor constant that it is approximated to 0,94 for graphitic samples [267], [268], [269]. λ is the X-ray wavelength, β is the Full Width at Half-Maximum (FWHM) of the corresponding peak expressed in radians and θ is the maximum position of the diffraction angle.

It must be pointed, however, that the use of the term crystallite is not correct in all cases as one cannot know whether the information relates to the size of

crystallites or stacked domains. In the case of GO, as it is not formed by crystallites, it would be more correct to talk about “size of the coherently diffracting domain” or, more condensed, “column length”. For this reason, in the thesis we will refer to that value as column length (L_c).

In the case of graphite, the typical distance between layers is broadly known, with a value of 26.5° 2θ, corresponding to the (002) plane and an interlayer distance of 3.36 Å [270].

In the case of GO, a signal corresponding to the (001) plane becomes strong in a range from 7º to 12º 2θ [271], with interlayer distances from 12.5 Å to 7.5 Å respectively. The (002) peak is still present in some cases but tends to show a lower signal shifted to 20-24º 2θ [272]. The increase in the distance between graphitic planes is caused by the insertion of oxygen atoms on both sides of the hexagonal carbon lattice during the reaction procedure.

Interlayer distance is not a generic parameter for all GO samples. The reasons that can change the position of the (001) signal are: the amount of water retained during the drying process of the GO solution [273], the use of different solvents [274], or differences in the reaction that alter the oxidation degree [116]. Changes on these parameters may displace the (001) signal of GO according to a higher or lesser interlayer distance of the GO layers.

In the case of performing a reduction of GO to rGO, the only signal that appears is in the range of 23-24º 2θ [261], [271], corresponding to the plane (002) and an interplanar distance around 3.7 Å, a similar distance than the obtained for graphite, indicating the effective removal of oxygen groups from the structure and the compaction of the layers. An example of typical diffractograms that can be obtained for graphite, GO and rGO is depicted in Figure 36.

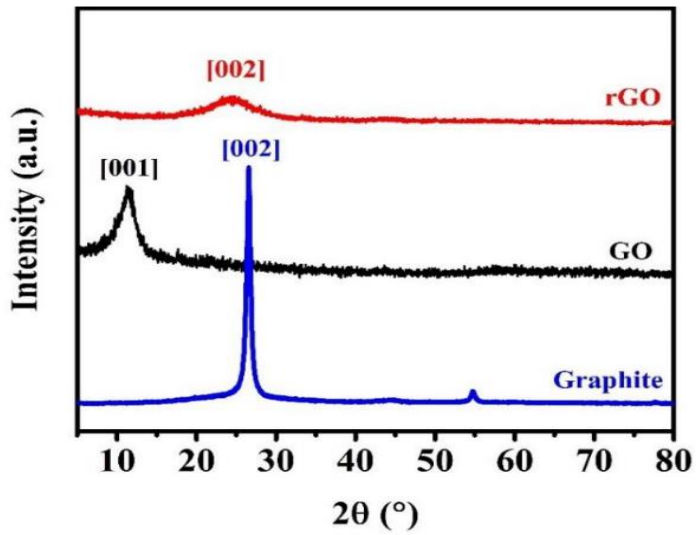

Figure 36: Example of typical diffractograms obtained for graphite, GO and rGO. Interlayer distance information can be extracted by the position of the peaks along 2θ. Reproduced with permission from [275].

3.1.6.1. Preparation of the samples and instrumentation used

In this thesis, XRD (X-ray diffraction) measurements were made using a *Siemens D5000* diffractometer (Bragg-Brentano parafocusing geometry and vertical θ-θ goniometer) fitted with a curved graphite diffracted-beam monochromator, incident and diffracted -beam Soller slits, a 0.06º receiving slit and scintillation counter as a detector. The data were collected with an angular step of 0.05º at 3s per step and sample rotation. Cu(k_α) radiation was obtained from a copper X-ray tube operated at 40 kV and 30 mA, corresponding to an X-ray wavelength of 1.5406 Å. LaB_6 SRM 660c was used as standard to obtain the instrumental broadening of the peaks.

Samples were prepared by drop-casting of 1.0 mL of each sample of diluted GO with a concentration of 3 mg/mL on a low background Si (510) wafer as a substrate. Samples were dried at room temperature to let the water evaporate

avoiding the formation of bubbles between the thin layer of GO. Afterwards, they were heated to 50 ºC to desorb the retained water and they were stored in a sealed desiccant box until the time of analysis, to avoid the samples to absorb moisture.

The XRD patterns were recorded firstly covering a range of 2θ between 5 and 45 º, where all the peaks of graphite and GO can be found and, later, a second round of analysis was performed focused in the area of interest which has the main peak of GO, corresponding to the plane (001), centering the analysis in the range of 2θ between 7.5 and 15.0 º. The samples were always analyzed set by set, so in each XRD graph, the samples depicted had been analyzed consecutively with the same atmospheric conditions.

Diffractograms were analyzed adjusting the peaks to a pseudo-Voigt function [276], obtaining the peak position and the Full Width at Half Maximum (FWHM).

3.1.7. Raman spectroscopy

Raman spectroscopy is a standard technique based on the inelastic interaction of light with the polarizable electron density of molecules or materials [277]. A monochromatic laser excites the sample to a virtual state and the energy decay can occur reemitting the light elastically at the same frequency as the original, known as Rayleigh scattering, or inelastically at higher or lower frequencies, called the Raman effect.

In the Raman effect, the light excites the molecule from the ground state to an excited virtual state and then decays to a vibrational state still above the ground state, emitting light with lower frequency. This shift in frequency provides information on vibrational, rotational and other low-frequency transitions characteristic of molecules and materials, giving a fingerprint spectrum that allow their identification.

The quality of graphitic materials can be investigated by Raman spectroscopy, as they are Raman sensitive to vibrations caused by the graphene lattice in-plane phonons.

For graphitic materials, Raman spectra have three important peaks about 1355 cm^{-1} (D band) 1590 cm^{-1} (G band) and 2700 cm^{-1} (2D band). The G band is assigned to the vibrational E2g degenerative mode in graphite single crystal and it is an indicator of the stacking structure [278]. For this reason, this band shows a low signal for graphene monolayer and increases progressively when accumulating layers of graphene, being extremely useful for discriminating monolayer from multilayer graphene [279]. The D band is assigned to the A1g mode, and it corresponds to the breathing mode of the six-member rings. For this reason, this band is related to the density of defects in the honeycomb structure [278], [280]. The 2D band is also present as an overtone of the D band, and is highly sensitive to the stacking order along the c axis [281].

In graphitic materials, it has been proven that the relation of the intensity of the D and G peaks (I_D/I_G) is related to the number of defects and the distance between these defects [282].

In Figure 37a, the Raman spectra of pristine graphene and defective graphene are compared. One can observe the presence of the G and 2D bands for the case of pristine graphene, and the evolution of the D band (and other related bands) when defects are introduced.

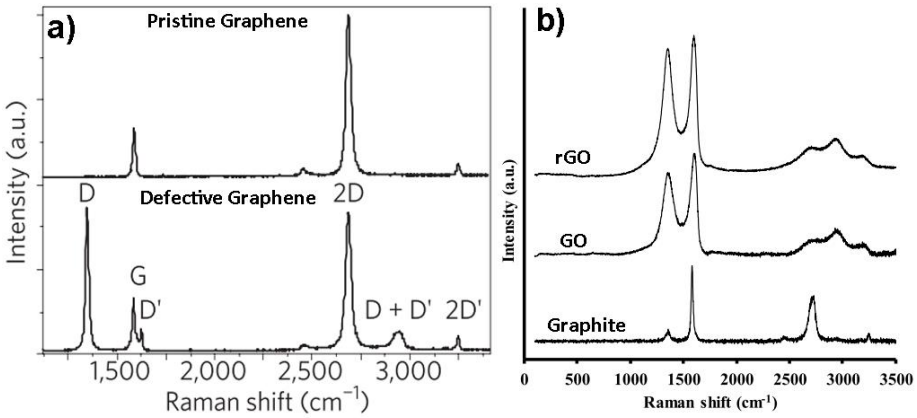

Figure 37: a) Raman spectra of pristine and defective graphene. Reproduced from [280] *with permission from Springer Nature. b) Raman spectra of graphite, GO and rGO. Reproduced from* [283].

In the case of GO and rGO, Raman spectroscopy is not sensitive enough to differentiate samples, due to the introduction of too many defects [284]. This can be observed in Figure 37b where Raman spectra of GO and rGO are quite similar but different from the graphite precursor. The increase of the D band from graphite to GO is caused by the creation of defects, that remain after the reduction to rGO [283].

3.1.7.1. Preparation of the samples and instrumentation used

In this thesis, Raman measurements were performed using a Renishaw inVia Reflex confocal Raman microscope equipped with a 514 nm Ar^+ laser and a 50x Leica objective. The same samples prepared for EDS (section 3.1.3) were used, consisting of 2 mg of dried GO deposited by drop-casting of the corresponding dispersions on silicon (1x1 cm^2) substrates. The surface of the samples was focused in 5 different zones and the spectra were obtained using

a laser power of 0,15 mW and 1 accumulation of 10 s each. The spectra of the 5 zones were averaged.

3.2. REACTION PROCEDURE

One of the main aims when producing GO, is the obtention of large and well-exfoliated flakes. It is already known that permitting more time and temperature during the reaction, leads to a higher degree of exfoliation of the graphite oxide particles, caused by a higher penetration and reactivity of the oxidants into the graphitic galleries. However, the excess of the same parameters also causes a higher oxidation of the sp^2 carbon lattice, inducing permanent defects and transformation of the aromatic carbons to CO_2, losing potential properties attributed to the continuous aromatic lattice. For this reason, an equilibrium of the reaction parameters must be achieved to obtain the optimal GO product.

Despite we introduced some variations in the parameters of our reactions to compare the morphology and chemistry of the different GOs obtained, we selected a specific reaction procedure to use it as a basis for our modifications. This reaction is the modification of Hummers' method performed by Eigler et al. [19] published in 2013. Eigler et al. used smooth reaction conditions to obtain a mildly oxidized GO to be afterwards reduced to graphene with the full recovery of the carbon sp^2 framework. In these years, graphene oxide was just starting to grow only as a precursor of the celebrated graphene. It was several years later that GO started to gain interest as a material itself.

3.2.1. Eigler's modification of Hummers' method

In Eigler's modification of Hummers' method, the authors dispersed 1 g of graphite and 0.5 g of sodium nitrate ($NaNO_3$) in concentrated sulfuric acid. They cooled the dispersion in an ice bath to about 5 ºC. Then, for a period of three hours they added 3.0 g of potassium permanganate ($KMnO_4$) and left the reaction to occur while stirring during three additional hours at 20-30 ºC.

Afterwards, the reaction mixture was poured on 500 mL of ice and 10 mL of hydrogen peroxide 3% (H_2O_2) were added to finish the reaction.

3.2.2. Our modifications of Hummers' method

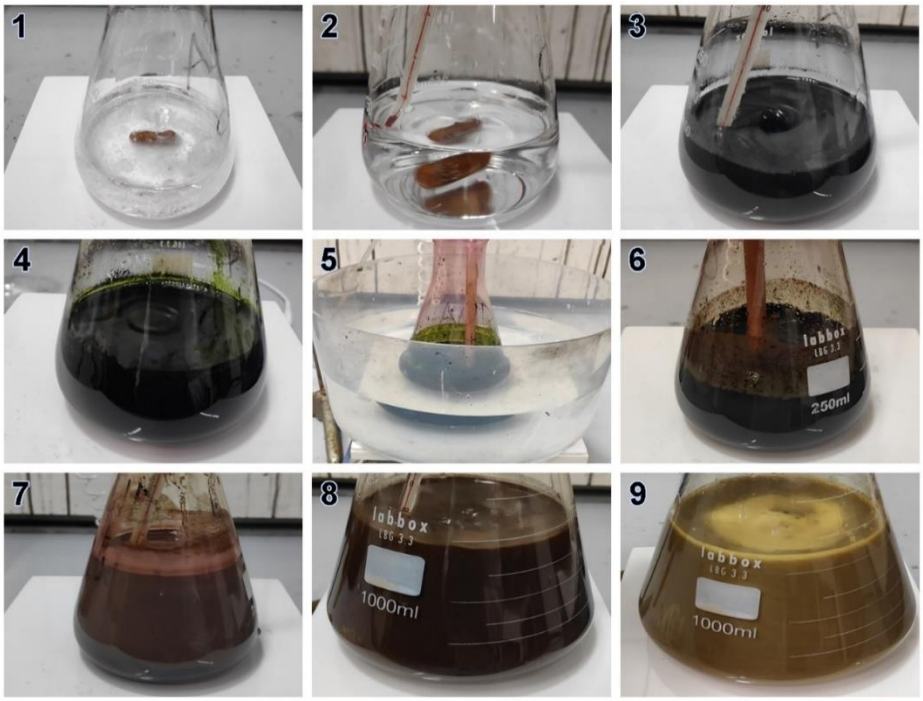

Figure 38. Images taken during the main steps of the reaction procedure: (1) Mixing of $NaNO_3$ and H_2SO_4 under magnetic stirring. (2) Total dissolution of $NaNO_3$ in the sulfuric acid media. (3) Addition of graphite. (4) Addition of $KMnO_4$ and start of the reaction. (5) Temperature control using an ice bath during the reaction. (6) Slurry obtained after the reaction. (7) Initial hydrolysis and acid quench with diluted H_2SO_4. (8) Quench with cooled water. (9) Addition of H_2O_2 to remove residual MnO_4^- and end of the reaction.

In our case, we used Eigler's methodology to elaborate a series of experiments varying the time and temperature of the reaction. We also introduced minor modifications about the procedure based on our experience on the oxidation of graphite gained in the course of the research. The main steps of our procedure for the oxidation of graphite are depicted in Figure 38 and are as follows:

1. *Preparation of acidic mix*. In a 250 mL Erlenmeyer flask, 2.5 g of $NaNO_3$ (extra pure, purchased from Scharlab) are added to 120 mL of H_2SO_4 95-98% (Pharmpur, purchased from Scharlab). The mix is magnetically stirred for some time (generally 15-45 min) to let the $NaNO_3$ fully dissolve. In Figure 38(1) this process can be observed where solid $NaNO_3$ is present in the medium.
2. *Dissolution of $NaNO_3$*. Figure 38(2) shows how $NaNO_3$ has been totally dissolved. In some procedures, as in Eigler's study mentioned above, they immediately add graphite in the first step together with $NaNO_3$, but this darkens the solution and the dissolution of $NaNO_3$ cannot be followed. Instead, we let $NaNO_3$ fully dissolve before the addition of graphite.
3. *Addition of graphite*. Next, 5.0 g of graphite flakes (99% carbon basis, -325 mesh, purchased from Sigma-Aldrich) are added to the flask with care to avoid contact with the sides of the flask, as the particles would stick and remain there during the rest of the process without being oxidized. An image of the mix can be observed in Figure 38(3). This mixture rests during 25 min. During this time, the mix is put in an ice bath in the cases for which the temperature of the reaction had to be kept low. Otherwise, the step is performed at room temperature without any bath.
4. *Anhydrous oxidation of graphite.* The next step is the addition of 15.0 g of $KMnO_4$ (pharma grade, purchased from ITW Reagents) to initialize the anhydrous oxidation of graphite. This step is the first that differs

from Eigler's procedure. In their methodology, they started the addition of $KMnO_4$ after cooling the mixture and maintained the temperature low during the addition. In our procedure, the temperature increase caused by the initial oxidation is controlled to avoid surpassing a certain reaction temperature. For example, if we perform the reaction at 5ºC, we cool the mix to 5ºC, and we add the $KMnO_4$ in small portions to avoid heating of the mix. If the reaction temperature is 50ºC, we add the $KMnO_4$ in bigger portions at room temperature while keeping the temperature from exceeding 50 ºC. This step takes from 5 to 60 min depending on the temperature. An image of the mixture after the addition of $KMnO_4$ can be observed in Figure 38(4) with a characteristic green color corresponding to the presence of manganese heptaoxide (Mn_2O_7) [133].

5. *Control of reaction temperature.* Immediately after all the $KMnO_4$ was added, the reaction is brought to the temperature set for each reaction. To do that, a hot plate with a temperature probe is used for heating, while an ice bath is used for cooling. The reaction tends to generate heat in the first minutes of the reaction, accelerating itself in a chain effect of temperature increase. However, with some care this step is not dangerous as the temperature is easy to decrease by simply putting the mixture in the ice bath. In Figure 38(5) this procedure can be seen where the flask is put in the ice bath to cool down the mix.
6. *Product of the reaction*. After the reaction time, which varies for each case, we obtain a brownish and dense slurry as we can observe in Figure 38(6). The density of the slurry is different in each case and gives a first view of the exfoliation degree of the graphite.
7. *Quenching with diluted acid*. The following step is the addition of 100 mL of H_2SO_4 10% (chilled to 5ºC). The reason to quench with a dilution of sulfuric acid is to avoid the sudden increase of temperature due to the dissociation energy of the acidic reaction when distilled water is added to the mix. With this intermediate step, the dissociation energy

is released in two steps: first with the addition of diluted sulfuric acid and later with the addition of distilled water. Thus, 100 mL of H_2SO_4 10% are added by small volumes while controlling the temperature of the mixture with the ice bath. This addition usually takes from 30 to 120 min depending on the temperature control specifics. An image of the product obtained after the addition of H_2SO_4 10% can be seen in Figure 38(7).

8. *Quenching with chilled water*. Then, the slurry was transferred to a 1 L Erlenmeyer flask and 500 mL of chilled distilled water (0 ºC) are added in one go. As can be observed in Figure 38(8), the mix turns a darker brown.
9. *Termination with hydrogen peroxide*. The final step is the addition of 100 mL of hydrogen peroxide 3% (dilution prepared from H_2O_2 30% extra pure, purchased from Scharlab) to complete the reaction. H_2O_2 neutralizes the oxidant permanganate residues with the formation of inert $MnSO_4$ [147]. After the addition, the mixture turns to a golden-brown color as can be seen in Figure 38 (9), and it is left in magnetic stirring for 24 hours to let all the H_2O_2 reduce the permanganate. After this step, the reaction ends, and the product is ready for the washing procedure. At this stage, GOs prepared with different conditions already displays different colors, which are related to different ratio of sp^2/sp^3 carbon atoms, reflecting the degree of oxidation [285].

3.2.3. Washing procedures of the obtained Graphite Oxide

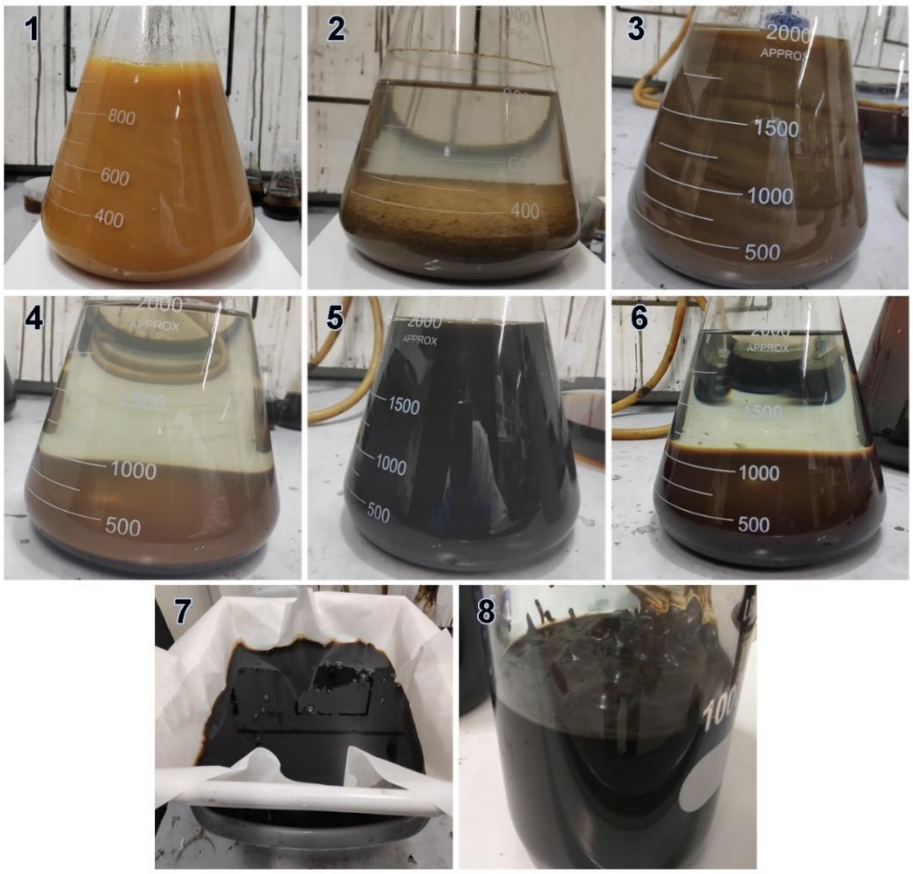

Figure 39. Images taken during the main steps of the washing procedures to obtain purified GO: (1) Raw GO from the reaction after the addition of H_2O_2 and 24 hours of stirring, displaying a golden color. (2) Sedimented raw GO. (3) GO after the first decantation and water addition, displaying a brownish color. (4) Still acidic GO fully sedimented after 24 h of rest. (5) GO after some steps of washing-decanting displaying a blackish color. In this step, GO is stable in dispersion and won't sediment anymore. (6) GO sedimented after the addition of HCl and some hours of rest. (7) Filtration of the sedimented GO using a large-area filter. (8) Obtained slurry of GO at the end of the first washing.

After the period of 24 h in H_2O_2, the mixture turns into a golden color as seen in Figure 39(1). At this point, the GO mixture constitutes a diluted but heavily acidic mix composed by SO_4^{2-}, Mn^{2+} [147] , Na^+, K^+, and polycyclic organic acids [148] generated from the carbon structures of the graphite [143]. In the mix, graphite oxide microparticles can be seen by naked eye, as they are formed by the aggregation of smaller flakes of GO stuck by Van der Waals forces [20]. This happens at pH≈0 as all functional groups of GO are protonated and the net charge of the surface is near 0 [162], [216], causing GO particles to have more affinity for themselves than for the aqueous medium [161].

After the final step of the reaction, the mix is left during 24 h in magnetic stir When this time completes, the stirrer is stopped and the microparticles start to sediment. This process is quite fast and after some hours, all the GO particles sediment to the bottom of the flask, as can be seen in Figure 39(2). Next, the upper acidic media was decanted from the sedimented GO. The transparent liquid, containing strong acids and contaminant heavy metals, was discarded properly, and the remaining solid fraction was transferred to a 2L Erlenmeyer flask, where distilled water was added to continue with the wash of the GO particles. As can be observed in Figure 39(3), the dispersion of particles turned brownish. Changes in the color of the mixtures indicate chemical transformations, which are related to an increase of the conjugation of the π-system [109]. Again, the mixture was left to sediment. After some more hours, the GO particles sedimented, as can be seen in Figure 39(4), and another decantation was performed.

This process consisting of addition of water-sedimentation-decantation was repeated three times, until the dispersion turned to a black color, as observed in Figure 39(5). This occurs because the acidic medium starts to weaken, the functional groups of the GO ionize into negatively charged oxo-derived groups and the affinity with H_2O molecules increase, with the consequent delamination of the monolayers of graphene oxide and the formation of a metastable

dispersion of GO in water. At this point, sedimentation cannot be achieved even after leaving the dispersion to sediment for a long time (days).

The objective behind washing is to get rid of the sulfate and manganese ions that were intercalated into the graphitic structure [127]. With the graphene oxide layers exfoliated and the intercalated contaminants released, pH can be lowered again with the addition of hydrochloric acid (HCl) to aggregate the GO flakes and facilitate a last sedimentation-decantation step. HCl is adequate as chlorides can be easily washed afterwards.

For this purpose, HCl 37% (Pharmpur, purchased from Sharlab), was used. The amount varied between 30-100 mL of the concentrated HCl, as the different obtained GOs had different sedimentation rates (due to differences in exfoliation degree). In Figure 39(6) the final sedimentation after the addition of HCl can be observed. The solid GO again shows a brownish color, due to the restacking of the GO flakes into microparticles attracted by Wan der Waals forces due to the decrease of the ionization and the decrease of electrostatic repulsive forces.

Finally, the last decantation is performed, and the solid part is transferred to a conventional filtration paper placed in a holed tray, as shown in Figure 39(7), and dead-end filtration was performed [164]. This common filtration technique has proved to be the most effective for us, as in pump filtration the GO flakes rapidly clogged the pores of the filter, ceasing the passage of water.

After the addition of 2L of water to the filter and resting time (around 3 days), the GO recovered its black color, and became a dense paste-like mass, as can be seen in Figure 39(8). The paste, with a pH~3 and a concentration around 25 mg/mL, was then gathered and stored at 5 ºC. The reason to keep GO in acid conditions and at low temperature is to avoid decomposition of the functional groups, which are unstable in non-acidic aqueous medium after long periods of time [221], [286], [287].

3.2.4. Samples of GO prepared at varying reaction parameters

GO samples were prepared with the procedure described above at different conditions of 'reaction time' and 'temperature' in step 4 (anhydrous oxidation of graphite). The time spent by quenching the acids was not considered in the reaction time. However, the temperature was controlled indeed in all the steps, including in the quenching steps (6) and (7). This is a significant difference from the original Hummers' method [101], where the temperature in the quenching steps rose to 98 ºC, potentially affecting the resultant chemistry of the GOs.

The total number of samples prepared was 8 and they are summarized in Table 1, indicating the chronology of the syntheses. Samples were prepared using temperatures of 5, 25, 50 and 75 ºC and times of 30, 60, 120, 300 and 540 min.

Table 1: Summary of the different GOs prepared at varying reaction times (set 1, highlighted in blue) and temperatures (set 2, highlighted in red). Colors indicate the groupings of samples into two sets. The value displayed indicates the order of the syntheses.

	Temperature			
Time	5 ºC	25 ºC	50 ºC	75 ºC
30 min		**1**		
60 min		**3**		
120 min	**7**	**4**	**8**	**6**
300 min		**2**		
540 min		**5**		

For a better comparison of the samples prepared, the samples are divided into two sets. Thus, the characterization of the samples was performed set by set and the results are presented in Chapters 4 and 5, as follows:

- Sample set 1 (Table 1, in blue) comprises five samples, which were prepared with a reaction temperature of 25ºC and times of reaction of 30, 60, 120, 300 and 540 min.
- Sample set 2 (Table 1, in red) comprises four samples, which were prepared with a reaction time of 120 min and temperatures of 5, 25, 50 and 75ºC.

The specific conditions of each reaction performed for each GO are gathered in Appendix 1. There, the quantity of GO obtained, the concentration and pH of the final dispersions are also shown.

3.2.5. Post-treatment protocol

To investigate whether further purification of the prepared GO samples influenced their chemical structure, another washing procedure was performed to a fraction of the obtained paste of each GO. The newly purified dispersions consisted of 250 mL with a GO concentration of 5 mg/mL. For each paste of GO obtained after washing (Section 3.2.3), the corresponding volumes (around 50 mL) were diluted, separately, in 3 L of distilled water, and, one by one, were poured over a dead-end filter paper. The paste was washed until the drained water reached a pH of 7. After the filtration, the paste was transferred to a flask, and distilled water was added to a volume of 300 mL, and the mix was put in strong magnetic stirring (800 rpm) during 24 h to exfoliate and disperse the GO particles. Afterwards, the dispersions were stored at 5ºC. A summary of the prepared samples is shown in Table 2. For each set, at the left, the untreated GO samples prepared with our modifications of Hummers' method. At right, the obtained post-treated GO after performing the post-treatment protocol. The

time and temperature from the reaction conditions are maintained in the naming of the post-treated GOs.

Table 2: Summary of all the samples prepared in this thesis. In bold, new series of samples prepared by applying a post-treatment protocol on the GO samples of set 1 and 2.

Set 1		**Set 2**	
Sample	Post-treated	Sample	Post-treated
GO-30 min	**ptGO-30 min**	GO-5 ºC	**ptGO-5 ºC**
GO-60 min	**ptGO-60 min**	GO-25 ºC	**ptGO-25 ºC**
GO-120 min	**ptGO-120 min**	GO-50 ºC	**ptGO-50 ºC**
GO-300 min	**ptGO-300 min**	GO-75 ºC	**ptGO-75 ºC**
GO-540 min	**ptGO-540 min**		

4 THE EFFECT OF REACTION TIME IN HUMMERS' METHOD TOWARDS WELL EXFOLIATED GRAPHENE OXIDE OF LOW OXIDATION DEGREE

Summary: Graphene oxide (GO) has been synthesized by a modification of Hummers' method using different times of reaction of 30, 60, 120, 300 and 540 min while maintaining all other parameters constant and avoiding aggressive post-treatments such as sonication and strong agitation that are known to affect the chemical and structural integrity of the flakes. The morphology of the obtained flakes has been investigated by optical and electron microscopies. Chemical properties of the GOs have been determined by TGA, XRD, XPS and EDS. The degree of exfoliation strongly increased with the reaction time, while no significant differences were found between the GOs in terms of their chemistry. Thus, we demonstrate that increasing reaction time is enough for the obtention of large-sized and well-exfoliated GO flakes, while maintaining a chemical richness that would be hindered by aggressive exfoliation techniques.

4.1. MORPHOLOGICAL CHARACTERISTICS BY OM AND SEM

4.1.1. Morphology of graphite precursor

Firstly, to put in context what can we encounter when we observe the morphology of our graphitic samples, we analyze the morphology of the graphite particles used as precursor. Optical microscopy and SEM images have been obtained of the distribution of particles, which are shown in Figure 40a-b, respectively. Our graphite had a specific size of -325 mesh, which corresponds to sieved particles of less than 44 µm [173].

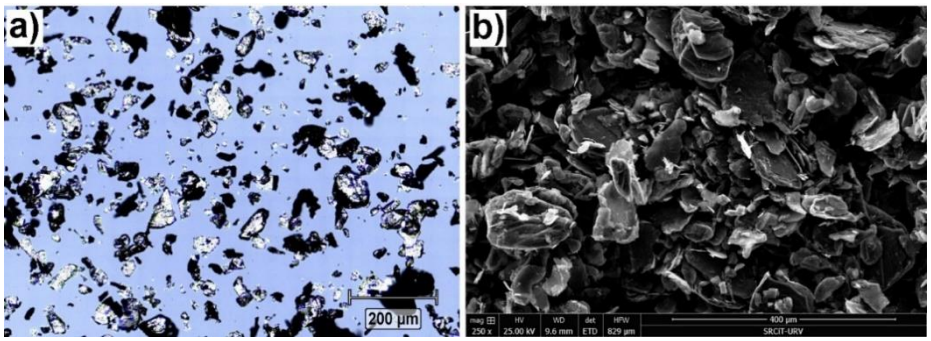

Figure 40: Morphology of the graphite flakes used for the GO syntheses. Obtained by a) Optical microscopy and b) SEM.

In the optical micrograph of Figure 40a the sizes of the particles can be observed. Note that some thick particles are out of focus, displaying a black shape. The importance of this image is that all our GO flakes will be comprised in the same range of sizes. Thus, the following optical images of the GO samples will be consistent with their parent distribution of graphite particles. In the SEM image of Figure 40b the individual flakes can be observed more

consistently, being able to perceive the layered structure and platelet shape typical of graphite.

4.1.2. Morphology of GOs of set 1 of samples

Using the optical microscope, GO samples prepared with different reaction times were observed, to obtain an overall overview about the size and thickness of the particles and observe how increasing the reaction time affects the morphology of the GO flakes. Optical micrographs of the GO samples of the set 1 are depicted in Figure 41.

Observing the dispersion of particles of the sample GO-30 min, we can notice in the center of the image that there exist several big graphitic particles. Some exfoliated flakes can be also observed, showing interference colors. These flakes are significantly smaller than the graphitic particles. Some bright flakes with thicknesses less than 80 nm are also detectable but it is important to note that most of these are very small in lateral dimensions, being observed as small dots, especially in the center-left part of the image.

Sample GO-60 min changes importantly compared to the previous sample. Flakes appear much more exfoliated, with an increase in their lateral dimensions. Tiny particles are still present but it is clear that large-sized flakes predominate. Some graphitic particles still exist but they are less numerous. Some bright and colored flakes indicate that most of the fraction belongs to flake thicknesses between 50 and 300 nm.

Sample GO-120 min consists, again, in large flakes. In this case, colored flakes are minority and almost all flakes are comprised in a thickness less than 80 nm, given by the bright blue color with low opacity. Graphitic particles are still present, but they show interference colors in their borders, indicating partial oxidation and an out-to-in exfoliation of the particles.

Sample GO-300 min presents much larger flakes compared to the previous samples, until reaching 200 µm from end to end in some individuals. Again, graphitic particles are present but most of the flakes are well-exfoliated presenting bright color with different opacities, which indicates a thickness less than 80 nm for all of them.

Sample GO-540 min is composed by large particles, in the same magnitude than the previous sample, but appears that the bright bluish flakes ere more transparent, which indicates even a lesser thickness related to a higher exfoliation. In this sample, just a few interference colors appear related to 3D graphitic particles not totally exfoliated, indicated by different colors in the same particle.

From the images observed, it can be concluded that more reaction time leads in general to a better exfoliation of the graphite particles into GO flakes.

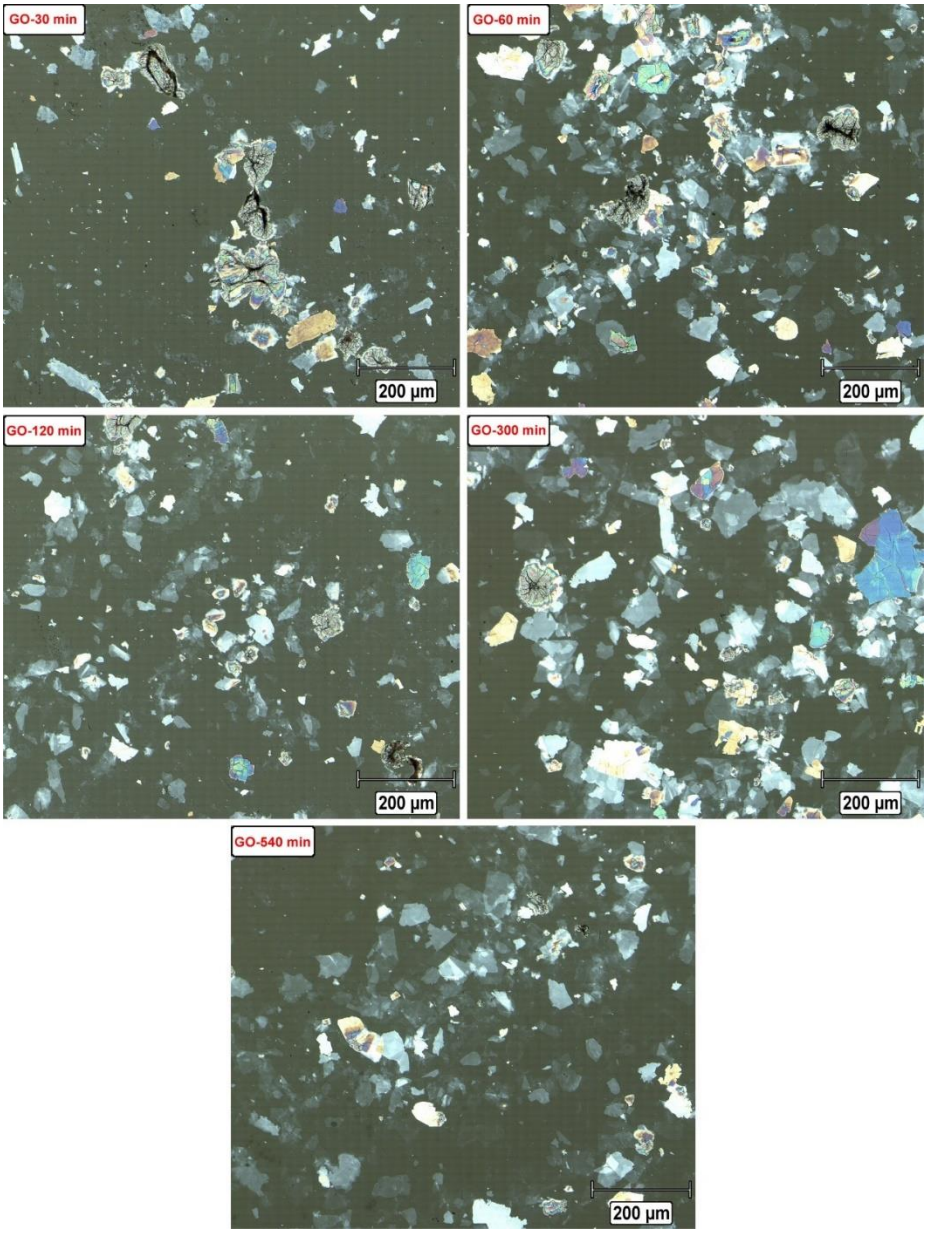

Figure 41: Optical reflection micrograph of GO samples deposited on a glass substrate. GOs belong to the set 1 of samples. Each micrograph corresponds to a sample prepared with different reaction times, as indicated.

SEM images of the micrographs of the GO samples prepared with different reaction time are shown in Figure 42. Individual flakes can be observed with different contrasts but with well-defined borders. Again, graphitic 3D particles can be observed coexisting with flat GO flakes, showing a range of contrasts with the substrate, related to their different thicknesses. The GO flat flakes tend to be smaller for the GO samples prepared with lower time, while for the samples prepared with higher reaction time larger flakes can be observed.

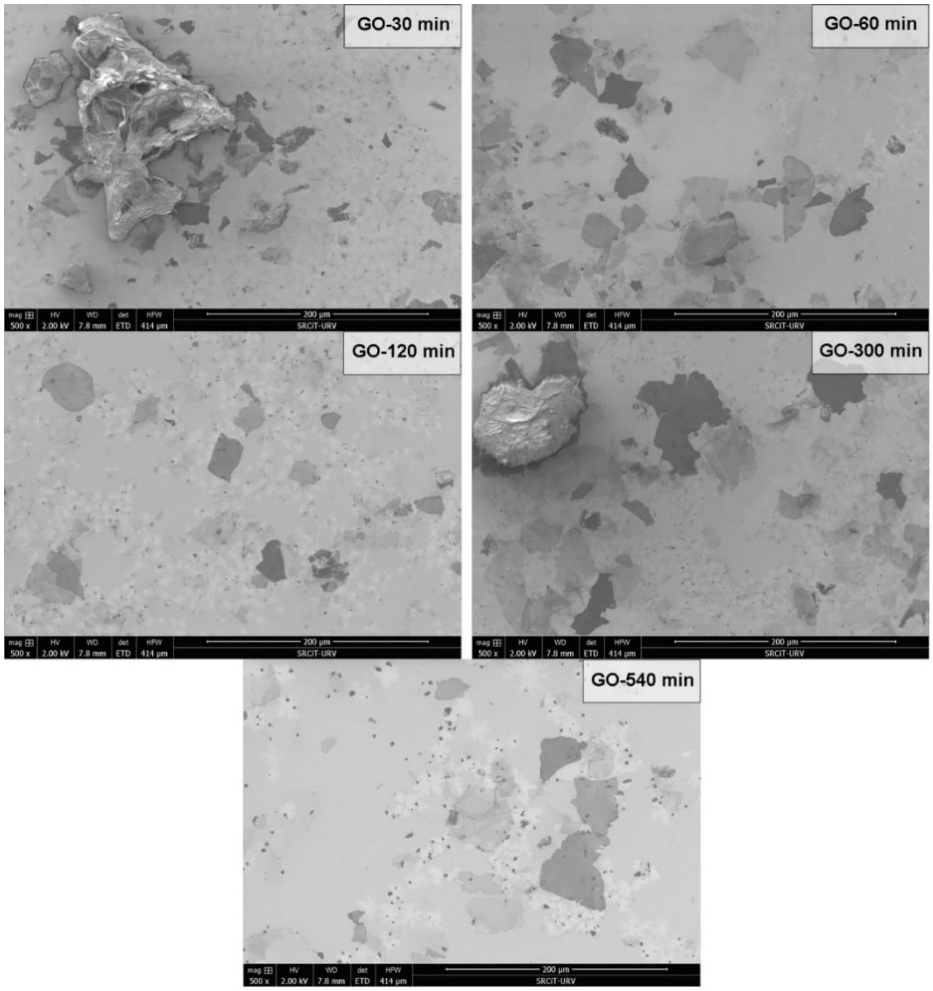

Figure 42: SEM images of the GO samples of the set 1, prepared with different reaction times.

4.1.3. Size distribution analyses of the GO flakes

In the following section we perform size statistics of the flakes from several images captured for each GO sample. Their average sizes are commonly

reported, often assuming that they follow a Gaussian distribution. However, the experimental data shows that the size distribution of GO flakes is highly asymmetric, responding better to the fitting of a log-normal model [288]. In addition, the Gaussian distribution is not adequate to characterize broad distributions of object sizes because it has finite value for negative values of the independent variable, whereas size cannot be negative.

We analyzed the lateral dimensions of the GO flakes prepared with different synthesis conditions. An example of a SEM image of the sample GO-300 min is shown in Figure 43a. The image shows that the flakes are dispersed enough to differentiate individual objects (flakes and particles). Using Adobe Photoshop, the contour of the flakes was traced to obtain their area in pixels, which can be used afterwards to obtain the area in microns. Not all the observable particles were used to perform the size statistics. The selection criteria for counting the flakes are displayed graphically in Figure 43b. Recognizable flakes of all sizes were selected (green contour). Granular, unrecognizable or flakes not fully captured were discarded (red lined). Some flakes were folded. In this case, the area of the fold was added to the area of the original flake (blue filled). Then, the area of each flake was calculated. The area of the flakes is a parameter whose values are difficult to visualize, as their range is very broad, roughly from 10 to 5000 μm^2. The high end of this range, even seeming a large number, can belong to a flake of only 50x100 µm. For this reason, instead of the sheet area the particle size was easier to visualize using a size parameter "*s*" defined as the square root of the sheet area "*A*" [289]: $s = \sqrt{A}$.

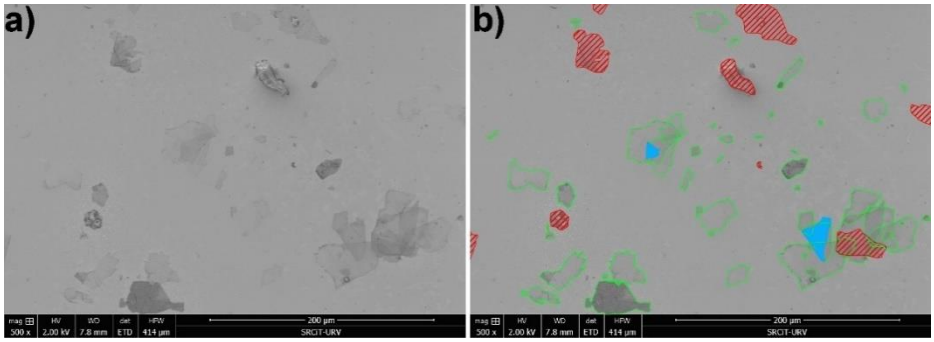

Figure 43: Methodology used to obtain size distributions from the area of the flakes through SEM images of the GO dispersions. a) Example of an original image of a GO sample. b) Same image with the selected flakes and determination of their areas. Green lines surround good flakes used for the counting. Blue lines represent clearly folded zones of the flake, which area was summed as part of a single flake. Red lines represent discarded flakes for the counting.

In Figure 44, the flake size distribution histograms of the GO samples are plotted along with lognormal distribution fits. Each was obtained from 250 flakes. The distributions tend to broaden with longer reaction time. This can be seen in the statistical information of the log-normal fittings provided in each graph. This trend can be seen in Figure 44f, in which the five log-normal fit curves are plotted together (as probability density functions with areas normalized to 100%). Whereas the extrema (mode) of the size distributions are similar, at around 10 µm, the distribution tails at large flake sizes become more prominent as the reaction time increases.

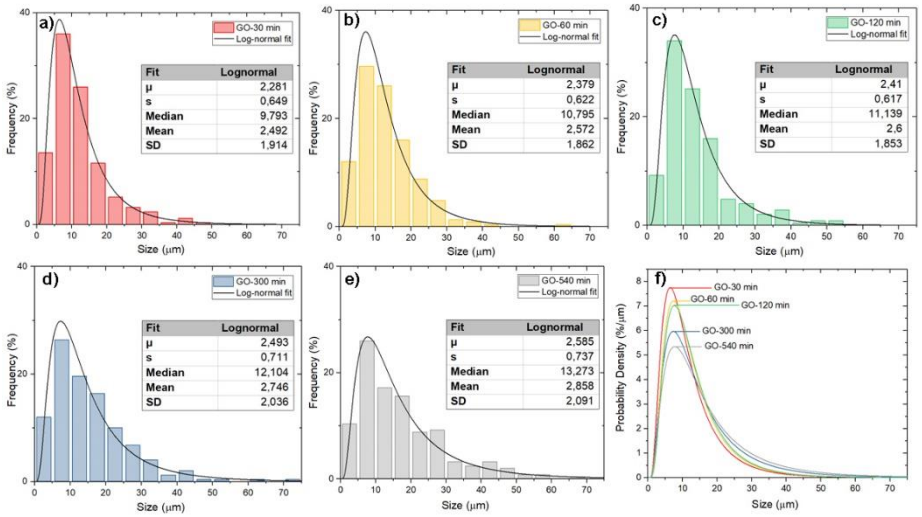

Figure 44: GO flake size histograms from 250 flakes of the GO samples prepared with varying reaction time: a) 30 min, b) 60 min, c) 120 min, d) 300 min, and e) 540 min. Log-normal fit of each distribution is show as the black line. Inset shows statistical information of each sample. f) The log-normal distributions plotted together for comparison, where the area under the curves have been normalized to 100%.

Considering that only flat flakes were counted, these results may reflect differences in the delaminating mechanism of the graphite polycrystalline particles, where small superficial flakes are the first to detach from the grain as the oxidants penetrate the particle. When the particle has been exposed for long enough to the oxidants, it splits into its larger subunits of ordered graphitic layers. This explains the behavior of the log-normal curves of broadening to higher sizes as the percentage of large flakes increases while maintaining a similar fraction of small particles, produced during the initial stages (first minutes) of the reaction.

4.2. THERMAL STABILITY BY THERMOGRAVIMETRY

Thermal stability of the GO samples belonging to the set 1 of samples were analyzed by TGA in the presence of air. For reference, the graphite used as the precursor in all the reactions was also analyzed in its as-used powder form.

Initially, we ran one TGA analysis on 1 sample per reaction time condition to have a general view of the behavior of the samples in all the range of temperatures and check the weight losses that develop until total combustion. The temperature of the furnace was brought to 1400 ºC in a ramp of 10 ºC/min.

The results obtained are represented in Figure 45a. All the GO samples follow the same thermal degradation trend regardless of the reaction time used in their synthesis, while being very different from the degradation trace of graphite. In the TGA curves of GO, three important variations of weight can be noticed, which can be verified by the first derivative trend shown in Figure 45b: (i) From 25 to 100 ºC, there is a first weight loss for the GO samples corresponding to the desorption of water [290], which constitutes around a 20% of the weight. (ii) From ~100 to 200 ºC, the thermal degradation of the oxo-functional groups, representing around a 25% of the total weight [264]. (iii) From 200 to 350 ºC, the decomposition of the organosulfates to SO_2, with a weight loss around 10%.

After the decomposition of all the functional groups, the GO samples should consist in a mildly-oxidized carbon frameworks, similar to rGO but with a bunch of holes and discontinuities in the graphitic structure [291], [292].

Later the samples stabilize until (iv) the decomposition of the carbon framework, which starts at 500 ºC and runs until 1100 ºC. At these temperatures, the graphitic framework decomposes to CO_2 in the presence of air. This is also true for graphite, which remains unaltered until 600 ºC and then, starts to decompose until the end of the analysis.

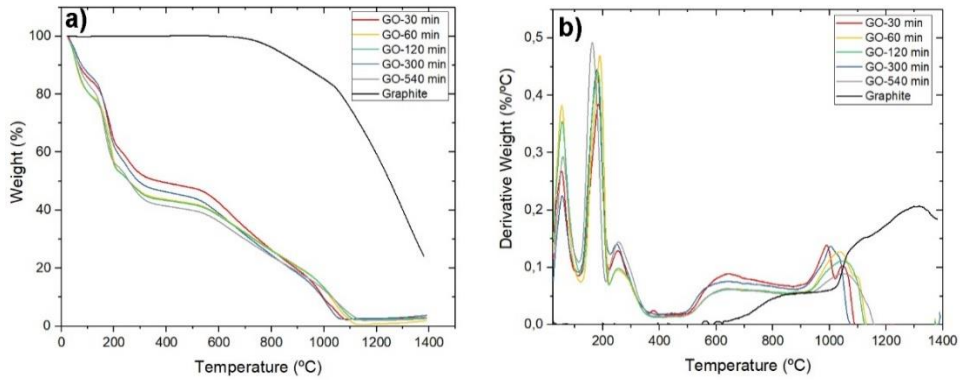

Figure 45: a) TGA curves for the GOs prepared with different reaction times and for the graphite precursor, using a ramp of 10 ºC/min in air. b) First derivative of the TGA curves.

The fact that all the GO samples follow the same trend is particularly interesting, especially for the GO-30 min sample. Considering its optical microscopy image (Figure 41), where large “graphitic” particles where present conforming the dispersion. One would have expected that the TGA curve of that sample would share similitudes with the curve of graphite. Instead, we find that the GO-30 min has a thermal decomposition behavior more similar to the GO-540 min case than that of the original graphite.

It should be pointed that the typical curves of GO have strong similarities to the TGA curves obtained for intercalated graphite compounds (GICs) [293], [294]. This could confirm the reaction mechanism of GO produced following Hummers’ method as explained in Section 1.2.2, where graphite rapidly interacts with the oxidizing media forming H_2SO_4-graphite intercalated compound (H_2SO_4-GIC) followed by the oxidation and detachment of the oxidized layers in a slower rate. Thus, we can conclude that in all the GOs, the H_2SO_4-GIC stage was reached during the reaction, while the oxidation of the inner parts of the H_2SO_4-GIC particles could have been more or less complete depending on the reaction time, causing then the slight differences between samples observable in the TGA curves.

To obtain a sharpened view of the weight losses, new thermogravimetric analyses were performed, from 25 to 400 ºC in air atmosphere, with a slower ramp of 2.5 ºC/min and repeating the samples by triplicate. In Figure 46a the median curve of the three measurements for each sample is represented. The derivative curves of the samples (DTG) have been calculated and they are shown in Figure 46b.

For all the conditions, the desorption of water already starts at 25 ºC and completes around 100 ºC. In Figure 45, the desorption of water appeared to complete at 150 ºC, but this may simply be a delay caused by the faster ramp (10 ºC/min). It is reasonable for water to be totally desorbed at 100 ºC.

After the desorption of water, the samples stabilize along a few ºC and, at 110-125 ºC, the first stage thermal decomposition of the functional groups starts taking place, ending at 175-200 ºC. The second stage of thermal decomposition immediately starts until approximately 350 ºC.

Looking closely to the derivatives, we observe that the decomposition of the oxo-functional groups, from 125 to 200 ºC has, in all the cases, a wide peak, formed probably by the sum of different peaks corresponding to different decomposition of the oxo-functional groups. For this reason, we went one step further and we analyzed the peaks of the DTG curve to find quantitative differences between samples. An example analysis of the DTG curve is represented in Figure 45d to highlight the significant weight loss events and associated temperatures. We also used these analyses to find the exact percentage of weight lost in each process and the corresponding temperatures. The methodology is explained hereafter:

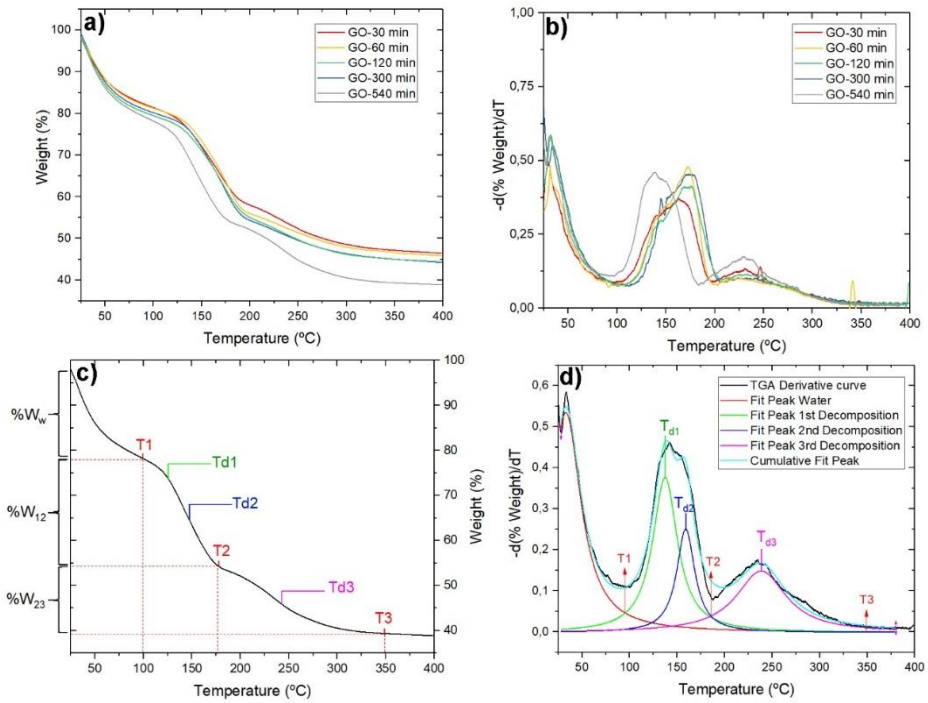

Figure 46: a) TGA performed for the quantitative analysis of the curves. a) TGA curves obtained from 25 to 400 ºC with a ramp of 2.5 ºC/min. b) Derivative curves of the TGA curves. c) Significant points for the quantitative analysis marked in one TGA curve. d) Example of how the significant points have been extracted of one derivative curve.

The DTG curves (in black) were deconvoluted in four peaks using Lorentzian fitting. The first peak is set in the first range of temperatures and corresponds to the desorption of water present in the GO samples (red line). The main peak attributed to the first stage decomposition of the functional groups (oxygen-based functional groups) is deconvoluted in two peaks. A first peak centered around 130 ºC (green line) and another peak centered around 200ºC (blue line). The center of these peaks will give us the information about the temperatures (T_{d1}) and (T_{d2}) where the different groupings of functional groups decompose. The splitting of the decomposition of oxo-functional groups in two groupings is arbitrary, but it will permit us to find differences between samples as this deconvolution allowed a good fitting of the peaks. The fourth peak is adjusted

around 250 ºC to find the temperature of decomposition of the organosulfates (T_{d3}).

From the intersection of the peaks, we extracted the starting and ending temperatures of each decomposition (T1, T2 and T3). From these values of temperature, the corresponding weights were obtained, and the weight losses were calculated as their difference, being the percentage of water lost ($\%W_w$): 100% - W_{T1}; the percentage of the oxo-functional groups degradation ($\%W_{12}$): $W_{T2} - W_{T1}$; and the percentage of the degradation of the organosulfates ($\%W_{23}$): $W_{T3}-W_{T2}$.

Hence, all the important data extracted from the derivative curves is depicted in Table 3 as a summary of the results of the GO samples of the set 1.

Table 3: Summary results table of temperatures of decomposition, percentage of weight lost on decomposition and percentage of water desorbed from each GO sample synthesized with different times of reaction.

	T_{d1} (ºC)	T_{d2} (ºC)	$\%W_{12}$	T_{d3} (ºC)	$\%W_{23}$	$\%W_w$
GO-30 min	145	172	24	246	10	19
GO-60 min	150	177	27	253	8	18
GO-120 min	149	176	26	250	8	20
GO-300 min	148	174	27	254	8	20
GO-540 min	140	163	26	240	13	21

From the quantitative data, some tendencies can be observed as a function of the reaction time of each sample. In general, temperatures of decomposition decrease with increasing reaction time. The % of weight lost in these degradations and the % of water increase. This could confirm a slight increase in the oxidation degree with the reaction time, although the samples behave too similarly to extract definitive conclusions.

4.3. INTERPLANAR DISTANCE BY X-RAY DIFFRACTION

XRD measurements were performed on sample set 1 prepared with different times of reaction and on the graphite used as a precursor in the reaction. The first measured spectra consisted in a wide scan over the 2θ range from 5º to 90º to observe all the diffraction planes that exist in our samples. These are shown in Figure 47a. The obtained curves were normalized, as graphite gave a much higher intensity, due to its high relative crystallinity. All the GO samples gave signals in the same magnitude of intensity. Graphite gave two diffraction peaks corresponding to the plane (002) at 26.6º and to the plane (004) at 54.75º. These values correspond to an interplanar distance of 3.36 Å along the c axis for graphite. For all the GO samples, the most intense peak appears around 11º, corresponding to the plane (001) and an interplanar distance of about 8 Å along the c axis. The increase of the interlayer distance in relation to graphite is caused by the expansion of the structure along the *c* direction caused by the creation of functional groups between the planes. There is a clear shift between the samples, as each GO has different properties that affect their interlayer distance. In GO samples, the plane (002) also shows a weak signal at the double 2θ value of the (001) position, at around 22º.

In Figure 47b-c, an expanded view of the low-intensity signals is shown for the GO samples and for graphite, respectively. Diffraction planes of graphite have been assigned to their corresponding signals according to reference [295]. From all the minor signals of graphite, it is worth commenting the two-dimensional lattice reflections corresponding to the (100) and (110) planes, which give signal at 42.45º and 77.55º 2θ, respectively. These two signals could be present in GO samples that conserved some aromatic domains, but they were not observed in our case.

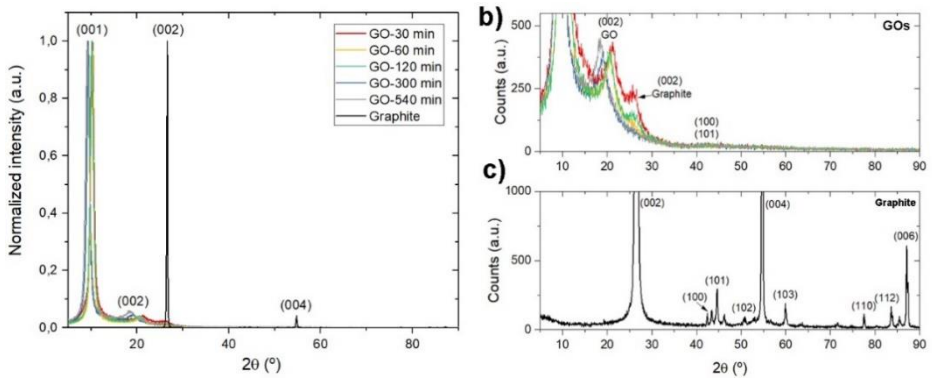

Figure 47: a) Normalized XRD patterns recorded for the GO samples of set 1 of samples, varying reaction time. Measured pattern of starting graphite has been added for comparison. On the right, an expanded view of the low-intensity signals of the b) GO samples and c) graphite.

In the expanded XRD patterns for GO (Figure 47b), a peak at 26º can be observed for some of the samples. That signal corresponds to the (002) diffraction plane of graphite residues, still present in the GO samples. The samples that show that signal are, from highest to lowest: GO-30 min, GO-120 min and GO-60 min. No apparent signal appears for the samples GO-300 min and GO-540 min. This suggests that in samples where the reaction time was lower, not all graphite was transformed to GO or was expanded by the intercalation of the oxidants. However, the intensity of the signal does not follow any monotonic trend with reaction time. Two possibilities could have caused graphite to be present in the samples: (i) too little time of reaction to fully convert graphite to GO, or (ii) remaining of graphite particles stuck to the glass walls, not exposed to the oxidants but collected with the GOs after the reaction.

In other studies [261], [296], [297], GO samples gave a signal corresponding to the (100) plane at 2θ around 42º. This signal is related to high crystallinity along the two-dimensional hexagonal lattice, being more prominent in mildly oxidized GOs samples and rGO. In our case, a very weak and broad signal can be perceived at that zone.

For a better observation and analysis of the (001) signal of GO samples, a second set of XRD measurements were performed focused on the 2θ range from 7.5 to 15º. The XRD patterns obtained are shown in Figure 48a. In this case, a shift of the peak along 2θ can be observed clearly for each sample. In Figure 48b the calculated d spacings and column lengths are represented versus time of reaction to observe the tendencies versus this parameter.

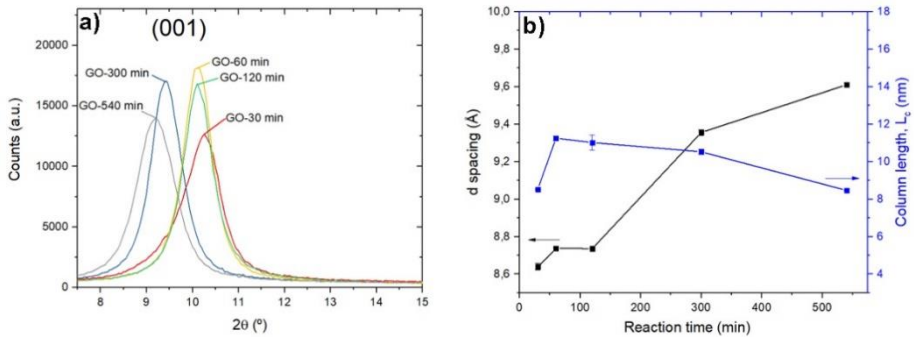

Figure 48.a) XRD patterns of GO samples prepared with different reaction times, recorded with the same ambient conditions focused on the (001) signal in the 2θ range between 7.5 and 15.0º. b) Plot of the corresponding interplanar spacing "d" obtained by the Bragg's law and column length obtained by the Scherrer equation versus the time of reaction of the preparation of each sample.

We can observe that the d-spacing increases with the time of reaction. However, it must be pointed that this increase is not very pronounced, with a difference of only 1.2 Å between the samples GO-30 min and GO-540 min. Such a distance is not enough to even fit one layer of water molecules between carbon planes [58]. This could be because the d spacing is an average obtained from many contributions over a large area of deposited GO. Therefore, the mild increase in the intercalated functional groups and water molecules in different locations of the sample may be responsible for the observed increase of the interlayer distance with reaction time, which, in addition, is consistent with the expectation that a longer reaction should generate more functional groups and greater exfoliation that retained more water molecules upon drying.

Regarding the column length, we determined values in a relatively narrow range, between 8.5 and 11.8 nm, while for the starting graphite powder the column length is 51.5 nm. There is a clear decrease in crystallinity for all the GO samples compared to graphite. However, no substantial differences between the GO samples indicates that there was no special correlation between the internal structure of the flakes and the reaction time. Thus, a greater exfoliation does not come with more disorder of the stacked layers.

4.4. DENSITY OF DEFECTS BY RAMAN SPECTROSCOPY

Raman spectra were obtained on the GOs prepared with different reaction times (set 1) and on the graphite flakes used as precursor. They are shown in Figure 49. The Raman spectrum of graphite differs greatly from the Raman spectra of the GO samples, which are similar. Graphite shows an intense G band at 1580 cm^{-1}, a minor D band at 1356 cm^{-1} and an intense 2D band at 2713 cm^{-1}. The large G and 2D to D intensity ratio indicates high stacking of the graphitic layers and low density of defects, respectively. All the GOs had similar spectra, with intense D and G bans at 1351 cm^{-1} and 1596 cm^{-1}, respectively, but a less intense 2D band at 2703 cm^{-1}, compared to graphite. The high intensity of the D band indicates a higher disorder and presence of defects for the GO samples than for graphite [278]. The shift of the G band of the GOs towards higher wavenumber with respect to graphite is attributed to the formation of new sp^3 carbon atoms by oxidation [281].

The I_D/I_G ratios of our GO samples have values of 0.96-0.97 in all cases, much larger than for graphite, which have a value of 0.24. This confirms the effective oxidation of graphite to GO in all the GO samples, as the oxygen introduction caused an increase of defects in the honeycomb structure, increasing the D band intensity. But the fact that the I_D/I_G ratios for GO are all similar indicate little differences in their quality (similar density of defects). However, when measuring GO with Raman spectroscopy, it is common to be unable to find differences related to the quality of different GO samples, because above a defect level of ~3% in the carbon sp^2 framework, the D and G bands will have the same relative intensity for all the samples [298].

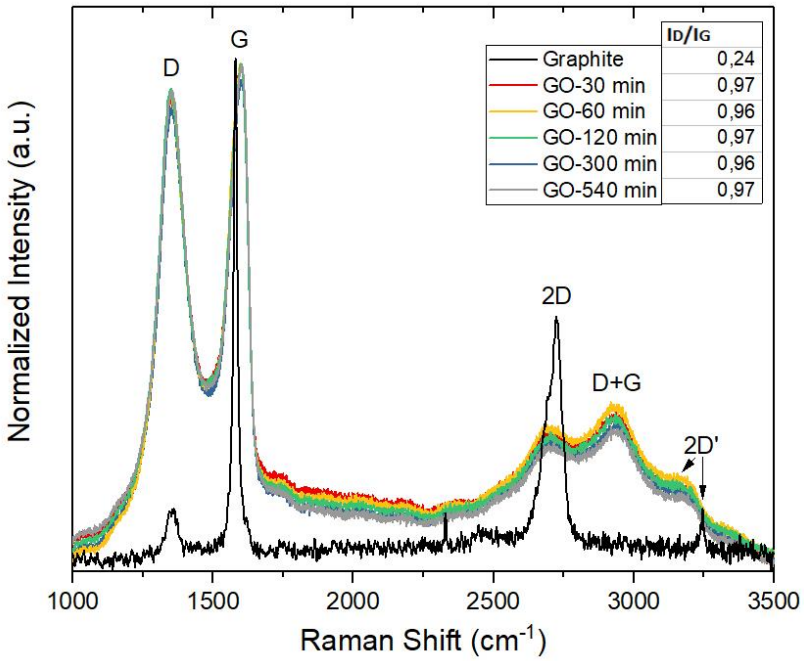

Figure 49: Raman spectra of the GOs prepared with different reaction times and for the graphite precursor. Inset: I_D/I_G ratios for each sample.

4.5. ELEMENTAL AND CHEMICAL ANALYSES BY EDS AND XPS

Energy-Dispersive X-ray Spectroscopy (EDS) and X-ray photoelectron spectroscopy (XPS) are complementary techniques that can be used to characterize the elemental composition of the GOs. EDS has a high penetration in samples, being able to obtain information from the inner parts of samples. EDS is very sensitive to detect the presence of different elements in low concentrations, however, for their quantification the limit is about 0.1 %at [250]. The technique shows even higher imprecision when the analyzed elements have low atomic number "Z" [299]. This weakness is prominent in the case of GO, which composition is mainly carbon and oxygen, but it is still useful to detect reaction remains and/or other contaminants present in the samples.

XPS's two important advantages when it is applied to GO: it provides elemental content of the sample and it is quantitative, also providing the percentage of the different oxygen functional groups on the structure. The elemental quantification is determined by running a survey spectrum where all elements constituting the samples can be detected. The most valuable information, which is the different chemical states of the carbon atoms, is obtained from the C 1s spectrum.

With the information of both techniques, the ratio between carbon and oxygen (C/O ratio) of the GO samples can be obtained, which is the main indicator used in the literature about the oxidation degree of GOs.

4.5.1. Elemental and chemical analyses of graphite

Our graphite powder used as a precursor for the reactions has been analyzed by EDS and XPS. In Figure 50, the EDS spectrum is shown, where an intensive

peak can be found at 0.3 keV corresponding to carbon, as the main constituting element of graphite. A relative intense band at 1.7 keV is present corresponding to silicon, coming from the silicon substrate holding the graphite flakes (SEM image shown in Figure 40b). Oxygen, which is usually found on the terminating carbon atoms of graphite [255], [300], was not detected.

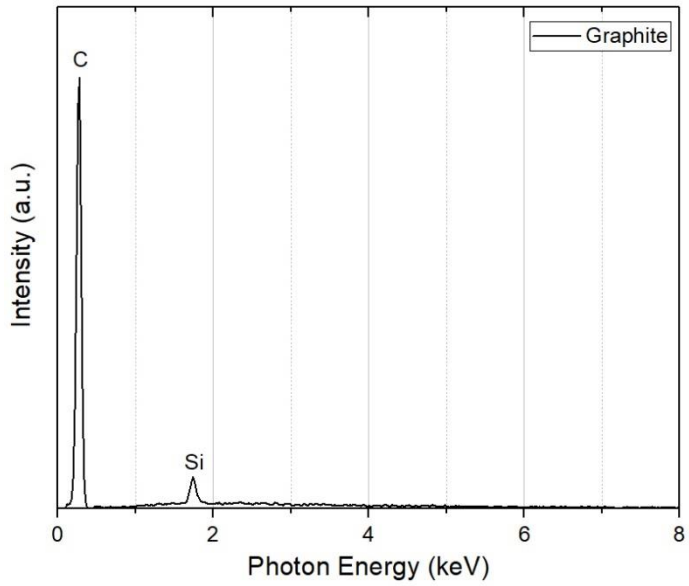

Figure 50: EDS spectra of graphite used as a precursor.

The elemental composition at the surface of our graphite flakes by XPS was obtained from survey spectrum shown in Figure 51a, which contains peaks corresponding to C 1s, O 1s and Si (2p and 2s) binding energies, the latter being due to the substrate, as for EDS. The relative abundances of carbon and oxygen obtained were 96.5% and 3.5%, respectively. The high amount of oxygen detected by XPS is probably because the edges of the graphitic structure are prone to be oxygen-terminated [300], which are detected in higher

concentration when probing only the surface of the graphite flakes instead of their bulk (by EDS).

In Figure 51b, the C 1s spectrum of graphite is shown, where we encounter a single band centered around 284.8 eV, which is the typical band of the graphitic framework, including C-C, C=C and C-H bonds [258]. This band is assigned to the graphitic domains, as long they are not chemically bound to oxygen atoms. Even if the carbon is not pure sp^2, it will generate a signal in this area. The asymmetry of the peak is due to the presence of a minor component around 286 eV originated from oxygen functional groups at the edges of the graphene layers [300]. Lastly, a low-intensity peak at 191.4 eV corresponds to π-π* interactions, proving the quality of the sp^2 graphitic structure [259].

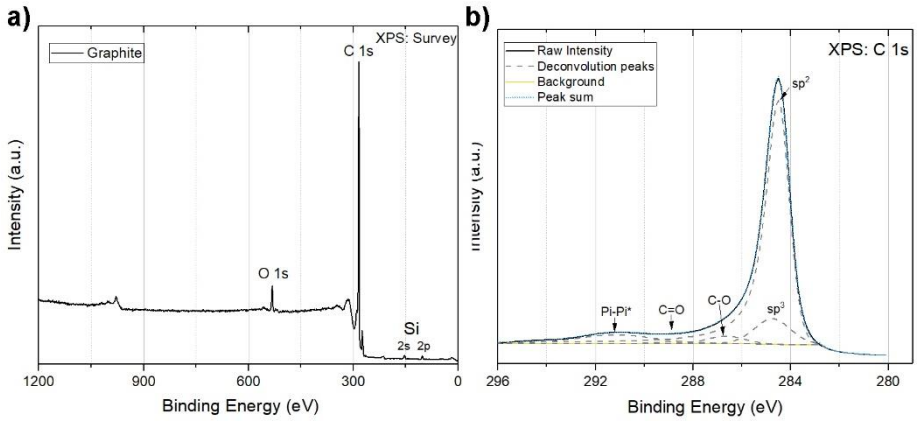

Figure 51: a) XPS survey spectra of graphite used as a precursor. a) Survey spectrum. b) High-resolution spectra of the C 1s band.

4.5.2. Bulk atomic composition of the GOs by EDX

Bulk samples of the GOs from samples' set 1 were analyzed by EDS to obtain the atomic concentration of each GO prepared at different times of reaction.

For each condition, the averaged EDS spectrum of 5 spectra obtained at different locations in each sample is shown in Figure 52.

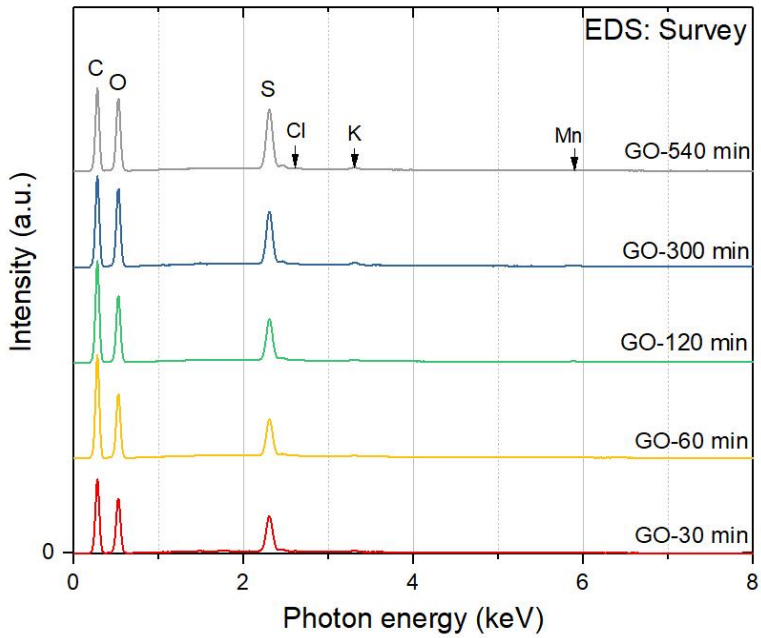

Figure 52: EDS spectra of the GO samples of the set 1 with the detected elements indicated.

The main elements detected are carbon (C), oxygen (O) and sulfur (S), as the known elements that form GO with its functionalities. Other elements detected by EDX are chlorine (Cl), potassium (K) and manganese (Mn). Chlorine is present in the samples because of the washing procedures where hydrochloric acid was used to acidify the dispersions of contaminated GO and facilitate the sedimentation-decantation steps (Section 3.2.3). Although the presence of chlorine is inelegant, as it is a deliberately added contaminant, its presence in GO samples is somewhat reiterative and accepted in the technical literature [107], [301], [254], [302]. Potassium and manganese remained in our GO

samples from the synthesis procedure, trapped in K_2SO_4 and $MnSO_4$ [107], [147].

The fact that the presence of chlorine is residual in the samples which were prepared with lower time of reaction and relatively high in samples with higher time of reaction responds only to the purification process performed. As seen in the morphology results (Section 4.1), using more time of reaction effectively led to a higher exfoliation of the GO sheets. This had an impact in the washing procedures of the GO samples: (i) in the sedimentation-decantation procedure, more HCl had to be added to accelerate the sedimentation, as well-exfoliated GO sheets tended to remain in suspension for too long periods of time, whereas high amounts of added HCl caused the particles to agglomerate and sediment. (ii) On the other hand, in the filtration process, the same circumstance was present. Well-exfoliated distributions tended to clog the filter faster and extensively, leading to a slow and less effective washing. Both factors have contributed retaining chloride ions between the GO sheets which was encouraged by the higher exfoliation of the flakes obtained for higher reaction times.

4.5.3. Surface chemistry of the GOs by XPS

Chemical surface of the GOs of the set 1 of samples was analyzed by XPS to obtain the atomic concentration and the quantification of functional groups present in the surface of each GO sample.

XPS survey spectra of the GOs is shown in Figure 53a, where all the samples reproduce the same typical pattern of GO, obtaining in all cases two intense peaks corresponding to the C 1s (around 285 eV) and the O 1s (around 530 eV) orbitals. The S 2p peak can be seen around 168 eV and has been also analyzed. Other peaks present in all samples are the S 2s (232 eV) and, surprisingly, an unexpected, although small, N 1s peak (401 eV) [303]. Nitrogen

was not detected by EDS in any of our samples despite being in the reagents as $NaNO_3$. Being detectable by XPS could mean that its presence is higher at the surface than in the core of the particles. However, the reason behind this is unclear. It could also be caused by external contamination.

Other elements detected by EDS are K, Cl and Mn, which would show binding energies around 295 eV (K 2p), 195 eV (Cl 2p) and 650 eV (Mn 2p). However, they were not detected by XPS. In this case, these elements could be trapped in the inner core of the unexfoliated particles but washed from the surface. For this reason, they can be detected by EDS but not by XPS.

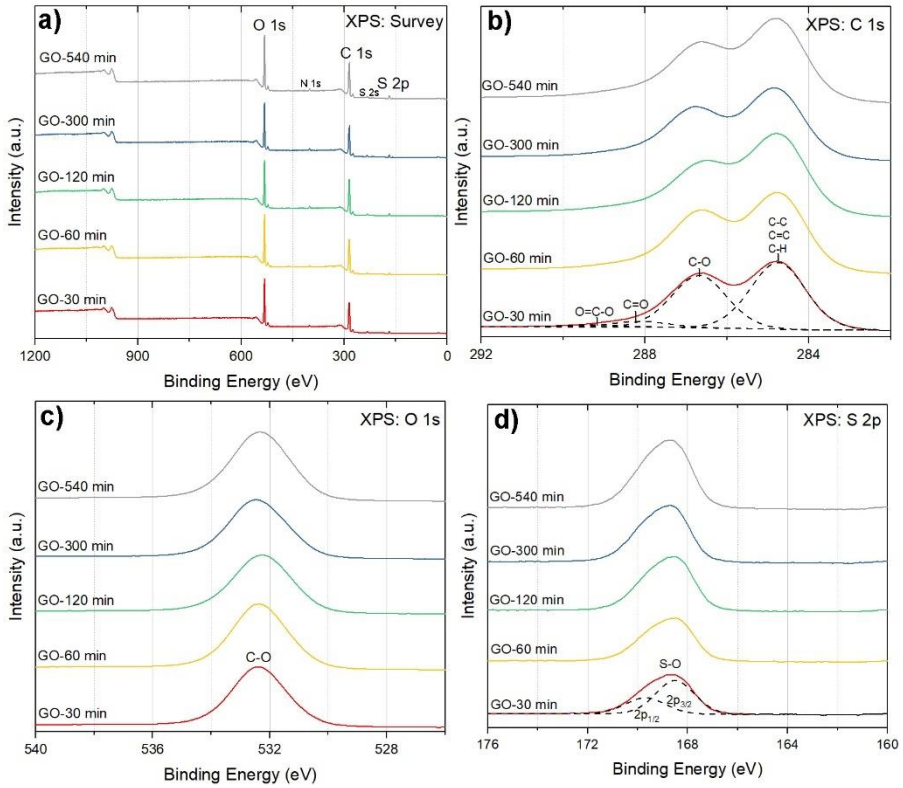

Figure 53: a) XPS survey spectra of the GOs prepared with different reaction times. High-resolution spectra of b) C 1s, c) O 1s and d) S 2p. Deconvolution was performed for all the spectra but is shown only for the 30-min lines.

For the analysis of the functionality of the GOs, high resolution spectra of the C 1s peak was obtained, which are shown in Figure 53b for the five samples. In the literature, different ways of deconvoluting the integral C 1s spectra can be found [260], [255], [261], where the C 1s spectra is deconvoluted in all sorts of functional groups that may constitute GO. However, the low binding energy shift between similar functional groups makes these deconvolutions highly speculative, even for comparative purposes. For this reason, we present the deconvolution of the C 1s spectrum of our GOs in just four components, with the following assignations [304]:

- C-C, C-H and C=C bonds to 284.8 eV;
- C-O bonds to 286.7 eV;
- C=O bonds to 288.2 eV;
- O-C=O bonds to 289.4 eV.

The deconvolution, despite being performed for all samples, it is represented visually only for the first line for clarity. The most intense peak at 284.8 eV is assigned to the graphitic domains. The peak at 286.7 eV is attributed to the carbon atoms of epoxides (C-O-C) and tertiary alcohols (C-OH). These two components, despite being the most important functional groups of the basal planes, are entangled and cannot be separated due to the large number of configurations that can be found in GO, leading to spectral broadening. The low intensity peak at 288.2 eV corresponds to ketones (C=O), quinones (O=C-C=O), and aldehydes (HC=O). Lastly, the less intense signal at 289.4 eV comprises the carboxylate derivates such as carboxyls (O=C-OH), lactols, and esters (O=C-O-C). It can be observed that the GO samples prepared with different times of reaction exhibit similar patterns with small changes in the relative intensity of the peak situated at 286.5 eV.

Although O 1s spectra of GO do not give much more information about the chemistry of GO, as all the C-O bonds are overlapped in the same band near 532 eV, they were recorded to check any observable deviation. The high-

resolution spectra of the O 1s spectra of the GO samples are shown in Figure 53c. The signal apparently corresponds to a single component. In the literature, however, this signal has been deconvolved into between 2 and 4 components [193], [255]. However, these deconvolutions are speculative and are generally assigned to match the quantification of the functional groups assigned with the C 1s spectra. For this reason, here we avoid assigning components to this peak, beyond identifying it as gathering the C-O contribution from all the functional groups.

Finally, the high-resolution spectra of the S 2p peaks has been obtained and is shown in Figure 53c. In this case, a 2p spin orbit splitting occurs, which causes the peaks to be formed by the sum of the areas of the two spin orbit peaks ($2p_{1/2}$ and $2p_{3/2}$) with an area ratio of 1:2 (corresponding to 2 electrons for the $2p_{1/2}$ level and 4 electrons for the $2p_{3/2}$ level). In the case of sulfur, the separation between the peaks is always 1.18 eV [305]. As both peaks correspond to the same S-O bond, this leads to the 100% of signal to be assigned to sulfur bonded to oxygen atoms in form of organosulfates.

Table 4 displays the elemental compositions of the samples as obtained by XPS and by EDS. The relative atomic abundances vary little from sample to sample, with no clear tendencies with the reaction time, except maybe an increase of the sulfur content. By XPS, carbon content is around 74%, oxygen around 24% and sulfur around 2%. The C/O ratios by XPS have values around 3, which are on the high end of the ranges reported by other XPS studies, such as [105], [142], [255], where typical C/O ratios range from 1 to 3. In fact, the C/O ratios obtained for these samples are in the low range of ratios obtained for mildly reduced GOs and thermally treated GOs, with C/O values of 3-6 [144], [306]. Chemically reduced GOs (rGOs) have higher C/O ratios, ranging between 5-15 [307]. We therefore conclude that our samples are less mildly oxidized because of the preservation of the low temperature during the reaction [19].

By EDS a higher oxygen abundance has been found than by XPS, thus lower relative abundance of C. This difference with the XPS analysis may be due to the greater penetration of the electron beam in EDS, and its detection of oxygen in retained water, which had been previously quantified at 20%wt by TGA. Interestingly, the C/O obtained by EDS, despite being lower than by XPS, follows the same tendency along the samples as the C/O ratio obtained by XPS.

A higher quantity of sulfur can be also detected by EDS than by XPS. This could be because organosulfates, which can be hydrolyzed to vicinal diols [109], are more prone to suffer hydrolysis if they are at the surface of the GO flake, whereas if they are intercalated in the graphitic structure, they are more protected from nucleophilic attack. For this reason, sulfur concentration could be lower at the flakes' surface than in their bulk.

Table 4: Relative atomic abundances of the GO samples from XPS and EDS elemental analyses.

	XPS Elemental composition (At%)				EDS Elemental composition (At%)				
	C	**O**	**S**	**C/O**	**C**	**O**	**S**	**Others***	**C/O**
Graphite	96.5	3.5	-	**27.57**	100.0	-	-	-	-
GO-30 min	74.0	24.2	1.8	**3.06**	48.5	48.5	2.8	0.3	**1.00**
GO-60 min	74.6	23.7	1.8	**3.15**	50.3	47.2	2.3	0.2	**1.07**
GO-120 min	75.0	22.7	2.3	**3.30**	49.8	47.5	2.5	0.2	**1.05**
GO-300 min	73.1	24.4	2.5	**3.00**	47.2	49.4	3.0	0.4	**0.96**
GO-540 min	72.6	24.8	2.6	**2.93**	47.1	49.1	3.5	0.3	**0.96**

* Others: Cl, K, and Mn.

The relative abundance of the deconvoluted components of the XPS C 1s spectra is shown in Table 5. From the C 1s assignations, C-O components, epoxides (C-O-C) and hydroxyls (C-OH) are the most abundant functional groups of all samples by far. A slight tendency with reaction time can be observed in which the C-O bonds decrease while C=O and O-C=O bonds increase, as the hydroxyls and epoxides oxidize to carbonyls and carboxyls.

Also, as the latter, most oxidized functional groups can only be present at the edges of the carbon grid, a higher amount could arise from a higher fragmentation of the carbon hexagonal lattice. But, again, the differences are not great, and we find less abundance of these most oxidized functional groups than have been reported in other studies. For example, the proportion of C-O/C=O/O-C=O tends to be around 35%/15%/5% for GO prepared with Hummers' method [142], [255], [36], which means that our GOs have a higher fraction of less-oxidized functional groups.

Table 5: XPS compositional analysis of the C 1s spectra of the prepared GOs.

	XPS C 1s (At%)			
	C-C, C-H, sp2	**C-O**	**C=O**	**O-C=O**
GO-30 min	52.7	41.2	4.5	1.6
GO-60 min	54.0	39.8	4.6	1.7
GO-120 min	57.7	35.2	5.3	1.8
GO-300 min	55.8	38.5	4.5	1.3
GO-540 min	55.5	36.8	5.7	2.0

4.6. CONCLUSIONS

We have reported a synthesis procedure of graphene oxide using a modification of Hummers' method, varying the time of reaction from 30 to 540 minutes. The morphological characterization of the samples showed that the reaction time correlates strongly with a greater exfoliation of the graphite oxide particles into thin flakes with large lateral dimensions. Thermal degradation by TGA showed that all the samples degrade similarly and very differently from the graphite precursor, with three weight losses corresponding to the desorption of water, the decomposition of the oxo-functional groups and the decomposition of the organosulfates. XRD patterns show a gentle increase of interlaminar spacing versus sample reaction time, attributed to the greater exfoliation of the flakes. The average number of stacked layers ranges from 9 to 13 units. Raman spectroscopy confirms the oxidation of graphite to GO in all the samples, with no differences in the density of defect of the GOs. Compositional characterization shows no significant differences between the GOs prepared at different reaction times, neither in the analysis of the flakes surface by XPS or in that of the bulk of the flakes by EDS. Yet, our GOs have a higher fraction of less-oxidized functional groups than are found in the literature. Thus, we conclude that increasing reaction time can be a splendid route to obtain well-exfoliated GO without causing over-oxidation of the material, avoiding high damage to the carbon honeycomb and preserving the relative quantity of functional groups. Hydrolysis of the organosulfates is avoided because of the sustaining of low temperature in all the reactions. Then, controlling reaction time is interesting in applications where well-oxidized GO of low functionalization or with high relative presence of thermally-unstable functional groups are sought.

THE EFFECT OF REACTION TEMPERATURE IN HUMMERS' METHOD ON THE CHEMISTRY AND MORPHOLOGY OF GO

5

Summary: The effect of the reaction temperature on the morphology and chemistry of the GO flakes is studied. The GO samples (set 2) prepared at constant reaction time of 120 min and at varying reaction temperatures of 5, 25, 50 and 75 ºC were characterized following the same methodology as used for the samples of the previous chapter. Both the exfoliation and chemical characteristics varied much depending on the temperature, obtaining an incomplete reaction when the temperature was too low, and a high oxidation when temperatures were increased. The exfoliation of the flakes was notably higher with high reaction temperature, but the chemical composition changed with the hydrolysis of the organosulfates and the relative increase of the most stable oxo-functional groups.

5.1. MORPHOLOGY OF THE GO FLAKES

The morphology of the set 2 GO samples prepared with different reaction temperatures (Table 1) was studied by optical and electron microscopy in the same manner as the GO samples prepared using different reaction times (Chapter 4).

Optical micrographs of the set 2 GO samples are shown in Figure 54. Notable differences between the distribution of sizes of the samples can be noticed, as it happened for the GOs prepared with different reaction time.

Sample GO-5 ºC appears to be fully constituted of relatively small particles and flakes. Some exfoliated flat flakes can be observed with low opacity, but numerous small colored tridimensional particles are also present. In this sample, no large flat flakes are observed. Sample GO-25 ºC corresponds to the sample GO-120 min of the set 1, and the observable distribution of flake sizes in the figure is similar as seen before in Figure 41 for this condition, being formed by large flat flakes displaying different opacities and colors of interference. Some graphitic big particles are also present in this sample. Sample GO-50 ºC shows that most flakes are flat, large, and semi-transparent, indicating high exfoliation degree. Colored flakes and graphitic particles are still present to some degree. The sample GO-75 ºC presents a great fraction of large and semi-transparent objects, which are well-exfoliated GO flakes. Compared to GO-50 ºC the flakes show less opacity, indicating that these flakes have smaller thickness. Some big graphitic particles are still present.

These results show a clear tendency of increased exfoliation with increasing temperature. The increase of the exfoliation with the oxidation temperature has been observed in studies where small temperature changes were applied to Hummers' method [191]. The reason for such a behavior would be the fastest intercalation and the formation of new functionalities on the basal planes of the GOs [124], forming more hydrophilic spots in the graphitic plates, increasing the negative potential of the surface of the flakes [192], and favoring the spontaneous exfoliation in water dispersion.

SEM images of the GOs of the set 2 of samples are shown in Figure 78.

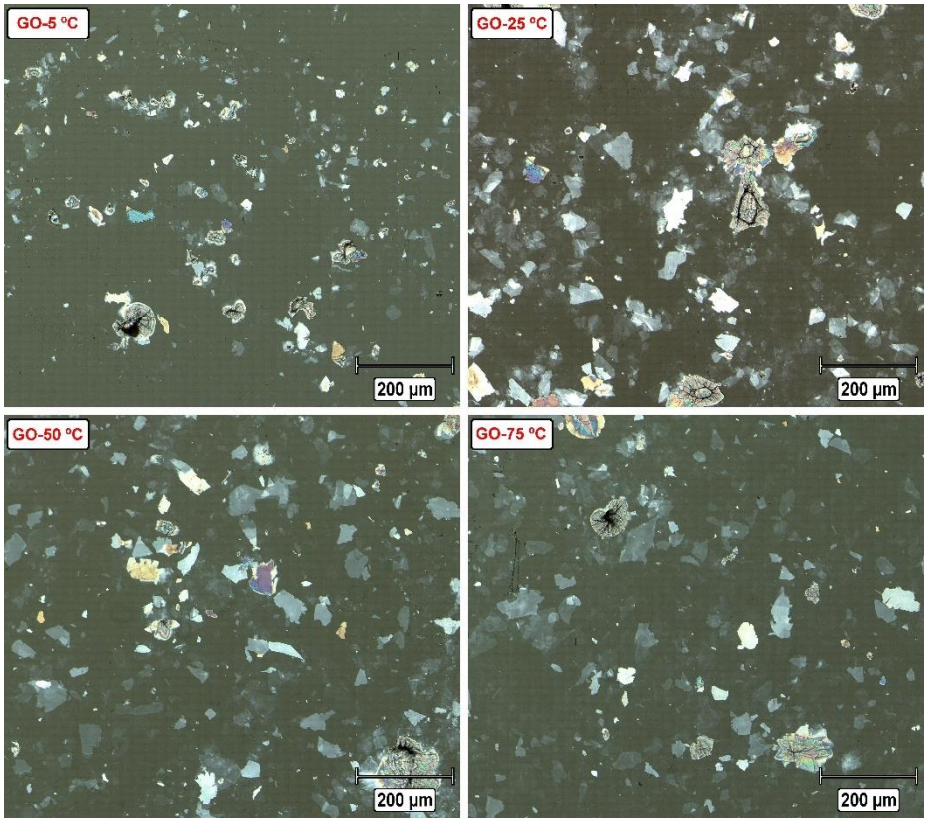

Figure 54: Optical reflection micrographs of GO samples deposited on a glass substrate, belonging to sample set 2. Each micrograph corresponds to a sample prepared with different reaction temperature, as shown.

In Figure 55, the GO flake size histograms of the samples prepared with different reaction temperature are presented, where an increasing tendency of the flake size versus the reaction temperature can be noticed, which confirms the effect of the higher reaction temperature leads to the effective exfoliation of the particles into larger flakes. In this case, a huge difference was found between the sample GO-5 ºC and the other samples, indicating for this sample the existence of only small flakes within the flat objects encountered, and of a clear ineffective oxidation of the graphite particles. Probably for this reason, Eigler et al., whose method served as a basis of our reactions, increased the reaction time over 16 h when they performed their reaction method with

temperatures below 10 ºC [19], as these low temperatures are not sufficient to obtain exfoliated GO flakes with an acceptable yield.

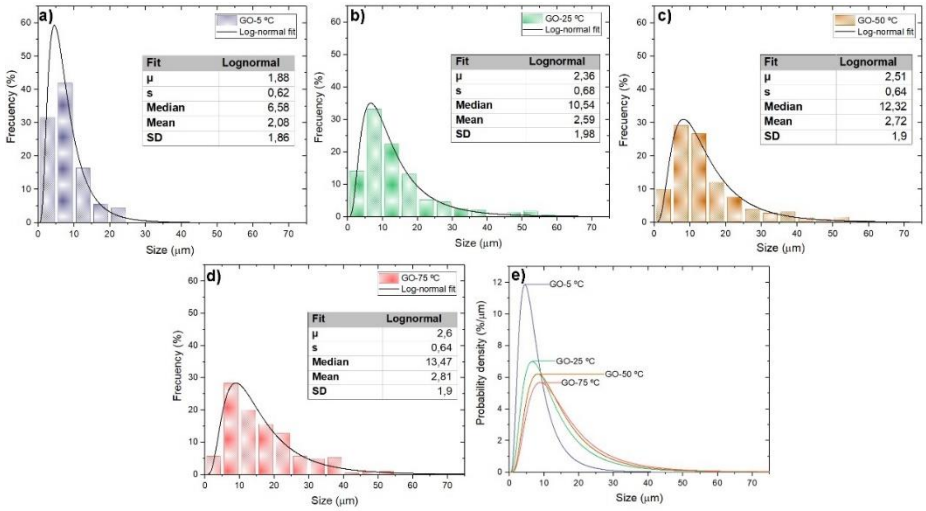

Figure 55: GO flake size histograms from 250 flakes of the GO samples prepared with varying reaction temperature: a) 5 ºC, b) 25 ºC, c) 50 ºC and d) 75 ºC. Log-normal fit of each distribution is show as the black line. e) The log-normal distributions plotted together for comparison, where the areas under the curves have been normalized to 100%.

5.2. THERMAL STABILITY OF THE BULK GOS

TGA experiments were performed on the GO samples prepared with different reaction temperatures. The TGA curves and their derivative are shown in Figure 56. Comparing the derivative curves, we can observe an important change of these samples compared to those of sample set 1 prepared with different reaction times, shown in Figure 46. The derivative curves of samples GO-5 ºC and GO-25 ºC have a similar shape to those obtained for set 1, with a wide weight loss along a range of temperatures from 100 to 200 ºC. However, samples GO-50 ºC and GO-75 ºC have a more sharpened weight decay centered at 200 ºC. This change in behavior indicates the possibility of differences in the chemical structure of the samples.

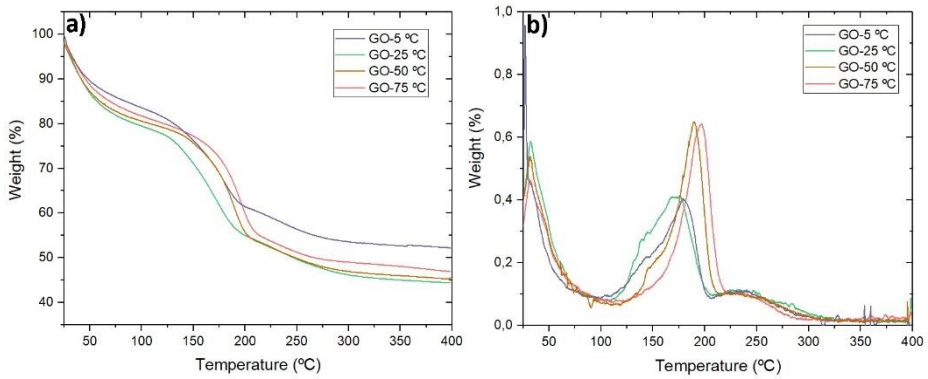

Figure 56: TGA curves (a) and their corresponding derivative curves (b) of the samples of the set 2 prepared with different reaction temperature.

In Table 6, the quantitative data obtained from the curves is presented. From these data a clear growing tendency of the temperatures of decomposition of the oxo-functional groups (Td1 and Td2) with reaction temperature, despite the percent weight loss in these decompositions (%W12) being similar for all the samples. The decomposition of organosulfates (Td3) occurs for all the samples

at the same temperature, around 250 ºC; but there is a clear decrease in the weight loss (%W23) on the samples prepared with higher reaction temperatures (from 8% to 5%). Absorbed water (%Ww) is similar in all the samples (~20%) except for the sample GO-5 ºC, with less amount of water in the sample, probably due to the low exfoliation degree of the particles. Well-exfoliated big flakes would retain more water upon drying at room temperature (see reparation of the TGA samples on section 3.1.5).

Table 6: Summary results table of temperatures of decomposition, percentage of weight lost on decomposition and percentage of water desorbed from each sample of sample set 2.

	Td1 (ºC)	Td2(ºC)	%W12	Td3(ºC)	%W23	%Ww
GO-5 ºC	151	179	24	246	8	16
GO-25 ºC	149	176	26	250	8	20
GO-50 ºC	168	190	28	257	5	21
GO-75 ºC	172	195	28	251	5	20

These TGA results indicate that the samples prepared with more reaction temperature have more stable oxo-functional groups and less amount of organosulfates. It is known that there is a relationship between the amount of functional groups and the weight loss of the GO samples (%W12), as more oxidized samples contain more defects and are thus more likely to decompose into CO and CO_2 [308]. In our case, the degree of oxidation is not clearly different between samples because the weight losses are similar in all cases. However, the temperatures of decomposition (Td1 and Td2) increase as the reaction temperature increases and, considering that the dissociation energies of the GO oxo-derived bonds increase in the following order: C-O-C < COOH < HO-C-C-OH [309], we infer that the samples prepared with higher reaction temperature have a greater amount of (more stable) hydroxyls than epoxides and carboxyls. Also, as organosulfates had hydrolyzed to vicinal diols in samples prepared with high temperatures [126], these samples would be rich

in hydroxyls, but at the expense of losing chemical diversity (organosulfates and epoxides) and of generating new holes in the carbon grid (due to loss of carbon in form of CO and CO_2) [49], [310].

The smaller presence of organosulfates for samples prepared with higher reaction temperature has been also found in studies where this parameter was studied [193], indicating that high temperatures during the quenching with diluted acid and water (steps 7 and 8) leads to the hydrolysis of the organosulfates [145].

5.3. INTERLAYER DISTANCE OF THE BULK GOS

XRD measurements were performed to the GO samples prepared with different reaction temperatures. In Figure 57a, the expanded XRD patterns of the samples is shown. The most intense signal corresponds to the (001) plane for all the samples, located around 2θ of 10º, while the (002) plane is also present with less intensity around 2θ of 20º. A signal at 26º is present for samples GO-5ºC and GO-50ºC, belonging to the (002) plane and corresponding to unreacted graphite particles. This signal is relatively intense for sample GO-5ºC, due to the greater presence of unreacted graphite in this sample. Furthermore, for this sample, a new signal is present at 16.3º. This signal has been identified as a (002) signal from an intermediary graphite intercalated compound present during the reaction [297], [311], but it is not commonly found in the GO literature. MnO_2 or $MnSO_4$ crystals, if present, would give a signal around 17º [312], [313], but they have been discarded as no presence of Mn was detected in this sample by EDS (see below)..

In Figure 57b, the expanded view of the (001) signal is shown. In this case, except sample GO-5 ºC, the samples follow a tendency of shifting towards higher angles with increasing reaction temperature. The interplanar distances and the column lengths, as calculated from Bragg's law and Scherrer's equation, respectively, are plotted as a function of reaction temperature in Figure 57c.

The d distances show a decrease versus reaction temperature, with exception of sample GO-5 ºC, which has the lowest d distance. The reason of this behavior is unknown, but could be related to an incomplete reaction caused by the low temperature used, causing the slow penetration of the oxidants into the graphitic galleries combined with a slow oxidation of the reactive points [127], [19], yielding graphite oxide particles with relatively less oxidated and compacted cores. Again, considering that graphite presents an interlayer distance of 3.3 Å, the GO-5 ºC sample is still more related to GO than to

graphite, in terms of its structure. The Lc values do not show a clear a tendency of the stacking order to increase or decrease as a function of reaction temperature.

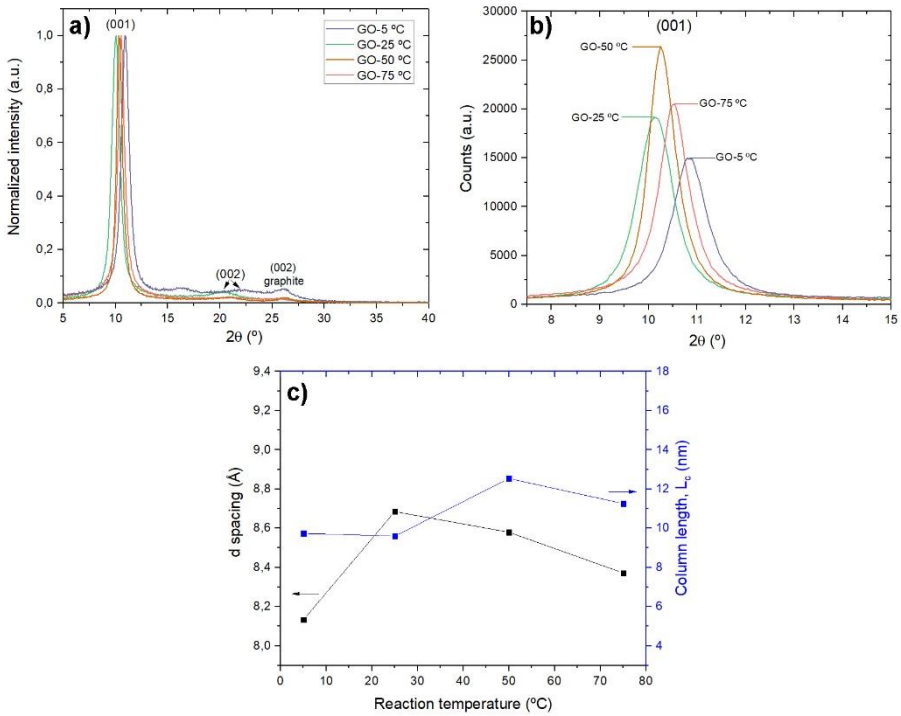

Figure 57.a) Normalized XRD patterns for the GO samples of the sample set 2 of samples, varying reaction temperature. b) (001) signal expanded view of the same samples in a 2θ range between 7.5 and 15.0º. c) d spacing and column length of the samples as calculated from Braggs law and Scherrer equation, plotted versus reaction temperature.

5.4. RAMAN SPECTRA

The GOs of sample set 2 prepared with different reaction temperatures were measured by Raman spectroscopy and the results are shown in Figure 58. As it happened for the samples of set 1 (Figure 49), all the GO samples of this set 2 present the same Raman spectra, with I_D/I_G ratios of 0.96-0.97. We conclude that discrimination by Raman spectroscopy of GO samples which differ only in the reaction temperature (made by our modified Hummer's method) is not possible or likely.

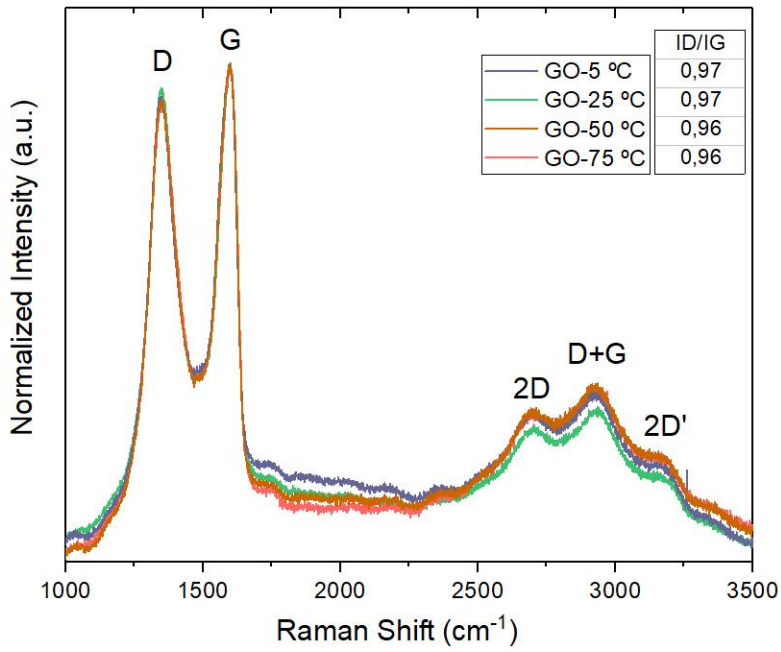

Figure 58: Raman spectra of the GO samples of the set 2. Inset: I_D/I_G ratios for each sample.

5.5. ELEMENTAL COMPOSITION OF THE GOS

Elemental compositions of the GO samples prepared with different reaction temperatures were obtained by EDS and XPS.

Bulk samples were analyzed by EDS, obtaining the atomic concentration of the elements present in the samples, including possible impurities coming from the reaction and washing procedures. The EDS spectra of the GO samples is shown in Figure 59, where the detected elements are indicated.

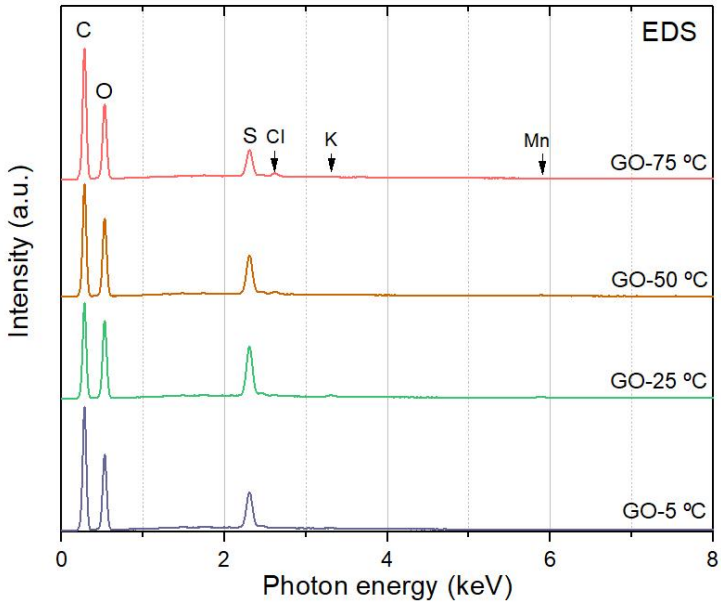

Figure 59: EDS spectra of the GOs prepared with different reaction temperature, with the detected elements indicated.

As it happened for the GO samples of sample set 1 (Figure 52), the main elements detected (C, O and S) belong to the chemical structure of GO, and

Cl, K and Mn are detected as impurities remaining from the reaction and washing procedures.

From the XPS analyses, information about the relative atomic abundances and the chemical functionalization was obtained. The XPS survey spectra are shown in Figure 60a and the high-resolution spectra of the C 1s, O 1s and S 2p orbitals are shown in Figure 60b-d, respectively. The C 1s spectra already shows important differences among the samples, with different relative intensities between the signal attributed to the C-O bonds and the signal of the graphitic domains (C-C, C=C, and C-H). Components were assigned as in the previous chapter: C-C, C=C and C-H (284.8 eV), C-O (286.7 eV), C=O (288.0 eV) and O-C=O (289.0 eV).

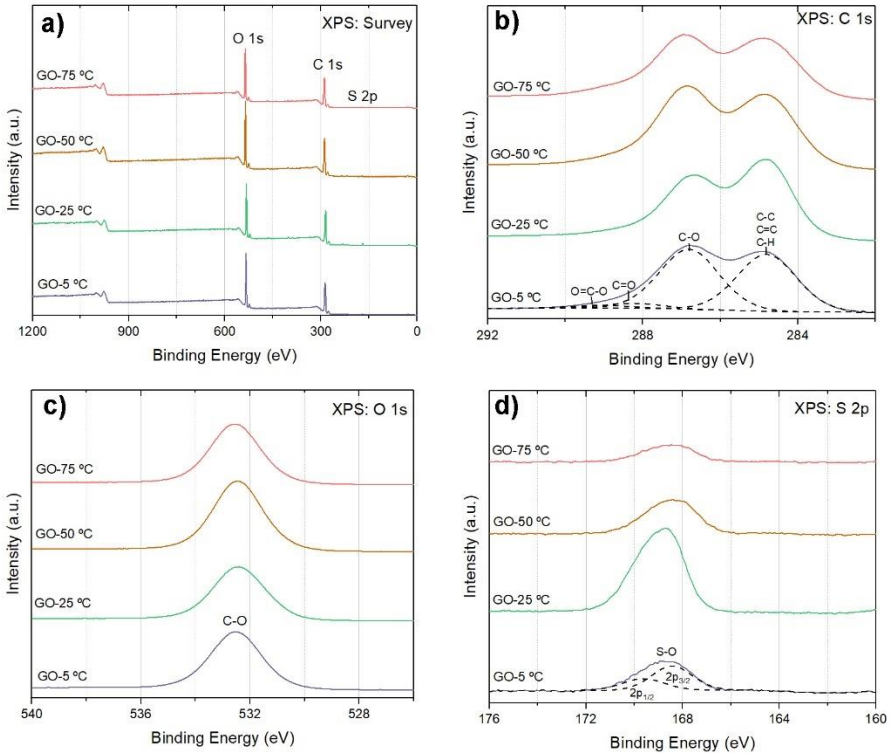

Figure 60: a) XPS survey spectra of the GOs prepared with different reaction temperatures. High-resolution spectra of b) C 1s, c) O 1s and d) S 2p. Deconvolution is shown for the first lines of C 1s and S 2p.

The relative atomic abundances obtained by XPS and EDS are displayed in Table 7. Apart from sample GO-5 ºC, there are tendencies related to the reaction temperature. The most observable difference between samples is the important decrease of the presence of sulfur with increasing the reaction temperature, shown by XPS and EDS. This result matches with the TGA analyses, which had previously indicated a lesser amount of organosulfate groups, confirming that the hydrolysis of the organosulfates during the reaction [127] is increased as a result of high temperatures [126], [197]. The relative content of carbon and oxygen varies little from sample to sample, with slight differences in the C/O ratios. For the surface of the GOs, as determined by XPS, the C/O ratios draw a decreasing tendency as a function of reaction

temperature. The C/O ratios for bulk GOs increase as a function of reaction temperature, possibly indicating that the hydrolysis and decomposition of the less-exposed functional groups is lower even at high temperatures. Considering that each sulfur is bonded to four oxygen atoms and their hydrolysis leads to vicinal diols (2 oxygen atoms) [126], the hydrolysis of organosulfates would be accompanied by the decrease of the relative amount of oxygen. Also, the high temperatures cause the hydrolysis and decomposition of some oxo-functional groups to CO_2 [194], [195], with the corresponding increase of the relative concentration of carbon, as 1 carbon atom is lost for every 2 oxygen atoms. Thus, the oxidation of graphite may have been greater with higher reaction temperatures, despite not being directly reflected in the C/O ratio values.

Table 7: Relative atomic abundances of the GO samples prepared with different reaction temperatures from XPS and EDS elemental analyses.

	XPS Elemental composition (At%)				**EDS Elemental composition (At%)**				
	C	**O**	**S**	**C/O**	**C**	**O**	**S**	**Others***	**C/O**
GO-5 ºC	73.6	25.7	0.7	**2.86**	50.6	47.5	2.0	0.0	**1.07**
GO-25 ºC	74.2	23.9	2.0	**3.11**	47.6	49.0	2.9	0.3	**0.97**
GO-50 ºC	74.1	25.3	0.7	**2.93**	49.4	48.2	2.1	0.3	**1.02**
GO-75 ºC	73.3	26.2	0.4	**2.79**	50.7	47.6	1.4	0.2	**1.06**

For GOs prepared by the conventional Hummers' method, which have a maximum temperature of 98 ºC in step 7 of the reaction [101], C/O ratios determined by XPS tend to be comprised between 1.6 and 2.7 [314]. Our GOs have higher C/O ratios, potentially indicating that our oxidations have been not as strong as that of the original Hummers' method. Dimiev et al. have suggested recently that water molecules in acid media are the actual attackers of the carbon atoms triggering the oxidation [50]. As water is added to the

anhydrous mixture in the step 2 of the reaction, it makes sense that our GOs, which were exposed to lower temperatures (5, 25, 50 or 75ºC) than in the actual Hummers' method (98ºC), would have lower C/O ratios than the GOs prepared by the conventional Hummers' reaction.

Apart from that, we find that the sample GO-5 ºC does not follow this tendency. The reason may be related to a better washing of the particles due their low exfoliation (OM results: section 5.1). This is corroborated by the fact that no impurities were detected by EDS and the dispersion had a higher pH after the washing procedures (Appendix 1). Thus, a base-driven hydrolysis of the functional groups could have led to the chemistry of this sample to change like the samples prepared with high temperature, where the functional groups have been degraded to CO_2, in this case not by temperature but by basification of the medium [126], [128], [315].

Table 8: XPS compositional analysis of the C 1s spectra of the GOs prepared with different reaction temperatures.

	XPS C 1s (At%)			
	C-C, C-H, sp^2	**C-O**	**C=O**	**O-C=O**
GO-5 ºC	45.7	48.2	3.9	2.2
GO-25 ºC	53.6	40.3	4.4	1.8
GO-50 ºC	46.0	48.9	2.2	2.9
GO-75 ºC	47.1	46.5	2.0	4.4

The relative abundance of the deconvoluted components of the C 1s spectra of the GO samples is shown in Table 8.

If we look for tendencies with reaction temperature, we will find that sample GO-25 ºC seems to break any tendency. The reason could be the high amount of organosulfates present only in this sample for this set. The deconvolution of spectra is a pure mathematical tool that can give us information by comparison, but when there are similar species causing shifts in the binding energies,

caution must be taken when the components are assigned. The binding energy of the C 1s orbital of the carbon atom linked to an organosulfate (-**C**-O-S-) is shifted to higher values than hydroxyl carbons (-**C**-O-H), due to the higher electronegativity of sulfur [316]. As sample GO-25 ºC has a higher amount of organosulfates than the other samples, it has a shift to about 287 eV (Figure 60b) caused by the organosulfate bonds that have falsely lowered the relative abundance of C-O components while increasing the relative abundance of C=O components.

Except for this sample, the carbonyls (C=O) appear to decrease and the carboxyls (O-C=O) to increase as reaction temperature increases. This behavior was also found in the literature [196], and could be related to a more aggressive oxidation driven by the high temperature, reaching for the C=O moieties in a higher oxidation state in O-C=O groups. The increase in the relative abundance of carboxylic acids was found in studies in which higher reaction temperatures [185] or multiple consecutive oxidation reactions of the same GO [181] were used, indicating the clear connection between this oxo-functional group with the oxidation level of GO. The C-O component of our GOs seem to remain constant, but since it involves both epoxides (C-O-C) and hydroxyls (C-OH), differences in the abundances of these functional groups cannot be detected, despite the likelihood of transformation of epoxides to hydroxyls in acidic medium via ring-opening, favored by high temperatures [197], [195], [135].

5.6. CONCLUSIONS

We have reported a synthesis procedure of graphene oxide using a modification of Hummers' method, varying the reaction temperature by 5, 25, 50 and 75 ºC, while maintaining the time of reaction on 120 min. The morphological characterization of the samples showed a clear relationship of the exfoliation degree of the GO particles with the reaction temperature, somewhat stronger than the exfoliation obtained in the last chapter by varying the reaction time at constant temperature of 25ºC. The chemical composition of the samples also changed as a function of reaction temperature. TGA measurements clearly showed a higher thermal stability of the functional groups for the GOs prepared with high reaction temperatures, indicating a higher presence of the most stable fraction of the oxo-functional groups. XRD, EDS and XPS showed the same tendencies of evolution of the interlaminar distance and the chemical composition of the GOs except for sample GO-5ºC, which behaved oddly, possibly due to its greater washing efficiency and concomitant increased pH of the dispersion caused by the low oxidation and exfoliation of the particles. In the other three samples, the compositional data showed a development of the functional groups as a function of reaction temperature, leading to a higher oxidation degree and hydrolysis of the organosulfates. Thus, we conclude that the effect of the temperature on the morphology and chemistry of the GOs is important and can be tailored to obtain GOs with different chemistries. However, when performing low-temperature oxidations, reaction time should be increased to permit a better exfoliation. With high temperatures, a high exfoliation of the flakes is achieved. However, the chemical composition of GO also varies, with a variation of the functionalization towards more stable functional groups, especially with the hydrolysis of the organosulfates.

UNIVERSITAT ROVIRA I VIRGILI
CHARACTERIZATION OF GRAPHENE OXIDE OBTAINED FROM MODIFICATIONS OF HUMMERS' METHOD AND ITS APPLICATION FOR REINFORCING TEXTILES
Jordi Aixart Forés

THE EFFECT OF BASIFICATION OF THE AQUEOUS GO DISPERSIONS AND STRONG AGITATION TO THE MORPHOLOGY AND CHEMISTRY OF GO

6

Summary: GO samples studied in the last two chapters, prepared using modifications of Hummer's method, have been post-treated. The post-treatments consisted in the neutralization on the aqueous media by washing each sample by dead-end filtration until the pH of the flowing water had pH=7. After that, the samples were subjected to strong magnetic stirring to increase the exfoliation degree of the particles. The resultant post-treated GO (ptGO) samples were characterized following the same methodology as used for the samples of the previous two chapters, comparing the results to their untreated counterparts. We found that the post-treatments were crucial, causing greater changes in the morphology and chemistry of the GO flakes than the reaction conditions (time and temperature) did, obtaining a high shattering of the GO flakes into smaller pieces with transformed functional groups due to hydrolysis.

6.1. MORPHOLOGY OF THE POST-TREATED FLAKES

The strong agitation on GO dispersions is known to usually have an important effect on the exfoliation and fragmentation of the size of the GO flakes [122], [199]. In our case, we performed an intense washing of the samples followed by strong magnetic agitation, which can have affected the exfoliation and fragmentation of the flakes. In this section, optical and SEM images of some of the post-treated GOs are presented to observe these effects. In Figure 61, optical micrographs of the samples GO-30 min, GO-540 min, belonging to sample set 1, GO-5ºC and GO-75ºC, belonging to sample set 2, and GO-120 min (GO-25 ºC), which is common in both sets, are presented. Under each of those micrographs, their corresponding post-treated GO counterparts (labelled pt) are shown, to effectively compare the effect of the post-treatments on each of these samples.

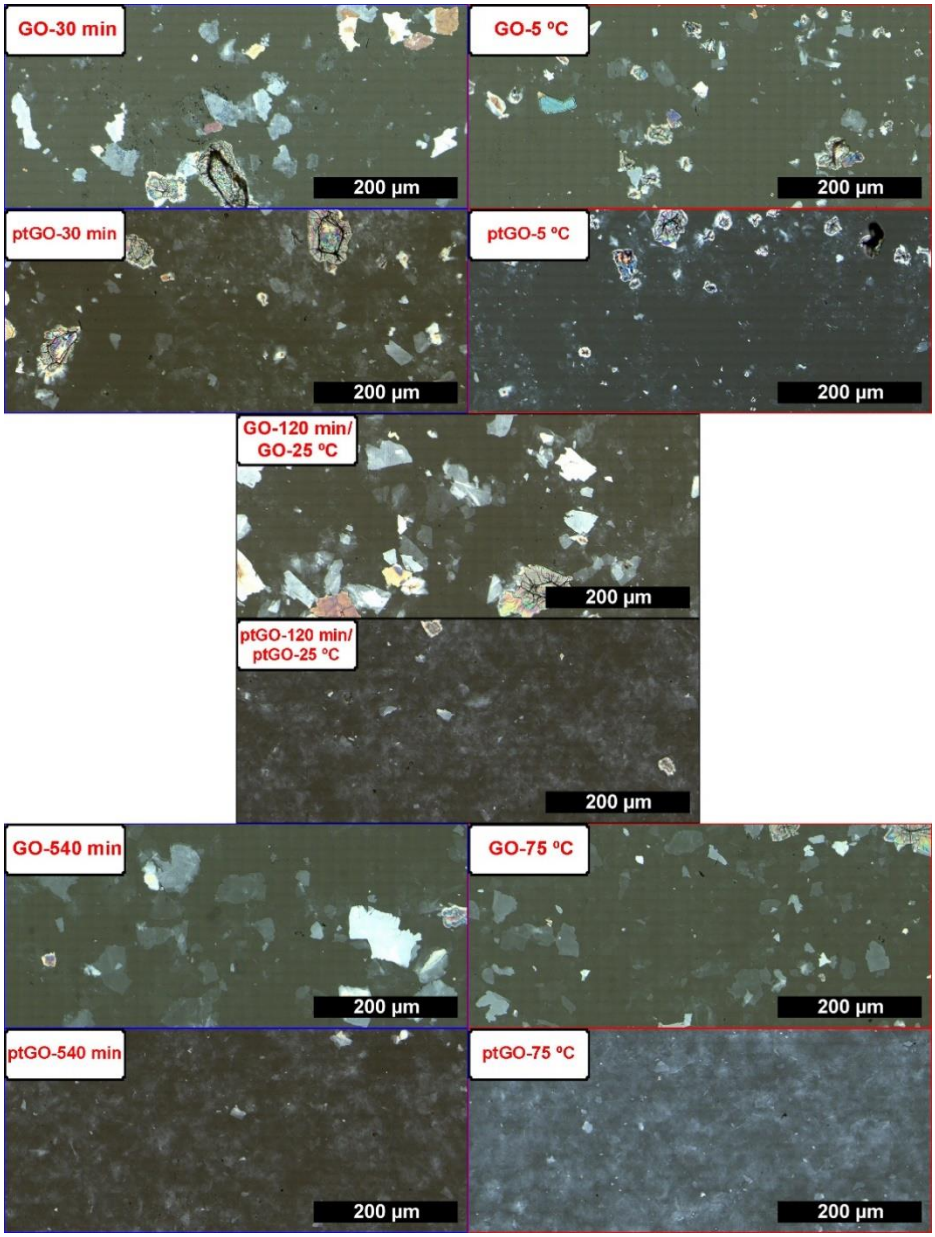

Figure 61: Optical reflection micrographs of a selection of untreated GOs and the corresponding post-treated GOs (ptGOs) where the effect of the post-treatments on each sample prepared with different conditions can be observed.

A clear effect of the post-treatments on the morphology of the GOs can be observed in the optical micrographs, as the aspect of the flakes is totally different after the post-treatments. A bluish “cloud” of small flakes, where individual particles can be hardly differentiated appeared after the post-treatments. For the samples prepared with low reaction time or temperature (30 min and 5 ºC) differences between untreated and post-treated samples are slight. 3D graphitic particles are present in all the cases, but the flat flakes seem to be shattered in smaller pieces in the ptGO samples, being notable the absence of large flat flakes. For the post-treated sample prepared with 120 min/25 ºC, the same effect occurs in a stronger manner: almost no large flakes are present despite some 3D particles that show interference colors, due to a higher thickness. Most of the flakes are thin and uniform. For the samples prepared with long reaction time or high temperature (540 min and 75 ºC), this effect is extensive. No recognizable individual objects can be observed except than the bluish cloud.

For the visualization of the shattered flakes in the ptGO samples, SEM images of these samples were obtained, and they are shown in Figure 62. In those micrographs, the huge difference between the size of the GO and ptGO flakes can be observed. In the case of ptGOs, the small, shattered flakes that form the distributions are well-defined, confirming that the bluish cloud of flakes observed in the optical micrographs corresponds to a distribution of flakes with smaller lateral sizes of a few micrometers.

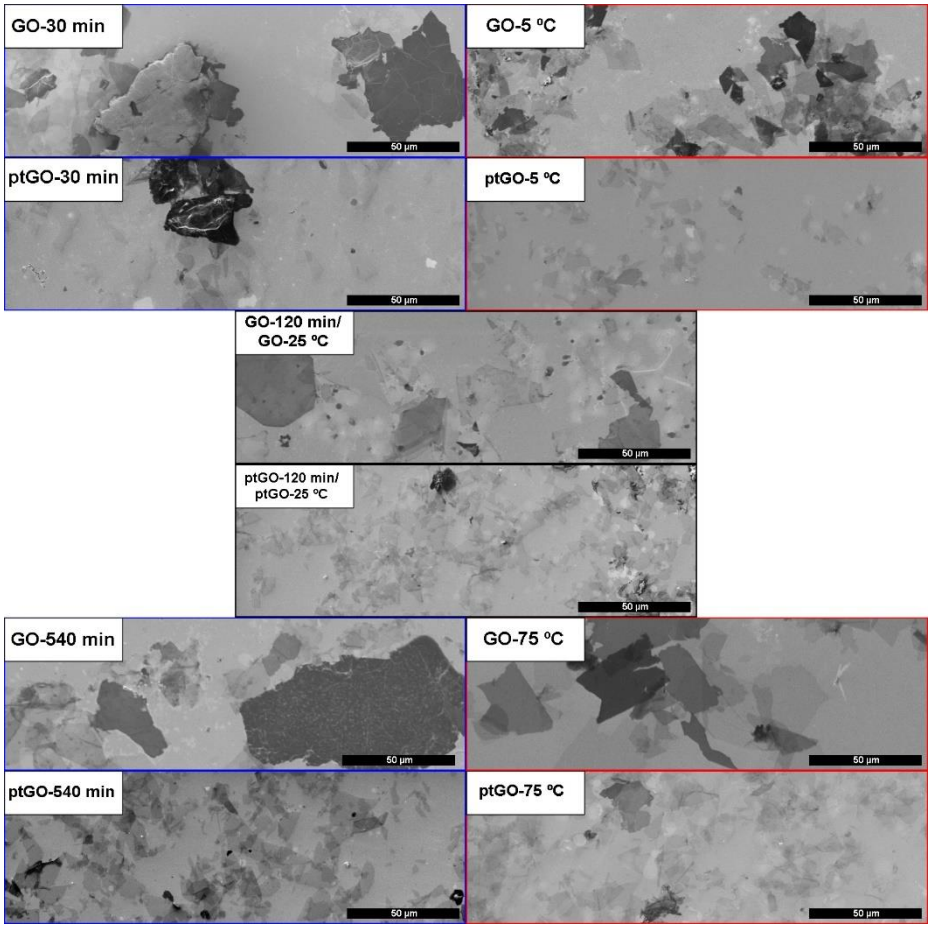

Figure 62: SEM micrographs of the selected GO and ptGO samples prepared with different reaction conditions where the effect of the post-treatments on the morphology of the flakes can be observed.

In the previous studies (Chapters 4 and 5) we found that the GOs exfoliate to a greater extent when more reaction time or temperature were permitted. The samples with long reaction times or high temperatures, which already had well-exfoliated flakes, tend to be shattered to by aggressive post-treatments. For samples prepared with short reaction times or low temperatures, some flakes are still shattered into small pieces, but some large, exfoliated particles remain, and, most importantly, some of the graphitic unexfoliated particles persist

despite the post-treatments. Nonetheless, thick flakes that show interference colors in the untreated GO samples, are totally absent after post-treatment, indicating that they have been totally exfoliated and shattered to smaller flakes by the post-treatments.

As had also been done for all the GO samples, size distributions of the ptGOs have been obtained for the size of the flakes obtained from the SEM images. The size histograms of all the ptGO samples are shown in Figure 79 and Figure 80. while the log-normal fittings of the distributions are represented in Figure 63. For a full comparison between the sizes of all the samples prepared in this thesis, both the GO and ptGO samples are presented for the samples (a) prepared with different reaction time and (b) prepared with different reaction temperature.

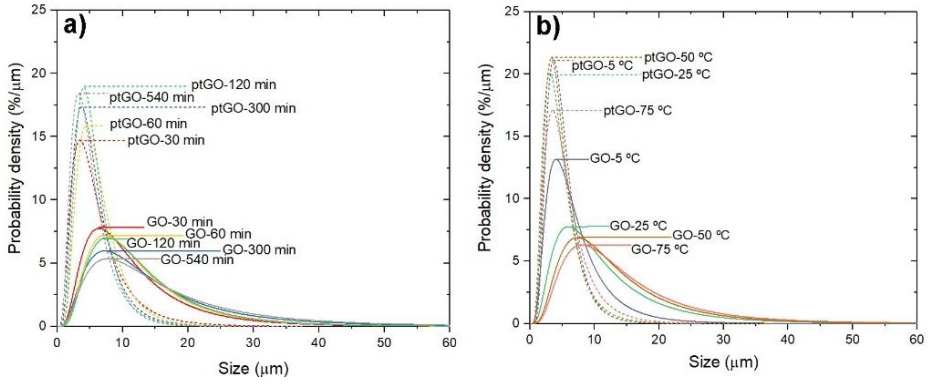

Figure 63: Log-normal size distribution curves of the untreated GO (solid lines) and post-treated GO (dashed lines) samples belonging to a) set 1, prepared with different reaction times and b) set 2 prepared with different reaction temperatures. Size histograms of each sample are presented in Figure 79 and Figure 80. The curve areas are normalized to 100% in all cases.

For the ptGOs corresponding to the sample set 1, shown in Figure 63a, all the distributions are centered (mode) around 5 μm, instead of the 10-13 μm for the majority of the untreated GO samples. Also, for the ptGOs, the size tendency

with reaction time is contrary to that for the untreated GOs. Here, the ptGO-30 min is the sample with larger flake sizes, while the GO-30 min was the sample with smaller flake sizes. This agrees with the optical micrographs (Figure 61) where some big flakes were observed for the sample ptGO-30 min, while for the others only the bluish cloud of small flakes was present. For the ptGO samples corresponding to the sample set 2 conditions (Figure 63b), the same difference occurs between the untreated and post-treated GOs, except for the sample GO-5 ºC that exhibits a high fraction of small flakes, with a size distribution comparable to the ptGOs. In this case, there does not exist a trend between size and reaction temperature for the ptGOs.

Table 9: Statistical information from the log-normal distributions of the flake size for each untreated GO and post-treated GO samples.

		GOs		ptGOs	
		Mode (µm)	**Median (µm)**	**Mode (µm)**	**Median (µm)**
Set 1: T= 25 ºC	**30 min**	6,42	9,79	3,49	5,22
	60 min	7,33	10,80	4,41	5,68
	120 min	7,61	11,14	4,06	5,04
	300 min	7,30	12,10	3,72	4,95
	540 min	7,70	13,27	3,28	4,50
Set 2: t= 120 min	**5 ºC**	4,49	6,58	3,65	4,53
	25 ºC	6,61	10,54	3,10	4,20
	50 ºC	8,17	12,32	3,31	4,25
	75 ºC	8,94	13,47	3,48	4,82

The main statistical information (mode and median) of the log-normal fitting is displayed in Table 9 for all the GO and ptGO samples, where all the commented differences and relations can be confirmed: The size of the flakes of the untreated GOs is much larger than for the post-treated GOs. The untreated GO follow a general trend of size increase versus reaction times and temperatures, which can be attributed to a better exfoliation of the flakes with these parameters. However, this clear trend is not shown in the ptGOs. The ptGOs

are all comprised in the same range of sizes (median between 4.2-5.2 µm), possibly indicating a limit of fragmentation of the flakes, regardless of initial conditions (due to different reaction conditions), at least when using the same protocol of post-treatments (Section 3.2.5). The same was observed in a follow-up study in which increasing times of sonication were performed to GO samples and the size of the flakes reached a lower limit no matter if more time of sonication was allowed [317], so 5-4 µm seems to be a lower size limit for our GO flakes, and applying more intense post-treatments would not further fragmentate the flakes.

6.2. THERMOGRAVIMETRIC ANALYSES OF THE PTGOS

TGA measurements were performed for ptGOs to reveal their thermal stability. The curves are shown in Figure 64, where the TGA and DTG curves are displayed for the ptGOs of the set 1 (a and b), respectively, and for the ptGOs of the set 2 (c and d). Here, an important variation can be observed compared to their untreated counterparts. All the ptGOs of the set 1 have the same decomposition behavior, as observed on their DTG (Figure 64b). The major weight loss has shifted to 200 ºC and sharpened. Observing the samples of the set 2 (Figure 64c and d), we find the same behavior. In this case we can observe a slight shift in the position of the DTG peak as a function of the reaction temperature. It is worth to comment that this behavior also happened for the GO samples prepared with high reaction temperature (GO-50 ºC and GO-75 ºC, Figure 56), so the chemical structure of the ptGOs could be related to the GOs prepared with high reaction temperatures.

Also, very important to note that for each of the ptGOs, there is almost no weight loss from 250 to 300 ºC, corresponding to the decomposition of the organosulfates, indicating the relative absence of this functional group.

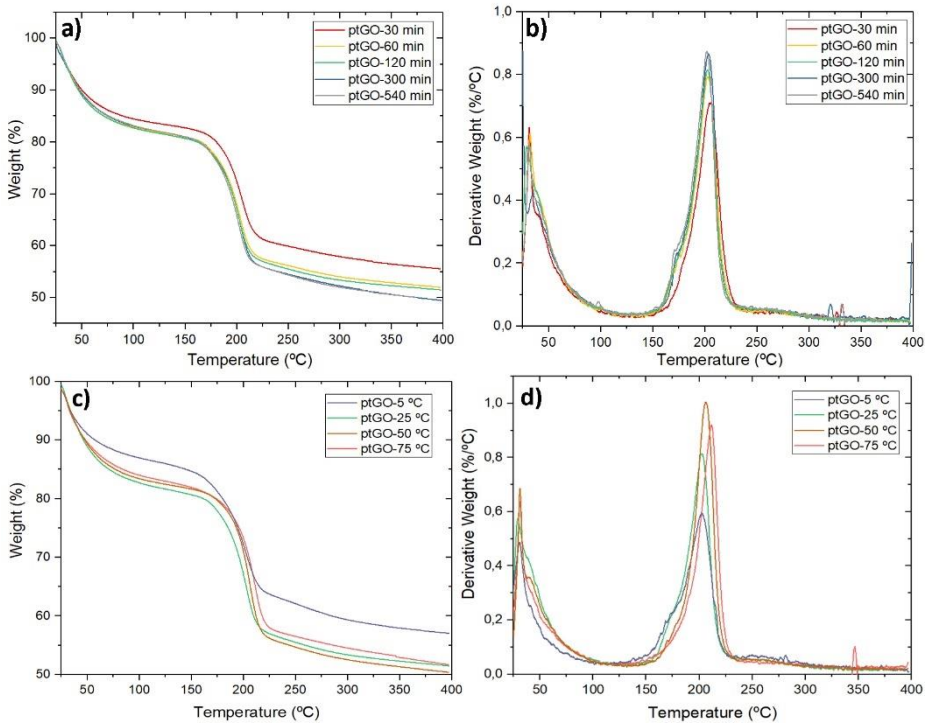

Figure 64: TGA curves and their corresponding derivative curves of the samples of all the post-treated GO samples. a) and c) TGA curves for set 1 and 2 reaction conditions, respectively. b) and d) their corresponding derivative curves.

The quantitative data extracted from the analyses of the derivative curves is gathered in Table 10. For the temperature and percentage of weight lost by the decomposition of the oxo-groups (Td1, Td2 and %W12), the values are similar among all the samples. Some slight tendencies could be observed like the decrease of the decomposition temperatures versus reaction time and their increase versus reaction temperature. The values for the decomposition of organosulfates (Td3 and %W23) and the amount of water absorbed (%Ww) are very similar for all the samples.

When comparing these results with those from the GOs of sample sets 1 and 2 (Table 3 and Table 6), we observe that Td1 and Td2 are about 40 ºC higher for the ptGOs than for the untreated GOs and the values Td1 and Td2 are

closer, indicating a higher slope of degradation for the post-treated samples. However, the %W12 is almost the same for both kinds of samples. This indicates that the untreated GOs decompose sooner and over a larger temperature range than the ptGOs, which decompose rapidly at around 200 ºC. This could indicate that the GOs have a higher diversity of oxo-functional groups, including the less-stable functional groups that decompose at low temperatures, while the ptGOs only have the most-stable fraction of oxo-functional groups.

The reason behind these differences could be because with the post-treatments, the less stable oxo-functional groups of the GOs developed to a more-stable version, from epoxides to hydroxyls via nucleophilic ring opening [135], or even decomposed from carboxyls to CO_2 [264], [181]. However, the ptGOs are more thermally stable, although with a similar degree of functionalization to the GOs, as the weight lost on decomposition of the oxo-groups (%W12) is similar for the GOs and the ptGOs. The fact that the GO-50 ºC and GO-75 ºC samples have similar TGA curves to the corresponding post-treated GOs, invites us to hypothesize that the modification of the functional groups caused by the post-treatments in these samples resembles that for the samples prepared with high reaction temperature (but no post-treatment), which would be the temperature-induced hydrolysis and decomposition of the less stable oxo-functional groups [315]. A decomposition that would be caused in the case of the ptGOs by the increase of the pH of the medium [318] and the higher exfoliation, allowing a better access of the nucleophiles to the functional groups.

Finally, the temperature corresponding to the decomposition of organosulfates (Td3) is the same for GOs and for ptGOs, but the %W23 is much lower for the ptGOs (8-13% for GOs and 3-4% for ptGOs), indicating less presence of organosulfates due to the washing procedures where the increased pH of the medium favored their hydrolysis [126].

Table 10: Summary TGA results of temperatures of decomposition, percentage of weight lost on decomposition and percentage of water desorbed from all the post-treated GO samples.

	Td1 (ºC)	Td2(ºC)	%W12	Td3(ºC)	%W23	%Ww
ptGO-30 min	193	206	24	246	3	17
ptGO-60 min	187	203	26	253	3	18
ptGO-120 min	188	203	26	250	3	18
ptGO-300 min	190	204	28	254	4	19
ptGO-540 min	187	201	28	240	4	18
ptGO-5 ºC	181	202	24	279	5	13
ptGO-25 ºC	188	203	26	250	3	18
ptGO-50 ºC	198	207	28	295	3	17
ptGO-75 ºC	200	212	27	300	3	16

6.3. X-RAY DIFFRACTION OF THE PTGOS

The XRD patterns of the post-treated GOs are shown in Figure 65 for the case of the ptGOs of set 1 (a) and set 2 (b) conditions. For the untreated GOs, in Chapters 4 and 5 we could observe variations in the position of the (001) peaks in function of with the reaction time and temperature. After post-treatment, the (001) signals of all the samples are conjoined around 10.7º, indicating a homogenization of the interlayer distances of all the GOs caused by the post-treatments.

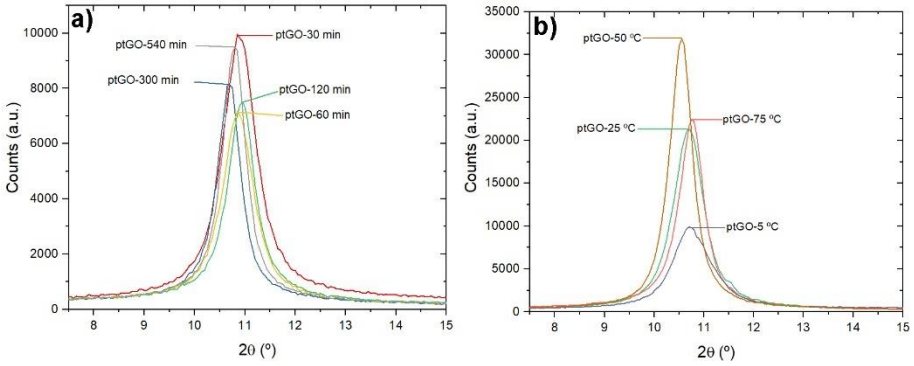

Figure 65: XRD patterns of the (001) signal of the ptGOs prepared with a) different reaction time and b) different reaction temperature.

In Table 11, gathers the d distances and diffraction column lengths (Lc) of all the GO and ptGO samples. The reader is advised to be careful when comparing the values across different sets of measurements (separated in the table by lines), as they were obtained in different days and the results were sensitive to atmospheric conditions, which varied for the two sets. As examples, GO-120 min and GO-25 ºC, ptGO-120 min and ptGO-25 ºC, that are the same samples (obtained at 120 min and 25 ºC), respectively, differ due to this factor.

Table 11: Summary of the interlaminar distances (d distances) and effective diffraction columns (Lc) for all the GO and ptGO samples, obtained by XRD.

		GOs		ptGOs	
		d distance (Å)	**Lc (nm)**	**d distance (Å)**	**Lc (nm)**
Set 1: T= 25 ºC	**GO-30 min**	8.6	8.5	8,1	10,5
	GO-60 min	8.7	11.3	8,1	11,4
	GO-120 min	8.7	11.0	8,1	12,9
	GO-300 min	9.4	10.5	8,2	14,9
	GO-540 min	9.6	8.5	8,1	15,2
Set 2: t= 120 min	**GO-5 ºC**	8.1	9.7	8,2	9,3
	GO-25 ºC	8.7	9.6	8,3	11,7
	GO-50 ºC	8.6	12.5	8,3	15,3
	GO-75 ºC	8.4	11.3	8,2	14,2

Samples have been compared within the same set of measurements to observe tendencies. All the ptGOs have lower d distances than their untreated counterparts and they are all comprised in a narrow range, between 8.1 and 8.3 Å. Also, their stacking order (Lc) has increased some nm. This behavior is related to the exfoliation and the structural homogenization caused by the post-treatments. The hydrolysis of the voluminous organosulfates and the decomposition of some oxo-functional groups would homogenize the chemical structure of the ptGOs. The higher exfoliation and shattering of the flakes caused by the agitation during sonication may release the compounds trapped in the graphitic structure [127] and reduce the oxygen moieties of the lattice [319], therefore compacting the resultant structures of the post-treated GOs (reducing the interplanar distance).

6.4. RAMAN SPECTROSCOPY

Recalling Chapters 4 and 5, Raman spectroscopy did not give any advantageous information for the GOs of the set 1 (Figure 49) and set 2 (Figure 58) samples, where all the spectra had the same characteristics with I_D/I_G ratios of 0.96-0.97. The situation changes for the ptGOs. Raman spectra of ptGOs are shown in Figure 66a-b, respectively for reaction conditions corresponding to sample sets 1 and 2. All the ptGOs have the typical Raman spectra of any GO material, with the characteristic D and G bands at 1347 cm^{-1} and 1595 cm^{-1}, respectively, and the 2D, D+G and 2D' bands at higher wavenumbers. The I_D/I_G ratio have values around 0.91-0.94, somewhat less than had been obtained for the untreated GOs (0.96-0.97). To explain this, the consensus in the technical literature is that a decrease in the I_D/I_G ratio would indicate a higher disorder and increase number of defects in GO [320], [321] , this observed decrease of the I_D/I_G ratio for the ptGOs (relative to the untreated samples) could indicate an increase in the density of defects, with the formation of new holes (by the generation of CO and CO_2 [322]) and/or transformation of sp^2 carbons to new sp^3 [323], [324].

However, based on the literature about Hummers' method, we believe that our GOs and ptGOs have a high degree of defects/functionalities. Then, with Raman spectroscopy it is not possible to extract solid conclusions about the relation between preparation conditions of GO [127], [284].

At least, though, we can conclude that obtaining for all the GOs the same I_D/I_G ratios while different and decreased I_D/I_G values for all the ptGOs, can be due to a structural transformation caused by the post-treatments, with the possibility of decomposition of functional groups or structural damage caused by the strong agitation.

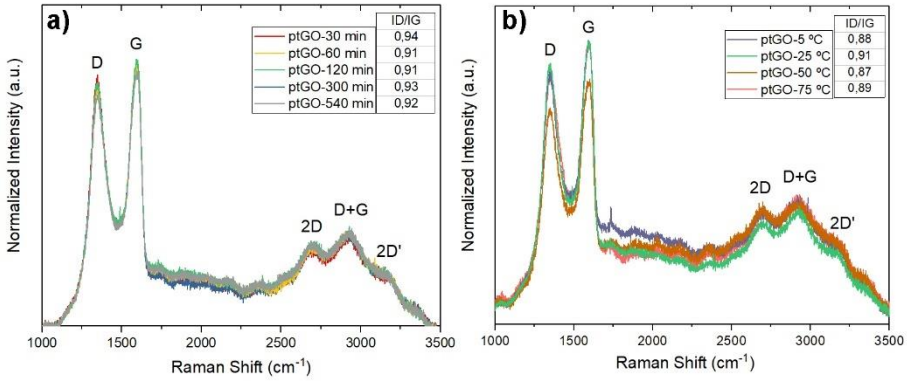

Figure 66: Raman spectra of the post-treated GO samples for the sample set 1 (a) and 2 (b) reaction conditions. Insets: I_D/I_G ratios for each sample.

6.5. ELEMENTAL COMPOSITION OF PTGOS

6.5.1. Elemental analyses by EDS

Post-treated GOs (ptGOs) have been analyzed by EDS. EDS spectra of the ptGOs for set 1, prepared with different reaction time, and set 2, prepared with different reaction temperature, are shown in Figure 67a and b, respectively. The spectra are similar for both sets, with the same elements being detected with similar relative intensities.

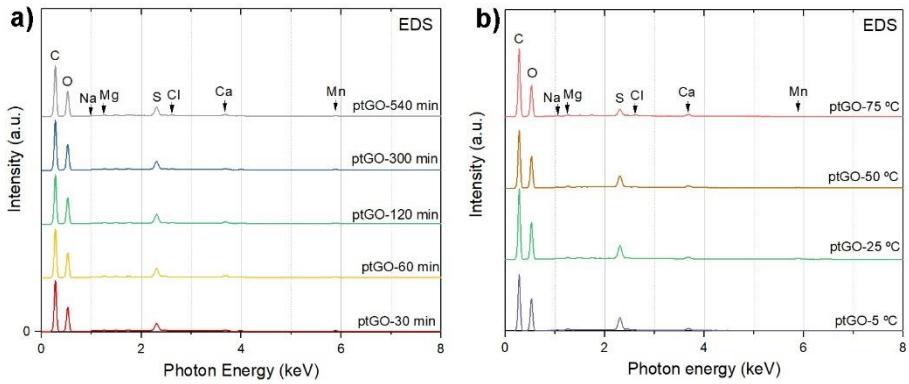

Figure 67: EDS spectra of the post-treated GO samples for reaction conditions of a) set 1, prepared with different reaction times, and b) set 2, prepared with different reaction temperatures. Detected elements are indicated.

The most intense signals are still the main elements of GO: carbon, oxygen and sulfur. Yet, new peaks from sodium, magnesium, and calcium are observed, which had not previously been detected for the untreated GOs. Chlorine and manganese are still present from the reaction procedure, but not potassium, which seems to have been removed completely during the post-treatments.

The appearance of sodium, magnesium and calcium is a little controversial, especially in such large quantities. The particularity of ptGOs is that they have

been washed intensively with high amounts of distilled water. Distilled water obtained from traditional water purification systems may retain some amount of alkali and alkaline earth metals present in tap water fed to the deionization process [325]. On the other hand, GO have been shown to form strong bonds with positive ions such as magnesium, calcium and aluminum [326], [327], [328]. As a curiosity, calcium chloride salt is used in coagulating baths to bring about the rapid agglomeration of GO flakes [329] when desired. Then, magnesium and calcium could come from the water used during washing procedures, despite being distilled water. Although we did not review them specifically, other works exist in which there is an unjustified detection of calcium in GO samples [261]. While sodium could remain in GO from the $NaNO_3$ used in the reaction, but not observing it when analyzing the untreated GO samples leads us to believe that it is a contamination from the distilled water.

Table 12: Relative atomic abundances of the post-treated GO samples from EDS elemental analysis.

	EDS Elemental composition (At%)					
	C	**O**	**S**	**Others***	**Others****	**C/O**
ptGO-30 min	52.3	45.9	1.1	0.1	0.4	**1.14**
ptGO-60 min	51.6	46.3	1.3	0.2	0.6	**1.11**
ptGO-120 min	50.8	46.9	1.3	0.3	0.6	**1.08**
ptGO-300 min	51.3	46.8	1.2	0.2	0.4	**1.09**
ptGO-540 min	52.0	45.9	1.3	0.2	0.5	**1.13**
ptGO-5 ºC	50.1	47.6	1.5	0.1	0.7	**1.05**
ptGO-25 ºC	51.2	46.6	1.4	0.2	0.6	**1.10**
ptGO-50 ºC	50.7	46.9	1.2	0.2	0.7	**1.08**
ptGO-75 ºC	52.1	46.4	0.7	0.1	0.6	**1.12**

*Others: Cl, K and Mn. **Others: Na, Mg, Ca

Table 12 displays the elemental compositions of the ptGO samples obtained by EDS, grouped into set 1 and 2 reaction conditions. In the table, C, O and S

contents are displayed as the constituent elements of GO, while the impurities are gathered separately in two “others” columns, dividing them if coming from the reaction and first washing procedures (*) and if introduced from the distilled water used in the intense wash and neutralization of the samples (**). We can observe that the impurities from the reaction (Cl, K and Mn) have similar percentage values to those obtained from the untreated samples (Table 4 for the GOs of the set 1 and Table 7 for the GOs of the set 2), which indicates that the intense washing of the samples was not able to get rid of these impurities. The reason could be that they are incorporated in the inner structure of the graphitic galleries and released upon exfoliation, but not washed. The impurities coming from the distilled water used to wash and neutralize the samples (Na, Mg, Ca) are present in relatively high quantities, pointing to the importance of using water of higher purity when performing this kind of washing procedures with large quantities of water.

Regarding the elements composing the ptGOs, C, O and S, all the samples show the same relative elemental abundances with no special relationships between the reaction conditions. Comparing the ptGOs with their complementary untreated GO samples (Table 4 for the GOs of the set 1 and Table 7 for the GOs of the set 2) we find that all the ptGOs have higher C/O ratios (by around 10 %) than their untreated counterparts and less presence of sulfur in all cases. This indicates the development of the functionalities with the hydrolysis of the organosulfates and the possible transformation of the oxo-functional groups to CO_2.

If we try to find differences among the ptGOs, the only remarkable value is the low sulfur amount of the sample ptGO-75 ºC. This result is not surprising because the corresponding untreated GO-75 ºC also has the lowest amount of sulfur. For all the other samples, the relative abundance of the main three elements is similar, possibly confirming a homogenization of the functionalities caused by the intense washing procedures and neutralization of the medium. This could mean that the less stable functional groups have developed into

more stable functionalities during sample post-treatment, reaching a stable chemical structure with poorer chemical diversity.

6.5.2. Elemental and compositional analyses by XPS

XPS has been performed to some ptGO samples. The samples analyzed are all the post-treated GOs from set 2 samples, prepared with different temperatures, and from one set 1 sample, namely ptGO-300 min. (In fact, it is two from set 1, as sample ptGO-25 ºC also belongs to the set 1, also named as ptGO-120 min). In Figure 68, the XPS spectra are presented as commonly in the thesis as: a) survey spectra, and high-resolution spectra of b) C 1s, c) O 1s and d) S 2p.

The relative atomic abundances and the compositional analysis of the C 1s spectra obtained are shown in Table 13. XPS reproduces the same tendencies as were obtained by EDS, with a slight increase in the atomic content of carbon and slight decrease of the content of oxygen due to the post-treatments, leading to higher C/O ratios, compared to their untreated GO counterparts. The important decrease of the sulfur content of the ptGO samples observed by EDS is also observed here.

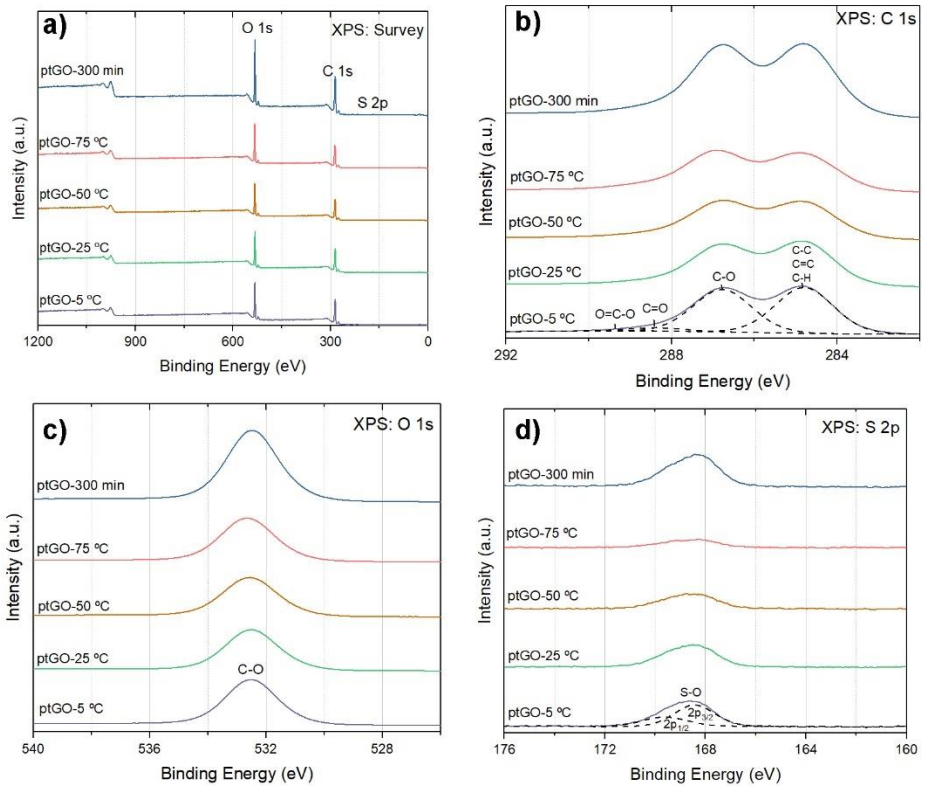

Figure 68: XPS spectra of the ptGOs of the set 2 and the sample ptGO-300 min of the set 1. a) Survey spectra. b) C 1s, c) O 1s and d) S 2p high resolution spectra of the mentioned samples. Deconvolution of the lines are shown for the first line when performed.

The compositional analysis of the C 1s orbital also shows, relative to untreated samples (Table 5 and Table 8), an increase of the bonds related to the carbon framework (C-C, C-H and sp^2) with a general decrease of the oxygen functionalities. However, the functional groups that reduced their presence to a greater extent are the carboxyls (O-C=O). The carbonyls (C=O) maintained their relative abundance, while the C-O bonds increased slightly. This behavior seems to indicate that the washing procedures and the increase in the pH affect mostly the carboxylic acids, which would decarboxylate to CO_2 [317], [330], [331]. Furthermore, O-C=O groups in GO also include lactols and esters [47],

which are prone to hydrolysis under basic conditions [332]. The obtention of the same C-O relative abundance for the ptGOs and GOs clearly indicates that C-O functionalities are do not decompose, but epoxides (C-O-C) may have developed to hydroxyls (C-OH) due to pH-driven nucleophilic ring-opening [333]. With XPS we cannot differentiate them, so we cannot know the true nature of the C-O bonds. Finally, the presence of alkaline earth metals may help to stabilize hydroxyls through the formation of electrostatic interactions [326].

Table 13: Relative atomic abundances and compositional analysis of the C 1s spectra of the ptGOs of the set 2 and the sample ptGO-300 min of the set 1.

	XPS Elemental composition (At%)				**XPS C 1s (At%)**			
	C	**O**	**S**	**C/O**	**C-C, C-H, sp^2**	**C-O**	**C=O**	**O-C=O**
ptGO-5 ºC	74.8	24.4	0.8	**3.07**	49.4	45.9	3.7	1.0
ptGO-25 ºC	75.8	23.5	0.7	**3.23**	50.6	45.1	2.8	1.4
ptGO-50 ºC	74.6	24.9	0.5	**3.00**	47.9	47.1	3.0	2.0
ptGO-75 ºC	74.3	25.4	0.3	**2.93**	47.0	47.5	2.0	3.5
ptGO-300 min	75.2	24.2	0.6	**3.11**	48.5	46.0	4.1	1.4

6.6. CONCLUSIONS

The GOs prepared and presented in this thesis were subjected to relatively mild post-treatments, consisting in the neutralization of the pH of the aqueous media, followed by stirring (section 3.2.5). The characterization reported in this chapter for these samples, labeled ptGOs, showed the tremendous effect of these post-treatments on the morphology of the flakes and the chemistry of all the samples. The well-exfoliated flakes which had been observed in the OM and SEM micrographs of untreated samples, reported in chapters 4 and 5, have now been strongly shattered into smaller pieces in the case of the ptGOs. The thermal stability of the post-treated samples has also increased, indicating the elimination or transformation of the less-stable oxo-functional groups present in the GOs. The interplanar distance of the samples has decreased after the post-treatments from 8.6-9.6 until 8.1-8.3 Å, losing, for all the post-treated samples, the dependence on the reaction parameters which had been found in the untreated samples. Raman spectra also indicated a change in the structure for the ptGOs, suggesting an increase of the density of defects. The compositional results obtained by EDS and XPS clearly indicate a deterioration of the chemical richness of the GOs by undergoing the post-treatments. The organosulfates have been hydrolyzed to a large extent and part of the carboxylic groups have been degraded to CO_2, due to the basification of the aqueous dispersions. Thus, we conclude that the post-treatments performed, while being still mild compared to the usual exfoliation techniques found in the technical literature (which often involve sonication), have a tremendous impact on the morphology and chemistry of the GO flakes. Importantly, the chemical richness which had been obtained through modifications of Hummers' method (increasing time and lowering temperature) has been diminished, homogenizing all the GOs into a more ordinary product with no remarkable connection to the reaction procedure.

LARGE-SCALE APPLICATION OF GO AS A COATING FOR TEXTILES TO INCREASE THEIR MECHANICAL STRENGTH

7

Summary: This thesis has been developed in the context of an industrial PhD focused on the application of a graphene-based derivative as textile coating for the improvement of mechanical characteristics, done for and in collaboration with Lenard BCN company (Tarragona, Spain). For this purpose, the GO with reaction conditions of 120 min and 25 ºC was prepared at large scale and was applied to textiles via dip-coating, a method used in the textile industry. The GO-based coating was formulated with a commercial polyurethane (PU) resin. Each parameter of the process has been optimized towards the mechanical resistance to puncture of the samples. The mechanical testing was performed using a universal testing machine adapted to the technical specification of a corresponding quality test standard. With the work performed, we obtained an improved fabric with higher mechanical resistance, maintaining its flexibility and processability and controlling the weight increase as a fundamental parameter for wearable textiles.

7.1. PRELIMINARY EXPERIMENTS: COATING TECHNICAL FABRICS WITH GO AND TESTING ITS MECHANICAL RESISTANCE

To design the path of the project, some preliminary experiments were performed initially aimed at enhancing the mechanical strength of fabrics by means of GO. We tested different kind of fabrics, and developed the methodology needed to apply GO, including the choice of resin needed to fix

the GO on the fabric, and the protocols for testing the resistance to puncture. One key concept we learned early on was that it was the composite GO plus resin, not only the GO alone, that which provided significant enhancement of the mechanical strength.

The fabric chosen for the project consisted in a technical fabric provided by the company involved in the project. It was designed to endure mechanical forces, and comprised yarns of polyester, polyethylene, and fiberglass. The yarn consists in a core of fiberglass and polyester covered by polyethylene. The resin used was a commercial resin consisting of an aqueous dispersion of aliphatic polyurethane (PU) based on polyether. The total content of PU in the resin was 40%wt. It was presented as a milky colored liquid that formed an elastic transparent film when drying.

The typical experiments consisted in a first coating of the fabric with an aqueous dispersion of GO. Then, the GO-coated fabric was let dry, and was coated with the PU resin. GO and PU were not mixed because they reacted, forming agglomerates. The reason for this could be the epoxy cross-linking of GO functional groups with PU [334]. After the GO was dried on the fabric, the reactivity of GO with PU was beneficial in helping the two coatings adhere to each other, thus strengthening the composite on the fabric.

Figure 69a shows an example of a fabric coated with GO and PU, next to the original uncoated fabric, which was initially white. It can be observed a uniform brownish color due to the presence of GO in the coating. The GO+PU coating tended to have a thickness around 0.5-1 mm.

The mechanical testing setup is shown in Figure 69b. A universal testing machine (Lloyd EZ50) was adapted with a purpose-designed and manufactured grip holding a tip according to the standard specifications for puncture testing on gloves EN 388:2016 [335]. A purpose-made stainless-steel frame was used to firmly hold the fabric, allowing the insertion of the puncture tip through a hole in the frame. Typical Load-Displacement curves are shown in Figure 69c where the load of the machine typically increases as the tip

presses on the fabric until a maximum (load at break or puncture resistance) is reached at the break point of the fabric. In the graph, the GO-coated fabric (yellow line) exhibits more resistance than the uncoated fabric (black line).

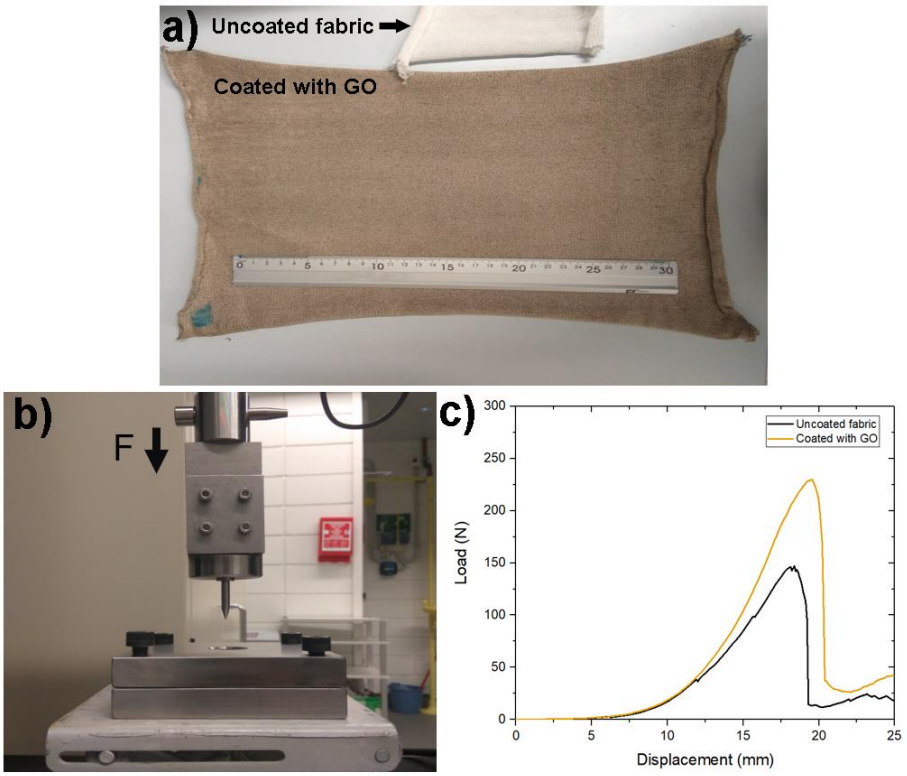

Figure 69: a) Example of a fabric coated with GO, 30 cm rule as a reference. b) Set up for the mechanical puncture testing of the fabrics, showing the purpose made tip, grip fixture to attach the tip to the upper arm, and base fixture for clamping the textile. c) Example tensile test curve of uncoated and coated GO fabrics.

The fabrics coated with GO and PU were observed with a stereo microscope and by environmental SEM (ESEM), working at low vacuum. The stereo microscope images are shown in Figure 70a-b for the uncoated fabric and the coated fabric, respectively. The GO covers the texture of the fabric

homogeneously. ESEM images are shown in Figure 70c-d, where the micrographs were obtained from the backscattered electrons and secondary electrons signal, respectively. In Figure 70c only some thick particles can be observed on the clear part of the fabric (fiberglass), while in Figure 70d, which has higher magnification, the fibers appear to be united with the GO+PU coating.

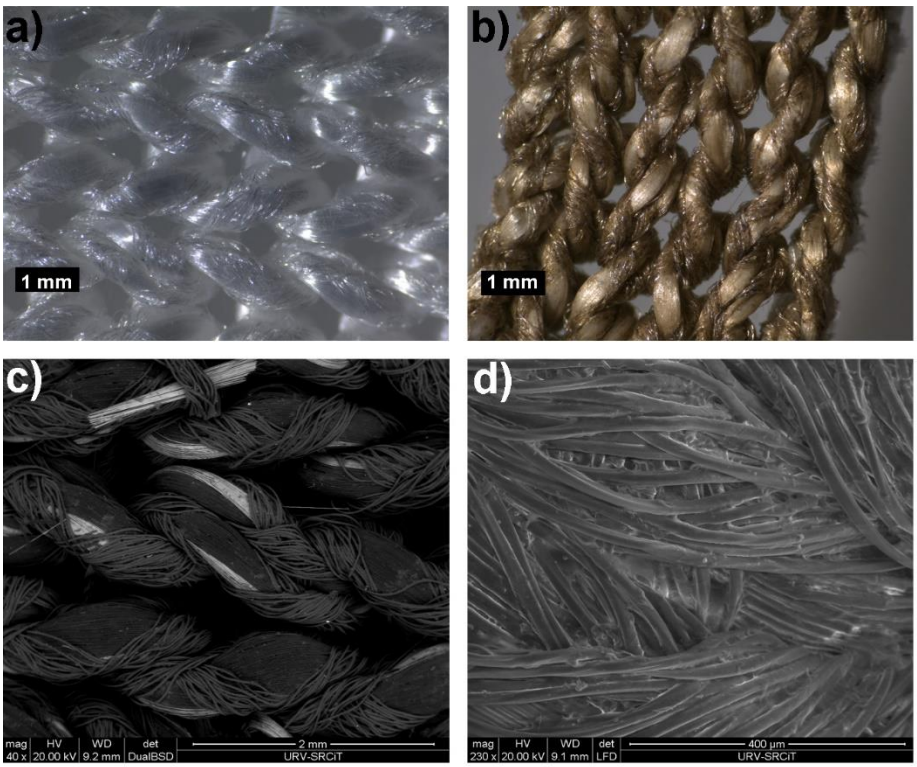

Figure 70: Stereo microscope micrographs of a) uncoated fabric and b) fabric coated with GO. ESEM images of the GO+PU coated fabric obtained from c) backscattered electrons and d) secondary electrons.

7.2. OPTIMIZATION OF THE PARAMETERS AND SCALE-UP OF THE COATING PROCESS

After the preliminary experiments, which validated the potential enhancements in mechanical properties of the test textile by coating with GO, the parameters involving the coating procedure were optimized, focusing on the possible scaling-up of the procedure to obtain higher quantity of coated fabric.

The first parameter that we optimized was the concentration of the GO dispersion used. The experiment consisted of the preparation of 20 GO-water dispersions with concentrations from 1 to 20 mg/mL. The fabric was cut into 7.5x15 cmxcm squares, and each one was dipped in GO dispersion, then draining off the excess of liquid and allowing them to dry at room temperature. The samples were then coated with 10%wt PU resin. This concentration of resin was chosen to fix the GO particles without adding much extra resistance provided by the resin itself.

Figure 71a shows the results of the maximum puncture resistance of the samples. An image of the prepared samples is displayed in the inset. We compare the results of the untreated fabric (red dot), the fabric coated only with PU (blue dot) and the fabrics coated with GO and PU (brown dots). GO-coated samples, even with the lowest concentrations (1 mg/mL), already increase the puncture resistance of the fabrics from that of the samples without GO. Among the GO-coated samples, the resistance does not increase indefinitely as the concentration of the GO dispersion increases. Initially, the resistance raises considerably at low concentrations until a few mg/mL, and then, the increase becomes more modest with a slight dip (10-14 mg/mL) and an asymptotic trend towards 280 N of maximum resistance.

It can be concluded that the best resistance/quantity of product ratio will be obtained at low concentrations, probably below 5 mg/mL. A low sensitivity of the function parameter to the design parameter (GO concentration) is also

beneficial from a manufacturing point of view. Therefore, we considered using a GO concentration of 5 mg/mL (instead of 2, for example), which represents an improvement in the maximum resistance of 250 N, being 60% more than the original fabric.

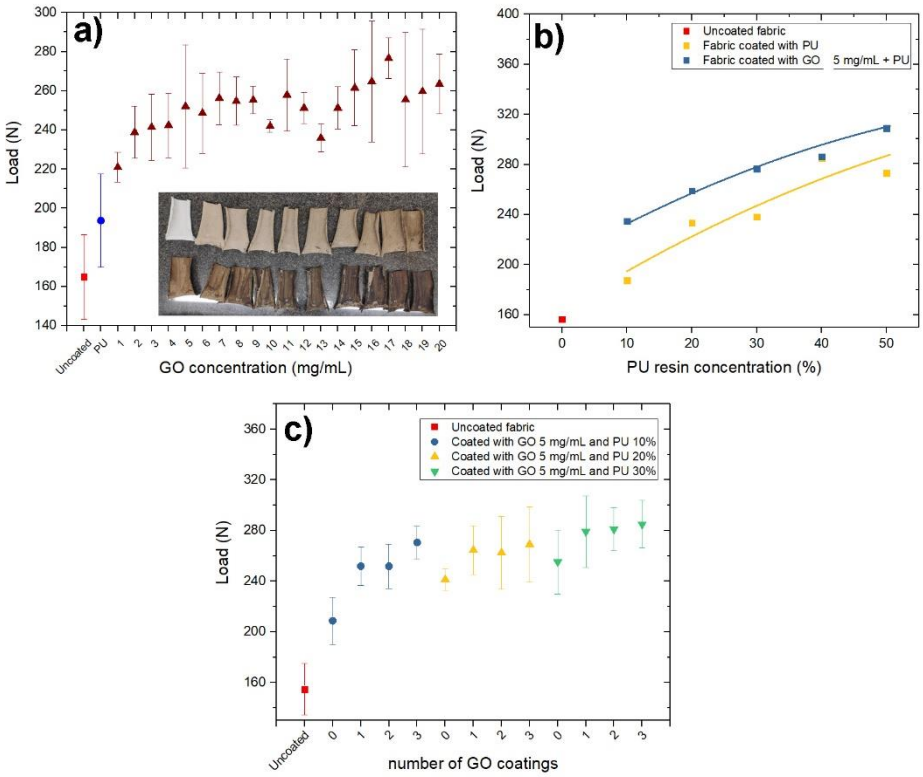

Figure 71: Results of the optimization of the coating parameters. a) Puncture resistance (load at puncture) of the fabrics coated with GO dispersions of different concentrations. b) Puncture resistance of the fabrics coated with different concentration of polyurethane and with GO (blue line) and without GO (yellow line), and of uncoated fabric (red dot). c) Puncture resistance of the fabrics coated with GO 5 mg/mL dispersion and varying PU concentrations for different number of consecutive coatings.

The next parameter to optimize was the quantity of resin used to fix the GO on the fabric. Firstly, the fabric pieces were coated with GO dispersion with a

concentration of 5 mg/mL and then, they were dip-coated in the PU resin diluted in water at different concentrations, ranging from 10 to 50%wt. Beyond 50% the application of resin resulted in a coated fabric with little flexibility, so we decided to discard using higher concentrations of resin. For comparative purposes, fabrics with the same concentrations of PU resin but without GO were prepared in a like manner.

The results are shown in Figure 71b. The resistance improves when the PU concentration is higher, since the PU membrane that covers the fabric becomes thicker (around 3 mm). It can be also seen that samples with GO have a higher resistance than their counterparts with only PU. This extra resistance is relatively greater, especially for low concentrations of PU in the resin. This is because the resistance contribution of the GO is approximately uniform and, therefore, is more noticeable when there is less PU.

Finally, the last optimization was the number of consecutive coatings of the dispersion of GO. In preliminary experiments we had observed that repeating cycles of GO coating and letting them dry between dip-coatings resulted in an increase of the amount of material deposited, more than using a single dip-coating of a higher concentration dispersion. For this experiment, therefore, fabric samples were prepared and dip-coated in the GO 5 mg/mL dispersion, letting them dry and repeating the dip-coating. Samples were prepared repeating the coating cycles 1, 2 and 3 times. This was done for three GO dispersions with the same GO concentration and PU with concentrations of 10, 20 and 30%wt. The results of maximum puncture resistance are shown in Figure 71c. In the graph it can be seen how the puncture resistance increases significantly for the samples coated with GO. However, it seems that additional coating cycles do not improve resistance significantly.

In this case, we monitored the weight variation when performing each cycle of coating. The results are shown in Table 14, which shows that when coating with GO, in the three cases that a single coating was made, the weight increased by about 1.25 g, increasing to 3.25 g for the second coating, and to 5.25 g for

the third. It can be observed that, despite depositing more material, the puncture resistance does not increase proportionally. The weight increase due to the PU resin coating is also shown, being consistent with the concentrations used. Considering that our objective is to increase the resistance of the fabric with as little impact on its weight as possible, we consider that the appropriate %resistance/%weight ratio is at the minimum amount of GO and PU resin: using 1 cycle of GO coating and PU resin at 10% of concentration, obtaining an increase in the puncture resistance of 62% relative to the uncoated fabric.

Original fabric max. resistance (N)	Sample	Weight before coatings (g)	Weight after GO coating (g)	Increment (%)	Weight after PU coating (g)	Increment (%)	Total weight increment (%)	Max. resistance (N)	Max resistance increment (%)
154,76									
PU 10%	Only PU	9,5294	n/a	n/a	10,0077	**5,02**	**5,02**	**208,82**	**34,93**
	GO 0,5% **1 coat.**	9,7584	9,8815	**1,26**	10,2977	**4,21**	**5,53**	**251,94**	**62,80**
	GO 0,5% **2 coat.**	9,2648	9,5485	**3,06**	9,9462	**4,17**	**7,35**	**251,87**	**62,75**
	GO 0,5% **3 coat.**	9,3962	9,8712	**5,06**	10,4365	**5,73**	**11,07**	**270,58**	**74,84**
PU 20%	Only PU	9,0275	n/a	n/a	9,8401	**9,00**	**9,00**	**241,38**	**55,97**
	GO 0,5% **1 coat.**	9,0045	9,1175	**1,25**	9,9239	**8,84**	**10,21**	**264,65**	**71,01**
	GO 0,5% **2 coat.**	9,2555	9,5505	**3,19**	10,4122	**9,02**	**12,50**	**262,57**	**69,66**
	GO 0,5% **3 coat.**	9,8898	10,395	**5,11**	11,2805	**8,52**	**14,06**	**269,11**	**73,89**
PU 30%	Only PU	9,6066	n/a	n/a	10,8653	**13,10**	**13,10**	**255,23**	**64,92**
	GO 0,5% **1 coat.**	9,3407	9,464	**1,32**	10,807	**14,19**	**15,70**	**279,10**	**80,35**
	GO 0,5% **2 coat.**	9,4628	9,81	**3,67**	11,1358	**13,51**	**17,68**	**281,07**	**81,62**
	GO 0,5% **3 coat.**	9,085	9,6022	**5,69**	10,845	**12,94**	**19,37**	**284,95**	**84,12**

Table 14: Maximum resistance data and increment of weight due to the deposition of coating material for the fabrics prepared on the optimization of the number of coating at different percentages of PU in the coating resin.

Once the experimental procedure was optimized at laboratory scale, it was transferred to a pilot scale, to manufacture fabric pieces in a continuous form, coating the textiles with GO 5 mg/mL and 10% PU resin, with a single coating cycle. For this experiment, we prepared 10 L of GO 5 mg/mL using one of our modifications of Hummers' method corresponding to the "GO-120 min/25º C" procedure explained in Section 3.2.2. In Figure 72a, the GO dispersion prepared for the experiment can be seen. We also prepared 5 L of 10% PU resin and two pieces of fabric with dimensions 50x500 cmxcm. In Figure 72b, the coating instrument, called foulard, can be observed. The image was taken while coating the fabric. In the process the white uncoated fabric passes through the GO dispersion bath and leaves it with darker color. Then it passes through two rollers that drain the excess of GO. After the coating with GO, the fabric was passed through a belt dryer at 60 ºC (not shown in the image). Afterwards, it was coated with the PU resin using the foulard, prior to the final drying at 60 ºC at the belt dryer. Figure 72c shows the final appearance of both samples with the GO and PU coatings.

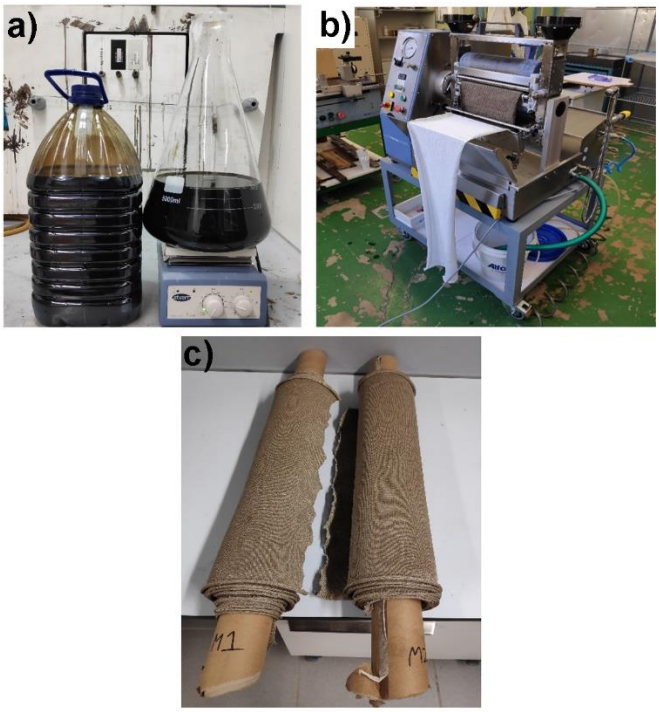

Figure 72: Images of the large-scale coating procedure. a) 10 L of GO 5 mg/mL prepared for the experiment. b) Foulard used to coat the fabrics with GO and PU. c) Coated final samples, consisting in two rolls of 1x5 m of fabric.

The mechanical resistance to the puncture was tested on these samples. The results are displayed in Table 1, where the information about the weight gain of the fabrics is also displayed. The original fabric weight of 430 g/m^2 was increased by 3.5%, averaged over the two samples. The puncture resistance has increased by 46.5%, which is slightly less than had been obtained in the lab samples. The difference may be due to the rollers of the foulard squeezing a higher volume of liquid than the manual procedure used in the lab.

We considered the results obtained in this last experiment to be good enough for the objective of the project as the resistance to penetration of the final fabric is above level 4, according to the EN 388:2016 standard. The samples were

manufactured then to prepare a textile piece with enhanced resistance to the puncture, closing the project with an actual prototype.

Table 15: Puncture resistance results of the samples coated using the industrial procedure.

Final samples	
Initial weight (g/m²)	430
Final weight sample 1 (g/m²)	447
Final weight sample 2 (g/m²)	443
Average increment (%)	**3,49**
Max resistance sample 1 (N)	227,21
Max resistance sample 2 (N)	223,23
Average increment (%)	**46,48**

7.3. CONCLUSION

During this project, a methodology to improve the mechanical resistance of textile materials has been investigated using GO as a coating in pure form. A major performance was achieved when combined with PU resin, thanks to epoxy cross-linking between PU and GO. Applying GO+PU gave a puncture resistance superior to that of the original fabric, reaching a resistance to penetration force above level 4, according to the EN 388:2016 standard. We optimized the relevant parameters to apply the GO+PU composite on the selected fabric, consistent with a viable industrially scalable procedure. We therefore optimized the amount of GO deposited, the amount of PU resin that should be applied to fix the GO without excessively increasing the weight of the product, and we translated these optimizations initially done in the lab to industrial machinery that is commonly used in the textile sector.

Large fabric pieces of GO-enhanced fabric with significant (~46%) increments in puncture resistance with minimal weight increase (~3.5%) were manufactured, being suitable for technical clothing, as was proved in the manufacture of a piece of clothing.

8 THESIS CONCLUSIONS AND OUTLOOK BEYOND THIS THESIS

The work done in this thesis has resulted in new contributions in the growing field of graphene oxide and has brought a private company to complete an ambitious industrial-R&D research project applying this novel nanomaterial. The successful development of the research made it possible to meet expectations on both aspects of the investigation: contributing to the scientific literature with a publication (a second one being in progress), and successfully conclude an industrial R&D project.

Regarding the fundamental research in the GO field, we investigated the most important reaction procedure for the obtention of GO: Hummers' method. We revealed how some of the reaction conditions affect the obtained GO without any post-treatment (which might modify its physicochemical properties). Thus, we reached the following main conclusions about the use of Hummers' method in our work:

- Reaction time can be increased to obtain better exfoliation of the graphite oxide particles into thin GO flakes. The increase of reaction time does not come necessarily with a higher oxidation of the flakes, so higher damage to the carbon honeycomb is avoided and the total and relative quantity of functional groups is preserved. Organosulfates, which are functional groups particularly prone to hydrolysis, are maintained despite the increase of the reaction time. This route may be interesting in applications where well-exfoliated GO with low functionalization or with high relative presence of thermally-unstable functional groups, including organosulfates, are sought.
- Reaction temperature also affects the degree of exfoliation of the GO flakes, with higher exfoliation for higher reaction temperatures. However, the chemical composition of GO also varies, obtaining a

higher oxidation degree for higher temperatures and a variation of the functionalization towards more stable functional groups, especially with the removal of organosulfates. Therefore, varying reaction temperature is a magnificent route to tailor the chemistry of the GO flakes.

Additionally, we investigated the effect of some post-treatments that are widely used in the technical literature on the as-synthesized GOs. The post-treatments were the neutralization of the acidic media, and the use of strong agitation (but without sonication, a significantly more aggressive approach). The main conclusions we reached are as follows:

- The strong agitation caused a tremendous effect on the morphology of the flakes, causing their shattering into smaller pieces. The neutralization of the media also affected the chemistry of the GOs, with loss of the chemical richness of the prepared GOs, with the development of the less-stable functional groups, including organosulfates, towards more stable functionalities, a similar effect as the one obtained for the GOs prepared with high reaction temperature.
- Furthermore, and most importantly, all the post-treated GOs have similar physicochemical characteristics, regardless the reaction conditions for their preparation. This would explain why some authors claim that GOs prepared with different reaction conditions differ little in their compositional characteristics, when, in fact, they could be observing the homogenizing effect of the post-treatments commonly applied.

Finally, the work performed for the industrial-R&D textile coating project arose with the following conclusions:

- The capacity of GO to be used as a reinforcing coating in textiles have been demonstrated. Its major performance is achieved when combined with a polyurethane resin to fix the GO on the fabric and form a GO+PU composite based on epoxy cross-linking. The mechanical resistance

tests of the prepared fabrics to puncture (according to standard EN 388:2016) showed a resistance increase for all the GO+PU coated fabrics around the 50%, compared to the original fabric. A large fraction of this increase is attributable to the GO.

The coating methodology has been scaled up to an industrial pilot scale, showing that GO can be effectively applied on textiles with currently used industrial procedures.

We conclude with an outlook beyond by this thesis' research. Clearly, GO is a complex nanomaterial which is still not fully understood, and which will likely have great importance in the future in many applications. The new knowledge obtained in this thesis regarding the influence of reaction parameters on the chemical richness of the GO could be used in applications in which GO with different compositions can greatly affect the performance of the material. For example, in combination with polymers, GOs with different chemistries may form composites with different characteristics, such as strength, flexibility, conductivity or processability. In the area of sensors, tailored GOs could be used to enhance the electrochemical interaction with the analyte. Also, further functionalization could be performed (and optimized) with GOs with adequate starting composition. The controlled exfoliation with low oxidation is also interesting when reduction to rGO is sought, which is of interest in capacitors, batteries or conductive thin films.

REFERENCES

[1] A. K. Geim and K. S. Novoselov, “The rise of graphene,” *Nat. Mater.*, vol. 6, no. 3, pp. 183–191, 2007.

[2] H. P. Boehm, R. Setton, and E. Stumpp, “Nomenclature and terminology of graphite intercalation compounds,” *Carbon N. Y.*, vol. 24, no. 2, pp. 241–245, 1986.

[3] A. K. Geim, “Graphene prehistory,” *Phys. Scr.*, vol. T146, p. 14003, 2012.

[4] K. S. Novoselov *et al.*, “Electric Field Effect in Atomically Thin Carbon Films,” *Science (80-.).*, vol. 306, no. 5696, pp. 666 LP – 669, Oct. 2004.

[5] “Press release. NobelPrize.org. Nobel Prize Outreach AB 2021. Thu. 24 Jun 2021. <https://www.nobelprize.org/prizes/physics/2010/press-release/>.” .

[6] C. Lee, X. Wei, J. W. Kysar, and J. Hone, “Measurement of the Elastic Properties and Intrinsic Strength of Monolayer Graphene,” *Science (80-.).*, vol. 321, no. 5887, pp. 385 LP – 388, Jul. 2008.

[7] J.-H. Chen, C. Jang, S. Xiao, M. Ishigami, and M. S. Fuhrer, “Intrinsic and extrinsic performance limits of graphene devices on SiO2,” *Nat. Nanotechnol.*, vol. 3, no. 4, pp. 206–209, 2008.

[8] D. E. Sheehy and J. Schmalian, “Optical transparency of graphene as determined by the fine-structure constant,” *Phys. Rev. B*, vol. 80, no. 19, p. 193411, Nov. 2009.

[9] S. Ghosh *et al.*, “Dimensional crossover of thermal transport in few-layer graphene,” *Nat. Mater.*, vol. 9, no. 7, pp. 555–558, 2010.

[10] R. Van Noorden, “Production: Beyond sticky tape,” *Nature*, vol. 483, no. 7389, pp. S32–S33, 2012.

[11] F. Tehrani, L. Reiner, and B. Bavarian, “Rapid Prototyping of a High Sensitivity Graphene Based Glucose Sensor Strip,” *PLoS One*, vol. 10, no. 12, p. e0145036, Dec. 2015.

[12] I. Forbeaux, J.-M. Themlin, and J.-M. Debever, “Heteroepitaxial graphite on 6H-SiC (0001): Interface formation through conduction-band electronic structure,” *Phys. Rev. B*, vol. 58, no. 24, pp. 16396–16406, Dec. 1998.

[13] C. Virojanadara, M. Syväjarvi, R. Yakimova, L. I. Johansson, A. A. Zakharov, and T. Balasubramanian, “Homogeneous large-area graphene layer growth on 6H-SiC(0001),” *Phys. Rev. B*, vol. 78, no. 24, p. 245403, Dec. 2008.

[14] X. Li *et al.*, “Large-Area Synthesis of High-Quality and Uniform Graphene Films on Copper Foils,” *Science (80-.).*, vol. 324, no. 5932, pp. 1312 LP – 1314, Jun. 2009.

[15] P. Li, C. Chen, J. Zhang, S. Li, B. Sun, and Q. Bao, “Graphene-Based Transparent Electrodes for Hybrid Solar Cells,” *Front. Mater.*, vol. 1, p. 26, 2014.

[16] S. Bae *et al.*, “Roll-to-roll production of 30-inch graphene films for transparent electrodes,” *Nat. Nanotechnol.*, vol. 5, no. 8, pp. 574–578, 2010.

[17] P. Y. Huang *et al.*, “Grains and grain boundaries in single-layer graphene atomic patchwork quilts,” *Nature*, vol. 469, no. 7330, pp. 389–392, 2011.

[18] A. Yu, P. Ramesh, M. E. Itkis, E. Bekyarova, and R. C. Haddon, “Graphite Nanoplatelet−Epoxy Composite Thermal Interface Materials,” *J. Phys. Chem. C*, vol. 111, no. 21, pp. 7565–7569, May 2007.

[19] S. Eigler *et al.*, “Wet Chemical Synthesis of Graphene,” *Adv. Mater.*, vol. 25, no. 26, pp. 3583–3587, Jul. 2013.

[20] D. Li, M. B. Müller, S. Gilje, R. B. Kaner, and G. G. Wallace, “Processable aqueous dispersions of graphene nanosheets,” *Nat. Nanotechnol.*, vol. 3, no. 2, pp. 101–105, 2008.

[21] S. Stankovich *et al.*, “Synthesis of graphene-based nanosheets via chemical reduction of exfoliated graphite oxide,” *Carbon N. Y.*, vol. 45, no. 7, pp. 1558–1565, 2007.

[22] Y.-J. Liou, B.-D. Tsai, and W.-J. Huang, “An economic route to mass production of graphene oxide solution for preparing graphene oxide papers,” *Mater. Sci. Eng. B*, vol. 193, pp. 37–40, 2015.

[23] B. C. Brodie, “XIII. On the atomic weight of graphite,” *Philos. Trans. R. Soc. London*, vol. 149, pp. 249–259, Jan. 1859.

[24] G. Eda and M. Chhowalla, “Chemically Derived Graphene Oxide: Towards Large-Area Thin-Film Electronics and Optoelectronics,” *Adv. Mater.*, vol. 22, no. 22, pp. 2392–2415, Jun. 2010.

[25] H. Chen, M. Wu, and C. Li, “Structural integrity versus lateral size: Enhancing graphene-based film materials by reducing planar defects

rather than flake boundary," *Carbon N. Y.*, vol. 139, pp. 216–225, 2018.

[26] V. C. Tung, M. J. Allen, Y. Yang, and R. B. Kaner, "High-throughput solution processing of large-scale graphene," *Nat. Nanotechnol.*, vol. 4, no. 1, pp. 25–29, 2009.

[27] H. C. Schniepp *et al.*, "Functionalized Single Graphene Sheets Derived from Splitting Graphite Oxide," *J. Phys. Chem. B*, vol. 110, no. 17, pp. 8535–8539, May 2006.

[28] D. Krishnan *et al.*, "Energetic graphene oxide: Challenges and opportunities," *Nano Today*, vol. 7, no. 2, pp. 137–152, 2012.

[29] N. A. Kotov, I. Dékány, and J. H. Fendler, "Ultrathin graphite oxide–polyelectrolyte composites prepared by self-assembly: Transition between conductive and non-conductive states," *Adv. Mater.*, vol. 8, no. 8, pp. 637–641, Aug. 1996.

[30] C. Gómez-Navarro *et al.*, "Electronic Transport Properties of Individual Chemically Reduced Graphene Oxide Sheets," *Nano Lett.*, vol. 7, no. 11, pp. 3499–3503, Nov. 2007.

[31] S. Pei and H.-M. Cheng, "The reduction of graphene oxide," *Carbon N. Y.*, vol. 50, no. 9, pp. 3210–3228, 2012.

[32] H.-J. Shin *et al.*, "Efficient Reduction of Graphite Oxide by Sodium Borohydride and Its Effect on Electrical Conductance," *Adv. Funct. Mater.*, vol. 19, no. 12, pp. 1987–1992, Jun. 2009.

[33] I. K. Moon, J. Lee, R. S. Ruoff, and H. Lee, "Reduced graphene oxide by chemical graphitization," *Nat. Commun.*, vol. 1, no. 1, p. 73, 2010.

[34] S. Y. Toh, K. S. Loh, S. K. Kamarudin, and W. R. W. Daud, "Graphene production via electrochemical reduction of graphene oxide: Synthesis and characterisation," *Chem. Eng. J.*, vol. 251, pp. 422–434, 2014.

[35] Y. Zhou, Q. Bao, L. A. L. Tang, Y. Zhong, and K. P. Loh, "Hydrothermal Dehydration for the 'Green' Reduction of Exfoliated Graphene Oxide to Graphene and Demonstration of Tunable Optical Limiting Properties," *Chem. Mater.*, vol. 21, no. 13, pp. 2950–2956, Jul. 2009.

[36] C. Mattevi *et al.*, "Evolution of Electrical, Chemical, and Structural Properties of Transparent and Conducting Chemically Derived Graphene Thin Films," *Adv. Funct. Mater.*, vol. 19, no. 16, pp. 2577–2583, Aug. 2009.

[37] S. Mao, H. Pu, and J. Chen, "Graphene oxide and its reduction: modeling and experimental progress," *RSC Adv.*, vol. 2, no. 7, pp.

2643–2662, 2012.

[38] M. Terrones *et al.*, “Graphene and graphite nanoribbons: Morphology, properties, synthesis, defects and applications,” *Nano Today*, vol. 5, no. 4, pp. 351–372, 2010.

[39] U. Hofmann and R. Holst, “Über die Säurenatur und die Methylierung von Graphitoxyd,” *Berichte der Dtsch. Chem. Gesellschaft (A B Ser.*, vol. 72, no. 4, pp. 754–771, Apr. 1939.

[40] G. Ruess, “Über das Graphitoxyhydroxyd (Graphitoxyd),” *Monatshefte für Chemie und verwandte Teile anderer Wissenschaften*, vol. 76, no. 3, pp. 381–417, 1947.

[41] W. Scholz and H. P. Boehm, “Untersuchungen am Graphitoxid. VI. Betrachtungen zur Struktur des Graphitoxids,” *Zeitschrift für Anorg. und Allg. Chemie*, vol. 369, no. 3-6, pp. 327–340, Oct. 1969.

[42] T. Nakajima and Y. Matsuo, “Formation process and structure of graphite oxide,” *Carbon N. Y.*, vol. 32, no. 3, pp. 469–475, 1994.

[43] D. R. Dreyer, S. Park, C. W. Bielawski, and R. S. Ruoff, “The chemistry of graphene oxide,” *Chem. Soc. Rev.*, vol. 39, no. 1, pp. 228–240, 2010.

[44] A. Lerf, H. He, M. Forster, and J. Klinowski, “Structure of Graphite Oxide Revisited,” *J. Phys. Chem. B*, vol. 102, no. 23, pp. 4477–4482, Jun. 1998.

[45] H. He, T. Riedl, A. Lerf, and J. Klinowski, “Solid-State NMR Studies of the Structure of Graphite Oxide,” *J. Phys. Chem.*, vol. 100, no. 51, pp. 19954–19958, Jan. 1996.

[46] A. M. Dimiev, “Mechanism of Formation and Chemical Structure of Graphene Oxide,” *Graphene Oxide*. pp. 36–84, 13-Oct-2016.

[47] P. P. Brisebois and M. Siaj, “Harvesting graphene oxide – years 1859 to 2019: a review of its structure, synthesis, properties and exfoliation,” *J. Mater. Chem. C*, vol. 8, no. 5, pp. 1517–1547, 2020.

[48] C. Gómez-Navarro *et al.*, “Atomic Structure of Reduced Graphene Oxide,” *Nano Lett.*, vol. 10, no. 4, pp. 1144–1148, Apr. 2010.

[49] K. Erickson, R. Erni, Z. Lee, N. Alem, W. Gannett, and A. Zettl, “Determination of the Local Chemical Structure of Graphene Oxide and Reduced Graphene Oxide,” *Adv. Mater.*, vol. 22, no. 40, pp. 4467–4472, Oct. 2010.

[50] A. M. Dimiev, K. Shukhina, and A. Khannanov, “Mechanism of the graphene oxide formation: The role of water, ‘reversibility’ of the oxidation, and mobility of the C–O bonds,” *Carbon N. Y.*, vol. 166, pp.

1–14, 2020.

[51] P. V Kumar, N. M. Bardhan, S. Tongay, J. Wu, A. M. Belcher, and J. C. Grossman, “Scalable enhancement of graphene oxide properties by thermally driven phase transformation,” *Nat. Chem.*, vol. 6, no. 2, pp. 151–158, 2014.

[52] Y. Zhu *et al.*, “Graphene and Graphene Oxide: Synthesis, Properties, and Applications,” *Adv. Mater.*, vol. 22, no. 35, pp. 3906–3924, Sep. 2010.

[53] N. V Medhekar, A. Ramasubramaniam, R. S. Ruoff, and V. B. Shenoy, “Hydrogen Bond Networks in Graphene Oxide Composite Paper: Structure and Mechanical Properties,” *ACS Nano*, vol. 4, no. 4, pp. 2300–2306, Apr. 2010.

[54] Z. Yang, Y. Sun, and F. Ma, “Interlayer spacing of multilayer graphene oxide: Influences of oxygen-containing group density, thickness, temperature and strain,” *Appl. Surf. Sci.*, vol. 529, p. 147075, 2020.

[55] T. Ben Issa and L. Benhamada, “Crystal Structure, Thermal Behavior and Vibrational Spectra of 4,4’Diamoniumdiphenylmethan Sulfate Hydrate,” *Open J. Inorg. Chem.*, vol. 07, no. 02, pp. 61–73, 2017.

[56] A. F. Fonseca, T. Liang, D. Zhang, K. Choudhary, and S. B. Sinnott, “Probing the accuracy of reactive and non-reactive force fields to describe physical and chemical properties of graphene-oxide,” *Comput. Mater. Sci.*, vol. 114, pp. 236–243, 2016.

[57] D. A. Dikin *et al.*, “Preparation and characterization of graphene oxide paper,” *Nature*, vol. 448, no. 7152, pp. 457–460, 2007.

[58] R. Liu *et al.*, “Graphene oxide membrane for liquid phase organic molecular separation,” *Carbon N. Y.*, vol. 77, pp. 933–938, 2014.

[59] A. Dimiev, D. V Kosynkin, A. Sinitskii, A. Slesarev, Z. Sun, and J. M. Tour, “Layer-by-Layer Removal of Graphene for Device Patterning,” *Science (80-.).*, vol. 331, no. 6021, pp. 1168 LP – 1172, Mar. 2011.

[60] A. T. Dideikin and A. Y. Vul’, “Graphene Oxide and Derivatives: The Place in Graphene Family,” *Front. Phys.*, vol. 6, p. 149, 2019.

[61] J. W. Suk, R. D. Piner, J. An, and R. S. Ruoff, “Mechanical Properties of Monolayer Graphene Oxide,” *ACS Nano*, vol. 4, no. 11, pp. 6557–6564, Nov. 2010.

[62] T. Kuilla, S. Bhadra, D. Yao, N. H. Kim, S. Bose, and J. H. Lee, “Recent advances in graphene based polymer composites,” *Prog. Polym. Sci.*, vol. 35, no. 11, pp. 1350–1375, 2010.

[63] H. Kim, A. A. Abdala, and C. W. Macosko, “Graphene/Polymer

Nanocomposites," *Macromolecules*, vol. 43, no. 16, pp. 6515–6530, Aug. 2010.

[64] Y. Wei *et al.*, "Influence of graphene oxide with different oxidation levels on the properties of epoxy composites," *Compos. Sci. Technol.*, vol. 161, pp. 74–84, 2018.

[65] T. Cheng-an, Z. Hao, W. Fang, Z. Hui, Z. Xiaorong, and W. Jianfang, "Mechanical Properties of Graphene Oxide/Polyvinyl Alcohol Composite Film," *Polym. Polym. Compos.*, vol. 25, no. 1, pp. 11–16, Jan. 2017.

[66] Y. Li, D. Pan, S. Chen, Q. Wang, G. Pan, and T. Wang, "In situ polymerization and mechanical, thermal properties of polyurethane/graphene oxide/epoxy nanocomposites," *Mater. Des.*, vol. 47, pp. 850–856, 2013.

[67] H.-D. Huang *et al.*, "Improved barrier properties of poly(lactic acid) with randomly dispersed graphene oxide nanosheets," *J. Memb. Sci.*, vol. 464, pp. 110–118, 2014.

[68] G. Eda, G. Fanchini, and M. Chhowalla, "Large-area ultrathin films of reduced graphene oxide as a transparent and flexible electronic material," *Nat. Nanotechnol.*, vol. 3, no. 5, pp. 270–274, 2008.

[69] O. C. Compton, B. Jain, D. A. Dikin, A. Abouimrane, K. Amine, and S. T. Nguyen, "Chemically Active Reduced Graphene Oxide with Tunable C/O Ratios," *ACS Nano*, vol. 5, no. 6, pp. 4380–4391, Jun. 2011.

[70] W. K. Chee *et al.*, "Performance of Flexible and Binderless Polypyrrole/Graphene Oxide/Zinc Oxide Supercapacitor Electrode in a Symmetrical Two-Electrode Configuration," *Electrochim. Acta*, vol. 157, pp. 88–94, 2015.

[71] D. Lin *et al.*, "Layered reduced graphene oxide with nanoscale interlayer gaps as a stable host for lithium metal anodes," *Nat. Nanotechnol.*, vol. 11, no. 7, pp. 626–632, 2016.

[72] S. Wang *et al.*, "Highly Stretchable and Self-Healable Supercapacitor with Reduced Graphene Oxide Based Fiber Springs," *ACS Nano*, vol. 11, no. 2, pp. 2066–2074, Feb. 2017.

[73] S.-S. Li, K.-H. Tu, C.-C. Lin, C.-W. Chen, and M. Chhowalla, "Solution-Processable Graphene Oxide as an Efficient Hole Transport Layer in Polymer Solar Cells," *ACS Nano*, vol. 4, no. 6, pp. 3169–3174, Jun. 2010.

[74] Y. Zhang, B. Shen, H. Huang, Y. He, B. Fei, and F. Lv, "BiPO4/reduced graphene oxide composites photocatalyst with high photocatalytic activity," *Appl. Surf. Sci.*, vol. 319, pp. 272–277, 2014.

[75] S. Padmajan Sasikala *et al.*, "Graphene oxide liquid crystals: a frontier 2D soft material for graphene-based functional materials," *Chem. Soc. Rev.*, vol. 47, no. 16, pp. 6013–6045, 2018.

[76] J. D. Renteria *et al.*, "Strongly Anisotropic Thermal Conductivity of Free-Standing Reduced Graphene Oxide Films Annealed at High Temperature," *Adv. Funct. Mater.*, vol. 25, no. 29, pp. 4664–4672, Aug. 2015.

[77] Z. Lu, C. Lu, C. K. Y. Leung, and Z. Li, "Graphene oxide modified Strain Hardening Cementitious Composites with enhanced mechanical and thermal properties by incorporating ultra-fine phase change materials," *Cem. Concr. Compos.*, vol. 98, pp. 83–94, 2019.

[78] B. Wicklein *et al.*, "Thermally insulating and fire-retardant lightweight anisotropic foams based on nanocellulose and graphene oxide," *Nat. Nanotechnol.*, vol. 10, no. 3, pp. 277–283, 2015.

[79] N. Wei, X. Peng, and Z. Xu, "Understanding Water Permeation in Graphene Oxide Membranes," *ACS Appl. Mater. Interfaces*, vol. 6, no. 8, pp. 5877–5883, Apr. 2014.

[80] H. Yan *et al.*, "Effects of the oxidation degree of graphene oxide on the adsorption of methylene blue," *J. Hazard. Mater.*, vol. 268, pp. 191–198, 2014.

[81] S. Thangavel and G. Venugopal, "Understanding the adsorption property of graphene-oxide with different degrees of oxidation levels," *Powder Technol.*, vol. 257, pp. 141–148, 2014.

[82] C. Feng *et al.*, "Superhydrophobic and Superoleophilic Micro-Wrinkled Reduced Graphene Oxide as a Highly Portable and Recyclable Oil Sorbent," *ACS Appl. Mater. Interfaces*, vol. 8, no. 15, pp. 9977–9985, Apr. 2016.

[83] C. I. L. Justino, A. R. Gomes, A. C. Freitas, A. C. Duarte, and T. A. P. Rocha-Santos, "Graphene based sensors and biosensors," *TrAC Trends Anal. Chem.*, vol. 91, pp. 53–66, 2017.

[84] D.-K. Lim, A. Barhoumi, R. G. Wylie, G. Reznor, R. S. Langer, and D. S. Kohane, "Enhanced Photothermal Effect of Plasmonic Nanoparticles Coated with Reduced Graphene Oxide," *Nano Lett.*, vol. 13, no. 9, pp. 4075–4079, Sep. 2013.

[85] Y. Wang, Z. Li, J. Wang, J. Li, and Y. Lin, "Graphene and graphene oxide: biofunctionalization and applications in biotechnology," *Trends Biotechnol.*, vol. 29, no. 5, pp. 205–212, 2011.

[86] D. R. Dreyer, A. D. Todd, and C. W. Bielawski, "Harnessing the chemistry of graphene oxide," *Chem. Soc. Rev.*, vol. 43, no. 15, pp.

5288–5301, 2014.

[87] A. Kasprzak, A. Zuchowska, and M. Poplawska, “Functionalization of graphene: does the organic chemistry matter?,” *Beilstein J. Org. Chem.*, vol. 14, pp. 2018–2026, Aug. 2018.

[88] Y. Xu *et al.*, “A Graphene Hybrid Material Covalently Functionalized with Porphyrin: Synthesis and Optical Limiting Property,” *Adv. Mater.*, vol. 21, no. 12, pp. 1275–1279, Mar. 2009.

[89] L. Zheng and W. Zhen, “Preparation and characterization of amidated graphene oxide and its effect on the performance of poly(lactic acid),” *Iran. Polym. J.*, vol. 27, no. 4, pp. 239–252, 2018.

[90] Z. Liu, J. T. Robinson, X. Sun, and H. Dai, “PEGylated Nanographene Oxide for Delivery of Water-Insoluble Cancer Drugs,” *J. Am. Chem. Soc.*, vol. 130, no. 33, pp. 10876–10877, Aug. 2008.

[91] E. S. Orth, J. E. S. Fonsaca, S. H. Domingues, H. Mehl, M. M. Oliveira, and A. J. G. Zarbin, “Targeted thiolation of graphene oxide and its utilization as precursor for graphene/silver nanoparticles composites,” *Carbon N. Y.*, vol. 61, pp. 543–550, 2013.

[92] M. K. Rabchinskii *et al.*, “From graphene oxide towards aminated graphene: facile synthesis, its structure and electronic properties,” *Sci. Rep.*, vol. 10, no. 1, p. 6902, 2020.

[93] M. Xu *et al.*, “Improved In Vitro and In Vivo Biocompatibility of Graphene Oxide through Surface Modification: Poly(Acrylic Acid)-Functionalization is Superior to PEGylation,” *ACS Nano*, vol. 10, no. 3, pp. 3267–3281, Mar. 2016.

[94] A. M. Shanmugharaj, J. H. Yoon, W. J. Yang, and S. H. Ryu, “Synthesis, characterization, and surface wettability properties of amine functionalized graphene oxide films with varying amine chain lengths,” *J. Colloid Interface Sci.*, vol. 401, pp. 148–154, 2013.

[95] S.-J. Qiao, X.-N. Xu, Y. Qiu, H.-C. Xiao, and Y.-F. Zhu, “Simultaneous Reduction and Functionalization of Graphene Oxide by 4-Hydrazinobenzenesulfonic Acid for Polymer Nanocomposites,” *Nanomaterials* , vol. 6, no. 2. 2016.

[96] J. S. Y. Chia, M. T. T. Tan, P. S. Khiew, J. K. Chin, and C. W. Siong, “A bio-electrochemical sensing platform for glucose based on irreversible, non-covalent pi–pi functionalization of graphene produced via a novel, green synthesis method,” *Sensors Actuators B Chem.*, vol. 210, pp. 558–565, 2015.

[97] L. Staudenmaier, “Verfahren zur Darstellung der Graphitsäure,” *Berichte der Dtsch. Chem. Gesellschaft*, vol. 31, no. 2, pp. 1481–1487,

May 1898.

[98] W. Luzi, “Beiträge zur Kenntnis des Graphitkohlenstoffs.,” *Z. Naturwiss*, vol. 64, pp. 224–269, 1891.

[99] G. Charpy, “Sur la formation de l’oxyde graphitique et la définition du graphite,” *C. R. Hebd. Séances Acad. Sci.*, vol. 148, pp. 920–923, 1909.

[100] H. P. Boehm, M. Eckel, and W. Scholz, “Untersuchungen am Graphitoxid V. Über den Bildungsmechanismus des Graphitoxids,” *Zeitschrift für Anorg. und Allg. Chemie*, vol. 353, no. 5-6, pp. 236–242, Sep. 1967.

[101] W. S. Hummers and R. E. Offeman, “Preparation of Graphitic Oxide,” *J. Am. Chem. Soc.*, vol. 80, no. 6, p. 1339, Mar. 1958.

[102] S. Shamaila, A. K. L. Sajjad, and A. Iqbal, “Modifications in development of graphene oxide synthetic routes,” *Chem. Eng. J.*, vol. 294, pp. 458–477, 2016.

[103] M. S. Chang *et al.*, “Guidelines for Tailored Chemical Functionalization of Graphene,” *Chem. Mater.*, vol. 29, no. 1, pp. 307–318, Jan. 2017.

[104] H.-P. Boehm and W. Scholz, “Untersuchungen am Graphitoxyd, IV1). Vergleich der Darstellungsverfahren für Graphitoxyd,” *Justus Liebigs Ann. Chem.*, vol. 691, no. 1, pp. 1–8, Feb. 1966.

[105] H. L. Poh, F. Šaněk, A. Ambrosi, G. Zhao, Z. Sofer, and M. Pumera, “Graphenes prepared by Staudenmaier, Hofmann and Hummers methods with consequent thermal exfoliation exhibit very different electrochemical properties,” *Nanoscale*, vol. 4, no. 11, pp. 3515–3522, 2012.

[106] B. K. Ong, H. L. Poh, C. K. Chua, and M. Pumera, “Graphenes Prepared by Hummers, Staudenmaier and Hofmann Methods for Analysis of TNT-Based Nitroaromatic Explosives in Seawater,” *Electroanalysis*, vol. 24, no. 11, pp. 2085–2093, Nov. 2012.

[107] O. Jankovský *et al.*, “Synthesis procedure and type of graphite oxide strongly influence resulting graphene properties,” *Appl. Mater. Today*, vol. 4, pp. 45–53, 2016.

[108] C. Schafhäutl, “Über weißes und graues Roheisen, Graphitbildung,” *J. Prakt. Chem.*, vol. 76, no. (1), pp. 257–310, 1859.

[109] A. Dimiev, D. V Kosynkin, L. B. Alemany, P. Chaguine, and J. M. Tour, “Pristine Graphite Oxide,” *J. Am. Chem. Soc.*, vol. 134, no. 5, pp. 2815–2822, Feb. 2012.

[110] C. Botas *et al.*, “Graphene materials with different structures prepared

from the same graphite by the Hummers and Brodie methods," *Carbon N. Y.*, vol. 65, pp. 156–164, 2013.

[111] H. Thiele, "Die Quellung des Graphit an der Anode und die mechanische Zerstörung von Kohlenanoden," *Zeitschrift für Elektrochemie und Angew. Phys. Chemie*, vol. 40, no. 1, pp. 26–33, Jan. 1934.

[112] S. Pei, Q. Wei, K. Huang, H.-M. Cheng, and W. Ren, "Green synthesis of graphene oxide by seconds timescale water electrolytic oxidation," *Nat. Commun.*, vol. 9, no. 1, p. 145, 2018.

[113] Y. Nishina and S. Eigler, "Chemical and electrochemical synthesis of graphene oxide – a generalized view," *Nanoscale*, vol. 12, no. 24, pp. 12731–12740, 2020.

[114] B. Gurzęda, P. Florczak, M. Kempiński, B. Peplińska, P. Krawczyk, and S. Jurga, "Synthesis of graphite oxide by electrochemical oxidation in aqueous perchloric acid," *Carbon N. Y.*, vol. 100, pp. 540–545, 2016.

[115] A. Metrot and J. E. Fischer, "Charge transfer reactions during anodic oxidation of graphite in H2SO4," *Synth. Met.*, vol. 3, no. 3, pp. 201–207, 1981.

[116] D. C. Marcano *et al.*, "Improved Synthesis of Graphene Oxide," *ACS Nano*, vol. 4, no. 8, pp. 4806–4814, Aug. 2010.

[117] L. Peng *et al.*, "An iron-based green approach to 1-h production of single-layer graphene oxide," *Nat. Commun.*, vol. 6, no. 1, p. 5716, 2015.

[118] "https://www.scbt.com/p/potassium-ferrate-vi-39469-86-8." .

[119] A. Romero, M. P. Lavin-Lopez, L. Sanchez-Silva, J. L. Valverde, and A. Paton-Carrero, "Comparative study of different scalable routes to synthesize graphene oxide and reduced graphene oxide," *Mater. Chem. Phys.*, vol. 203, pp. 284–292, 2018.

[120] E. M. Deemer *et al.*, "Consequence of oxidation method on graphene oxide produced with different size graphite precursors," *Mater. Sci. Eng. B*, vol. 224, pp. 150–157, 2017.

[121] L. Shen *et al.*, "Analysis of oxidation degree of graphite oxide and chemical structure of corresponding reduced graphite oxide by selecting different-sized original graphite," *RSC Adv.*, vol. 8, no. 31, pp. 17209–17217, 2018.

[122] A. M. Dimiev, *Mechanism of Formation and Chemical Structure of Graphene Oxide In Graphene Oxide (eds A.M. Dimiev and S. Eigler)*.

2016.

[123] J.-L. Li, K. N. Kudin, M. J. McAllister, R. K. Prud'homme, I. A. Aksay, and R. Car, "Oxygen-Driven Unzipping of Graphitic Materials," *Phys. Rev. Lett.*, vol. 96, no. 17, p. 176101, May 2006.

[124] G. Shao, Y. Lu, F. Wu, C. Yang, F. Zeng, and Q. Wu, "Graphene oxide: the mechanisms of oxidation and exfoliation," *J. Mater. Sci.*, vol. 47, no. 10, pp. 4400–4409, 2012.

[125] D. W. Boukhvalov, "Oxidation of a Graphite Surface: The Role of Water," *J. Phys. Chem. C*, vol. 118, no. 47, pp. 27594–27598, Nov. 2014.

[126] A. M. Dimiev, L. B. Alemany, and J. M. Tour, "Graphene Oxide. Origin of Acidity, Its Instability in Water, and a New Dynamic Structural Model," *ACS Nano*, vol. 7, no. 1, pp. 576–588, Jan. 2013.

[127] A. M. Dimiev and J. M. Tour, "Mechanism of Graphene Oxide Formation," *ACS Nano*, vol. 8, no. 3, pp. 3060–3068, Mar. 2014.

[128] A. M. Dimiev and T. A. Polson, "Contesting the two-component structural model of graphene oxide and reexamining the chemistry of graphene oxide in basic media," *Carbon N. Y.*, vol. 93, pp. 544–554, 2015.

[129] Y. Yosida, S. Tanuma, and K. Okabe, "In situ observation of x-ray diffraction in a synthesis of H2SO4-GICS," *Synth. Met.*, vol. 34, no. 1, pp. 341–346, 1989.

[130] P. C. Eklund, C. H. Olk, F. J. Holler, J. G. Spolar, and E. T. Arakawa, "Raman scattering study of the staging kinetics in the c-face skin of pyrolytic graphite-H2SO4," *J. Mater. Res.*, vol. 1, no. 2, pp. 361–367, 1986.

[131] D. Roy Chowdhury, C. Singh, and A. Paul, "Role of graphite precursor and sodium nitrate in graphite oxide synthesis," *RSC Adv.*, vol. 4, no. 29, pp. 15138–15145, 2014.

[132] J. Chen, B. Yao, C. Li, and G. Shi, "An improved Hummers method for eco-friendly synthesis of graphene oxide," *Carbon N. Y.*, vol. 64, pp. 225–229, 2013.

[133] O. Glemser and H. Schröder, "Über Manganoxyde. II. Zur Kenntnis des Mangan(VII)-oxyds," *Zeitschrift für Anorg. und Allg. Chemie*, vol. 271, no. 5-6, pp. 293–304, Mar. 1953.

[134] S. Eigler and A. Hirsch, "Chemistry with Graphene and Graphene Oxide—Challenges for Synthetic Chemists," *Angew. Chemie Int. Ed.*, vol. 53, no. 30, pp. 7720–7738, Jul. 2014.

[135] T. Taniguchi *et al.*, “pH-driven, reversible epoxy ring opening/closing in graphene oxide,” *Carbon N. Y.*, vol. 84, pp. 560–566, 2015.

[136] M. Trömel and M. Russ, “Dimanganese Heptoxide for the Selective Oxidation of Organic Substrates,” *Angew. Chemie Int. Ed. English*, vol. 26, no. 10, pp. 1007–1009, Oct. 1987.

[137] J.-A. Yan, L. Xian, and M. Y. Chou, “Structural and Electronic Properties of Oxidized Graphene,” *Phys. Rev. Lett.*, vol. 103, no. 8, p. 86802, Aug. 2009.

[138] S. Zhou and A. Bongiorno, “Origin of the Chemical and Kinetic Stability of Graphene Oxide,” *Sci. Rep.*, vol. 3, no. 1, p. 2484, 2013.

[139] C. Li, X. Chen, L. Shen, and N. Bao, “Revisiting the Oxidation of Graphite: Reaction Mechanism, Chemical Stability, and Structure Self-Regulation,” *ACS Omega*, vol. 5, no. 7, pp. 3397–3404, Feb. 2020.

[140] Y. Gao and K. B. Sharpless, “Vicinal diol cyclic sulfates. Like epoxides only more reactive,” *J. Am. Chem. Soc.*, vol. 110, no. 22, pp. 7538–7539, Oct. 1988.

[141] O. V Yazyev and Y. P. Chen, “Polycrystalline graphene and other two-dimensional materials,” *Nat. Nanotechnol.*, vol. 9, no. 10, pp. 755–767, 2014.

[142] R. Muzyka, S. Drewniak, T. Pustelny, M. Chrubasik, and G. Gryglewicz, “Characterization of Graphite Oxide and Reduced Graphene Oxide Obtained from Different Graphite Precursors and Oxidized by Different Methods Using Raman Spectroscopy,” *Mater. (Basel, Switzerland)*, vol. 11, no. 7, p. 1050, Jun. 2018.

[143] J. Červenka, M. I. Katsnelson, and C. F. J. Flipse, “Room-temperature ferromagnetism in graphite driven by two-dimensional networks of point defects,” *Nat. Phys.*, vol. 5, no. 11, pp. 840–844, 2009.

[144] Y. C. G. Kwan, G. M. Ng, and C. H. A. Huan, “Identification of functional groups and determination of carboxyl formation temperature in graphene oxide using the XPS O 1s spectrum,” *Thin Solid Films*, vol. 590, pp. 40–48, 2015.

[145] S. Eigler, C. Dotzer, F. Hof, W. Bauer, and A. Hirsch, “Sulfur Species in Graphene Oxide,” *Chem. – A Eur. J.*, vol. 19, no. 29, pp. 9490–9496, Jul. 2013.

[146] A. G. Bannov, A. Manakhov, A. A. Shibaev, A. V Ukhina, J. Polčák, and E. A. Maksimovskii, “Synthesis dynamics of graphite oxide,” *Thermochim. Acta*, vol. 663, pp. 165–175, 2018.

[147] M. J. Yoo and H. B. Park, “Effect of hydrogen peroxide on properties of

graphene oxide in Hummers method," *Carbon N. Y.*, vol. 141, pp. 515–522, 2019.

[148] J. P. Rourke *et al.*, "The Real Graphene Oxide Revealed: Stripping the Oxidative Debris from the Graphene-like Sheets," *Angew. Chemie Int. Ed.*, vol. 50, no. 14, pp. 3173–3177, Mar. 2011.

[149] H. R. Thomas, C. Vallés, R. J. Young, I. A. Kinloch, N. R. Wilson, and J. P. Rourke, "Identifying the fluorescence of graphene oxide," *J. Mater. Chem. C*, vol. 1, no. 2, pp. 338–342, 2013.

[150] A. Bonanni, A. Ambrosi, C. K. Chua, and M. Pumera, "Oxidation Debris in Graphene Oxide Is Responsible for Its Inherent Electroactivity," *ACS Nano*, vol. 8, no. 5, pp. 4197–4204, May 2014.

[151] I. Rodriguez-Pastor, G. Ramos-Fernandez, H. Varela-Rizo, M. Terrones, and I. Martin-Gullon, "Towards the understanding of the graphene oxide structure: How to control the formation of humic- and fulvic-like oxidized debris," *Carbon N. Y.*, vol. 84, pp. 299–309, 2015.

[152] I. Martin-Gullon, J. M. Pérez, D. Domene, A. J. A. Salgado-Casanova, and L. R. Radovic, "New insights into oxygen surface coverage and the resulting two-component structure of graphene oxide," *Carbon N. Y.*, vol. 158, pp. 406–417, 2020.

[153] A. Piñeiro-García, F. Tristan, D. Meneses-Rodríguez, V. Semetey, and S. M. Vega-Díaz, "Tuning the nucleophilic attack and the reductive action of glycine on graphene oxide under basic medium," *Mater. Today Chem.*, vol. 19, p. 100386, 2021.

[154] S. H. Dave, C. Gong, A. W. Robertson, J. H. Warner, and J. C. Grossman, "Chemistry and Structure of Graphene Oxide via Direct Imaging," *ACS Nano*, vol. 10, no. 8, pp. 7515–7522, Aug. 2016.

[155] J. P. Rourke and N. R. Wilson, "Letter to the Editor: A defence of the two-component model of graphene oxide," *Carbon N. Y.*, vol. 96, pp. 339–341, 2016.

[156] A. S. Kuzenkova *et al.*, "New insights into the mechanism of graphene oxide and radionuclide interaction," *Carbon N. Y.*, vol. 158, pp. 291–302, 2020.

[157] M. Hada *et al.*, "Selective Reduction Mechanism of Graphene Oxide Driven by the Photon Mode versus the Thermal Mode," *ACS Nano*, vol. 13, no. 9, pp. 10103–10112, Sep. 2019.

[158] J. Zhang, C. Xiong, Y. Li, H. Tang, X. Meng, and W. Zhu, "The critical contribution of oxidation debris on the acidic properties of graphene oxide in an aqueous solution," *J. Hazard. Mater.*, vol. 402, p. 123552, 2021.

[159] Z. Clemente, V. L. S. S. Castro, L. S. Franqui, C. A. Silva, and D. S. T. Martinez, “Nanotoxicity of graphene oxide: Assessing the influence of oxidation debris in the presence of humic acid,” *Environ. Pollut.*, vol. 225, pp. 118–128, 2017.

[160] M. M. Gudarzi, “Colloidal Stability of Graphene Oxide: Aggregation in Two Dimensions,” *Langmuir*, vol. 32, no. 20, pp. 5058–5068, May 2016.

[161] R. L. D. Whitby *et al.*, “pH-driven physicochemical conformational changes of single-layer graphene oxide,” *Chem. Commun.*, vol. 47, no. 34, pp. 9645–9647, 2011.

[162] X. Wang, H. Bai, and G. Shi, “Size Fractionation of Graphene Oxide Sheets by pH-Assisted Selective Sedimentation,” *J. Am. Chem. Soc.*, vol. 133, no. 16, pp. 6338–6342, Apr. 2011.

[163] N. I. Kovtyukhova *et al.*, “Layer-by-Layer Assembly of Ultrathin Composite Films from Micron-Sized Graphite Oxide Sheets and Polycations,” *Chem. Mater.*, vol. 11, no. 3, pp. 771–778, Mar. 1999.

[164] F. J. Tölle, K. Gamp, and R. Mülhaupt, “Scale-up and purification of graphite oxide as intermediate for functionalized graphene,” *Carbon N. Y.*, vol. 75, pp. 432–442, 2014.

[165] H. A. Becerril, J. Mao, Z. Liu, R. M. Stoltenberg, Z. Bao, and Y. Chen, “Evaluation of Solution-Processed Reduced Graphene Oxide Films as Transparent Conductors,” *ACS Nano*, vol. 2, no. 3, pp. 463–470, Mar. 2008.

[166] P. Bhunia, M. Kumar, and S. De, “Fast purification of graphene oxide solution by continuous counter current hollow fibre dialysis: A step towards large scale production,” *Can. J. Chem. Eng.*, vol. 97, no. S1, pp. 1596–1604, Jun. 2019.

[167] J. Chen, X. Zhang, X. Zheng, C. Liu, X. Cui, and W. Zheng, “Size distribution-controlled preparation of graphene oxide nanosheets with different C/O ratios,” *Mater. Chem. Phys.*, vol. 139, no. 1, pp. 8–11, 2013.

[168] J. Chen, Y. Li, L. Huang, C. Li, and G. Shi, “High-yield preparation of graphene oxide from small graphite flakes via an improved Hummers method with a simple purification process,” *Carbon N. Y.*, vol. 81, pp. 826–834, 2015.

[169] G. Ceriotti, A. Y. Romanchuk, A. S. Slesarev, and S. N. Kalmykov, “Rapid method for the purification of graphene oxide,” *RSC Adv.*, vol. 5, no. 62, pp. 50365–50371, 2015.

[170] A. Kausar, I. Rafique, and B. Muhammad, “Aerospace Application of

Polymer Nanocomposite with Carbon Nanotube, Graphite, Graphene Oxide, and Nanoclay," *Polym. Plast. Technol. Eng.*, vol. 56, no. 13, pp. 1438–1456, Sep. 2017.

[171] I. Zambrano-Andazol *et al.*, "Reduced graphene oxide membranes in ocular regenerative medicine," *Mater. Sci. Eng. C*, vol. 114, p. 111075, 2020.

[172] S. P. Figerez, S. Patra, G. Rajalakshmi, and T. Narayanan, "Graphene Oxide based Rechargeable Respiratory Masks," *ChemRxiv*, 2020.

[173] "https://www.sigmaaldrich.com/chemistry/stockroom-reagents/learning-center/technical-library/particle-size-conversion.html (Consulted 14-01-21)." .

[174] L. Shen *et al.*, "Analysis of oxidation degree of graphite oxide and chemical structure of corresponding reduced graphite oxide by selecting different-sized original graphite," *RSC Adv.*, vol. 8, no. 31, pp. 17209–17217, 2018.

[175] C. Botas *et al.*, "The effect of the parent graphite on the structure of graphene oxide," *Carbon N. Y.*, vol. 50, no. 1, pp. 275–282, 2012.

[176] U. Hofmann and A. Frenzel, "Quellung von Graphit und die Bildung von Graphitsäure," *Berichte der Dtsch. Chem. Gesellschaft (A B Ser.*, vol. 63, no. 5, pp. 1248–1262, May 1930.

[177] L. Sun and B. Fugetsu, "Mass production of graphene oxide from expanded graphite," *Mater. Lett.*, vol. 109, pp. 207–210, 2013.

[178] Y.-R. Shin, S.-M. Jung, I.-Y. Jeon, and J.-B. Baek, "The oxidation mechanism of highly ordered pyrolytic graphite in a nitric acid/sulfuric acid mixture," *Carbon N. Y.*, vol. 52, pp. 493–498, 2013.

[179] S. Ding *et al.*, "Preparation and adsorption property of graphene oxide by using waste graphite from diamond synthesis industry," *Mater. Chem. Phys.*, vol. 221, pp. 47–57, 2019.

[180] E. H. Sujiono *et al.*, "Graphene oxide based coconut shell waste: synthesis by modified Hummers method and characterization," *Heliyon*, vol. 6, no. 8, p. e04568, 2020.

[181] M. Nováček *et al.*, "Tuning of graphene oxide composition by multiple oxidations for carbon dioxide storage and capture of toxic metals," *J. Mater. Chem. A*, vol. 5, no. 6, pp. 2739–2748, 2017.

[182] R. Ikram, B. M. Jan, and W. Ahmad, "An overview of industrial scalable production of graphene oxide and analytical approaches for synthesis and characterization," *J. Mater. Res. Technol.*, vol. 9, no. 5, pp. 11587–11610, 2020.

[183] J. Guerrero-Contreras and F. Caballero-Briones, “Graphene oxide powders with different oxidation degree, prepared by synthesis variations of the Hummers method,” *Mater. Chem. Phys.*, vol. 153, pp. 209–220, 2015.

[184] T. F. Emiru and D. W. Ayele, “Controlled synthesis, characterization and reduction of graphene oxide: A convenient method for large scale production,” *Egypt. J. Basic Appl. Sci.*, vol. 4, no. 1, pp. 74–79, 2017.

[185] C. Li, Y. Shi, X. Chen, D. He, L. Shen, and N. Bao, “Controlled synthesis of graphite oxide: Formation process, oxidation kinetics, and optimized conditions,” *Chem. Eng. Sci.*, vol. 176, pp. 319–328, 2018.

[186] F. Pendolino, N. Armata, T. Masullo, and A. Cuttitta, “Temperature influence on the synthesis of pristine graphene oxide and graphite oxide,” *Mater. Chem. Phys.*, vol. 164, pp. 71–77, 2015.

[187] R. Muzyka, M. Kwoka, Ł. Smędowski, N. Díez, and G. Gryglewicz, “Oxidation of graphite by different modified Hummers methods,” *New Carbon Mater.*, vol. 32, no. 1, pp. 15–20, 2017.

[188] M. F. R. Hanifah *et al.*, “Facile synthesis of highly favorable graphene oxide: Effect of oxidation degree on the structural, morphological, thermal and electrochemical properties,” *Materialia*, vol. 6, p. 100344, 2019.

[189] C. Hontoria-Lucas, A. J. López-Peinado, J. d. D. López-González, M. L. Rojas-Cervantes, and R. M. Martín-Aranda, “Study of oxygen-containing groups in a series of graphite oxides: Physical and chemical characterization,” *Carbon N. Y.*, vol. 33, no. 11, pp. 1585–1592, 1995.

[190] L. Zhang, J. Liang, Y. Huang, Y. Ma, Y. Wang, and Y. Chen, “Size-controlled synthesis of graphene oxide sheets on a large scale using chemical exfoliation,” *Carbon N. Y.*, vol. 47, no. 14, pp. 3365–3368, 2009.

[191] D.-W. Kang and H. S. Shin, “Control of size and physical properties of graphene oxide by changing the oxidation temperature,” *Carbon Lett.*, vol. 13, no. 1, pp. 39–43, Jan. 2012.

[192] K. Krishnamoorthy, M. Veerapandian, K. Yun, and S. J. Kim, “The chemical and structural analysis of graphene oxide with different degrees of oxidation,” *Carbon N. Y.*, vol. 53, pp. 38–49, 2013.

[193] A. Alkhouzaam, H. Qiblawey, M. Khraisheh, M. Atieh, and M. Al-Ghouti, “Synthesis of graphene oxides particle of high oxidation degree using a modified Hummers method,” *Ceram. Int.*, vol. 46, no. 15, pp. 23997–24007, 2020.

[194] P. Feicht *et al.*, “Systematic evaluation of different types of graphene

oxide in respect to variations in their in-plane modulus," *Carbon N. Y.*, vol. 114, pp. 700–705, 2017.

[195] N. Morimoto *et al.*, "Real-Time, in Situ Monitoring of the Oxidation of Graphite: Lessons Learned," *Chem. Mater.*, vol. 29, no. 5, pp. 2150–2156, Mar. 2017.

[196] M. Lojka, B. Lochman, O. Jankovský, A. Jiříčková, Z. Sofer, and D. Sedmidubský, "Synthesis, Composition, and Properties of Partially Oxidized Graphite Oxides," *Materials* , vol. 12, no. 15. 2019.

[197] J. Chen *et al.*, "Water-enhanced oxidation of graphite to graphene oxide with controlled species of oxygenated groups," *Chem. Sci.*, vol. 7, no. 3, pp. 1874–1881, 2016.

[198] X. Zhou and Z. Liu, "A scalable, solution-phase processing route to graphene oxide and graphene ultralarge sheets," *Chem. Commun.*, vol. 46, no. 15, pp. 2611–2613, 2010.

[199] X. H. Yau, F. W. Low, C. S. Khe, C. W. Lai, S. K. Tiong, and N. Amin, "An investigation of the stirring duration effect on synthesized graphene oxide for dye-sensitized solar cells," *PLoS One*, vol. 15, no. 2, p. e0228322, Feb. 2020.

[200] F. W. Low, C. W. Lai, and S. B. Abd Hamid, "Easy preparation of ultrathin reduced graphene oxide sheets at a high stirring speed," *Ceram. Int.*, vol. 41, no. 4, pp. 5798–5806, 2015.

[201] F. Kim, J. Luo, R. Cruz-Silva, L. J. Cote, K. Sohn, and J. Huang, "Self-Propagating Domino-like Reactions in Oxidized Graphite," *Adv. Funct. Mater.*, vol. 20, no. 17, pp. 2867–2873, Sep. 2010.

[202] S. Stankovich, R. D. Piner, X. Chen, N. Wu, S. T. Nguyen, and R. S. Ruoff, "Stable aqueous dispersions of graphitic nanoplatelets via the reduction of exfoliated graphite oxide in the presence of poly(sodium 4-styrenesulfonate)," *J. Mater. Chem.*, vol. 16, no. 2, pp. 155–158, 2006.

[203] J. I. Paredes, S. Villar-Rodil, A. Martínez-Alonso, and J. M. D. Tascón, "Graphene Oxide Dispersions in Organic Solvents," *Langmuir*, vol. 24, no. 19, pp. 10560–10564, Oct. 2008.

[204] G. Eda and M. Chhowalla, "Graphene-based Composite Thin Films for Electronics," *Nano Lett.*, vol. 9, no. 2, pp. 814–818, Feb. 2009.

[205] C. Botas *et al.*, "Optimization of the size and yield of graphene oxide sheets in the exfoliation step," *Carbon N. Y.*, vol. 63, pp. 576–578, 2013.

[206] J. Jia, C.-M. Kan, X. Lin, X. Shen, and J.-K. Kim, "Effects of processing

and material parameters on synthesis of monolayer ultralarge graphene oxide sheets," *Carbon N. Y.*, vol. 77, pp. 244–254, 2014.

[207] S. Ye and J. Feng, "The effect of sonication treatment of graphene oxide on the mechanical properties of the assembled films," *RSC Adv.*, vol. 6, no. 46, pp. 39681–39687, 2016.

[208] W. Gao, N. Zhao, W. Yao, Z. Xu, H. Bai, and C. Gao, "Effect of flake size on the mechanical properties of graphene aerogels prepared by freeze casting," *RSC Adv.*, vol. 7, no. 53, pp. 33600–33605, 2017.

[209] Z. Luo, Y. Lu, L. A. Somers, and A. T. C. Johnson, "High Yield Preparation of Macroscopic Graphene Oxide Membranes," *J. Am. Chem. Soc.*, vol. 131, no. 3, pp. 898–899, Jan. 2009.

[210] D. Pan, J. Zhang, Z. Li, and M. Wu, "Hydrothermal Route for Cutting Graphene Sheets into Blue-Luminescent Graphene Quantum Dots," *Adv. Mater.*, vol. 22, no. 6, pp. 734–738, Feb. 2010.

[211] Z. Li, W. Zhang, Y. Luo, J. Yang, and J. G. Hou, "How Graphene Is Cut upon Oxidation?," *J. Am. Chem. Soc.*, vol. 131, no. 18, pp. 6320–6321, May 2009.

[212] M. Lotya, P. J. King, U. Khan, S. De, and J. N. Coleman, "High-Concentration, Surfactant-Stabilized Graphene Dispersions," *ACS Nano*, vol. 4, no. 6, pp. 3155–3162, Jun. 2010.

[213] C. Xiang *et al.*, "Large Flake Graphene Oxide Fibers with Unconventional 100% Knot Efficiency and Highly Aligned Small Flake Graphene Oxide Fibers," *Adv. Mater.*, vol. 25, no. 33, pp. 4592–4597, Sep. 2013.

[214] C. Mellado, T. Figueroa, R. Baez, M. Meléndrez, and K. Fernández, "Effects of probe and bath ultrasonic treatments on graphene oxide structure," *Mater. Today Chem.*, vol. 13, pp. 1–7, 2019.

[215] "https://www2.chemistry.msu.edu/faculty/reusch/virttxtjml/acidity2.htm (Consulted 22/06/21)." .

[216] B. Konkena and S. Vasudevan, "Understanding Aqueous Dispersibility of Graphene Oxide and Reduced Graphene Oxide through pKa Measurements," *J. Phys. Chem. Lett.*, vol. 3, no. 7, pp. 867–872, Apr. 2012.

[217] M. D. Moreira and V. R. Coluci, "Initial stages of graphene oxide cracking in basic media," *Carbon N. Y.*, vol. 142, pp. 217–223, 2019.

[218] C. K. Chua and M. Pumera, "Light and Atmosphere Affect the Quasi-equilibrium States of Graphite Oxide and Graphene Oxide Powders," *Small*, vol. 11, no. 11, pp. 1266–1272, Mar. 2015.

[219] L. Guardia, S. Villar-Rodil, J. I. Paredes, R. Rozada, A. Martínez-Alonso, and J. M. D. Tascón, “UV light exposure of aqueous graphene oxide suspensions to promote their direct reduction, formation of graphene–metal nanoparticle hybrids and dye degradation,” *Carbon N. Y.*, vol. 50, no. 3, pp. 1014–1024, 2012.

[220] M. R. Karim, M. M. Rahman, and A. M. Asiri, “Termination of Structural Deformation and Proton–Electron Conductive Inflection of Graphene Oxide in Six Years,” *ACS Appl. Electron. Mater.*, vol. 2, no. 5, pp. 1304–1312, May 2020.

[221] S. Kim *et al.*, “Room-temperature metastability of multilayer graphene oxide films,” *Nat. Mater.*, vol. 11, no. 6, pp. 544–549, 2012.

[222] S. Choudhary, H. P. Mungse, and O. P. Khatri, “Hydrothermal Deoxygenation of Graphene Oxide: Chemical and Structural Evolution,” *Chem. – An Asian J.*, vol. 8, no. 9, pp. 2070–2078, Sep. 2013.

[223] V. Kohlschütter and P. Haenni, “Zur Kenntnis des Graphitischen Kohlenstoffs und der Graphitsäure,” *Zeitschrift für Anorg. und Allg. Chemie*, vol. 105, no. 1, pp. 121–144, Dec. 1919.

[224] A. R. Horrocks, B. K. Kandola, P. J. Davies, S. Zhang, and S. A. Padbury, “Developments in flame retardant textiles – a review,” *Polym. Degrad. Stab.*, vol. 88, no. 1, pp. 3–12, 2005.

[225] T. Ruiz-Calleja, M. Bonet-Aracil, J. Gisbert-Payá, and E. Bou-Belda, “Analysis of the influence of graphene and phase change microcapsules on thermal behavior of cellulosic fabrics,” *Mater. Today Commun.*, vol. 25, p. 101557, 2020.

[226] K. S. Chavali *et al.*, “Graphene-based intumescent flame retardant on cotton fabric,” *J. Mater. Sci.*, vol. 55, no. 29, pp. 14197–14210, 2020.

[227] J. Zhao *et al.*, “Graphene Oxide-Based Antibacterial Cotton Fabrics,” *Adv. Healthc. Mater.*, vol. 2, no. 9, pp. 1259–1266, Sep. 2013.

[228] Y. A. Samad, Y. Li, S. M. Alhassan, and K. Liao, “Non-destroyable graphene cladding on a range of textile and other fibers and fiber mats,” *RSC Adv.*, vol. 4, no. 33, pp. 16935–16938, 2014.

[229] X. Li *et al.*, “Multifunctional graphene woven fabrics,” *Sci. Rep.*, vol. 2, no. 1, p. 395, 2012.

[230] X. Xiang *et al.*, “In situ twisting for stabilizing and toughening conductive graphene yarns,” *Nanoscale*, vol. 9, no. 32, pp. 11523–11529, 2017.

[231] Y. J. Yun, W. G. Hong, W.-J. Kim, Y. Jun, and B. H. Kim, “A Novel

Method for Applying Reduced Graphene Oxide Directly to Electronic Textiles from Yarns to Fabrics," *Adv. Mater.*, vol. 25, no. 40, pp. 5701–5705, Oct. 2013.

[232] J. Molina *et al.*, "Plasma treatment of polyester fabrics to increase the adhesion of reduced graphene oxide," *Synth. Met.*, vol. 202, pp. 110–122, 2015.

[233] X. Hu, M. Tian, L. Qu, S. Zhu, and G. Han, "Multifunctional cotton fabrics with graphene/polyurethane coatings with far-infrared emission, electrical conductivity, and ultraviolet-blocking properties," *Carbon N. Y.*, vol. 95, pp. 625–633, 2015.

[234] Q. Jing, W. Liu, Y. Pan, V. V Silberschmidt, L. Li, and Z. Dong, "Chemical functionalization of graphene oxide for improving mechanical and thermal properties of polyurethane composites," *Mater. Des.*, vol. 85, pp. 808–814, 2015.

[235] T. K. Gupta *et al.*, "Superior nano-mechanical properties of reduced graphene oxide reinforced polyurethane composites," *RSC Adv.*, vol. 5, no. 22, pp. 16921–16930, 2015.

[236] H. Li *et al.*, "Rapid and Reliable Thickness Identification of Two-Dimensional Nanosheets Using Optical Microscopy," *ACS Nano*, vol. 7, no. 11, pp. 10344–10353, Nov. 2013.

[237] D. T. Grubb, "2.17 - Optical Microscopy," K. Matyjaszewski and M. B. T.-P. S. A. C. R. Möller, Eds. Amsterdam: Elsevier, 2012, pp. 465–478.

[238] M. W. Davidson and M. Abramowitz, "Optical Microscopy," *Encyclopedia of Imaging Science and Technology*. 15-Jan-2002.

[239] G. Delly, "The Michel-Lévy Interference Color Chart – Microscopy's Magical Color Key," *Hooke College of Applied Sciences*, 2012. [Online]. Available: https://www.mccrone.com/wp-content/uploads/2020/10/Using-the-Michel-Levy-Chart.pdf.

[240] X. Lin *et al.*, "Fabrication of Highly-Aligned, Conductive, and Strong Graphene Papers Using Ultralarge Graphene Oxide Sheets," *ACS Nano*, vol. 6, no. 12, pp. 10708–10719, Dec. 2012.

[241] F. Perrozzi, S. Prezioso, and L. Ottaviano, "Graphene oxide: from fundamentals to applications," *J. Phys. Condens. Matter*, vol. 27, no. 1, p. 13002, 2014.

[242] I. Jung, J.-S. Rhyee, J. Y. Son, R. S. Ruoff, and K.-Y. Rhee, "Colors of graphene and graphene-oxide multilayers on various substrates," *Nanotechnology*, vol. 23, no. 2, p. 25708, 2011.

[243] W. Ouyang, X. Z. Liu, Q. Li, Y. Zhang, J. Yang, and Q. S. Zheng, “Optical methods for determining thicknesses of few-layer graphene flakes,” *Nanotechnology*, vol. 24, no. 50, 2013.

[244] P. De Marco, M. Nardone, A. Del Vitto, M. Alessandri, S. Santucci, and L. Ottaviano, “Rapid identification of graphene flakes: alumina does it better,” *Nanotechnology*, vol. 21, no. 25, p. 255703, 2010.

[245] I. Jung, J. Y. Son, S.-J. Park, and K.-Y. Rhee, “Study on optical interference effect of graphene oxide films on SiO2 and Si3N4 dielectric films,” *Res. Chem. Intermed.*, vol. 40, no. 7, pp. 2477–2486, 2014.

[246] N. H. Nordin and Z. Ahmad, “Monitoring chemical changes on the surface of borosilicate glass covers during the silanisation process,” *J. Phys. Sci.*, vol. 26, no. 2, pp. 11–22, 2015.

[247] S. Mukherjee, A. Saha, P. K. Santra, S. Sengupta, and D. D. Sarma, “Beyond the ‘Coffee Ring’: Re-entrant Ordering in an Evaporation-Driven Self-Assembly in a Colloidal Suspension on a Substrate,” *J. Phys. Chem. B*, vol. 118, no. 9, pp. 2559–2567, Mar. 2014.

[248] K. Akhtar, S. A. Khan, S. B. Khan, and A. M. Asiri, “Scanning Electron Microscopy: Principle and Applications in Nanomaterials Characterization BT - Handbook of Materials Characterization,” S. K. Sharma, Ed. Cham: Springer International Publishing, 2018, pp. 113–145.

[249] V. E. Calado, G. F. Schneider, A. M. M. G. Theulings, C. Dekker, and L. M. K. Vandersypen, “Formation and control of wrinkles in graphene by the wedging transfer method,” *Appl. Phys. Lett.*, vol. 101, no. 10, p. 103116, Sep. 2012.

[250] www.Bruker-nano.com, “Principles of Electron Beam Microanalysis.”

[251] J. C. Russ, “Ultra - Low Energies,” *Fundam. Energy Dispersive X-ray Anal.*, pp. 174–180, 1984.

[252] M. Lojka and B. Lochman, “Oxidized Graphite Oxides,” 2019.

[253] A. T. Abdel-Motagaly, W. M. A. El Rouby, S. I. El-Dek, I. M. El-Sherbiny, and A. A. Farghali, “Fast technique for the purification of as-prepared graphene oxide suspension,” *Diam. Relat. Mater.*, vol. 86, pp. 20–28, 2018.

[254] S. You, S. M. Luzan, T. Szabó, and A. V Talyzin, “Effect of synthesis method on solvation and exfoliation of graphite oxide,” *Carbon N. Y.*, vol. 52, pp. 171–180, 2013.

[255] R. Al-Gaashani, A. Najjar, Y. Zakaria, S. Mansour, and M. A. Atieh,

"XPS and structural studies of high quality graphene oxide and reduced graphene oxide prepared by different chemical oxidation methods," *Ceram. Int.*, vol. 45, no. 11, pp. 14439–14448, 2019.

[256] "https://www.phi.com/surface-analysis-techniques/xps-esca.html (Consulted 24/11/20)." .

[257] "https://xpssimplified.com/whatisxps.php (Consulted 24/11/20)."

[258] D.-Q. Yang and E. Sacher, "s–p Hybridization in highly oriented pyrolytic graphite and its change on surface modification, as studied by X-ray photoelectron and Raman spectroscopies," *Surf. Sci.*, vol. 504, pp. 125–137, 2002.

[259] S. Eigler and A. M. Dimiev, "Characterization Techniques," *Graphene Oxide*. 30-Sep-2016.

[260] P. L. Chiu *et al.*, "Microwave- and Nitronium Ion-Enabled Rapid and Direct Production of Highly Conductive Low-Oxygen Graphene," *J. Am. Chem. Soc.*, vol. 134, no. 13, pp. 5850–5856, Apr. 2012.

[261] L. Stobinski *et al.*, "Graphene oxide and reduced graphene oxide studied by the XRD, TEM and electron spectroscopy methods," *J. Electron Spectros. Relat. Phenomena*, vol. 195, pp. 145–154, 2014.

[262] D. A. Skoog, J. Holler, and C. Stanley, *Principios de Análisis Instrumental*, 6ª Edición. McGraw-Hill, 2008.

[263] H.-P. Boehm and W. Scholz, "Der „Verpuffungspunkt" des Graphitoxids," *Zeitschrift für Anorg. und Allg. Chemie*, vol. 335, no. 1-2, pp. 74–79, Jan. 1965.

[264] S. Eigler, C. Dotzer, A. Hirsch, M. Enzelberger, and P. Müller, "Formation and Decomposition of CO2 Intercalated Graphene Oxide," *Chem. Mater.*, vol. 24, no. 7, pp. 1276–1282, Apr. 2012.

[265] "https://myscope.training/#/XRDlevel_2_1 (Consulted 17/10/20)." .

[266] P. Scherrer, "Bestimmung der Größe und der inneren Struktur von Kolloidteilchen mittels Röntgenstrahlen," *Nachrichten von der Gesellschaft der Wissenschaften zu Göttingen, Math. Klasse*, vol. 1918, no. 98, p. 100, 1918.

[267] J. I. Langford and A. J. C. Wilson, "Scherrer after sixty years: A survey and some new results in the determination of crystallite size," *J. Appl. Crystallogr.*, vol. 11, no. 2, pp. 102–113, Apr. 1978.

[268] N. Iwashita, C. R. Park, H. Fujimoto, M. Shiraishi, and M. Inagaki, "Specification for a standard procedure of X-ray diffraction measurements on carbon materials," *Carbon N. Y.*, vol. 42, no. 4, pp. 701–714, 2004.

[269] J. Biscoe and B. E. Warren, “An X-Ray Study of Carbon Black,” *J. Appl. Phys.*, vol. 13, no. 6, pp. 364–371, Jun. 1942.

[270] C. Botas *et al.*, “Critical temperatures in the synthesis of graphene-like materials by thermal exfoliation-reduction of graphite oxide,” *Carbon N. Y.*, vol. 52, pp. 476–485, 2013.

[271] T. N. Blanton and D. Majumdar, “Characterization of X-ray irradiated graphene oxide coatings using X-ray diffraction, X-ray photoelectron spectroscopy, and atomic force microscopy,” *Powder Diffr.*, vol. 28, no. 2, pp. 68–71, 2013.

[272] B. Gurzęda, T. Buchwald, M. Nocuń, A. Bąkowicz, and P. Krawczyk, “Graphene material preparation through thermal treatment of graphite oxide electrochemically synthesized in aqueous sulfuric acid,” *RSC Adv.*, vol. 7, no. 32, pp. 19904–19911, 2017.

[273] R. Liu, T. Gong, K. Zhang, and C. Lee, “Graphene oxide papers with high water adsorption capacity for air dehumidification,” *Sci. Rep.*, vol. 7, no. 1, p. 9761, 2017.

[274] A. V Talyzin, B. Sundqvist, T. Szabó, I. Dékány, and V. Dmitriev, “Pressure-Induced Insertion of Liquid Alcohols into Graphite Oxide Structure,” *J. Am. Chem. Soc.*, vol. 131, no. 51, pp. 18445–18449, Dec. 2009.

[275] M. Thalji, G. Ali, S. P. Lee, and K. F. Chong, “Solvothermal Synthesis of Reduced Graphene Oxide as Electrode Material for Supercapacitor Application,” vol. 4, pp. 17–26, Dec. 2019.

[276] F. Cruz-Gandarilla, J. Cabanas-Moreno, and M. Ortega, *Aplicaciones de la Difracción de Rayos X a Materiales Policristalinos.* 2005.

[277] C. N. Banwell, E. M. McCash, and E. M. McCash, *Fundamentals of molecular spectroscopy*, 4th ed. London: McGraw-Hill Book Company, 1994.

[278] F. Tuinstra and J. L. Koenig, “Raman Spectrum of Graphite,” *J. Chem. Phys.*, vol. 53, no. 3, pp. 1126–1130, Aug. 1970.

[279] D. Graf *et al.*, “Spatially Resolved Raman Spectroscopy of Single- and Few-Layer Graphene,” *Nano Lett.*, vol. 7, no. 2, pp. 238–242, Feb. 2007.

[280] A. C. Ferrari and D. M. Basko, “Raman spectroscopy as a versatile tool for studying the properties of graphene,” *Nat. Nanotechnol.*, vol. 8, no. 4, pp. 235–246, 2013.

[281] C. A. Amarnath, C. E. Hong, N. H. Kim, B.-C. Ku, T. Kuila, and J. H. Lee, “Efficient synthesis of graphene sheets using pyrrole as a

reducing agent," *Carbon N. Y.*, vol. 49, no. 11, pp. 3497–3502, 2011.

[282] M. M. Lucchese *et al.*, "Quantifying ion-induced defects and Raman relaxation length in graphene," *Carbon N. Y.*, vol. 48, no. 5, pp. 1592–1597, 2010.

[283] M. Ruidíaz-Martínez, M. A. Álvarez, M. V López-Ramón, G. Cruz-Quesada, J. Rivera-Utrilla, and M. Sánchez-Polo, "Hydrothermal Synthesis of rGO-TiO2 Composites as High-Performance UV Photocatalysts for Ethylparaben Degradation," *Catalysts* , vol. 10, no. 5. 2020.

[284] S. Eigler, F. Hof, M. Enzelberger-Heim, S. Grimm, P. Müller, and A. Hirsch, "Statistical Raman Microscopy and Atomic Force Microscopy on Heterogeneous Graphene Obtained after Reduction of Graphene Oxide," *J. Phys. Chem. C*, vol. 118, no. 14, pp. 7698–7704, Apr. 2014.

[285] D. W. Lee and J. W. Seo, "sp2/sp3 Carbon Ratio in Graphite Oxide with Different Preparation Times," *J. Phys. Chem. C*, vol. 115, no. 6, pp. 2705–2708, Feb. 2011.

[286] J. Nuncira, L. M. Seara, R. D. Sinisterra, V. Caliman, and G. G. Silva, "Long-term colloidal stability of graphene oxide aqueous nanofluids," *Fullerenes, Nanotub. Carbon Nanostructures*, vol. 28, no. 5, pp. 407–417, May 2020.

[287] F. Pendolino, E. Parisini, and S. Lo Russo, "Time-Dependent Structure and Solubilization Kinetics of Graphene Oxide in Methanol and Water Dispersions," *J. Phys. Chem. C*, vol. 118, no. 48, pp. 28162–28169, Dec. 2014.

[288] J. Russier *et al.*, "Evidencing the mask effect of graphene oxide: a comparative study on primary human and murine phagocytic cells," *Nanoscale*, vol. 5, no. 22, pp. 11234–11247, 2013.

[289] K. Kouroupis-Agalou *et al.*, "Fragmentation and exfoliation of 2-dimensional materials: a statistical approach," *Nanoscale*, vol. 6, no. 11, pp. 5926–5933, 2014.

[290] C. Botas *et al.*, "Critical temperatures in the synthesis of graphene-like materials by thermal exfoliation–reduction of graphite oxide," *Carbon N. Y.*, vol. 52, pp. 476–485, 2013.

[291] X. Chen *et al.*, "Rapid thermal decomposition of confined graphene oxide films in air," *Carbon N. Y.*, vol. 101, pp. 71–76, 2016.

[292] Y. Qiu, F. Guo, R. Hurt, and I. Külaots, "Explosive thermal reduction of graphene oxide-based materials: Mechanism and safety implications," *Carbon N. Y.*, vol. 72, pp. 215–223, 2014.

[293] Y. Lin, Z.-H. Huang, X. Yu, W. Shen, Y. Zheng, and F. Kang, “Mildly expanded graphite for anode materials of lithium ion battery synthesized with perchloric acid,” *Electrochim. Acta*, vol. 116, pp. 170–174, 2014.

[294] M. Salvatore, G. Carotenuto, S. De Nicola, C. Camerlingo, V. Ambrogi, and C. Carfagna, “Synthesis and Characterization of Highly Intercalated Graphite Bisulfate,” *Nanoscale Res. Lett.*, vol. 12, no. 1, p. 167, 2017.

[295] J. Y. Howe, C. J. Rawn, L. E. Jones, and H. Ow, “Improved crystallographic data for graphite,” *Powder Diffr.*, vol. 18, no. 2, pp. 150–154, 2003.

[296] S. Park, J. An, J. R. Potts, A. Velamakanni, S. Murali, and R. S. Ruoff, “Hydrazine-reduction of graphite- and graphene oxide,” *Carbon N. Y.*, vol. 49, no. 9, pp. 3019–3023, 2011.

[297] M. M. Storm, R. E. Johnsen, and P. Norby, “In situ X-ray powder diffraction studies of the synthesis of graphene oxide and formation of reduced graphene oxide,” *J. Solid State Chem.*, vol. 240, pp. 49–54, 2016.

[298] S. Eigler, C. Dotzer, and A. Hirsch, “Visualization of defect densities in reduced graphene oxide,” *Carbon N. Y.*, vol. 50, no. 10, pp. 3666–3673, 2012.

[299] J. C. Russ, “Chapter 14 - Ultra - Low Energies,” in *Butterworths Monographs in Materials*, J. C. B. T.-F. of E. D. X. A. Russ, Ed. Butterworth-Heinemann, 1984, pp. 174–180.

[300] X. Li, S. Biswas, and L. T. Drzal, “High Temperature Vacuum Annealing and Hydrogenation Modification of Exfoliated Graphite Nanoplatelets,” *J. Eng.*, vol. 2013, p. 638576, 2013.

[301] E. Burresi *et al.*, “Influence of the synthesis conditions on the microstructural, compositional and morphological properties of graphene oxide sheets,” *Ceram. Int.*, vol. 46, no. 14, pp. 22067–22078, 2020.

[302] Z. Sofer *et al.*, “Insight into the Mechanism of the Thermal Reduction of Graphite Oxide: Deuterium-Labeled Graphite Oxide Is the Key,” *ACS Nano*, vol. 9, no. 5, pp. 5478–5485, May 2015.

[303] J. R. J. R. C.D. Wagner, A.V. Naumkin, A. Kraut-Vass, J.W. Allison, C.J. Powell, “NIST Standard Reference Database 20, Version 3.4 (web version) (http:/srdata.nist.gov/xps/) (consulted 28-11-20).” .

[304] S. Yumitori, “Correlation of C1s chemical state intensities with the O1s intensity in the XPS analysis of anodically oxidized glass-like carbon

samples," *J. Mater. Sci.*, vol. 35, no. 1, pp. 139–146, 2000.

[305] D. Briggs, *XPS: Basic Principles, Spectral Features and Qualitative Analysis, in: Surface Analysis by Auger and X-ray Photoelectron Spectroscopy.* Chichester: IM Publications, 2003.

[306] S. Rella *et al.*, "X-ray photoelectron spectroscopy of reduced graphene oxide prepared by a novel green method," *Vacuum*, vol. 119, pp. 159–162, 2015.

[307] C. K. Chua and M. Pumera, "Chemical reduction of graphene oxide : a synthetic chemistry viewpoint," *Chem Soc Rev*, pp. 291–312, 2014.

[308] A. V Talyzin *et al.*, "Brodie vs Hummers graphite oxides for preparation of multi-layered materials," *Carbon N. Y.*, vol. 115, pp. 430–440, 2017.

[309] S. Pan and I. A. Aksay, "Factors Controlling the Size of Graphene Oxide Sheets Produced via the Graphite Oxide Route," *ACS Nano*, vol. 5, no. 5, pp. 4073–4083, May 2011.

[310] K. P. Loh, Q. Bao, G. Eda, and M. Chhowalla, "Graphene oxide as a chemically tunable platform for optical applications," *Nat. Chem.*, vol. 2, no. 12, pp. 1015–1024, 2010.

[311] A. M. Dimiev *et al.*, "Direct Real-Time Monitoring of Stage Transitions in Graphite Intercalation Compounds," *ACS Nano*, vol. 7, no. 3, pp. 2773–2780, Mar. 2013.

[312] X. Li *et al.*, "Electrochemically active MnO2/RGO nanocomposites using Mn powder as the reducing agent of GO and the MnO2 precursor," *Electrochim. Acta*, vol. 130, pp. 305–313, 2014.

[313] Q. Lin, G. Gu, H. Wang, R. Zhu, Y. Liu, and J. Fu, "Preparation of manganese sulfate from low-grade manganese carbonate ores by sulfuric acid leaching," *Int. J. Miner. Metall. Mater.*, vol. 23, no. 5, pp. 491–500, 2016.

[314] J. Park, Y. S. Cho, S. J. Sung, M. Byeon, S. J. Yang, and C. R. Park, "Characteristics tuning of graphene-oxide-based-graphene to various end-uses," *Energy Storage Mater.*, vol. 14, pp. 8–21, 2018.

[315] X. Fan *et al.*, "Deoxygenation of Exfoliated Graphite Oxide under Alkaline Conditions: A Green Route to Graphene Preparation," *Adv. Mater.*, vol. 20, no. 23, pp. 4490–4493, Dec. 2008.

[316] S. Tardio and P. J. Cumpson, "Practical estimation of XPS binding energies using widely available quantum chemistry software," *Surf. Interface Anal.*, vol. 50, no. 1, pp. 5–12, 2018.

[317] G. T. T. Le, N. Chanlek, J. Manyam, P. Opaprakasit, N. Grisdanurak, and P. Sreearunothai, "Insight into the ultrasonication of graphene

oxide with strong changes in its properties and performance for adsorption applications," *Chem. Eng. J.*, vol. 373, pp. 1212–1222, 2019.

[318] H. WU *et al.*, "pH-dependent size, surface chemistry and electrochemical properties of graphene oxide," *New Carbon Mater.*, vol. 28, no. 5, pp. 327–335, 2013.

[319] P. Pérez-Martínez, J. M. Galvan-Miyoshi, and J. Ortiz-López, "Ultrasonic cavitation effects on the structure of graphene oxide in aqueous suspension," *J. Mater. Sci.*, vol. 51, no. 24, pp. 10782–10792, 2016.

[320] D. López-Díaz, M. López Holgado, J. L. García-Fierro, and M. M. Velázquez, "Evolution of the Raman Spectrum with the Chemical Composition of Graphene Oxide," *J. Phys. Chem. C*, vol. 121, no. 37, pp. 20489–20497, Sep. 2017.

[321] P. Vecera *et al.*, "Degree of functionalisation dependence of individual Raman intensities in covalent graphene derivatives," *Sci. Rep.*, vol. 7, no. 1, p. 45165, 2017.

[322] F. Grote, C. Gruber, F. Börrnert, U. Kaiser, and S. Eigler, "Thermal Disproportionation of Oxo-Functionalized Graphene," *Angew. Chemie Int. Ed.*, vol. 56, no. 31, pp. 9222–9225, Jul. 2017.

[323] M. Sahoo, R. P. Antony, T. Mathews, S. Dash, and A. K. Tyagi, "Raman studies of chemically and thermally reduced graphene oxide," *AIP Conf. Proc.*, vol. 1512, no. 1, pp. 1262–1263, Feb. 2013.

[324] K. N. Kudin, B. Ozbas, H. C. Schniepp, R. K. Prud'homme, I. A. Aksay, and R. Car, "Raman Spectra of Graphite Oxide and Functionalized Graphene Sheets," *Nano Lett.*, vol. 8, no. 1, pp. 36–41, Jan. 2008.

[325] D. Phillips, J. Foster, D. Ph, and T. F. Scientific, "Trace Metal Analysis of Water Produced From a Thermo Scientific Barnstead GenPure UV / UF-TOC Water Purification System," pp. 20–22, 2014.

[326] S. Park, K.-S. Lee, G. Bozoklu, W. Cai, S. T. Nguyen, and R. S. Ruoff, "Graphene Oxide Papers Modified by Divalent Ions—Enhancing Mechanical Properties via Chemical Cross-Linking," *ACS Nano*, vol. 2, no. 3, pp. 572–578, Mar. 2008.

[327] C.-N. Yeh, K. Raidongia, J. Shao, Q.-H. Yang, and J. Huang, "On the origin of the stability of graphene oxide membranes in water," *Nat. Chem.*, vol. 7, no. 2, pp. 166–170, 2015.

[328] N. H. Othman, W. Z. N. Yahya, M. Che Ismail, M. Mustapha, and Z. K. Koi, "Highly dispersed graphene oxide–zinc oxide nanohybrids in epoxy coating with improved water barrier properties and corrosion

resistance," *J. Coatings Technol. Res.*, vol. 17, no. 1, pp. 101–114, 2020.

[329] R. Cruz-Silva, M. Endo, and M. Terrones, "Graphene oxide films, fibers, and membranes," *Nanotechnol. Rev.*, vol. 5, no. 4, pp. 377–391.

[330] H. Bai *et al.*, "Insight into the Mechanism of Graphene Oxide Degradation via the Photo-Fenton Reaction," *J. Phys. Chem. C*, vol. 118, no. 19, pp. 10519–10529, May 2014.

[331] C. K. Chua and M. Pumera, "The reduction of graphene oxide with hydrazine: elucidating its reductive capability based on a reaction-model approach," *Chem. Commun.*, vol. 52, no. 1, pp. 72–75, 2016.

[332] E. Aliyev, V. Filiz, M. M. Khan, Y. J. Lee, C. Abetz, and V. Abetz, "Structural Characterization of Graphene Oxide: Surface Functional Groups and Fractionated Oxidative Debris," *Nanomaterials* , vol. 9, no. 8. 2019.

[333] X. Li, Z. Yang, and J. Xu, "Comprehensive Theoretical Investigation on the Regioselectivity in the Nucleophilic Ring Opening of Epoxides," *Current Organic Synthesis*, vol. 10, no. 1. pp. 169–177, 2013.

[334] J. Cui, J. Xu, J. Li, H. Qiu, S. Zheng, and J. Yang, "A crosslinkable graphene oxide in waterborne polyurethane anticorrosive coatings: Experiments and simulation," *Compos. Part B Eng.*, vol. 188, p. 107889, 2020.

[335] Instituto Nacional de Seguridad e Higiene en el Trabajo, "Guantes de protección contra riesgos mecánicos," *Ntp 882*, vol. 3, no. Junio, p. 4, 2010.

[336] N. a Ibraheem, M. M. Hasan, R. Z. Khan, and P. K. Mishra, "Understanding Color Models : A Review," *ARPN J. Sci. Technol.*, vol. 2, no. 3, pp. 265–275, 2012.

[337] "http://colorizer.org/ (Consulted 08-01-2021)." .

[338] H. Ren and Q. Zhong, "A new image segmentation method based on HSI color space for biped soccer robot," in *2008 IEEE International Symposium on IT in Medicine and Education*, 2008, pp. 1058–1061.

APPENDIX

8.1. COLORS OF GO FLAKES UNDER REFLECTION OPTICAL MICROSCOPY, A COLORIMETRIC STUDY FOR THICKNESS EVALUATION

Few-layer graphite oxide (GO), with thicknesses around 10 nm, can be “seen” under optical microscopy, by observing small changes in the opacity of the flakes in contrast with the substrate. In our case, as we avoided aggressive post-treatments, the GO flakes obtained directly from the synthesis procedures performed were relatively thick GO particles. Interference phenomena of light, as explained in section 3.1.1.1, enabled us to observe a higher abundance of interference colors in our distributions of flakes. In Figure 74, an example of the colors displayed for a distribution of GO flakes can be observed in a white-light optical reflection microscopy micrograph.

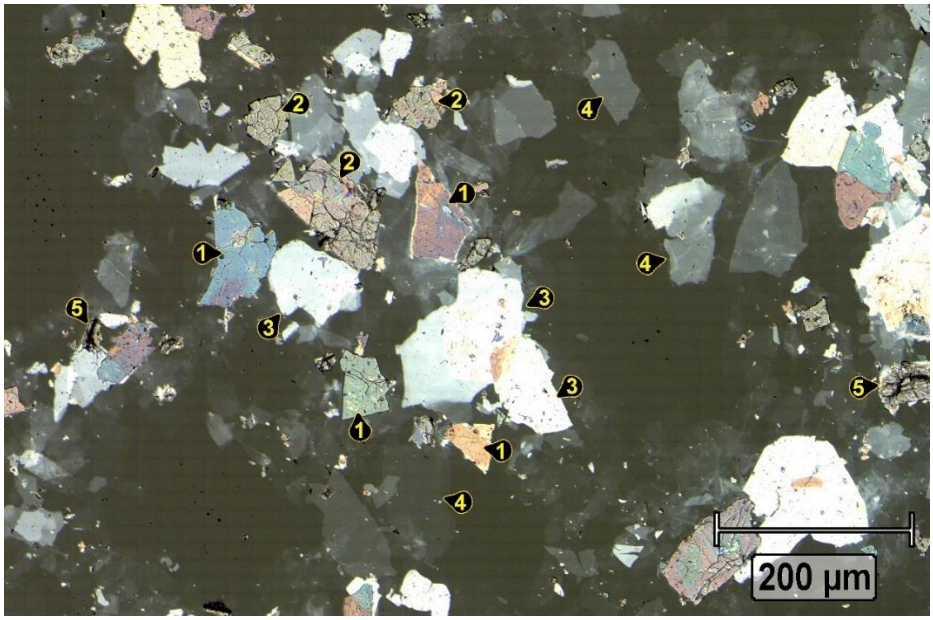

Figure 73: White-light optical reflection microscopy micrograph of different-thick GO flakes deposited on a glass slide. Depending on the thickness of each flake , different colors can be seen due to interference of light.

In the picture, several kinds of GO flakes can be observed, some of them displaying interference colors. In the center of the image, red, blue, green, and orange flakes can be found, some of which are labeled as **(1)**. These flakes will have different thicknesses, in a range between 80 and 300 nm, where the colors are related to a specific thickness. Also, some brownish particles, with a cracked appearance, can be seen, some of which are labeled as **(2)**. These particles are usually bigger than 300 nm. Bright flakes also appear in the image, some of which are labeled as **(3)**. These flakes have a thickness lower than 80 nm, and, as their thickness decreases, they tend to show less brightness, displaying the same color as that of the substrate, until reaching the appearance of a grey shape, some of which being labeled as **(4)**. These nearly observable flakes have thicknesses around 10 nm. Finally, some particles with no flat appearance can also be noticed, some of which being labeled as **(5)**. These particles are non-exfoliated graphitic remains, which are easy to detect

when observing the sample as they show out-of-focus portions, indicating a 3D structure along the z-axis.

8.1.1. Thickness of GO, a study towards the facile determination via interference colors of light

Before facing the morphological evaluation of the GO dispersions characterized in this Chapter 4, we introduced a previous study performed to create a tool in form of a color chart that helps relate the thickness of the flakes with the observable color under reflection optical microscopy. With this tool, we could estimate thicknesses of the flakes by only observing the colors of the flakes.

The experiment consisted in the preparation of a well dispersed distribution of GO flakes on a glass slide. White-light optical micrographs of individual flakes were captured. Then, the same distribution was put under a laser confocal microscope and the 3D topographies of the same flakes were obtained. An example of a pair of micrograph/topography pictures of a single GO flake can be observed in Figure 74. In Figure 74a the white light optical micrograph of the flake is depicted. In this case, it can be observed that it is a multilayered flake, with three recognizable heights by three different colors (yellow, red and blue). In Figure 74b the topography obtained by laser confocal microscopy is depicted. This test proves that the three colors stood for three different thicknesses, where yellow corresponded to ~100 nm, red to ~150 nm and blue to ~200 nm.

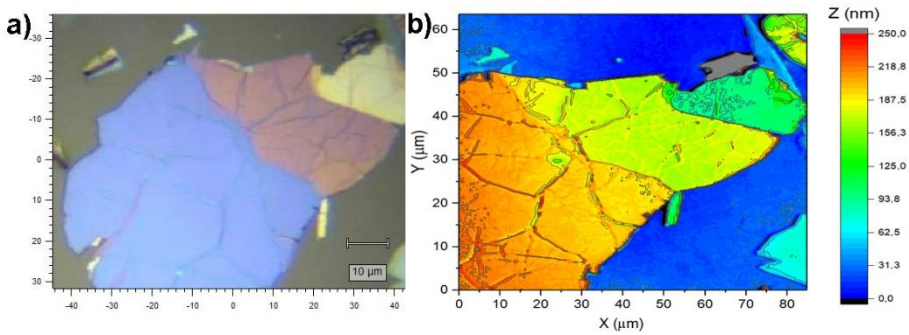

Figure 74: a) White light optical reflection microscopy image of a multilayered GO flake displaying blue, red and yellow colors. b) Confocal 3D topography map of the same flake, where the three apparent colors have been translated to three different thicknesses.

This test was repeated for approximately 100 different flakes. For each of them and from the optical micrograph, 10 different points were selected obtaining their RGB colors. RGB stands for Red-Blue-Green. It is an additive color model to determine a digital color using the combination of the intensities of these three primarily colors [336]. The RGB color model generally is the model used by image-capturing devices. However, the values of R, G and B will not change in a coherent trend with the interference phenomena, as they have no actual connection to wavelength of visible light. Fortunately, RGB colors can be transformed into other color models, being the most appropriate for us here the HSL model [337]. HSL stands for Hue, Saturation and Lightness and fits better with the perception of human eyes [338]. In fact, the value of Hue, expressed as an angle with values between 0 and 360º, follow the same linearity as the visible spectrum through wavelength values. For this reason, the Hue value will be used as a representative of the color of each flake. Schemes of the RGB and HSL models are presented in Figure 77.

Then, once the colors were obtained from a specific zone of the flake, the same points in x and y axis were used from the topography of the flake to find the correlated thickness, obtaining the color-thickness relation of approximately 1000 points. Then, with the Hue angle values and the thicknesses, a polar plot was constructed, which is depicted in Figure 75.

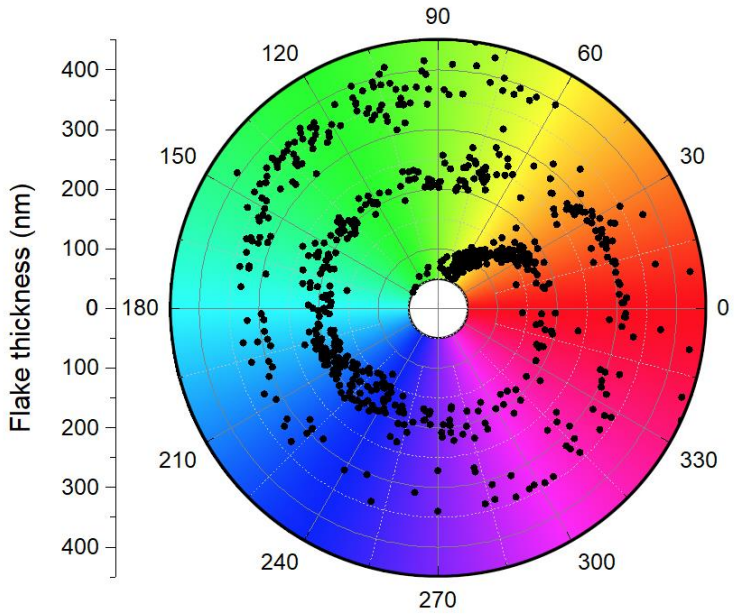

Figure 75: Flake thickness-Hue color angle relation for the measured samples. Flake thickness ranges from 50 to 400 nm. A clear tendency can be observed, matching to the theoretical calculations of the colors from thin film optics theory.

In the plot, a clear tendency can be noticed, where the color angle changes as a function of the increasing thickness, clustering the measured points in a spiral. Due to the nature of polar plots, a spiral tendency reveals an actual monotonic relation between color and thickness of the flakes. It can be proved that the

relation of color with thickness in our data matches with the calculated values from [242].

Our experimental plot ranges from 50 to 400 nm. For less than 50 nm, the flakes appear with the same blue color as coming from the glass substrate, as shown in Figure 73, with only a change in opacity. For more than 400 nm, the flakes appeared to have the same brownish color displayed by the GO dispersions, indicating that no more interference colors can be seen.

8.2. SELECTION OF THE CONDITIONS FOR THE XRD MEASUREMENTS TO AVOID MOISTURE ABSORPTION EFFECTS

A XRD experiment was performed to observe the effect of ambient humidity changes in the position of the peaks. The procedure we followed for this experiment consisted in the XRD measurements of GO samples in sequence over a period of 24 h. For a better comparison of the results, two samples were selected to perform the experiment. The samples were the post-treated GOs of sample set 1 prepared with reaction times of 30 and 540 min, namely ptGO-30 min and ptGO-540 min. These were selected as we suspected that they could absorb water to a different degree because their preparation procedures differed greatly.

The samples were analyzed 5 times over a period of 24 h after drying at 50 ºC and storage in a desiccant box until the measurement time. When extracted from the desiccant box, the samples were put in the diffractometer queue while allowing moisture absorption from the ambient during the next 24 h and the subsequent XRD measurements. Humidity at the start of the experiment, was 62%. After 12 h it was 49%. And after 24 h, it was 61%, very close to the starting value.

The measurement of the two samples in sequence over a period of 24 h was performed in the following form:

ptGO-30 min (t=0 h), ptGO-540 min (t=0 h), ptGO-30 min (t=5 h), ptGO-540 min (t=5 h), ptGO-30 min (t=12h), … etc.

Each measurement lasted 2h, so between the first sample ptGO-30 min (t=n) and ptGO-30 min (t=n) there was a 2 h time shift. The results are shown in Figure 76.

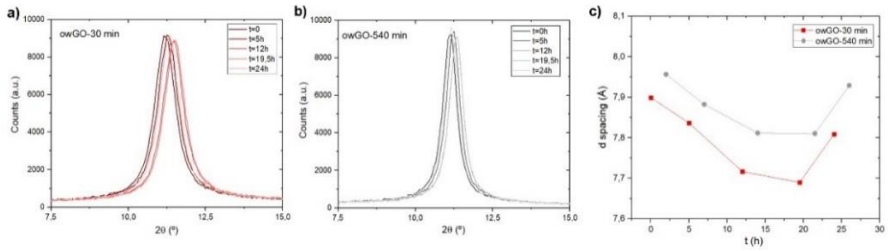

Figure 76: Consecutive XRD measurements of the same prepared GO samples along different times: 0, 5, 12, 19,5 and 24 h. a) Over-washed GO sample prepared with 30 min of reaction. b) Over-washed GO sample prepared with 540 min of reaction. c) Plot of the interlayer distance "d" of the two samples as a function of the time of measurement.

In Figure 76a and Figure 76b the diffractograms of these two samples are depicted, where shifts of the peak position along 2θ can be noticed in both cases for the different measurements. In Figure 76c the variation of interlayer distance "d", obtained from Bragg's law and the angles of the center of the peaks, is plotted as a function of time of the measurement. Both samples vary in the same form as a function of time. The 2 h shift between the two samples is also noticeable. Interestingly, the interlayer distance of each sample varies reversibly which could indicate that the peak position evolves in the same form that humidity does, as the humidity decreased during the first half of the experiment and increased in the second half. Interlayer distance expands with presumed more water absorption at higher humidity and contracts when the excess of water is released when the moisture decreases. Although the two samples reproduced the same overall tendency, there still exists a shift in d spacing between them, which must be attributed exclusively to their chemical characteristics and maybe also to their capacity to retain water. However, the variation of d spacing along time is greater than the d spacing shift between the two samples. This means that the effect of humidity on the interlayer distance value is much more important than the intrinsic interlayer distance of each sample. Therefore, while duing XRD experiments with our GOs, RH must be controlled being necessary to perform the measurements under specific

conditions to avoid seeing differences due to changes in moisture absorption at different times.

Thus, we performed the following XRD measurements grouping the samples set by set, and the comparative measurements were performed only from the range of 2θ were the (001) peak is situated, between 7.5º and 15.0º. Each measurement lasted only 15 min and after completing the XRD spectra collection from all the samples, the measurements were repeated two more times, so we could present the average of the interlayer distance.

8.3. GO synthesis procedure and results

		Reaction parameters						Quenching				Final GO obtained			
Sample	Date	Starting temperature (ºC)	Time addition KMnO4 (min)	Reaction time (min)	Reaction temp (ºC)	Temp. H2SO4 10% (ºC)	Addition H2SO4 10% (min)	T. max (ºC)	Temp. H2O (ºC)	Addition H2O (min)	T. max (ºC)	Volume (mL)	Conc. (mg/mL)	pH	Total GO (g)
GO1	03/12/2019	20	15	30	24	5	42	29	15	8	22	356,2	24,15	4	8,60
GO2	10/12/2019	21	10	300	22	4	60	28	15	7	26	310,9	26,82	2	8,34
GO3	11/12/2019	21	11	62	24	4	50	31	12	6	23	417,7	21,28	3	8,89
GO4	17/12/2019	22	12	121	27	5	61	33	10	4	27	361,8	26,06	3	9,43
GO5	08/01/2020	17	2	540	23	5	34	29	10	4	27	351,0	23,45	2	8,23
GO6	10/02/2020	21	10	120	79	10	20	86	20	5	42	361,1	22,60	2	8,16
GO7	19/02/2020	3	47	120	3	1	123	10	0	5	8	338,9	30,75	6	10,42
GO8	03/03/2020	26	3	120	52	7	10	55	25	5	50	322,6	27,07	2	8,73

Appendix 1: Summary of the information about the reaction procedures of each GO.

8.4. *Supplementary images*

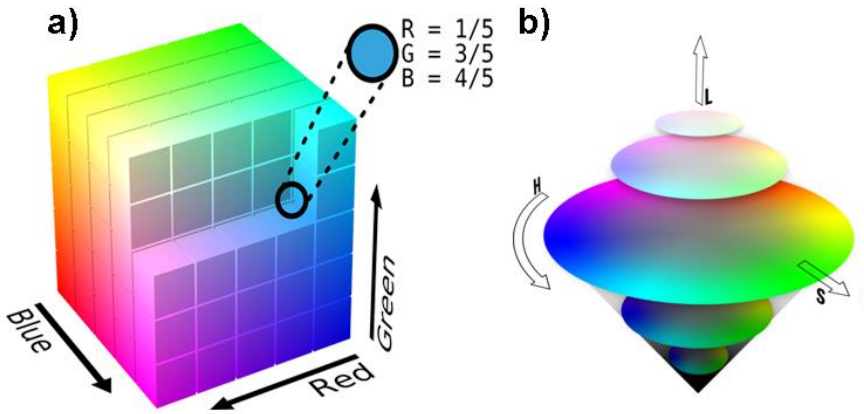

Figure 77: Visual representations of the a) RGB and b) HSL color models. All digital colors can be obtained by the combination of the parameters Red, Blue and Green in the case of RGB and Hue, Saturation and Lightness in the case of HSL. Images from Wikipedia.org (a) and Colorizer.org (b).

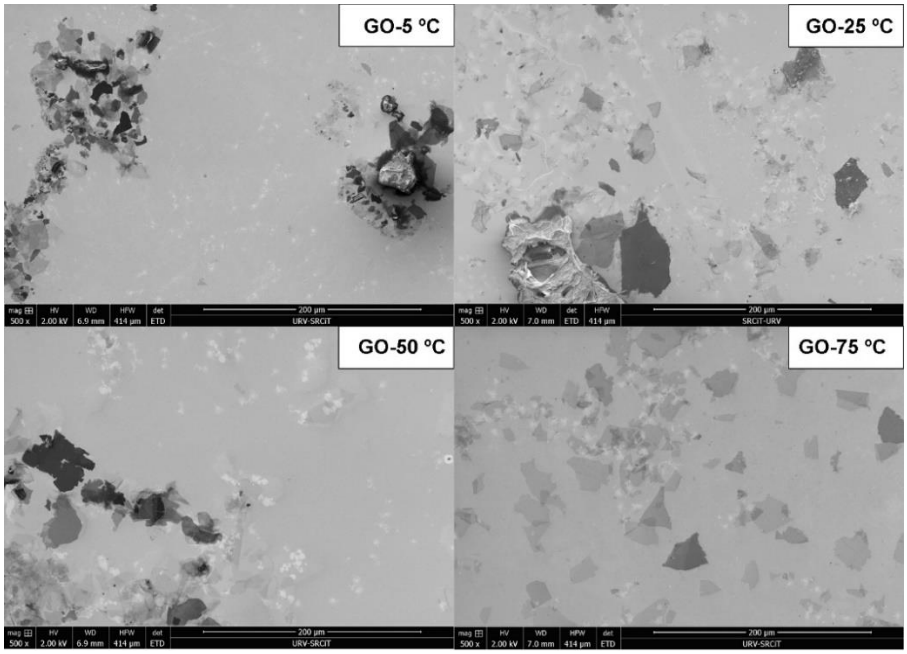

Figure 78: SEM images of the samples from sample set 2 prepared with different reaction temperature.

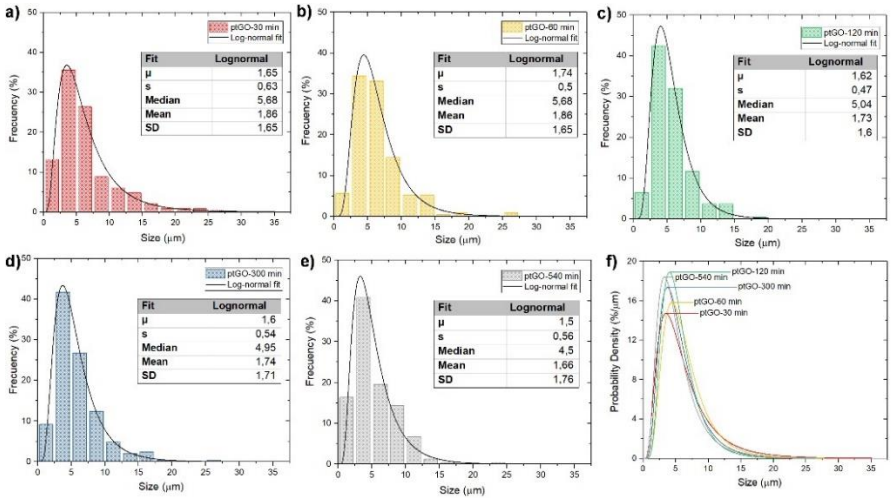

Figure 79: Size histograms of the GO flakes belonging to the post-treated samples from sample set 1, originally prepared with different reaction times.

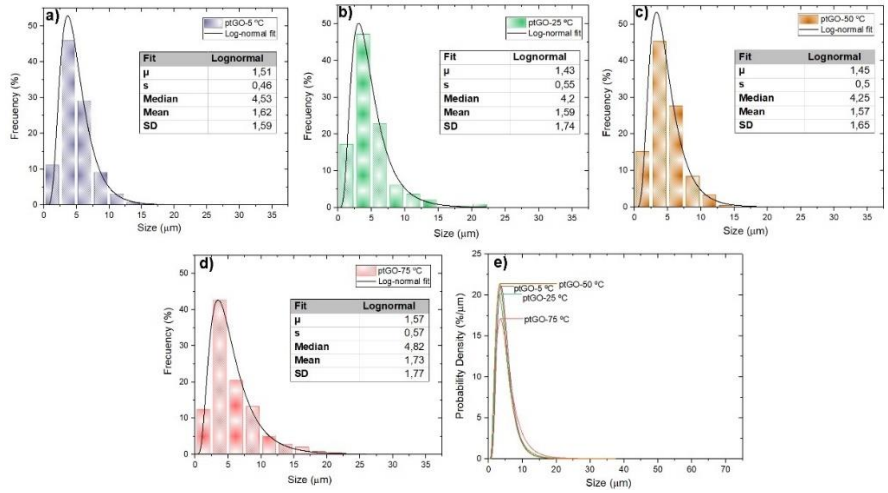

Figure 80: Size histograms of the GO flakes belonging to the post-treated samples from sample set 2, originally prepared with different reaction temperature.

UNIVERSITAT ROVIRA I VIRGILI
CHARACTERIZATION OF GRAPHENE OXIDE OBTAINED FROM MODIFICATIONS OF HUMMERS' METHOD AND ITS APPLICATION FOR REINFORCING TEXTILES
Jordi Aixart Forés

UNIVERSITAT ROVIRA I VIRGILI
CHARACTERIZATION OF GRAPHENE OXIDE OBTAINED FROM MODIFICATIONS OF HUMMERS' METHOD AND ITS APPLICATION FOR REINFORCING TEXTILES
Jordi Aixart Forés

UNIVERSITAT
ROVIRA i VIRGILI